

WARSAW UNIVERSITY OF TECHNOLOGY

DISCIPLINE OF SCIENCE - MATERIALS ENGINEERING

FIELD OF SCIENCE - TECHNICAL SCIENCES

Ph.D. Thesis

Edyta Wyszowska, M.Sc. Eng.

**Impact of radiation damage on the structural and mechanical
properties of *fcc* $\text{Ni}_x\text{Fe}_{1-x}$ single crystal alloys**

Supervisor

Łukasz Kurpaska, Ph.D. Eng., D.Sc., Assoc. Prof.

Co-supervisor

Cyprian Mieszczyński, Ph.D.

WARSAW 2025

To my beloved Husband, Daughter and Parents...

“Imagination is more important than knowledge. For knowledge is limited, whereas imagination embraces the entire world, stimulating progress, giving birth to evolution.”

Albert Einstein

“My brain is only a receiver, in the Universe there is a core from which we obtain knowledge, strength and inspiration. I have not penetrated into the secrets of this core, but I know that it exists.”

Nikola Tesla

The work presented in this thesis was supported by two granted projects obtained by the author:

- *National Science Centre (NCN) - Preludium21, 2022/45/N/ST5/02980, “Impact of radiation damage on the structural and mechanical properties of fcc $\text{Ni}_x\text{Fe}_{1-x}$ single crystal alloys”*
- *Ministry of Science and Higher Education (MNiSW) - “Young Scientist project”, 212727/E-78/M/2018, “The influence of ion irradiation on mechanical and structural changes of $\text{Ni}_x\text{Fe}_{1-x}$ single crystals”.*

Abstract

The core of a nuclear reactor experiences an extreme environment of high temperature, high stress, chemical reactivity, and intense radiation flux. In particular, the structural materials for Generation IV concept fission reactors will be subjected to exceptional fluxes of high-energy neutrons and extreme operating temperatures. One of the main consequences of the interaction of high-energy particles with materials is **the formation of lattice defects** resulting from the energy transfer to the atoms. The defects can take many forms: an atom can be kicked out from its initial lattice site, leaving an empty site (a vacancy) behind and creating an atom at an interstitial site in front, there may be defect clusters (aggregation of small defects), dislocation loops or three-dimensional defects. Importantly, **energetic ions** can be used to understand the effects of neutron irradiation in reactor components, avoiding high residual radioactivity and the decline of neutron sources for materials irradiation. As opposed to extremely costly, lengthy, and complicated neutron irradiation, ion irradiation has been widely adopted due to its low costs, short irradiation times, and controllable irradiation conditions.

Due to the structural degradation of the materials under the influence of radiation, the operating environment of a nuclear reactor requires **the use of materials with increased resistance to radiation, characterized by good mechanical and structural properties, especially at high temperatures**. Traditional construction materials are not able to withstand the extreme conditions inside the reactor, which can result in failure of their structural components. For this reason, **it is necessary to develop and characterize new materials and fundamentally understand the mechanisms of radiation defect formation**. In this context, the single-crystalline materials serve as good references, as they can be used as templates for modeling radiation resistance thanks to the uniform arrangement of atoms in the entire volume of their crystal lattice. **Single crystals allow for a fundamental understanding of the properties of materials at the electronic and atomic level and offer the possibility of tuning the properties of alloys**. By manipulating the chemical composition in single crystals, it is possible to directly influence the increased radiation resistance of the tested material.

Therefore, the aim of the presented study is to conduct a holistic analysis of the effect of radiation and Fe addition in the range from 0 to 62 at.% on the evolution of defects, microstructure, and mechanical properties using a model material such as single-crystal fcc $\text{Ni}_x\text{Fe}_{1-x}$ alloy. State-of-the-art experimental techniques, such as ion implantation and Rutherford backscatter spectrometry in channeling mode (RBS/C), were utilized to assess the

radiation resistance of the proposed materials. Then, the RBS/c spectra were fitted by Monte Carlo (MC) simulations using the McChasy code developed at the National Center for Nuclear Research (NCBJ), which allowed to determine the number of defects, their distribution, and migration within the single crystals. The RBS/C technique helped to identify the level of radiation damage for the considered compositions at a specific ion fluence. Moreover, the kinetics of defect formation was calculated based on the Multi-Step Damage Accumulation Model (MSDA). The level of radiation damage (displacement per atom) was calculated using the Stopping and Range of Ions in Matter (SRIM) program. Subsequently, studies were carried out using a scanning electron microscope equipped with a focused ion beam system (SEM/FIB) and transmission electron microscopy (TEM) to verify the types of radiation defects and their concentration/density as a function of ion fluence and iron addition. This made it possible to understand the mechanism of defect migration, their accumulation, and to distinguish between individual types of radiation defects. Additionally, a number of molecular dynamics simulations with the Large-Scale Atomic/Molecular Massively Parallel Simulator (MD-LAMMPS) were performed to understand the formation mechanisms of specific types of defects in various chemical compositions. The nanoindentation technique was used to determine the mechanical changes as a function of ion fluence, and as a function of iron addition in the initial state and after ion implantation. To verify the effect of elevated temperature, a Ni single crystal was irradiated at a temperature of $\sim 526^{\circ}\text{C}$ to determine the number of defects, depth profiles, mechanical and structural properties.

The experimental and numerical results obtained in this work **fill the gaps in the literature related to the analysis of defect formation at specific radiation damage levels and in specific chemical compositions**. Additionally, the knowledge about tuning the chemical composition in single crystals revealed by the conducted study expands the understanding of important element-specific properties that effectively mitigate radiation damage and control the material's response in extreme environments. The study also establishes basic methods, techniques, and interpretation of results obtained from the investigation of ion-irradiated Ni_xFe_{1-x} single crystals. Therefore, the study outcomes are crucial for complementing the research on new structural materials considered for the construction of advanced Generation IV Nuclear Reactors or related applications.

Keywords: fcc Ni_xFe_{1-x} single crystals, Ion channeling (RBS/c), Transmission Electron Microscopy (TEM), Radiation defects, Generation IV Nuclear Reactors, Nanoindentation, Monte Carlo Simulations

Streszczenie

Materiały konstrukcyjne przeznaczone do budowy reaktorów jądrowych IV generacji muszą sprostać wymagającym warunkom pracy takim jak: wysoka temperatura, złożone pole naprężeń czy intensywny strumień neutronów. Jedną z głównych konsekwencji oddziaływania cząstek o wysokiej energii z materiałami jest powstawanie tzw. **defektów radiacyjnych**. Tworzą się one w wyniku transferu energii przez bombardujące cząstki do struktury materiału. Defekty te mogą przybierać różne formy: atom może zostać wybity ze swojej pozycji sieciowej, pozostawiając po sobie puste miejsce (wakans) lub tworząc tzw. atom międzywęzłowy. Ponadto, pojedyncze defekty punktowe mogą aglomerować i tworzyć skupiska defektów: pętle i linie dyslokacyjne lub tzw. błędy ułożenia (ang. Stacking Fault Tetrahedra, SFT). W celu zrozumienia procesu tworzenia się defektów w materiale wykorzystuje się **defektowanie strumieniem jonów**. Technika ta pozwala na wytworzenie defektów radiacyjnych podobnych z generowanymi przez promieniowanie neutronowe, nie powodując aktywacji próbki. Metoda ta jest znacznie tańsza od klasycznego napromieniowywania w reaktorze i oferuje szybki proces tworzenia się defektów radiacyjnych.

W związku z degradacją struktury materiałów w wyniku promieniowania, środowisko pracy reaktorów jądrowych wymaga **zastosowania materiałów o zwiększonej odporności na promieniowanie, charakteryzujących się dobrymi własnościami mechanicznymi w wysokich temperaturach i stabilnością strukturalną**. Tradycyjne materiały konstrukcyjne nie są w stanie sprostać ekstremalnym warunkom panującym w reaktorze, grożąc awarią jego elementów konstrukcyjnych. Z tego powodu konieczne jest opracowywanie i charakteryzacja nowych materiałów oraz fundamentalne zrozumienie mechanizmów tworzenia się defektów radiacyjnych, które odpowiadają za powstałe zmiany właściwości funkcjonalnych. Dobrym przykładem są materiały monokrystaliczne, które ze względu na uporządkowanie atomów w całej objętości sieci krystalicznej mogą posłużyć, jako wzorzec do modelowania odporności radiacyjnej. **Monokryształy pozwalają na fundamentalne zrozumienie własności materiałów na poziomie interakcji elektronów i atomów oraz oferują możliwość dostrajania właściwości stopów**. Poprzez manipulację składem chemicznym w monokryształach, można bezpośrednio wpłynąć na zwiększenie odporności radiacyjnej badanego materiału.

Mając na uwadze wymienione aspekty, celem prowadzonych w niniejszej pracy badań jest przeprowadzenie holistycznej analizy wpływu promieniowania oraz dodatku Fe w zakresie od 0 do 62% at. na ewolucję defektów, mikrostruktury i właściwości mechanicznych wykorzystując monokrystaliczne stopy fcc Ni_xFe_{1-x}. Do oceny odporności radiacyjnej proponowanych materiałów

zostały wykorzystane techniki eksperymentalne, takie jak defektowanie strumieniem jonów, spektrometria z rozpraszaniem wstecznym Rutherforda w trybie kanałowania (RBS/C). Następnie widma RBS/c zostały dopasowane za pomocą symulacji Monte Carlo (MC) wykorzystując kod McChasy rozwijany w Narodowym Centrum Badań Jądrowych (NCBJ). Kinetyka, powstawania defektów radiacyjnych, została zbadana na podstawie modelu MSDA. Poziom zniszczeń radiacyjnych (ang. displacement per atom) został obliczony przy użyciu programu Stopping and Range of Ions in Matter (SRIM). Dodatkowo przeprowadzono badania z wykorzystaniem skaningowego mikroskopu elektronowego wyposażonego w system zogniskowanej wiązki jonów (SEM/FIB) oraz transmisyjnej mikroskopii elektronowej (TEM) w celu weryfikacji typów defektów radiacyjnych i ich koncentracji/gęstości w funkcji fluencji jonów oraz dodatku żelaza. Pozwoliło to zrozumieć mechanizm migracji defektów, ich akumulacji oraz rozróżnić poszczególne typy defektów radiacyjnych. Ponadto wykonano szereg symulacji z wykorzystaniem dynamiki molekularnej (MD-LAMMPS) w celu zrozumienia mechanizmów tworzenia się konkretnych typów defektów w różnych składach chemicznych na poziomie atomowym. Wykonano również szereg testów nanomechanicznych. W tym celu wykorzystano technikę nanoindentacji, która pozwoliła określić zmiany twardości w funkcji fluencji jonów, a także w funkcji dodatku żelaza w stanie wyjściowym oraz po implantacji jonowej. W celu weryfikacji wpływu podwyższonej temperatury na badane materiały wykorzystano wysokotemperaturowe defektowanie strumieniem jonów w temperaturze $\sim 526^\circ\text{C}$ na przykładzie monokryształu Ni, w celu określenia liczby defektów, profili głębokości, własności mechanicznych oraz strukturalnych.

Przedstawione w niniejszej pracy wyniki eksperymentalne i numeryczne **uzupełniają braki literaturowe** związane z analizą powstawania defektów **przy konkretnych poziomach zniszczeń radiacyjnych oraz w danych składach chemicznych**. Ponadto wiedza na temat dostrajania składu chemicznego w monokryształach poszerza zrozumienie istotnych właściwości, specyficznych dla danego pierwiastka, które skutecznie łagodzą uszkodzenia radiacyjne i kontrolują reakcję materiału w ekstremalnych środowiskach. Rezultaty niniejszej pracy pozwalają również ustalić podstawowe metody, techniki i sposób interpretacji wyników badań monokryształów $\text{Ni}_x\text{Fe}_{1-x}$ napromieniowanych jonami. Przedstawione rezultaty są, zatem kluczowe w uzupełnieniu badań nowych materiałów konstrukcyjnych, rozważanych do użycia w zaawansowanych koncepcjach Reaktorów Jądrowych IV Generacji, jak również w innych, powiązanych zastosowaniach.

Słowa kluczowe: Monokryształy fcc $\text{Ni}_x\text{Fe}_{1-x}$, Kanałowanie jonów (RBS/C), Transmisyjny Mikroskop Elektronowy (TEM), Defekty radiacyjne, Reaktory Jądrowe IV Generacji, Nanoindentacja, Symulacje Monte Carlo.

Table of Contents

ABSTRACT	7
STRESZCZENIE	9
TABLE OF CONTENTS	11
LIST OF ACRONYMS.....	14
THESIS STRUCTURE	15
CHAPTER 1 BACKGROUND.....	17
1.1 INTRODUCTION	17
1.2 STRUCTURAL MATERIALS FOR NUCLEAR APPLICATIONS – CHALLENGES	19
1.3 RADIATION DAMAGE EVENT	21
1.4 RADIATION DAMAGE IN METALS.....	22
1.4.1 Radiation-induced defects	22
1.4.2 Irradiation-induced hardening.....	27
1.5 APPLICATION OF THE ION IMPLANTATION TECHNIQUE TO SIMULATE NEUTRON RADIATION	29
CHAPTER 2 STATE OF THE ART.....	31
2.1 INTRODUCTION	31
2.2 THE NEW CLASS OF SP-CSAs	31
2.2.1 Fcc Ni-Fe solid-solution model system	32
2.3 TUNABLE CHEMICAL AND PHYSICAL PROPERTIES IN CONCENTRATED ALLOYS	33
2.3.1 Electronic level properties.....	35
2.3.2 Atomic level properties.....	36
2.3.3 Point defect energetics in SP-CSAs alloys.....	36
2.4 DEFECT FORMATION AND EVOLUTION IN SP-CSAs	38
2.4.1 Point defect and defect clusters	40
2.5 SUMMARY OF THE STATE OF THE ART	41
CHAPTER 3 THESIS GOALS	42
3.1 MOTIVATION	42
3.2 HYPOTHESES.....	42
3.3 OBJECTIVES	43
3.4 SCOPE	44
CHAPTER 4 METHODS	45
4.1 EXPERIMENTAL TECHNIQUES.....	45
4.1.1 Ion irradiation.....	45
4.1.2 Rutherford Backscattering Spectrometry (RBS).....	46
4.1.3 Nanoindentation.....	49
4.2 SIMULATIONS	50
4.2.1 Stopping and Range of Ions in Matter (SRIM)	50
4.2.2 Monte Carlo simulations of RBS spectra; McChasy program	52
4.2.3 Molecular Dynamic Simulations (MD)	52
4.2.4 Hybrid MC/MD simulations	54
4.3 MULTI-STEP DAMAGE ACCUMULATION (MSDA) MODEL	54
CHAPTER 5 DESCRIPTION OF PUBLISHED ARTICLES IN THE THESIS'S CONTEXT	57
5.1 ARTICLE A'S DESCRIPTION	57
5.2 ARTICLE B'S DESCRIPTION.....	58
5.3 ARTICLE C'S DESCRIPTION.....	59
5.4 ARTICLE D'S DESCRIPTION	60
5.5 ARTICLE E'S DESCRIPTION	61
5.6 SUMMARY.....	62

ARTICLE A: TUNING HETEROGENEOUS ION-RADIATION DAMAGE BY COMPOSITION IN Ni_xFe_{1-x} BINARY SINGLE CRYSTALS	63
A.1 ABSTRACT	64
A.2 INTRODUCTION	64
A.3 EXPERIMENT AND METHODS	66
A.3.1 <i>Single crystal production and sample preparation</i>	66
A.3.2 <i>Ion irradiation</i>	66
A.3.3 <i>RBS/C measurements and simulations</i>	67
A.3.4 <i>Nanoindentation</i>	68
A.3.5 <i>TEM defect characterization</i>	68
A.4 RESULTS	68
A.4.1 <i>RBS/C analysis and simulations</i>	68
A.4.2 <i>Irradiation-induced hardening</i>	73
A.5 DISCUSSION	75
A.6 CONCLUSIONS	82
ARTICLE B: THE FE ADDITION AS AN EFFECTIVE TREATMENT FOR IMPROVING THE RADIATION RESISTANCE OF FCC Ni_xFe_{1-x} SINGLE-CRYSTAL ALLOYS	83
B.1 ABSTRACT	84
B.2 INTRODUCTION	84
B.3 MATERIAL AND METHODS	87
B.3.1 <i>Material Production and Sample Preparation</i>	87
B.3.2 <i>Ion Irradiation</i>	87
B.3.3 <i>RBS/C (ion channeling) and MSDA model</i>	88
B.3.4 <i>Hybrid MC/MD simulation</i>	89
B.3.5 <i>Nanoindentation</i>	90
B.3.6 <i>TEM Analysis</i>	90
B.4 RESULTS	91
B.4.1 <i>RBS/C channeling</i>	91
B.4.2 <i>Damage kinetics</i>	94
B.4.3 <i>Mechanical properties</i>	95
B.4.4 <i>Hybrid MC/MD simulation</i>	98
B.5 CONCLUSIONS	105
ARTICLE C: NANOSCALE DEFECT FORMATION IN FCC NI AND LOW FE CONTENT Ni_xFe_{1-x} SINGLE CRYSTALS UNDER SELF-ION IRRADIATION	107
C.1 ABSTRACT	108
C.2 INTRODUCTION	108
C.3 EXPERIMENTS AND METHODS	110
C.3.1 <i>Ion Irradiation and SRIM Calculations</i>	110
C.3.2 <i>Computational modeling</i>	111
C.3.3 <i>RBS/C (ion channeling) and Multi-step damage accumulation (MSDA) model</i>	113
C.3.4 <i>TEM analysis</i>	114
C.4 RESULTS	114
C.4.1 <i>Computational modeling</i>	114
C.4.2 <i>The Multi-step damage accumulation (MSDA) model</i>	116
C.4.3 <i>TEM analysis</i>	118
C.5 DISCUSSION	121
C.5.1 <i>Defects evolution under irradiation</i>	121
C.5.2 <i>Defect formation mechanisms</i>	125
C.6 CONCLUSIONS	131
ARTICLE D: COMBINING MD-LAMMPS AND MC-MCCHASY2 CODES FOR DISLOCATION SIMULATIONS OF NI SINGLE CRYSTAL STRUCTURE	135
D.1 ABSTRACT	136
D.2 INTRODUCTION	136

D.3 METHODS.....	138
D.4 RESULTS AND DISCUSSION	140
<i>D.4.1 Atomic Positions Given by External Codes</i>	<i>140</i>
<i>D.4.2 Challenges – Atomic Positions from MD-Relaxed Structure.....</i>	<i>142</i>
<i>D.4.3 Challenges – MERGING Procedure.....</i>	<i>143</i>
<i>D.4.4 Monte Carlo Simulations.....</i>	<i>144</i>
D.5 CONCLUSIONS	146
ARTICLE E: DAMAGE KINETICS IN HIGH-TEMPERATURE IRRADIATED NI CRYSTALS.....	149
E.1 ABSTRACT	150
E.2 INTRODUCTION	150
E.3 MATERIAL AND METHODS	152
<i>E.3.1 Sample preparation</i>	<i>152</i>
<i>E.3.2 Experimental techniques</i>	<i>154</i>
<i>E.3.3 Simulation methods.....</i>	<i>155</i>
E.4 RESULTS AND DISCUSSION	157
<i>E.4.1 TEM results</i>	<i>157</i>
<i>E.4.2 Nanomechanical results</i>	<i>159</i>
<i>E.4.3 RBS/c simulations and MSDA using McChasy-1</i>	<i>161</i>
<i>E.4.4 RBS/C simulations using McChasy-2.....</i>	<i>163</i>
E.5 CONCLUSIONS.....	165
CHAPTER 6 CONCLUSIONS.....	167
6.1 SUMMARY OF OBTAINED RESULTS	167
6.2 THESIS VERIFICATION	171
6.3 FUTURE WORKS.....	172
REFERENCES	175
LISTS OF FIGURES	183
LISTS OF TABLES	184
ACKNOWLEDGMENTS	185
SCIENTIFIC ACHIEVEMENTS	186
SCIENTOMETRIC DATA	186
LISTS OF SCIENTIFIC PUBLICATIONS CONSTITUTING THE SUBJECT OF THE DOCTORAL DISSERTATION:.....	186
SCIENTIFIC PUBLICATIONS NOT INCLUDED IN THE SCOPE OF THE DOCTORAL DISSERTATION:	186
CONFERENCE PRESENTATIONS.....	188
DISTINCTIONS	190
CURRICULUM VITAE.....	190

List of acronyms

AES - Auger electron spectroscopy
APT - atom probe tomography
CCAs - complex concentrated alloys
DAF - diamond area function
DPA - displacements per atom
EAM - Embedded Atom Method
FCC - face centered cubic
FIB - focused ion beam
FIRE - Fast Inertial Relaxation Engine
HEAs - high entropy alloys
HTGR - High Temperature Gas Cooled Reactor
LAMMPS - large-scale atomic/molecular massively parallel simulator
MC simulations - Monte Carlo simulations
MD simulations - Molecular Dynamics simulations
MEAs - medium-entropy alloys
MSDA model – Multi-Step Damage Accumulation model
MNiSW - Ministry of Science and Higher Education
NCBJ - Narodowe Centrum Badań Jądrowych
NCN - National Science Centre
NEP - nuclear encounter probability
PKA - primary knock on atom
PDL - prismatic dislocation loops
RBS/C - Rutherford backscattering spectrometry in channeling mode
RDA - randomly displaced atoms
RPV - Reactor Pressure Vessel
RIP - radiation-induced precipitation
RIS - radiation-induced segregation
SCC - stress corrosion cracking
SEM - scanning electron microscope
SFT - stacking fault tetrahedron
SIAs - self-interstitial atoms
SP-CSAs - single phase concentrated solid solution alloys
SRIM - stopping and range of ions in matter
SCWR - Super Critical Water Reactor
TEM - transmission electron microscope
TMs - transition metals
VHTR - Very High Temperature Reactor
XRD - x-ray diffraction
ZBL - Ziegler-Biersack-Littmark

Thesis structure

This dissertation is elaborated in the form of a compendium of articles. Its core consists of five published interrelated scientific articles denoted with letters A-E, accompanied by six chapters denoted with numbers 1-6, which present the overall context of the thesis. The content of the chapters and articles is briefly described below:

- **Chapter 1** discusses the contemporary challenges associated with designing materials for nuclear applications, introducing the issues related to the formation of radiation defects and their influence on material properties. It also presents factors justifying the use of ion irradiation over neutron irradiation.
- **Chapter 2** describes the state of the art regarding single-phase concentrated solid-solution alloys (SP-CSSAs), including an explanation of their unique properties resulting from their atomic and electronic structure and how this relates to the radiation response of these materials. The choice of NiFe single-phase alloys as the subject of the dissertation is justified.
- **Chapter 3** outlines the motivation, hypotheses and specific objectives of the thesis, as well as the scope of the conducted research.
- **Chapter 4** describes the methods used in the conducted research, covering the explanation of lesser-known experimental techniques and simulations, as well as the models that enable the study of defect formation kinetics.
- **Chapter 5** provides a brief description of the five published articles in the context of the research hypotheses, in order to facilitate the understanding of their essence and the interpretation of the obtained results (descriptions are provided in Polish).
 - **Article A** – presents the results of the first published work from a series of five publications. In this work, the addition of Fe to Nickel in the proportions of 38% at and 62% is assessed in the context of the radiation resistance. Fcc Ni, Ni_{0.62}Fe_{0.38} and Ni_{0.38}Fe_{0.62} single crystals were irradiated over a wide fluence range (4×10^{13} to 4×10^{15} ions/cm², from 0.1 to 12 dpa) at room temperature. The irradiation-induced defect evolution has been studied using RBS/C spectrometry, MC simulations, TEM, and nanoindentation.
 - **Article B** describes five different compositions of *fcc* Ni and Ni_xFe_{1-x} single crystal alloys, namely Ni, Ni_{0.88}Fe_{0.12}, Ni_{0.77}Fe_{0.23}, Ni_{0.62}Fe_{0.38}, Ni_{0.38}Fe_{0.62} subjected to ion irradiation at room temperature in a wide fluence range (4×10^{13} to 4×10^{15} ions/cm², from

- 0.1 to 12 dpa). The role of Fe addition on the radiation resistance of the Ni_xFe_{1-x} single crystals has been studied by hybrid Monte Carlo / Molecular dynamics simulations combined with transmission electron microscopy (TEM), ion channeling technique (RBS/C), and nanoindentation techniques.
- **Article C** demonstrates the role of Fe content in its low range (0, 12, and 23 at.%) on the defect formation morphology in Ni_xFe_{1-x} fcc single crystals subjected to self-ion irradiation at room temperature in a wide fluence range corresponding to damage of 0.1-12 displacements per atom (dpa). The samples were analyzed using the RBS/C technique combined with TEM, with the aim of distinguishing different types of defects and calculating damage kinetics based on the MSDA model. Moreover, an overlap collision cascade method based on the molecular dynamics approach was used to simulate the early-stage formation of irradiation-induced defects in these materials.
 - **Article D** refers to the unique capability of the new version of the McChasy code (called McChasy2) to provide the possibility to simulate experimental energy spectra delivered by RBS/C in channeling direction using large atomic structures (ca. 10⁸ atoms). The extended defect models were created using ATOMSK and the MD-LAMMPS thermalization process. The models were then used to create virtual samples and fit experimental RBS/C spectra.
 - **Article E** describes structural and mechanical properties changes of nickel single crystals subjected to high-temperature irradiation (~800 K) with 380 keV using Ar ions. The implantation ion fluence ranged from 1×10¹⁴ cm⁻² up to 1×10¹⁶ cm⁻² (i.e. from 0.25 to 25 dpa). The structural characteristics were performed by RBS/C associated with SEM and TEM. The experimental results were supported by MC and MD-LAMMPS simulations and by nanoindentation.
 - **Chapter 6** summarizes the obtained results, discusses the verification of the hypotheses and discusses further research plans.

Chapter 1

Background

In this chapter, the context of the conducted research is presented. Firstly, the contemporary challenges associated with designing materials for nuclear applications are introduced. Next, the issues related to the formation of radiation defects, their types, and their impact on material properties are explained. Finally, the factors justifying the use of ion irradiation over neutron irradiation are discussed.

1.1 Introduction

The core of a nuclear reactor experiences extreme environments of high temperature, high stress, chemical reactivity, and intense radiation flux. In particular, the structural materials for Generation IV concept fission reactors will be subjected to exceptional fluxes of high-energy neutrons and extreme operating temperatures ^{1,2}. Besides the nuclear applications, materials requiring high radiation resistance are also needed for high-energy accelerators, such as the next-generation high-power rare isotope beam facilities ³. Highly focused, high-energy ion pulses create high-energy deposition densities in target materials and other accelerator components, leading to changes in structure, thermo-mechanical properties, and reduced lifetimes ^{4,5}.

One of the main consequences of irradiating high-energy particles (electrons, ions, neutrons, protons, etc.) onto materials is the lattice damage in the form of defects resulting from the energy transfer to the atoms. The lattice defects are formed during irradiation due to the knock-off of atoms from their lattice sites, creating vacancies and interstitials. Other consequences include the production of non-damage-producing phonons, excitons, and plasmons, secondary electrons and photons, and heating of the material. The irradiation-induced damage can be categorized into two stages, namely primary and secondary damage. The primary damage occurs immediately (within a few picoseconds) after ion/neutron/electron impact by atomic collision processes far from thermodynamic equilibrium ⁶. The secondary damage is a long-timescale (nanoseconds to years) evolution caused by thermally activated processes ⁶. During the secondary damage stage, the crystal defects evolve into more complex microstructural

features, including defect clusters, amorphous zones, dislocation loops, and three-dimensional defects such as voids and bubbles (Figure 1). The damage can also manifest as craters and ripples on surfaces.

Radiation damage in crystalline metallic metals has been studied extensively for decades. The primary purpose of this was to control the degradation of fission reactor materials induced by neutron irradiation. Three competing processes can describe the evolution of radiation-induced defect concentrations in metals across the primary and secondary damage stages: (i) defect production from atomic collision cascades; (ii) subsequent vacancy-interstitial recombination within the diffusion volume; and (iii) point defect absorption by different types of sinks such as dislocations and grain and phase boundaries ⁷. The point defects that survive recombination and sink absorption may cause different effects. For example, defects may migrate into the bulk material, grain boundaries or to the surface at a high level of mechanical stress induced by ion irradiation. This can result in an extended damage region due to enhanced defect migration with increasing ion fluence. Thus, point defects can diffuse and subsequently generate dislocation loops ⁸, and SFT under the stress gradient, depending on the material.

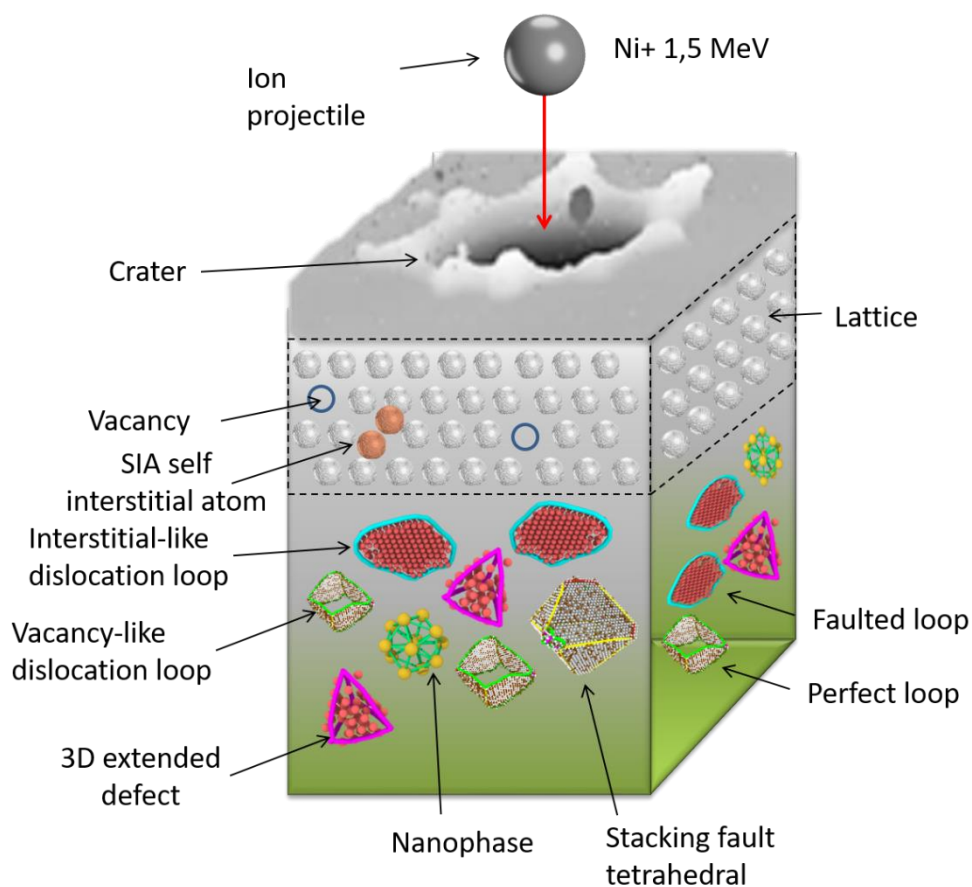


Figure 1. Structure degradation during irradiation of Ni and $\text{Ni}_x\text{Fe}_{1-x}$ single crystal – different radiation-induced defects.

Additionally, the formation of large vacancy clusters significantly deteriorates the performance of materials, as vacancies may lead to void swelling. Therefore, controlling vacancy cluster migration and effectively annihilating vacancies is crucial in selecting new advanced structural materials for nuclear applications^{9–11}. Hence, it is critical to understand the defect dynamics; however, research focused on enhancing defect recombination and controlling defect migration¹² in metallic alloys is scarce. There is evidence that tuning the chemical composition of a single-phase alloy may significantly change the features of defect clusters⁸, which warrants further elaboration.

Furthermore, the defect clusters may lead to macroscopically observable degradation effects, such as irradiation hardening, embrittlement, and irradiation-induced creep. These phenomena adversely affect materials used in advanced Generation IV fission and fusion reactors. This is because the materials are subjected to harsh operating conditions such as temperatures greater than 600°C, radiation fluences of more than 50 displacements per atom (dpa), high-mechanical stresses, and corrosive environments^{1,13,14}. Conventional metal alloys, such as ferritic and austenitic stainless steel, fail under such reactor conditions due to the aforementioned effects. Thus, the selection of new materials needs special attention for high radiation tolerance in a high fluence scope, high thermal and phase stabilities, and high mechanical properties⁹. Several articles and reports have described materials for advanced reactors^{2,10,13,15–18}; however, it is still an emerging research field with great scope for exploration. Hence, the research objective is to develop novel metallic alloys for advanced nuclear reactor structural material applications and assessing them to understand defect dynamics and mechanical properties.

1.2 Structural materials for nuclear applications – challenges

The energetic neutrons produced by the nuclear fission and fusion reactions have sufficient kinetic energy to displace significant numbers of atoms in structural materials from their lattice locations over the expected life of the reactors, creating defects associated with the missing lattice atoms (vacancies) and the moved atoms that reside in the lattice interstices (*self-interstitial atoms, SIAs*)¹⁴. The amount of radiation damage resulting from these ballistic collisions is quantified in terms of *displacements per atom, dpa*. Therefore, dpa is widely used as an exposure unit to predict the operating lifetime of materials in radiation environments. It determines the number of times that an atom is displaced for a given fluence. For instance, a damage level of 1 dpa corresponds to “stable” displacement of every atom from its position in the lattice site once during the lifetime of the material¹⁴. When designing radiation-resistant

materials, efforts should be made to effectively eliminate defects in the material structure. Unfortunately, we are unable to completely avoid damage to the material caused by neutron radiation; however, we can design the material in such a way as **to significantly increase its radiation resistance**, effectively facilitating the recombination of defects. The biggest challenge is to design a "self-healing" defect recombination process in construction materials with an extremely high efficiency e.g. ~99.99%. This is particularly necessary for the materials devoted to Gen. IV nuclear reactors applications, where they which will be exposed to damage exceeding 100 dpa. The next challenge is that these designed defect recombination structures must be resistant to the vigorous transient (~1 fs to 1 ps) atomic mixing that occurs within fast neutron-induced displacement cascades ¹⁴.

Radiation damage poses **five main risks** to the performance of construction materials, which occur at varying operating temperatures and damage levels. **First, at low temperatures** where, radiation-induced defect clusters serve as strong obstacles to dislocation motion. This *causes radiation hardening in materials*, which is usually accompanied by significant reductions in uniform elongation and macroscopic work hardening capacity ¹⁹. Because the radiation-induced hardening occurs at relatively low doses (0.001 to 0.1 dpa), radiation hardening and embrittlement often provide a lower limit for the operating temperature of structural materials in neutron irradiation environments. **At intermediate temperatures**, we are dealing with three phenomena that occur for doses between ~1 to 10 dpa:

- radiation-induced segregation and precipitation that can lead to localized corrosion or mechanical property degradation,
- void swelling from vacancy accumulation that can create unacceptable volumetric expansion,
- radiation-induced creep and/or anisotropic growth (that can produce dimensional expansion along directions of high stress and/or specific crystallographic directions) ¹⁴.

At very high temperatures and under applied mechanical stress, helium produced by neutron transmutation reactions in the structural material can migrate to grain boundaries and form cavities, thus causing ductility-limited intergranular cracking in materials subjected to stress. This high-temperature *helium grain boundary embrittlement* typically occurs for helium concentrations above 10 to 100 appm (~1 to 100 dpa, depending on material and neutron spectrum) and becomes increasingly severe with increasing temperature, applied stress, and decreasing deformation rate ¹⁴. In addition to chemical compatibility and thermal creep strength,

high-temperature embrittlement of helium may determine the maximum acceptable operating temperature for a structural material in neutron irradiation environments.

For advanced Generation IV reactors, the performance and integrity of construction materials are critical. Although the chosen material may be a different alloy (or ceramic), the material must still have well-established and efficient mechanical properties (including good thermal creep resistance), long-term phase stability, and reactor coolant compatibility^{14,20}. As the materials could be used in an intense high-energy neutron field, they must exhibit good dimensional, mechanical, and microstructural stability to neutron displacement damage. The radiation-resistance assessment is often the most difficult requirement to evaluate because the key degradation mechanisms are sensitive to the specific radiation conditions. Figure 2 compares the proposed operating temperatures and lifetime displacement damage levels for structural materials in the six Generation IV concepts and three fusion energy systems with the existing knowledge base¹⁴.

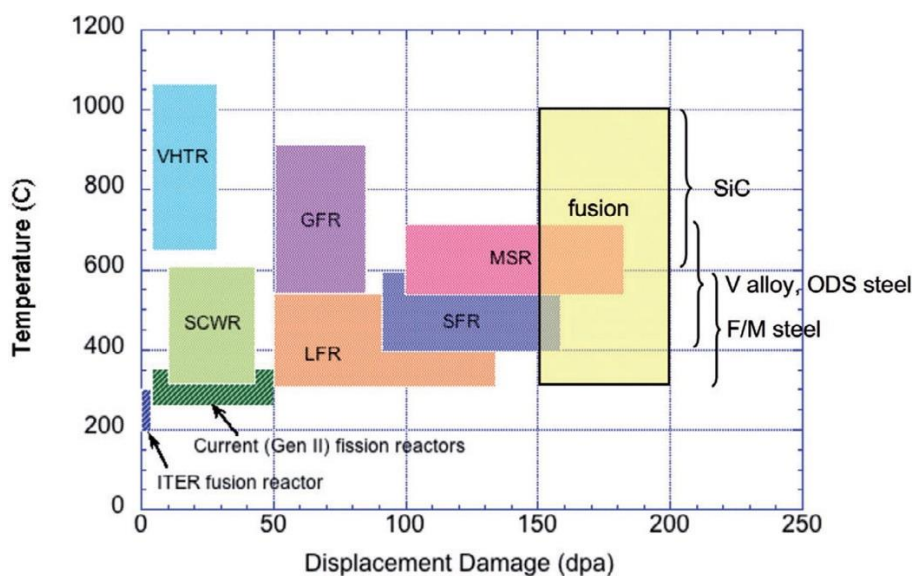


Figure 2. Operating temperatures and displacement damage dose regimes for structural materials in current (generation II) and proposed future (Generation IV) fission and fusion energy systems¹⁴.

1.3 Radiation damage event

The radiation damage event is composed of several distinct processes, which are as follows:

- The interaction of an energetic incident particle with a lattice atom.
- The transfer of kinetic energy to the lattice atom, giving rise to a primary knock on atom (PKA).
- The displacement of the atom from its lattice site.

- The passage of the displaced atom through the lattice and the concomitant formation of additional knock-on atoms.
- The creation of a displacement cascade (a set of point defects created by the PKA).
- The expiration of the PKA as an interstitial.

The radiation damage event ends when the PKA is retained in the lattice as an interstitial. The result of a radiation damage event is the creation of a set of point defects (vacancies and interstitials) and clusters of these defects in the crystal lattice. Subsequent events involving the migration of the point defects and defect clusters, and additional clustering or dissolution of the clusters are classified as *radiation damage effects* ²¹.

1.4 Radiation damage in metals

Radiation damage is inevitable and occurs in all materials. However, in this work I will focus on the interaction of radiation with metals. Energetic particles can affect a metal in two ways: first, through **displacement damage production**, where lattice atoms are removed from their regular lattice sites, and secondly, where the chemical composition of the target can be changed by ion implantation or transmutation, notably helium production via (n, α) reactions. This second aspect of radiation damage is particularly important for the nucleation of secondary defects. During the displacement damage, an atom can be displaced from its position if it receives a high enough energy: a vacancy is left at the place previously occupied by the recoiling atom, which becomes an interstitial atom. The minimum energy transfer for an atom to be displaced in a bulk crystal is called the **threshold displacement energy, E_d**; in most crystals, its value is about **25 eV**, i.e. several times higher than the sum of the formation energies of 1 vacancy plus 1 interstitial because this Frenkel pair formation is highly irreversible ²².

1.4.1 Radiation-induced defects

During the analysis of the irradiation effects in materials, it is crucial to understand, on the atomic level, **the nature of radiation damage**. The recoiling lattice atom moves through the crystal, colliding with its neighbors and displacing them from their sites. A cascade of atomic collisions is created by the original particle with the result being a number of vacant lattice sites and an equal number of displaced atoms wedged into the interstices of the lattice. The basic defects (vacancies and interstitials) form the foundation for all observed effects of irradiation on the physical and mechanical properties of materials.

We distinguish the following types of defects:

- Point defects (0D): vacancies and interstitials.
- Line defects (1D): dislocation lines (screw dislocation, edge dislocation).
- Planar defects (2D): dislocation loops.
- Volume defects (3D): voids, bubbles, stacking fault tetrahedral ²¹.

An example of several irradiation-induced defects is schematically presented in Figure 3.

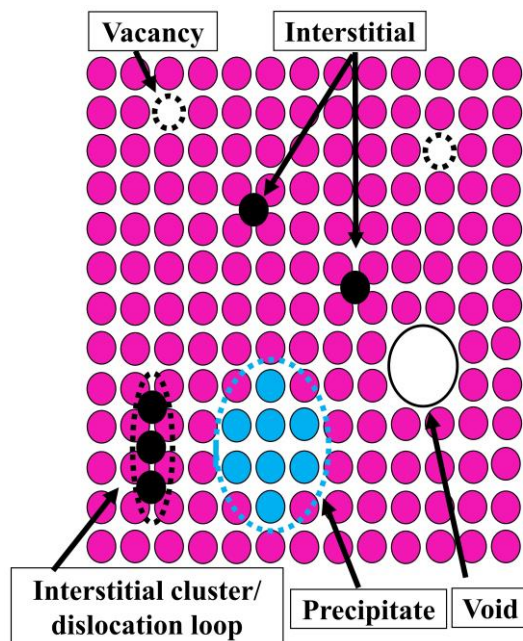


Figure 3. Schematic representation of several irradiation induced-defects (vacancy, interstitial, dislocation loop, precipitate, void).

Interstitials

Interstitial atom is an atom occupying a position outside the nodes of the crystal lattice. It is a type of point defect in the crystal lattice. The interstitial atom can be either a native atom or an impurity atom. The existence of such defects in crystal structures is the cause of two important diffusion mechanisms in solids: direct and indirect interstitial. Stable configuration of self-interstitial atoms (SIA) in metals is the **dumbbell** or **split-interstitial** configuration, where two atoms are associated with or “share” a single lattice site. Since the atom cores repel each other, the atoms arrange themselves in the lowest energy orientation. This turns out to be the case with dumbbell axis along the $\langle 100 \rangle$ direction for fcc metals, the $\langle 110 \rangle$ direction for bcc metals and the $\langle 0001 \rangle$ direction for hcp crystals ²¹.

Multiple interstitials form by the agglomeration of mobile SIAs at elevated temperatures and have a high binding energy approximately 1eV. Since the energy needed to dissociate a SIA from a large cluster approaches the SIA formation energy (2–4eV), SIA clusters are very stable

against dissociation at low temperatures. Impurity atoms in metals are **efficient traps for SIAs**. Stable complexes consisting of undersized atoms and interstitials do not dissociate thermally below a temperature where vacancies become mobile. One possible configuration is the mixed dumbbell, where one of the dumbbell atoms is replaced by the impurity atom. Binding energies are of the order of 0.5–1.0 eV. Weaker trapping is observed with oversized impurities. Interstitial–impurity complexes require only a small activation energy to reorient themselves by so-called cage motion. The impurity can jump between the indicated positions of the central octahedron, forming a new mixed dumbbell with the adjacent host atom. Since all of the mixed dumbbells have the impurity end toward the center of the cage, no long-range motion is associated with cage motion. The activation energy of the re-orientation jump in the cage is about 0.01 eV ²¹.

Vacancies

The vacancy, or missing lattice atom, is the simplest point defect in metal lattices. All calculations and computer simulations show that the single vacancy structure is a missing lattice atom with the nearest neighbors relaxing inward toward the vacancy. SIAs have a high formation energy (>2.0eV), a large relaxation volume (~2Ω) and a low migration energy (< 0.15eV) leading to a high mobility. Vacancies, on the other hand, have low formation energies (< 2eV), low relaxation volume (0.1–0.5Ω) and high migration energy (>0.5eV) and are therefore much less mobile than SIAs ²¹.

It is worth mentioning that atoms in a lattice are in a constant motion due to thermal vibration, which means that point defects in the lattice are also in motion. The random nature of thermal vibration gives rise to a random walk of the atoms via the defects that are in thermal equilibrium with their surroundings, known as self-diffusion. If foreign atoms are present in a pure metal, their diffusion is known as hetero-diffusion. Self-diffusion arises when a local concentration gradient of defects appears in the crystal, driving atoms to move in the direction that eliminates the gradient. Forces other than the concentration gradient, such as stress or strain, electric fields, temperature, etc. drive diffusion.

Dislocation lines

The dislocation line is the line where part of the lattice is shifted or distorted. The two basic types of dislocations lines are the **edge** and the **screw**. In an edge dislocation, atoms over the cut surface are shifted in a direction perpendicular to the dislocation line. An edge dislocation occurs due to the introduction or elimination of an extra row of atoms. In this dislocation,

Burger's vectors always perpendicular to the dislocation line. In a screw dislocation, the atoms over the cut surface are shifted in a direction parallel to the dislocation line.

Stacking fault tetrahedral

SFT is another dislocation configuration that can form in irradiated metals. A three-dimensional stacking fault configuration is in the shape of a tetrahedron. SFTs are believed to evolve directly from vacancy clusters produced in cascades or to evolve from Frank loops²³. It is the most common type of irradiation-induced defects in the Ni-based alloys^{24,25}. The lower stacking fault energy results in a larger tetrahedron in various alloys²⁶.

Dislocation loops

Dislocation loops resulting from vacancies and interstitial condensation arise from clusters of corresponding defects and either shrink or grow depending on the flux of defects reaching the embryo. Once a critical size is reached, the loops become stable and grow until they are damaged/changed by interactions with other loops leading to their high dislocation density increase in the lattice²³.

Voids

Can have a significant effect on material properties because solids undergo volumetric swelling as voids form and grow. The driving force behind the formation of voids in solids is the supersaturation of vacancies due to irradiation. During irradiation, defects react to form clusters that either grow by absorbing defects of the same type or shrink by absorbing defects of the opposite type. For a vacancy cluster to become a void, there must be a net increase in the number of vacancies relative to the number of interstitials absorbed²³. Void swelling should be inhibited by adding fine elements that bind the voids or interstitial spaces with sufficient strength to reduce the effective mobility, thereby preventing defects from entering the sinks and promoting recombination²³. For example, in the case of simple austenitic Fe–Cr–Ni alloys, the swelling decreases rapidly with increasing nickel content, reaching a minimum at about 50 at%. The effect of Ni content on swelling is mainly due to the change in the incubation dose, as shown in the Figure 4²³.

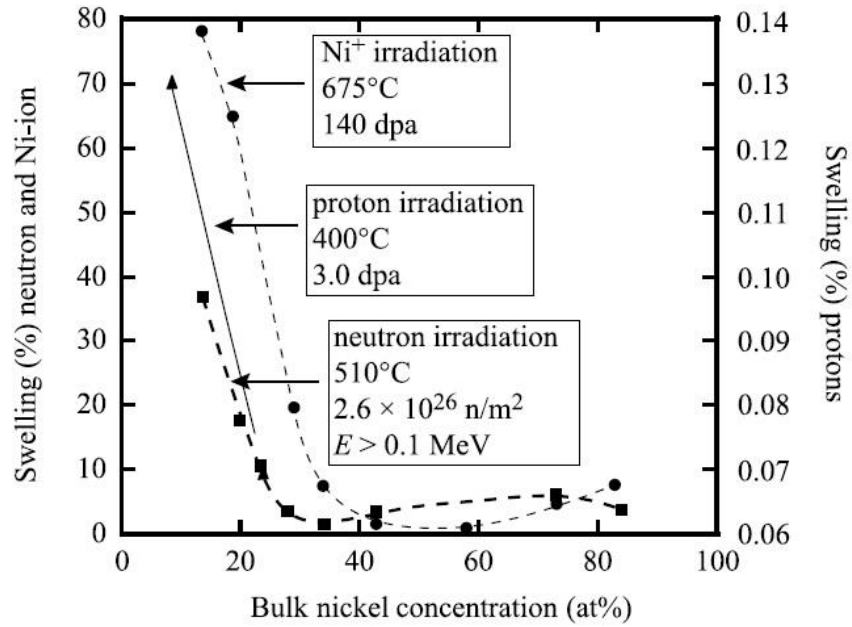


Figure 4. The effect of bulk nickel concentration on swelling resulting from irradiation with different particles: neutrons, nickel ions and protons²³.

More examples of void swelling in pure Ni and Ni-Fe alloys can be found in^{27,28}.

Bubbles

Under the influence of irradiation, a large number of inert gas bubbles can be formed, which significantly change the physical and mechanical properties of metals. Fast reactors and thermal reactors produce helium by transmutation, and the first wall of a fusion reactor is prone to bubble formation due to the high gas loading from the reaction products in the plasma. An example of bubbles formed during high-temperature irradiation in a pure Ni single crystal is shown in Figure 5.

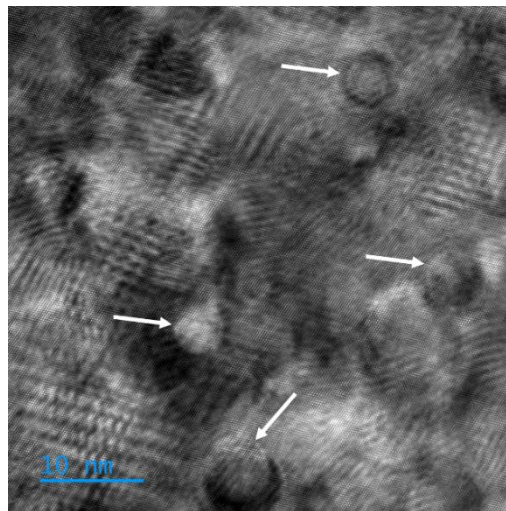


Figure 5. HRTEM image of bubbles in Ni bombarded samples with the fluences of $1 \times 10^{16} \text{ cm}^{-2}$ at temperature $\sim 800 \text{ K}$ with 380 keV Ar⁺ ions.

Bubble formation depends on the mobility of the gas (as single atoms or complexes), the minimum number of gas atoms that are capable of forming a stable nucleus, and the rate at which vacancies can be supplied to the lattice to increase the stability of the nucleated core. Under the influence of irradiation, the bubbles nucleate and then grow or dissolve again. The bubble density varies inversely as the square root of the diffusion coefficient of the gas atom and therefore increases with decreasing temperature ²³.

1.4.2 Irradiation-induced hardening

The radiation hardening phenomenon is closely related to the mechanisms of atomic-scale interaction between mobile dislocations and radiation-induced defects like defect clusters, dislocation loops, dislocation lines, voids, and bubbles or precipitates ²⁹.

In general, irradiation of the metal causes strengthening by source hardening and friction hardening. Source hardening is the increase in stress required to initiate dislocation movement in the glide plane. The applied stress required to release a dislocation into its slip plane is called the unpinning or unlocking stress ²³. Source hardening occurs in irradiated fcc metals where clusters of irradiated defects near Frank-Read sources increase the stress required to expand the loop and enable source multiplication. When the stress level is sufficient to release the source, the mobile dislocations can destroy the small clusters and reduce the stress needed to continue deformation. In unirradiated fcc metals the stress required to initiate dislocation motion is: the Frank-Read source unpinning stress in the metal and is defined by the equation as:

$$\sigma_{FR} = \frac{\mu b}{l} \quad (1)$$

Where, μ is the elastic modulus, b is the Burgers vector, and $l(= 2R)$ is the distance between the pinning points. It should be noted that the tension is inversely proportional to the distance between the pinning points. The gradual emergence of plasticity characteristics in fcc metals can generally be explained by the stress distribution required for the action of the sources. At low applied stress, the easiest dislocation sources to handle (with large spacing between attachment points) start to generate dislocations. As dislocations form and move through the lattice, they begin to accumulate and exert reverse stress on the dislocation source, stopping its action and thus plastic deformation. As the applied stress increases, more dislocation sources are activated and the dislocation multiplication increases ²³.

Friction hardening refers to the stress required to sustain plastic deformation, also known as flow stress or friction stress. The forces responsible for opposing the movement of dislocations

in the crystal lattice arise from the dislocation network and obstacles such as defect clusters, loops, precipitates, and voids. These sources of dislocations are characterized by either long-range or short-range hardening. Long-range stresses are caused by dislocation-dislocation interaction due to their stress fields. Short-range stresses originate from the interaction between the sliding displacement and discrete obstacles in the slip plane. The total applied shear stress necessary to overcome the long-range and short-range forces to move the dislocation is:

$$\sigma_F = \sigma_{LR} + \sigma_{SR} \quad (2)$$

where, σ_F is the friction stress, and the subscripts LR and SR denote the long-range and short-range contributions, respectively, and σ_{SR} is given by:

$$\sigma_{SR} = \sigma_{ppt} + \sigma_{void} + \sigma_{loops} \quad (3)$$

where, the terms on the right-hand side of the equation correspond to precipitates, voids, and loops, respectively. Long-range forces arise from the repulsive interaction between a moving dislocation and the components of the dislocation network of the solid. Dislocations on parallel slip planes exert forces on each other due to their stress fields, which are long-range stress fields. Short range forces arise from the interaction of a moving displacement with an obstacle lying in its slip plane. Short-range forces only arise when the dislocation contacts an obstacle. Short range forces can be divided into **athermal and thermally activated interactions**. The action of athermal stresses is independent of temperature and causes bending of dislocations around the obstacle. In thermally activated processes, a dislocation overcomes an obstacle by cutting or climbing it. Both processes require the addition of energy by increasing the temperature²³.

When a dislocation come across an obstacle, like an incoherent precipitate, a short-range interaction occurs upon physical contact with the obstacle. In the case of strong obstacles, the applied stress will cause a dislocation bending between the obstacles. The bending will continue until adjacent segments touch and destroy each other. This “pinching” process is identical to that used for the Frank-Read source. Once pulled away, the dislocation is free to continue along its sliding plane until it encounters another obstacle and the process repeats. Obstacles remain surrounded by a dislocation loop, which creates a stronger obstacle for the next one to appear. Bending dislocations provide the greatest amplification by obstacles. However, cutting down obstacles can also provide reinforcement. Cutting obstacles results in hardening through various mechanisms, which Dieter³⁰ summarizes as follows:

Shearing a particle creates a step of width b on both sides of the particle, and increasing the surface area requires additional work to shear the particle.

If the particles are ordered structures, e.g., intermetallic compounds, then shearing will also create a new interphase boundary in the particle, which will require additional energy.

The hardening is also due to the difference in the elastic moduli of the matrix and the particle, which affects the tension of the dislocation line requiring additional stress to cut the particle.

Strengthening also occurs due to the difference in Peierls stresses between the particle and the matrix.

Dislocations can also intersect voids, although the structure of the void is the same before and after intersection. Precipitates and voids are considered to be hard barriers with $\alpha \sim 1$. The only difference between the passage of a mobile dislocation through precipitates and voids is that in the case of voids the dislocation segments always meet the void surface at right angles and do not leave a dislocation ring after passing through the void ²³.

1.5 Application of the ion implantation technique to simulate neutron radiation

Heavy ion irradiation was developed in the 1960s and 1970s to simulate neutron damage for the breeder reactor program ²³. There is a considerable incentive to use ion irradiation to study neutron damage, as this technique can provide answers to fundamental processes, and also provides enormous savings in time and money. Neutron radiation experiments are not suitable for studies covering a wide range of conditions, which is exactly what is required **to study fundamental damage processes**. Simulation of radiation damage using ions enables easy variation of irradiation parameters such as dose, dose rate, and temperature over a wide range of values.

Energetic ions can be used to understand the effects of neutron irradiation on reactor components. Interest in this application of ion irradiation has increased in recent years for several reasons, including the avoidance of high residual radioactivity and the decline of the neutron sources for irradiating materials. Table 1 presents an overall comparison of the two techniques, highlighting their advantages and disadvantages.

Table 1. Comparison of the pros and cons of neutron and ion irradiation

	Neutron irradiation	Ion irradiation
Pros	<ul style="list-style-type: none"> ☑ Uniform distribution of radiation defects throughout the sample volume ☑ Neutron radiation reflects the actual conditions in a nuclear reactor 	<ul style="list-style-type: none"> ☑ Obtaining high damage levels (hundreds of dpa) in a short time ☑ The irradiated material is inactive, which makes it easier to conduct various tests ☑ Much lower cost of material modification
Cons	<ul style="list-style-type: none"> ☒ Obtaining low radiation damage with loge exposure time (several dozen years) ☒ Expensive irradiation process ☒ Material is active and its examination requires the preparation of a large number of safety protocols ☒ Material testing in its active state requires specialized staff and equipment, i.e. hot cells 	<ul style="list-style-type: none"> ☒ The damage is uneven and accumulated only in the top layer of the material ☒ Although the nature of radiation damage formation is similar to that in the neutron flux, verification of the results is still a challenge ☒ Irradiated material is not suitable for conventional (accredited) mechanical tests such as tensile, bending etc.

Typical neutron irradiation experiments in test reactors require 1–3 years of baseline exposure to achieve noticeable fluence levels for accelerated post-irradiation testing. However, this will involve at least another year of capsule design and preparation, as well as disassembly and cooling. It is worth mentioning that analysis of microchemical changes by Auger electron spectroscopy (AES) or microstructural changes by scanning electron microscopy-energy dispersive spectroscopy (STEM-EDS) and evaluation of mechanical properties or stress corrosion cracking (SCC) may take several additional years due to the precautions, special facilities and instrumentation required for handling radioactive samples. As a result, a single cycle from irradiation through microanalysis and mechanical/SCC testing can take three to five years. Such a long cycle does not allow for iterative assessment of irradiation and material condition, which is critical in any experimental research program. The long time required for design and irradiation also reduces the flexibility to change irradiation programs as new data become available. Due to the long cycle time, the need for special equipment and special sample handling, the costs of neutron irradiation experiments are very high. Unlike neutron irradiation, ion irradiation (heavy, light or electron) offers significant advantages in both cycle length and cost. Ion irradiation of any type rarely requires more than several tens of hours to achieve damage levels in the range of 1–10 dpa. Ion irradiation produces little or no residual radioactivity, allowing samples to be handled without the need for special precautions. These features translate into significant reductions in cycle times and costs ²³.

Chapter 2

State of the art

Due to their importance in the context of this dissertation, this chapter is dedicated to the presentation of the single-phase concentrated solid-solution alloys (SP-CSSAs). Firstly, an explanation of their unique properties resulting from their atomic and electronic structure is provided, with a special attention paid to the simplest model system of NiFe alloys. This information is then utilized for justifying why the two-element Ni_xFe_{1-x} single crystal alloys have been selected for deep studies presented in this thesis. Finally, the chapter is concluded by summarizing the state of the art and highlighting the gaps addressed in this thesis.

2.1 Introduction

A recent study of the family of Ni-containing equiatomic SP-CSAs (ranging from binary to five-component high-entropy alloys) has demonstrated that changing the number and type of constituent elements can have a significant positive impact on the radiation tolerance of SP-CSAs. **The number, type and concentration of alloying elements are the three fundamental components of compositional complexity.** It has been shown that the **type of alloying elements** may be **more important than the number of elements** for the response to irradiation, as well as for several mechanical and physical properties^{31,32}. For example, studies on the family of Ni-containing equiatomic cubic (fcc) alloys have shown that the addition of Fe can retard defect development more effectively upon room temperature irradiation compared to alloying with Co^{9,33}. At high temperature, the addition of Fe to Ni can significantly reduce the volumetric swelling, which is more effective than the addition of Co and Cr³¹. **As a result, Ni-Fe based alloys are expected to be an interesting system in the development of SP-CSA.**

2.2 The new class of SP-CSAs

SP-CSAs³⁴ are a unique group of complex concentrated alloys (CCAs). These chemically complex CSAs, including medium-entropy alloys (MEAs, e.g., with three alloying elements) and high-entropy alloys (HEAs, commonly containing five or more alloying elements^{35,36}), form random solid solutions on simple crystalline lattices, such as body-centered cubic (bcc), hexagonal close-packed (hcp), or face-centered cubic (fcc) structures³⁷. The new class of

single-phase CSAs, including high entropy alloys (HEAs), show remarkable mechanical, chemical, and magnetic properties, including high yield strength, fracture toughness, wear resistance, and corrosion resistance, compared to conventional alloys^{38–41}. Long time since observed that specific substitution additives in diluted alloys or certain CSA compositions improved structural stability and radiation resistance compared to their pure metal counterparts. The multi-element space in SP-CSA implies tunable chemical complexity at the electron and atomic level. As a unique system, SP-CSA enables scientific endeavors at the most fundamental level. In many applications of structural alloys like nuclear reactors, power plants, automotive, aerospace and space industries, defense, involve extreme conditions (such as temperature/heat, pressure, radiation, corrosion, oxidation, and mechanical deformation) that can cause the structural alloys to transition from an equilibrium state to a non-equilibrium state or a state far from equilibrium. In the case of SP-CSAs containing different transition metals (TMs) stochastically distributed on simple underlying crystal lattice sites, pronounced chemical disorders occur that influence the energy dissipation and defect evolution processes, not limited to thermal equilibrium states. Ongoing discoveries and new properties of single-phase medium-entropy alloys (MEAs) and HEAs point to completely new avenues for designing materials with desired properties⁴².

2.2.1 Fcc Ni-Fe solid-solution model system

The Ni_xFe_{1-x} alloys may be considered as the simplest fcc solid-solution model systems. It is worth mentioning that fcc unit cell has atoms not only at the corners but also at the center of each face. Thus, it has eight lattice points at the corners and six at the face centers. This arrangement results in a highly efficient packing of atoms, with an atomic packing factor of 0.74, making it one of the most space-efficient crystal structures. The fcc structure is presented in Figure 6 b.

Due to their unique physical properties, Ni-Fe alloys occupy one of the key places among modern materials of mechanical and device engineering, state-of-the-art microelectronic components and are widely used as materials of structural, precision, and magneto-sensitive elements in numerous devices, aircraft, space, and nuclear components. It has now been established that most of the physical properties of these alloys are determined by the coexistence and significant interaction of the spatial atomic configuration and the orders of magnetic moments⁴³. The phase diagram (Figure 6 a) shows that the decrease in temperature causes two sequential phase transitions, namely a paramagnetic-ferromagnetic transition of the second

order (at the Curie points) and an order-disorder transition of the first order (at the Kurnakov points) according to the symmetries of the L_{12} -type or L_{10} -type ordered-type and A1-type disordered phases. The ordered alloys with the L_{12} -type substitution superstructure (which is unambiguously observed in experiments for the Ni_3Fe stoichiometry and has been theoretically predicted for the NiFe_3 stoichiometry) and the L_{10} -type substitution superstructure (with the equiatomic NiFe composition) are derived from the disordered (A1-type) fcc⁴³.

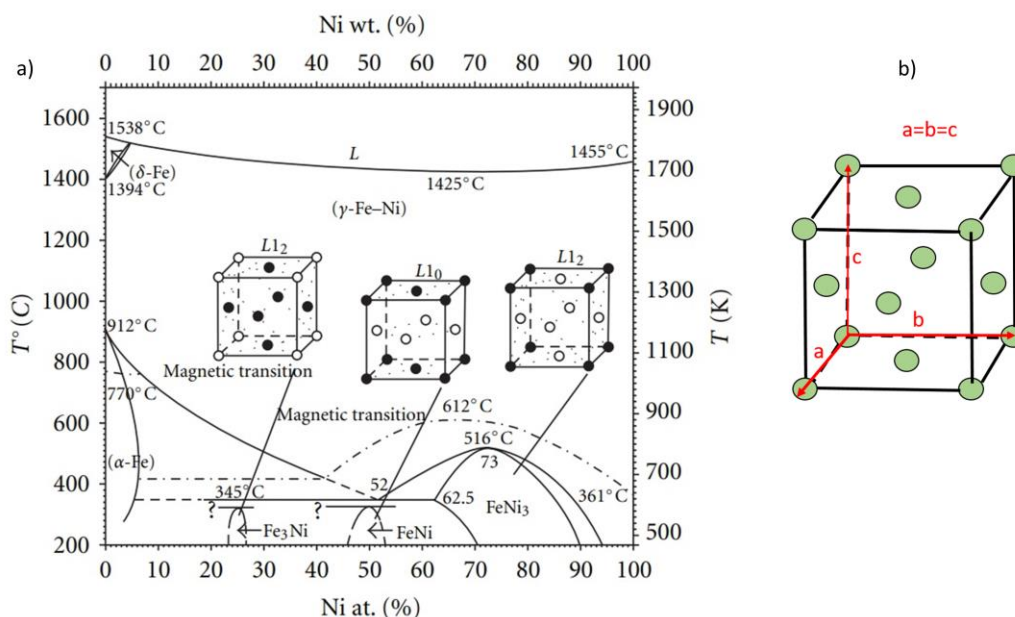


Figure 6. Experimentally obtained “metastable” phase diagram of Ni–Fe alloys taken from⁴³ a). The symbol “?” denotes the unidentified authentic structural and/or magnetic states of alloys. γ -Fe, α -Fe, and δ -Fe are the fcc., low-, and high-temperature bcc. crystal lattice modifications of iron. L is the Ni–Fe liquid solution. The equilibrium crystal structures of the three stoichiometric ordered phases at $T = 0$ K (from right to left), L_{12} -Ni₃Fe (Permalloy), L_{10} -NiFe (Elinvar), and L_{12} -NiFe₃ (Invar), are also shown ($\circ = \text{Ni}$, $\bullet = \text{Fe}$)⁴³. Face-Centered Cubic (fcc) unit cell b).

2.3 Tunable chemical and physical properties in concentrated alloys

It should be emphasized that the internal properties of materials are determined by chemistry at the level of atoms and electrons. In dilute alloys, there are generally no interactions with solutes, and all the solute atoms are neighbors. The conceptual difference between dilute alloys or ordered intermetallic compounds and CSA and CCA is that in the latter the same chemical species can occur in the same vicinity, whereas dilute alloys appear near the corners of the phase diagrams. SP-CSAs are composed of many elements, making the differences between solvents and solutes negligible. The enormous elemental diversity distinguishes CSA alloys from traditional solvent-solute alloys, allows for fundamental knowledge at the electronic and atomic level, and enables tuning of alloy properties. Although maximum compositional

disorder occurs at equiatomic composition, maximum chemical complexity depends on the strength of the coupling of the alloying chemical species involving local electronic, magnetic, and phonon interactions that may not be present at equiatomic composition. Controlled chemical disorder leads to controlled alloy properties. In chemically disordered fcc SP-CSAs, significant modification and reduction of the energy dissipation rate have been shown to be controlled at the electronic level via coupled electronic and magnetic interactions. Increasing chemical disorder significantly reduces thermal conductivity and has a significant impact on defect processes³⁷.

At the atomic level, chemical disorder between sites leads to complex, nonperiodic energy landscapes (e.g., nonuniform formation and migration energies, and the formation of anisotropic diffusion channels) that influence defect evolution. The lack of a unified fundamental description of the influence of alloy chemical complexity on energy dissipation and defect evolution is a serious obstacle to the development of alloys for applications in radiation environments. A tunable disordered chemical state opens the possibility of modifying the coupling strength of electrons, phonons, and magnons; thus it influences the paths and rates of energy dissipation and changes the energetics of point defects and atomic mass transport. More importantly, the tunable chemical disorder in concentrated alloys opens unique opportunities for developing fundamental knowledge of the energy dissipation mechanisms that control defect formation and atomic diffusion in a radiation environment³⁷.

In complex alloys composed of different TMs, there are two distinct but related types of chemical disorder at the most fundamental levels: the electronic and the atomic levels. Chemical disorder at the electronic level results from differences in the number of valence electrons, whereas chemical disorder at the atomic level results from differences in atomic volume and atomic mass. Chemical disorder effects arise from, and can be controlled by, the specific alloying elements and crystal structure of the alloy (e.g. fcc vs bcc). The influence of chemical disorder on the properties of SP-CSA is determined after determining the distribution of alloying elements, preferably random. SP-CSA alloys, including binary, ternary, quaternary and quinary alloys of different TMs, are characterized by a large compositional diversity and, consequently, different and tunable electronic structures. In alloys containing elements characterized by large variations in the number of valence electrons (e.g. from left to right in the d-block, as seen in many three-dimensional CSA analyses), valence electron disorder can have a significant effect on energy dissipation via intra-atomic electron rearrangement and interatomic charge transfer. In CSAs containing early TMs there may be significant differences

in atomic volume and atomic mass. Since atoms can deviate from their ideal positions in the lattice, positional disorder is expected to lead to a controllable lattice distortion^{41,42}.

2.3.1 Electronic level properties

The properties of many alloys are largely determined by the number of valence electrons and bonding characteristics of their constituent atoms^{37,44,45}. For example, heat conduction and energy flow depend on how far electrons can travel in metals and alloys without scattering. Electrical resistivity is one of the most fundamental properties and reflects the internal random scattering, which is directly related to the maximum electron flow velocity or their lifetime at the Fermi energy³⁷. The Fermi energy is the highest occupied energy level at 0 K. All electrons occupy energy states at or below the Fermi energy, and only electrons with energies close to the Fermi energy can participate in energy conduction^{37,46}.

The results presented in these works^{32,44,46,47} reveal that for SP-CSAs containing alloying elements with different 3d valence electrons, the electrical resistivity results from the spin-dependent electron scattering and strong electron–electron scattering can result in high residual resistivity. Examination of the Bloch spectral function for both spin-up majority and spin-down minority channels reveals that little or no blurring in Ni implies a long or infinite electron mean-free paths (MFP), and the heat is dissipated rapidly. However, significant blurring means significantly reduced MFP. The lower electrical thermal conductivity of the CSAs, compared to Ni, is attributed to band structure effects and higher random scattering³⁷. For example, NiFeCoCrMn quinary HEA contains five 3d TMs arranged on an fcc structure. These 3d TMs, from Cr to Ni, have increasing numbers of valence electrons, and thus the quinary HEA contains elements with large fluctuations in the number of valence electrons. Using *ab initio* methods, the researchers uncovered the electron scattering mechanisms in CSAs and demonstrated that electron MFPs range from ~ 10 to ~ 103 Å, corresponding to strong or weak scattering limits, respectively. The results presented herein³⁷ showed that NiFe and NiCoCr have higher resistivity than NiCoFe and NiFeCoCr, respectively, and therefore relatively lower electrical thermal conductivity. The results suggest that the resistivity values do not increase monotonically with the number of alloyed TMs. Additional evidence is provided by the electrical resistance measured at 2 K for two ternary alloys, NiCoFe ($4.8 \mu\Omega \text{ cm}$) and NiCoCr (94.3 or $94.0 \mu\Omega \text{ cm}$). The modeling work focuses attention on alloying effects at the Fermi surface resulting from partially filled d-bands of Cr and Mn compared to the nearly full d-bands of Co and Ni. This suggests that the electronic transport in SPCSA can be modified by selecting

the number, type, and concentration of alloying elements, more precisely d-band occupancy (i.e., the difference in electron number)^{32,37}. The results clearly show that the alloy complexity may depend not only on the larger number of major elements, such as NiFe vs. NiCoFe or NiCoCr vs. NiFeCoCr. Instead, the level of chemical disorder depends fundamentally on the specific alloying elements, such as NiCoFe vs NiCoCr.

2.3.2 Atomic level properties

In addition to the tuned electronic band structure, SP-CSAs also have tuned local lattice distortions. The chemical disorder in CSA alloys at the atomic level is usually attributed to differences in the atomic volume and atomic mass of the alloy components and is also determined by the local electron density distribution. Significant site perturbation resulting from differences in atomic volume and atomic mass is expected to lead to lattice distortion, which in turn causes compressive or tensile stress-strain properties at the atomic level.

Local lattice distortion occurs in both fcc and bcc crystallographic structures of SP-CSA, which is a result of the presence of different elements with different atomic size mismatches and random occupation of sites in the crystallographic lattice. In CSA, each atom can have a local environment with a different configuration of alloying atoms; lattice distortion and therefore displacement dissipation resulting from the relaxation of atoms away from their ideal lattice sites is expected. Local occupational and displacement disturbances can be determined directly by anisotropic analysis of the atomic vapor distribution function based on synchrotron X-ray or neutron diffraction measurements³⁷.

2.3.3 Point defect energetics in SP-CASs alloys

Differences in chemical complexity and inherent properties lead to a broad distribution of point defect energetics. Since valence electron number disorder and site disorder are related, local incompatibilities are interrelated at the electronic and atomic level. The combined electronic and atomic properties provide insight into the complex energy landscape and into the nanoscale inhomogeneities and short-range order. The energetics of defects (i.e. the formation energies and migration energies of interstitials or vacancies) are strictly dependent on the local environment. The characteristic energetics of point defects not only shows the expected distribution of formation and migration energies, but also reveals element-specific influences on the distributions. As the Fe concentration increases, the alloys change from dilute to

concentrated, and the forming energy distributions for Ni–Ni, Ni–Fe and Fe–Fe dumbbells become broader. When 30% Fe is alloyed with Ni, the distributions of different defect types begin to overlap. The overlap of defect formation energies is a result of reduced symmetry in concentrated alloys, where chemical disorder is increased ³⁷.

The migration barriers of vacancies in randomly disordered $\text{Ni}_{80}\text{Fe}_{20}$ and NiFe (or $\text{Ni}_{50}\text{Fe}_{50}$) CSAs were calculated by the elastic band method with a climbing image ⁴⁸. Calculations of randomly selected migration jumps of Ni and Fe atoms show that the distributions strongly depend on the Fe concentration or the alloy composition, but the average energy of Fe atom jumps (i.e., the average migration energy barrier for Fe vacancies, 1.17 and 1.06 eV in $\text{Ni}_{80}\text{Fe}_{20}$ and NiFe, respectively) is always lower than that for Ni vacancies (1.26 and 1.32 eV in $\text{Ni}_{80}\text{Fe}_{20}$ and NiFe, respectively). Moreover, the higher the Fe concentration, the broader the distribution and the larger the differences between the average migration energies of Fe and Ni vacancies (i.e. 1.06 and 1.32 eV in NiFe versus 1.17 and 1.26 eV in $\text{Ni}_{80}\text{Fe}_{20}$) ^{41,42,48}.

The energies of defect formation and migration are closely related to the specific element and its surrounding atoms (local chemical environment), which additionally influences the diffusion properties of the elements. Examination of the calculated energies ^{32,42} in the equiatomic CSAs reveals that the formation energies of the interstitial dumbbells can be much lower than 4.0 eV, lower than the formation energy of 4.27 eV for pure Ni, but most of the vacancy formation energy is higher than in pure Ni (1.47 eV) ⁴⁹. The calculated migration barriers are 0.11 and 1.01 eV for interstitial and vacancy, respectively, in pure Ni ⁴⁹. Interestingly, the range of point defect energies, especially the migration energies for interstitial and vacancy, increases from NiCo to NiFe and to NiCoCr as well as to NiFeCoCr.

In a radiation environment, point defects can be formed ballistically under the influence of irradiation at any location in the lattice, even in those that are locally unfavorable, at higher formation energies under thermal equilibrium conditions. The broad distributions indicate that the behavior of the defects can be significantly modified by the local chemical environments. Interactions between interstitial structures and vacancies may contribute to more efficient defect annealing. Since the energetics of point defects, including both formation and migration energies, are fundamental to understanding and predicting the properties of materials subjected to irradiation, tunable energetics can enable the creation of desired properties by manipulating distinct electronic structures in concentrated alloys ^{47,49}.

2.4 Defect formation and evolution in SP-CSAs

In a radiation environment, energetic particles carry significant momentum and interact with target atoms via the Coulomb force. Meaningful energy transfer to target electrons and nuclei induces far-from-equilibrium athermal processes and radiation-enhanced mass transfer and defect diffusion. Compared to thermally or temperature-driven activities, athermally driven processes are generally weakly temperature dependent or independent. In reality, athermal processes often occur at much lower temperatures than those required to overcome energy barriers and thermal migration. Ion or neutron bombardments cause energetic recoils that then initiate very localized collisional cascades (i.e., several nanometers), but at extremely high pressures and temperatures (of the order of 10–50 GPa and several thousand degrees Kelvin)⁵⁰. In a broader sense, these collisional cascades can be considered as ultrafast phase transitions at the nanoscale through complex dynamical and kinetic processes that leave the atomic structure essentially intact but give rise to point defects and small defect clusters^{41,42}.

In conventional metals and alloys, energy is believed to dissipate rapidly through delocalized electrons in the electronic subsystem. Recent studies have shown that increasing the compositional complexity in CSAs can significantly reduce the MFP of electrons, phonons, and magnons, modify the coupling strength, and thus can significantly affect the defect production and microstructure evolution^{28,44}. Chemical disorder, such as that in CSAs consisting of TMs with large differences in the number of valence electrons, has been shown to give rise to configurable electronic configurations that offer a forward path to modify energy dissipation and defect evolution^{34,37}. For example, in the high-quality Ni crystal, the energy dissipates rapidly via electrons because there is little scattering and an infinite MFP (i.e., low ρ and high κ), and consequently it has less influence on the defect dynamics at the atomic level. In the case of SP-CSA polymers, TM alloying with large differences in the number of valence electrons can cause significant chemical disturbances, resulting in a significant shortening of the MFP and thus a significant reduction in electrical and thermal conductivity.

The processes of producing radiation damage can be divided mainly into two phases: the ballistic phase and the rethermalization phase. In the ballistic phase, a large number of atoms are displaced as the high-energy atoms come closer to each other. This process creates a highly disordered, liquid-like volume. In the rethermalization phase, most of the displaced atoms return to their normal locations in the lattice, and a much smaller number of stable Frenkel pairs and point defect clusters remain.

Modeling of random Ni–Fe alloys has shown that slow chemically mediated diffusion can be improved by increasing the Fe content ^{41,42}. The combination of modeling and experiments suggests that the higher the chemical complexity, the slower the defect diffusion.

The slower the defect diffusion, the greater the probability that irradiated voids and interstitial spaces will interact and recombine, preventing the accumulation of radiation damage (and increasing radiation resistance). Although all SP-CSAs outperform pure Ni, the experimental results show that the major alloying elements and concentrations, as well as the level of chemical complexity, are important aspects of the performance ⁴⁴. Under Ni irradiation up to $1 \times 10^{14} \text{ cm}^{-2}$ (with a peak dose of $\sim 0.3 \text{ dpa}$), a marked reduction in the backscattering efficiency was observed in NiFe and NiCoFe, demonstrating the enhanced radiation resistance. Further inhibition of damage accumulation was observed in NiCoCr and NiFeCoCr alloys, where the defect density expressed in backscattering efficiency was about 4 times lower than in Ni alloys. The results show that defect formation and subsequent recombination are closely dependent on the alloy complexity. The key issue is that controlling chemical complexity is an effective approach in SP-CSA to modify the intrinsic properties, such as modifications at the electronic and atomic levels can influence both equilibrium and nonequilibrium defect dynamics ³⁷.

The MD analysis results for pure Ni show that the interstitial regions form $\langle 111 \rangle$ Frank loops in the $1/3$ range and the vacancies form stacking fault tetrahedra (SFT), which is consistent with the STEM images ^{44,51}. Similar work was performed for NiFe and Ni₈₀Cr₂₀. Although defect clusters were also formed, the kinetics were much slower for NiFe and Ni_{0.8}Cr_{0.2} than for pure Ni ^{44,51}. Additionally, experimental results showed that irradiation-induced defects extend beyond the predicted damage range and the damage becomes deeper with increasing ion fluence ⁸. The observed damage range was wider for Ni than for NiCo but was most refined for NiFe. One of the presented hypotheses suggest that high mechanical stresses induced by ion irradiation promote the propagation of defects in the bulk, resulting in a wider range of damage. Another hypothesis is that the interaction of an energetic particle with the material creates a continuous elastic wave along the ion trajectory, leading to a larger extent of damage. However, defect clusters were more prevalent in Ni than in NiCo and NiFe under room temperature radiation, which is consistent with the increasing chemical complexity (from Ni to NiCo and then to NiFe) and the resulting slower defect diffusion.

2.4.1 Point defect and defect clusters

Irradiation-induced point defects are annihilated by thermal or athermal recombination of a vacancy and an interstitial atom or by annihilation at absorption points such as free surfaces and microstructural inhomogeneities. However, the migration and evolution of radiation-induced point defects and small defect clusters can lead to long-range redistribution of elements due to kinetic coupling of fluxes between point defects and directional mass transport and may result in radiation-induced segregation (RIS) or radiation-induced precipitation (RIP)^{42,52,53}. It is therefore important to characterize the defect energies and the stability of the associated defects.

Understanding the migration of interstitial atoms, due to their low migration energy is important in studying the effects of radiation. For example MD simulations conducted on a NiFe model system revealed the migration behavior of a cluster composed of nine interstitials²⁷. As the Fe concentration increases from 0% to 10, 35, and 50%, the interstitial cluster motion changes from long-range 1D sliding to short-range three-dimensional (3D) migration²⁷. The evolution from long-range 1D motion in Ni to short-range 3D motion in Ni_xFe_{1-x} alloys is not abrupt but continuous, and the gradually increasing slow diffusion can be attributed to the progressively increasing chemical complexity. Similar MD simulations were performed for NiCo and NiFe²⁸. Compared with pure Ni, increasingly slow interstitial cluster motion was observed in NiCo and was more noticeable in NiFe.

While the interstitial structures tend to migrate by exchange with Ni atoms, the vacancies in NiFe prefer to migrate by exchange with Fe atoms^{37,54}. The presence and origin of slow vacancy-based diffusion is attributed to the differences in energy barriers between the alloying elements and the vacancies. Vacancy-driven slow diffusion is a combination of site percolation and local vacancy migration energies of the chemical environment (also composition dependent) and occurs when the concentration of the associated element approaches the corresponding percolation threshold of ~18% for the fcc lattice⁵⁵. In SP-CSA, low-energy time traps, in which mobile defects are trapped for a longer time, play an important role in defect evolution. As a result of the interaction of defects with temporal traps, initial defect states can become "frozen". As an example, Fe atoms have lower exchange barriers with the vacancy in NiFe. A relatively low or high diffusion barrier (i.e., the barrier between a vacancy and a neighboring atom) of Fe or Ni vacancies (i.e., exchange of the vacancy with surrounding Fe or Ni atoms) suggests that Fe vacancies are more mobile than Ni vacancies⁴⁹. If a Fe atom is in

the immediate vicinity of a vacancy, the vacancy can exchange positions with the Fe atom (i.e., exchange mainly with the Fe atom) by jumping back and forth, which retards the overall diffusion. Due to the low probability of exchange with a Ni atom, the diffusion path will continue only if the vacancy finds another Fe atom to exchange. In dilute alloys the number of such traps is small. As the Fe concentration increases closer to ~20%, almost to the site percolation threshold, more traps become available, leading to a significantly increased probability of retarding vacancy diffusion. Above this threshold, the probability that junctions will form between vacancies and their surrounding Fe atoms increases. The diffusion coefficient therefore becomes higher with increasing Fe concentration, and the maximum retarding effect observed in the vacancy diffusion mechanism occurs at ~20 at. % Fe. Primary damage initiation and defect accumulation involve the collective motion of large numbers of atoms over long periods of time (which may be much longer than seconds). A complete ab initio approach is beyond the capabilities of current computing power, but multi-scale simulation techniques can be used to solve these problems ³⁷.

2.5 Summary of the state of the art

Albeit chemical complexity can be tuned to increase radiation efficiency, knowledge of the interaction between energy dissipation and defect evolution in CSAs remains very preliminary. Knowledge gaps make it challenging to predict microstructural evolution and mechanical properties in cases of coupled extremes, such as irradiation and high temperature.

It is expected that further exploration will lead to a better understanding of the chemical and physical properties of CSA under both equilibrium and non-equilibrium irradiation conditions, as well as to greater interest in these complex alloys. Furthermore, it is obvious that much more work is needed to build and expand the knowledge base.

Chapter 3

Thesis goals

This chapter outlines the motivation, hypotheses and specific objectives of the thesis, as well as the scope of the conducted research.

3.1 Motivation

As outlined in the previous chapter, the research on fcc $\text{Ni}_x\text{Fe}_{1-x}$ single crystals is still limited. In particular, there is a lack of detailed studies that would clarify the defect dynamics, their evolution, distribution and mechanical properties after irradiation and high temperature. Hence, the motivation of the presented work is to provide a comprehensive study of irradiated $\text{Ni}_x\text{Fe}_{1-x}$ single crystal alloys, contributing towards their potential consideration for use in nuclear applications.

3.2 Hypotheses

Two major outcomes can be hypothesized in the proposed research, which are subsequently mentioned here based on the current knowledge about $\text{Ni}_x\text{Fe}_{1-x}$ alloys. In this work it is demonstrated that the introduction of compositional complexity with the addition of Fe into Ni will reduce the defect migration, concentration, and thus improve the radiation resistance of $\text{Ni}_x\text{Fe}_{1-x}$ single crystal alloys. With increasing Fe concentration, the damage build-up speed is decreased in the low fluence and the saturation fluence usually increases. This suggests that the addition of Fe delays the defect evolution process in $\text{Ni}_x\text{Fe}_{1-x}$ alloys.

Hence, the following **research hypothesis** has been formulated:

“By tuning the chemical composition in $\text{Ni}_x\text{Fe}_{1-x}$ single crystals, it is possible to tailor the radiation tolerance of these materials”.

And,

“The integration of structural characterization techniques with computational simulations enables not only quantitative analysis of radiation-induced defects in materials, but also allows for prediction of their type and distribution”.

3.3 Objectives

Modifying the compositional complexity of metallic alloys is a strategy for developing novel materials for advanced nuclear reactor applications. Such efforts gave rise to a unique group of alloys known as CSAs, with the addition of multiple elements into pure metals^{7–11,13,31,37}. In particular, Ni-based CSAs are promising materials for the structural components of advanced nuclear reactors. A simple class of Ni-based CSAs (serving as a basic composition for more complicated systems) can be examined for an easy understanding of the compositional complexity problem in $\text{Ni}_x\text{Fe}_{1-x}$ (x is the percentage of Ni content in the alloy) single-crystal alloys. These alloys are promising due to their extraordinary mechanical properties and high radiation tolerance, which are attributed to their simple structure and lack of grain boundaries^{8–11,13,31}. Ion irradiation can induce material degradation, which is observable by creating dislocation loops, voids, and SFT. Therefore, the main scientific purpose of this study is to identify the grade level of radiation damage and types of radiation defects of single-crystalline Ni-based alloys to understand the mechanisms and phenomenon of radiation-induced hardening, defect formation and its mobility in $\text{Ni}_x\text{Fe}_{1-x}$ single-crystalline alloys.

The current literature is limited in its understanding of $\text{Ni}_x\text{Fe}_{1-x}$ single crystals after ion irradiation, particularly at various fluences; therefore, various knowledge gaps and research questions remain. Some of the major research questions are listed here:

1. What are the types of defects created during irradiation in these model alloys?
2. What are the sizes, density, and distribution of the defects in fcc $\text{Ni}_x\text{Fe}_{1-x}$ single crystals?
3. How does the defect evolution/migration occur with varying irradiation fluences and concentration of Fe?
4. What is the dynamics of radiation defect formation for the tested chemical compositions as a function of the increase in ion fluence?
5. How do various defect microstructures impact the mechanical properties?
6. What is the impact of varying Fe concentration and irradiation fluences on the mechanical properties of Ni and $\text{Ni}_x\text{Fe}_{1-x}$ single crystals?

In general, the main objective of the proposed work is to answer these fundamental research questions and, thus, address the knowledge gaps by comprehensively understanding the effects of irradiation and Fe concentration on the microstructure and mechanical properties of some of the $\text{Ni}_x\text{Fe}_{1-x}$ single crystals and the correlation between these aspects.

3.4 Scope

The following scope of the thesis has been established to achieve objectives and confirm the righteousness of the hypothesis:

1. Simulating the level of radiation damage (dpa) using the SRIM program to determine the ion fluence and the depth of damage embedding in the material, the selection of energy, and the type of doping element.
2. Performing Ni⁺ ion irradiation (neutron radiation simulation) with an energy of 1.5 MeV at room temperature on the following compositions: Ni, Ni_{0.88}Fe_{0.12}, Ni_{0.77}Fe_{0.23}, Ni_{0.62}Fe_{0.38}, Ni_{0.38}Fe_{0.62} in a wide fluence range.
3. Performing high-temperature Ar⁺ ion irradiation at ~800 K with 380 keV on the fcc Ni single crystal.
4. Performing the RBS/C experiment using He⁺ ions with an energy of 1.6 MeV along the [001] direction in order to qualitatively and quantitatively assess the radiation defects generated in individual compositions.
5. Simulation of experimentally obtained RBS/C spectra using the Monte Carlo McChasy code developed at NCBJ. These include simulation of extended defects and randomly displaced atom distributions over the depth (quantitative analysis) based on ion channeling results. Additionally, RBS/C spectra will be used to calculate the kinetics of radiation defect formation for individual ion fluences using the MSDA model.
6. Carrying out nanomechanical investigations on the virgin compositions and after ion irradiation at room and at high temperature.
7. Performing hybrid simulations using molecular dynamics (MC/MD) of compositions in their virgin state to check their structural stability.
8. Carrying out structural analysis using TEM of all the compositions after ion beam irradiation.
9. Application of MD simulations with the LAMMPS software, renowned for its versatility in studying material behavior under various conditions. Simulation of radiation defect formation with ion fluence at the atomic level.
10. Creation of extended defect models using molecular dynamics LAMMPS. These models are used to create virtual samples and fit experimental RBS/C spectra for more precise radiation defect analysis.

Chapter 4

Methods

This chapter describes the selected research techniques, models and simulation methods that have been leveraged for the modeling and analysis of the radiation-induced defects.

4.1 Experimental Techniques

This section describes the selected, lesser-known experimental techniques leveraged in the conducted research, namely the ion irradiation, RBS/C and nanoindentation. While other well-known techniques have been utilized as well, such as SEM/FIB/TEM, their detailed presentation is skipped, as they are well-known and widely utilized in the field of materials science. Nevertheless, all of the utilized methods are well described in the published articles that are a part of this dissertation.

4.1.1 Ion irradiation

The ion implantation technique is widely used by scientists around the world, as evidenced by numerous publications in the field of nuclear research and beyond^{37,41,50,56–59}. Ion implantation is a process in which ions of a material are accelerated by an electric field to strike a solid. This technique involves bombarding the target with a beam of ions with energies ranging from several keV to several MeV. Due to the stochastic nature of the elastic collision process, the ions settle into a Gaussian distribution with the Gaussian mean centered around R_p , the predicted range, with a FWHM of $\sim 2.35\Delta R_p$, where ΔR_p is the standard deviation from the mean²³. If the ions differ in composition from the target, i.e., the sample to be implanted, they will change the elemental composition of the target and possibly change the physical, chemical, and/or electrical properties of the sample. In particular, the use of energetic ions enables the introduction of a wide range of atomic species independent of thermodynamic factors, thus enabling the achievement of concentrations and distributions of contaminants of particular importance. The ion implantation equipment consists of an ion source to produce ions of the desired element, an accelerator to accelerate the ions to high energy, and a target chamber⁵⁶.

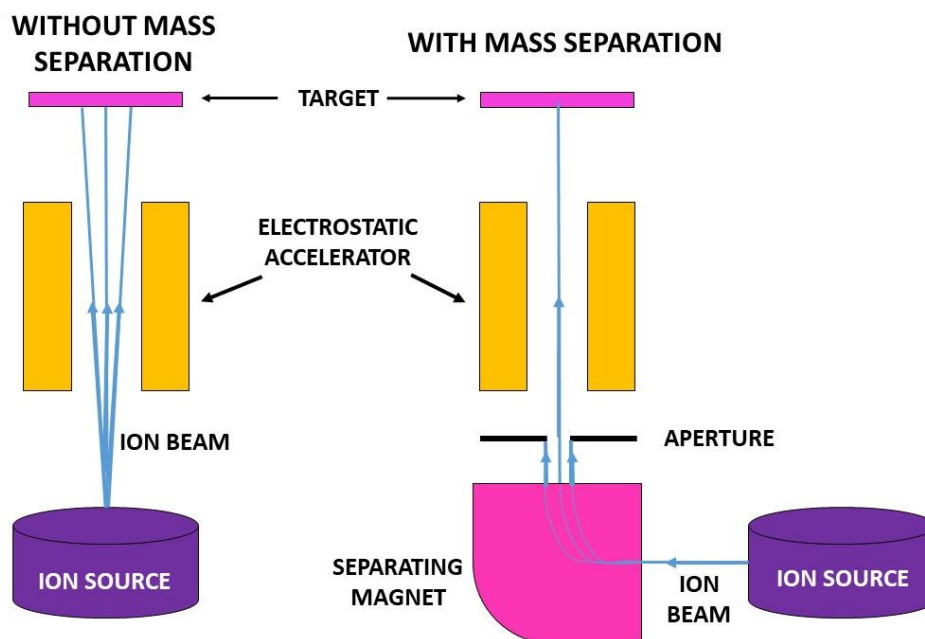


Figure 7. Diagram of an ion implanter without mass separation (left) and with mass separation (right).

There are two main types of ion implanters, i.e. implanters without mass separation (with direct ion beam) and with mass separation (without direct ion beam) as shown in Figure 7. A separating magnet is used for mass separation of the ion beam in order to obtain a homogenous beam in terms of a constant e/m ratio. The ion beam generated by an ion implanter without mass separation contains several kinds of ions with different degrees of ionization ⁶⁰.

4.1.2 Rutherford Backscattering Spectrometry (RBS)

RBS is a nuclear microanalysis method used to examine the subsurface layers of solids. High-energy light ions used in the RBS method enable for deep penetration of samples, without significantly affecting their structure. The scattering cross section, flux distribution, and energy losses of ions as they move through the crystal are known, which makes this method extremely useful. The duration of a single measurement does not exceed several dozen minutes, allowing for a relatively quick examination of many samples. Measurements do not have to be carried out in a very high vacuum ⁶¹.

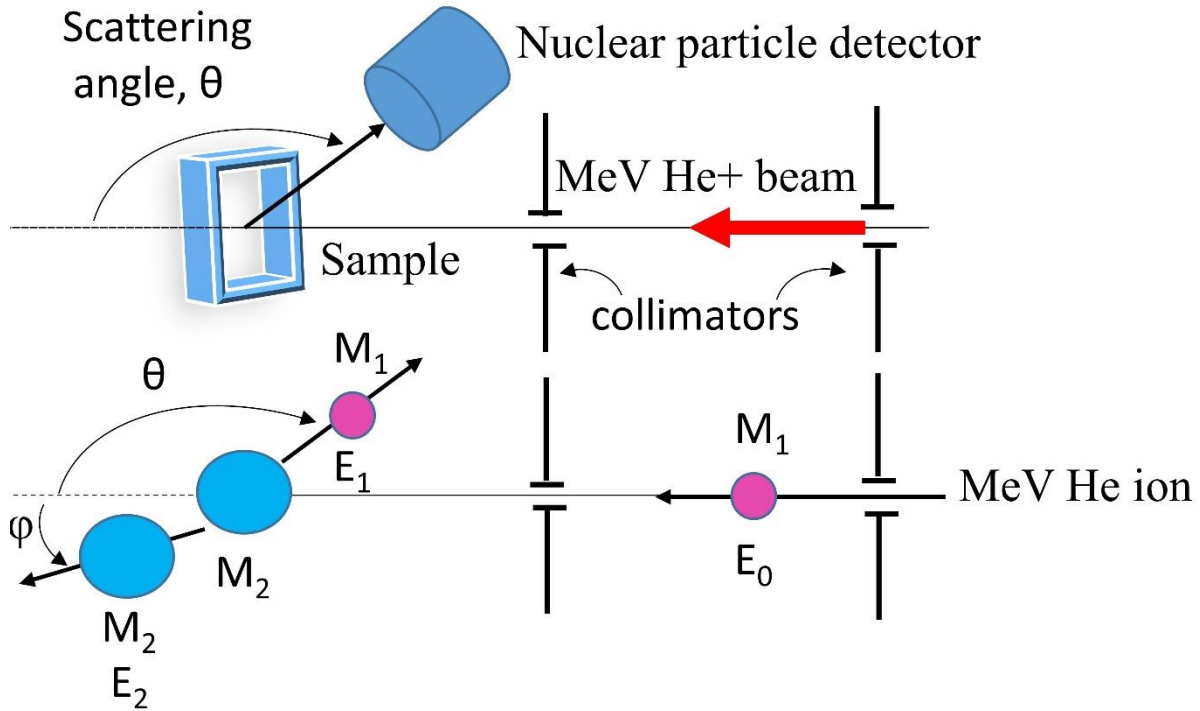


Figure 8. Flowchart of a typical RBS experiment.

The basic elements of the RBS research system (as shown in Figure 8) are: a source of a collimated beam of light ions (usually $^4\text{He}^+$), a detector of ions scattered back at a fixed angle, and a goniometer that allows for manipulating the position of samples, which are usually placed in a vacuum chamber. A mass separator is used in the ion path, and often an additional magnet deflects the beam by several degrees to eliminate potential uncharged particles. The ion beam can cause various effects in the tested sample, e.g., the emission of electrons, charged particles, or gamma or X quanta, so RBS is usually just one of the research lines associated with a given accelerator. Because of the Coulomb interaction with the target atoms, the ions of the analyzing beam of fixed energy are scattered in different directions, simultaneously losing some of their energy. The ratio of the ion energy after collision with the target atom E_1 to the initial energy E_0 is called the kinematic coefficient. It takes positive values less than one and can be determined from the principles of conservation of energy and momentum for any interacting ions – it is then a solution of the quadratic trinomial with respect to the variable being the ratio of the velocity (kinetic energy) of the incident ion after scattering to its initial velocity (kinetic energy):

$$k = \frac{E_1}{E_0} = \left(\frac{m_1 \cos \theta \pm \sqrt{m_2^2 - m_1^2 (\sin \theta)^2}}{m_1 + m_2} \right)^2 \quad (4)$$

where, $m_{1,2}$ are the masses of the ion and the target atom, respectively, and θ is the angle between the velocity vectors of the ion before and after scattering, depending on the collision parameter b .

Dependence (1) indicates that with the increase of θ , the energy and mass resolution of the RBS increases. The detection of ions scattered at a sufficiently large angle (e.g. 170°) therefore allows for the reliable separation of signals from the elements contained in the sample. Ions scattered at a fixed angle are recorded by a silicon detector, which performs their energy analysis and counts ions with energy values corresponding to individual energy channels. Their width on the energy scale (usually of the order of several hundred eV) is determined before starting the measurement. The result of the RBS measurement is therefore the energy spectrum of ions backscattered at a selected angle, presenting the number of ions recorded by the detector as a function of their energy ⁶¹.

Ion channeling mode (RBS/C)

The orientation of single-crystalline materials relative to the analyzing ion beam used in the RBS method is of great importance for the recorded spectrum. If the ion beam is directed parallel to one of the main crystallographic directions of the sample being examined (with an accuracy of $\sim 1^\circ$), then from the perspective of the ions, the structure spreading in front of them looks like a system of channels formed between the target atoms ⁶¹.

RBS measurements performed with such sample orientation relative to the beam are called RBS/Channeling (RBS/C). The spectra recorded in such a case are called aligned and are characterized by a significant decrease (even by 95-99% compared to the random spectrum) in the number of backscattered ions. From the perspective of the beam, the target atoms are somehow hidden in the shadow of the surface atoms, which forces the movement of most He ions in the channels created between the atomic rows. On the other hand, the aligned spectrum is characterized by the so-called surface peak, created as a result of the beam scattering on the surface atoms. Moreover, the crystal surface acts as a grid collimating the beam in the channels - ions not scattered on the surface atoms, but running near them with collision parameters sufficient to create relatively small deviations from the direction of movement are directed towards the center of the channel. This transverse momentum change need not be the cause of direct scattering, but contributes to the subsequent oscillatory motion between the channel walls.

In order to quantitatively evaluate RBS/C spectra recorded for ion-bombarded crystals, the ion beam used in the RBS analysis is assumed to consist of two fractions: **the random fraction** and the **aligned (channeled)** one. In the presence of defects, two mechanisms contribute to increasing the intensity of the measured RBS spectrum:

- **dechanneling**: ions from the aligned fraction are deflected into a random direction thus increasing the random fraction; the probability of dechanneling depends on the defect density at a given depth $n_D(z)$ and can be described by a defect dechanneling factor σ_D ;
- **direct scattering**: ions from the aligned fraction are instantly backscattered by displaced atoms; the intensity of the process depends on $n_D(z)$ and on an associated defect scattering factor f .

Both factors σ_D and f are characteristic of every type of defects. For example, dislocations have a very low contribution to direct scattering (f approaching zero) and reveal the high impact on dechanneling of ions, while point defects contribute to both mechanisms (with the value of f reaching unity). In contrast to point defects, dislocations provide few scattering centers and cause a rather strained distortion of the surrounding structure ⁶².

4.1.3 Nanoindentation

Nanoindentation is the state-of-the-art technique, which allows the measurement of hardness and elastic modulus of the thin layers even at several nanometers depth. A hard tip whose mechanical properties are known (frequently made of a hard material like diamond) is pressed into a sample whose properties are unknown. The load placed on the indenter tip is increased as the tip penetrates further into the specimen until it reaches a user-defined value. At this point, the load may be held constant for a period or removed. The area of the residual indentation in the sample is measured, and the hardness is defined as the maximum load, divided by the residual indentation area: $H = P_{\max}/A$, where P_{\max} represents the maximum load, and A is the projected contact area at a specific peak load. A schematic representation of nanoindentation is presented in Figure 9.

In this work, nanoindentation was performed utilizing the NanoTest Vantage system from Micro Materials Ltd. A Synton-MDP diamond Berkovich-shaped indenter was used to measure mechanical properties such as hardness of the ion-implanted Ni-Fe single crystals. The tests were conducted in multiple load cycles with increasing load from 0.5 mN up to 10 mN (in a total of ten cycles) using the load-controlled method. At least 16 indentations were made at

each load with 50 μm spacing between the indents. Before the indentation campaign started, a Diamond Area Function (DAF) of the indenter tip was calculated. Calibration was performed using fused silica material over a wide load range to assess a reliable indenter shape for a given indentation depth. The described method allows hardness extraction from indentation load-displacement curves during one cycle of loading and unloading⁶³. Once the contact area is determined, the hardness is estimated from $H = P_{\text{max}}/A$.

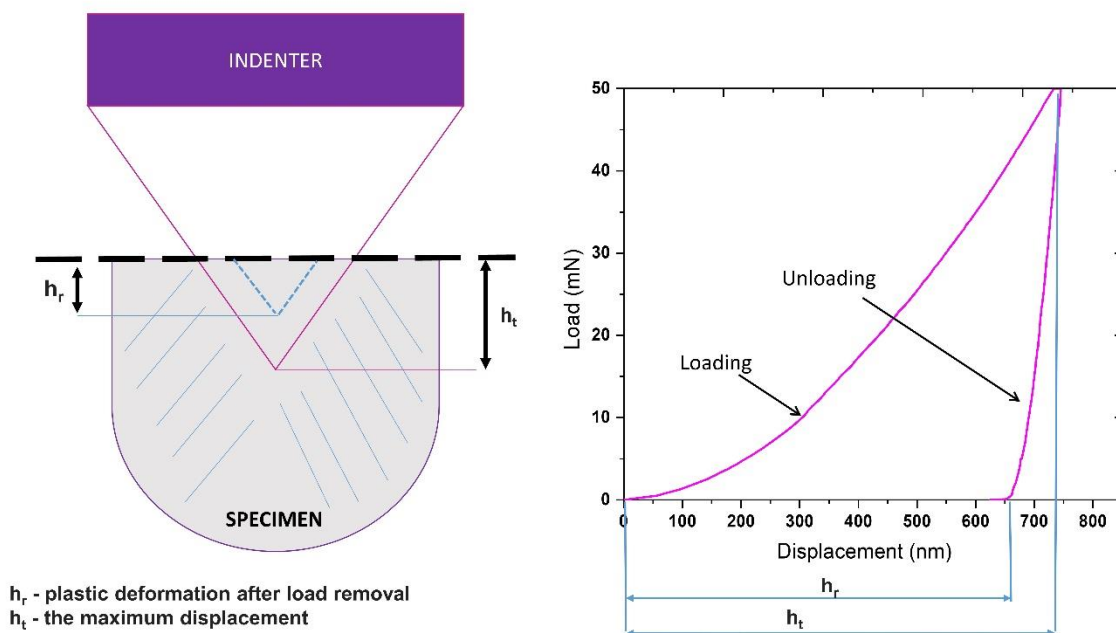


Figure 9. A schematic representation of nanoindentation experiment (left side) and generated load-displacement curve (on the right side)

4.2 Simulations

In this subsection, SRIM, Monte Carlo simulations of RBS spectra using McChasy code, Molecular Dynamic S, and Hybrid MC/MD will be described in the context of the thesis.

4.2.1 Stopping and Range of Ions in Matter (SRIM)

SRIM is a group of programs that calculate the stopping and ranging of ions (up to 2 GeV/amu) in matter using the quantum mechanics of ion-atom collisions (assuming that the moving atom is an "ion" and all target atoms are "atoms"). These calculations are made very efficient by the use of statistical algorithms that allow the ion to jump between calculated collisions and then average the results of the collisions in the interval between them⁶⁴. During collisions, the ion and the atom undergo a shielded Coulomb collision involving exchange and correlation

interactions between the overlapping electron shells. The ion enters into long-range interactions, causing electron excitations and plasmons within the target. These are described by including a description of the bulk electronic structure of the target and the interatomic bond structure during the calculation setup (tables of nominal values are provided). The charge state of the ion in the target is described using the effective charge concept, which includes a velocity-dependent charge state and long-range screening due to the collective electron sea of the target⁶⁴.

SRIM includes quick calculations that produce tables of stopping powers, range and straggling distributions for any ion at any energy in any elemental target. This software is particularly useful for:

- *Ion Implantation*, where ion beams are used to modify samples by injecting atoms to change the target chemical and electronic properties. The ion beam also causes damage to solid targets by atom displacement.
- *Sputtering*, where the ion beam may knock out target atoms. The calculation of sputtering, by any ion at any energy, is included in the *SRIM* package.
- *Ion Transmission*, where ion beams can be followed through mixed gas/solid target layers, such as occurs in ionization chambers or in energy degrader blocks used to reduce ion beam energies.
- *Ion Beam Therapy*, where ion beams are widely used in medical therapy, especially in radiation oncology.

The radiation damage characteristics of the ion-irradiated samples were evaluated using the SRIM program^{64–66}. The simulation results were necessary to calculate damage level for the particular ion fluence and specific chemical composition. In this work, the ion distribution was estimated from the RANGE.txt file. The corresponding dpa profiles were calculated using two files, VACANCY.txt and NOVAC.txt, under an assumed displacement energy threshold of 40 eV for all elements. The dpa profile is the sum of the vacancy concentrations using the column of "Knock-Ons" for Ni ions and the columns of "Vacancies" from target elements (the sum of Ni vacancies and Fe vacancies in the case of Ni_xFe_{1-x}) in VACANCY.txt, together with the replacement collisions in NOVAC.txt⁶⁷. Ion-induced damage in monoatomic and multi-elemental targets was predicted using full-cascade simulations^{68–71}.

The dpa has been calculated based on the following equation⁶⁹.

$$dpa = \frac{\text{fluence} \times \frac{\text{total vacancies}}{A\text{-ion}} \times \text{unit factor (f)}}{\text{atomic density}} \quad (5)$$

Where, fluence is the number of ions that fall on a unit surface in a given time (ion/cm²), total vacancies is the sum of the vacancy concentration + replacement collisions, and atomic density is the number of atoms or nuclides per unit volume, often expressed as atoms per cm³.

4.2.2 Monte Carlo simulations of RBS spectra; McChasy program

The use of the MC simulations in ion channeling studies was inspired by Barrett ⁷². In his pioneering work, he proposed the sampling of the scattering probability distribution to calculate the integral RBS spectrum. This probability distribution is known as nuclear encounter probability (NEP). It is the measure of a chance that the ion is scattered by an encountered atom and is calculated for every single ion-atom interaction. The cumulated distribution of the scattering probability can eventually be converted into an RBS spectrum. Moreover, NEP can also be used in simulations of such phenomena as nuclear reactions or atomic recoils ⁷³.

One of the most powerful MC codes to evaluate ion channeling spectra is called ‘McChasy’. The greatest virtues of the code are computing separate contributions from point defects and edge dislocations to the simulated spectra, as well as the possibility to run it on common PCs.

The McChasy code uses MC simulations to reproduce trajectories of light MeV ions (⁴He, ²H, and ¹H) in monocrystalline structures. It is run by an input file prepared by the user (a SIP file: Simple Input Protocol). The file contains commands that regulate simulations (if not provided, the default values are loaded). The most important input parameters to be provided to the code are:

- the energy of the beam and energy resolution,
- calibration of the energy channels width and offset,
- backscattering angle,
- the sample structure,
- defect profiles,
- initial dispersion and straggling of the beam,
- scattering on electrons and local energy loss corrections ⁷³.

4.2.3 Molecular Dynamic Simulations (MD)

MD simulations with the Large-scale Atomic/Molecular Massively Parallel Simulator (LAMMPS) software ⁶, are known for their versatility in studying material behavior under

various conditions, including radiation damage. In this work, interatomic potentials developed by Bonny *et al.* ^{74,75}, which are based on the Embedded Atom Method (EAM) with Ziegler-Biersack-Littmark (ZBL) corrections to account for short-range interactions ⁷⁶ have been utilized. Thus, modeling irradiation in materials, began by defining the *fcc* Ni sample with a dimension of (10.23, 10.58, 10.94) nm³ and 107 880 atoms along the [001] orientation, followed by optimizing the system's energy using the FIRE (Fast Inertial Relaxation Engine) 2.0 protocol ⁷⁷. This optimization continued until achieving a homogeneous temperature and pressure profile at a density of 8.88 g/cm³ ^{78,79} aligning well with experimental values. Subsequently, the prepared sample underwent a relaxation step for 10 ps to dissipate any artificial heat. To create the *fcc* Ni_xFe_{1-x} alloys, randomness was introduced by substituting 12% and 23% of Ni atoms Fe, following experimental results ^{76,80}. The optimization process focused on reaching the nearest local minimum of the energy structure, with criteria ensuring minimal change in energy between iterations and maintaining a global force vector length of all atoms below 10⁻⁸ eV/Å. The subsequent steps mirrored those of the pristine case, considering a series of MC simulations to search for each possible metastable configuration at room temperature ^{76,80}.

To model the generation of defects at low irradiation doses, MD simulations are commonly employed to depict the mechanisms of point defect formation during recoils within the range of 1 to 100 keV of primary knock-on atoms (PKAs) ^{81,82}. Subsequently, at low irradiation doses, clusters of defects begin to merge, leading to the formation of an extended defect that, can be observed as a dislocation network. This network, in conjunction with the continuous generation of isolated defects through irradiation, plays a role in the formation of dislocation loops and more complex defects like a SFT for example. Thus, the Ni, Ni_{0.88}Fe_{0.12}, and Ni_{0.77}Fe_{0.23} alloys are irradiated using cumulative overlapping collision cascade simulations at 5 keV recoils with temperature of 300 K. The dpa dose is calculated as $(n/N) (0.8E_{\text{PKA}}/2E_d)$ ^{83,84} with n as the number of cascades, $N = 107880$ as the total number of atoms in the numerical cell, E_{PKA} is the impact energy, and E_d is the threshold energy set at 40 eV for Ni ⁸⁵. Requiring a number of $n = 215$ and 1080 consecutive recoil MD simulations to obtain dpa values of 0.1 and 0.5, respectively ^{84,86}, which correspond to fluences in the range of 10¹³-10¹⁴ ions/cm². The process ensures that heat spikes generated by the recoils were fully developed within the cell and that periodic boundary conditions did not influence the final outcomes. Established simulation techniques for irradiation effects were employed, including adaptive time step algorithms, border cooling, electronic stopping power considerations, and the use of an EAM interatomic potential tailored for repulsion and defect properties ^{76,83,85}. To mitigate cascade-induced shock

waves, border cooling and damping were implemented by applying a thermostat on a 5 Å thick shell around the periodic borders of the cell ^{76,86}. Each recoil event was simulated for 20 ps, followed by an additional 10 ps under the NPT ensemble to allow for stress release and swelling. Random shifts of the simulation cell were applied between each recoil to ensure homogeneous irradiation. Each set of N-recoils was repeated three times, utilizing different seed numbers in the random number generator and different initial random cells. This extensive approach aimed to demonstrate that the results were not influenced by stochastic anomalies. To comprehend the nucleation of defects in irradiated fcc Ni and Ni_xFe_{1-x} single crystals, MD simulations of overlap collision cascades, tracing dislocation nucleation across various dpa doses using the DXA method implemented in OVITO ⁸⁵ have been conducted.

4.2.4 Hybrid MC/MD simulations

The hybrid MC/MD algorithm ^{87,88} was employed to facilitate thermally induced kinetics and anneal each alloy system. For each composition, a simulation cell with fcc crystal and a random distribution of constituent elements was created, containing 32000 atoms. Periodic boundary conditions have been applied in all three directions, and the sample was equilibrated at 300 K using the NPT ensemble. The following hybrid MC/MD steps ⁸⁸ have been utilized:

- 1- Two different atom types (Fe and Ni) are selected randomly in the simulations and tried to swap the positions so that the kinetic energy remains.
- 2- Metropolis criterion is used and each swap attempt is accepted if $\epsilon < \frac{P_f}{P_i}$, where ϵ is a random number between [0,1] and $P_i = e^{-\beta U_i}$, where β is the inverse of $k_B T$ and U_i is the potential energy of the system.
- 3- To relax any local residual stress induced by swapping, 50 molecular dynamic time steps under constant pressure (NPT) conditions are performed.

These three steps have been repeated until the system's potential energy reaches a reasonable level of convergence. The ordered crystal structures are analyzed using a polyhedral template matching algorithm ⁸⁹ that is implemented in OVITO software ⁸⁵.

4.3 Multi-step damage accumulation (MSDA) model

Multi Step Damage Accumulation is a model of multi-step creation of defects as a result of damage accumulation. It is a theoretical model that describes the process of defect accumulation

as a function of the deposited dose of bombarding ions. It assumes that the process of accumulation of defects is the result of subsequent transformations of defect structures⁹⁰. Each subsequent stage takes place when the energy deposited in the form of defects exceeds a certain critical value. When the critical value is reached, the current defect structure of the bombarded material is destabilized, and this becomes energetically unfavorable. This is the reason for the transition to the next stage, in which another type of defect dominates. As for the free energy of a crystal containing defect structures, it is always higher than the energy for a perfect crystal. However, it is always the case that between different possible defect structures, for one of them the free energy of the crystal is lower than for the others. From this, it was assumed, that each incident ion causes transformations of defect structures to such a configuration that will be the most energetically favorable at a given stage. So, to simulate the transformations takes place in a sample of a given material, it is enough to experimentally select these stages and determine the most important type of defect at a given moment⁹¹.

Based on the RBS/C spectra for pure Ni and Ni_xFe_{1-x} alloys irradiated with different fluences, the energy of the backscattered particle can be directly related to the depth at which the close encounter scattering event occurred. The bulk scattering arises from particles that have been deflected by atomic rows and have crossed over to another row, where they undergo a close-encounter event^{90,92}. This model is based on the equation assuming that the damage accumulation occurs through a series of structural transformations caused by the destabilization of the present crystal structure. The type of defect, which is associated with a given step is determined by the lowest free energy of this specific atomic configuration⁹¹. MSDA can be described as follows:

$$f_d = \sum_{i=1}^n (f_{d,i}^{sat} - f_{d,i-1}^{sat}) G [1 - \exp(\sigma_i (\Phi - \Phi_{i-1}))] \quad (6)$$

where,

σ_i - cross-section for the formation of a given kind of defect

$f_{d,i}^{sat}$ - level of damage at saturation for i-th kind of defects

Φ_i - fluence threshold for triggering the formation of i-th kind of defects

Chapter 5

Description of published articles in the thesis's context

The aim of this Chapter is to discuss the findings presented in the published articles in the context of this dissertation, answering the question: “how does it relate to the thesis?”.

5.1 Article A's description

W niniejszym artykule zaprezentowano wyniki badań monokrystalicznych stopów fcc Ni i Ni_xFe_{1-x} (z zawartością żelaza 0.38 i 0.62 % at), które zostały poddane defektowaniu strumieniem jonów w temperaturze pokojowej. Próbkę do badań strukturalnych i nanomechanicznych zostały zdefektowane jonami ⁵⁸Ni⁺ o energii 1,5 MeV osiągając fluencje: 4×10^{13} , 2×10^{14} , 5×10^{14} i 4×10^{15} jon/cm², co odpowiada zniszczeniom radiacyjnym na poziomie ok. 0.1, 0.5, 1.5 i 12 dpa (wartości dpa są różne w zależności od zawartości procentowej żelaza, co świadczy o zróżnicowanych mechanizmach powstawania zniszczeń radiacyjnych, wymienione wartości dpa dotyczą składu Ni_{0.38}Fe_{0.62}). Następnie zastosowano technikę spektrometrii rozpraszania wstecznego Rutherforda (w trybie kanałowania RBS/C) do jakościowej i ilościowej oceny uszkodzeń radiacyjnych. Analizę wykonano dla fluencji 4×10^{13} , 2×10^{14} , 1×10^{15} i 2×10^{15} jon/cm². Ponadto widma RBS/C przeanalizowano przy użyciu rodzimego kodu McChasy-1 i McChasy-2 wykorzystując symulacje Monte Carlo (MC), co pozwoliło określić liczbę defektów i ich rozkład w monokryształach. Technika RBS/C pozwoliła zidentyfikować poziom uszkodzeń radiacyjnych dla rozważanych kompozycji materiałowych i różnych fluencji jonów w funkcji głębokości penetracji jonów. Następnie, przeprowadzono badania przy użyciu transmisyjnej mikroskopii elektronowej (TEM), aby zweryfikować rodzaje defektów radiacyjnych i ich gęstość w funkcji fluencji jonów oraz dodatku żelaza. Technikę nanoindenatcji wykorzystano w celu zbadania poziomu utwardzania radiacyjnego, a także wykonano badania materiałów wyjściowych w celu określenia zmian mechanicznych w funkcji dodatku żelaza.

W pracy wykazano, że różne kompozycje osiągają nasycenie defektami przy różnych fluencjach jonów. Oznacza to, że ewolucja defektów jest opóźniona przez dodanie większej ilości Fe do Ni. Jest to związane zarówno z generowaniem defektów, jak i wzrostem defektów.

Zwykle przy wyższej fluencji, co oznacza, że do próbki wprowadzana jest większa ilość jonów Ni (powodując znaczne zniekształcenie sieci w wyniku jej interakcji z jonami, w tym przypadku jonami He), może nastąpić generowanie nowych defektów i ich transformacja obserwowana poprzez zwiększanie ich rozmiaru. Opisane zjawisko transformacji może również prowadzić do uwolnienia naprężeń, wpływając na wydajność rozpraszania wstecznego, co zaobserwowano w opisanych badaniach. Ponadto, wykazano, że jeśli krzywe RBS/C nakładają się na siebie, najprawdopodobniej mamy do czynienia z podobnymi rozmiarami defektów i ich gęstościami. Analiza koncentracji oraz rozkładu defektów rozciągłych wraz z fluencją jonów wykazała najmniejszy wzrost liczby defektów w stosunku do innych kompozycji w przypadku $\text{Ni}_{0.38}\text{Fe}_{0.62}$. Liczba defektów w $\text{Ni}_{0.38}\text{Fe}_{0.62}$ jest około dwukrotnie mniejsza niż w czystym Ni. Wyniki wykazały, że defekty akumulują się na różnych głębokościach, co może sugerować zmianę typu defektów i zdolności do migracji.

Analiza strukturalna wykonana za pomocą transmisyjnej mikroskopii elektronowej wykazała ponadto, że defekty mają tendencję do aglomerowania się w jednym miejscu w Ni i $\text{Ni}_{0.62}\text{Fe}_{0.38}$, podczas gdy w $\text{Ni}_{0.38}\text{Fe}_{0.62}$, nie uchwycono żadnej strefy akumulacji defektów (charakterystycznego piku uszkodzeń) ani przy niskich, ani przy wysokich fluencjach. Ponadto wykazano, że zmiana twardości wraz ze wzrostem zawartości Fe wynika z różnego ułożenia atomów Fe w strukturze krystalicznej, co wpływa na uzyskane właściwości mechaniczne $\text{Ni}_x\text{Fe}_{1-x}$ w stanie pierwotnym i po implantacji jonowej.

Podsumowując, w pracy wykazano, że manipulacja zawartością Fe ma wpływ na ogólną odpowiedź radiacyjną monokryształów $\text{Ni}_x\text{Fe}_{1-x}$, ponieważ dodatek Fe skutecznie wpływa na transport energii podczas defektowania strumieniem jonów poprzez elektrony podczas tworzenia i dystrybucji defektów. Wyniki badań przedstawione w artykule wskazują na zwiększoną tolerancję na promieniowanie składu $\text{Ni}_{0.38}\text{Fe}_{0.62}$, w porównaniu do czystego Ni i $\text{Ni}_{0.62}\text{Fe}_{0.38}$.

5.2 Article B's description

W kolejnym artykule poddano analizie pięć monokryształów o różnej koncentracji żelaza, mianowicie, czysty Ni oraz $\text{Ni}_{0.88}\text{Fe}_{0.12}$, $\text{Ni}_{0.77}\text{Fe}_{0.23}$, $\text{Ni}_{0.62}\text{Fe}_{0.38}$, $\text{Ni}_{0.38}\text{Fe}_{0.62}$, które zdefektowano strumieniem jonów $^{58}\text{Ni}^+$ o energii 1,5 MeV w zakresie fluencji jonów od 4×10^{13} do 4×10^{15} jon/cm². W tej pracy rola dodatku Fe na odporność radiacyjną monokryształów $\text{Ni}_x\text{Fe}_{1-x}$ została zbadana za pomocą hybrydowych symulacji Monte Carlo/dynamiki

molekularnej połączonych z transmisyjną mikroskopią elektronową (TEM), techniką kanałowania jonów (RBS/C) i techniką nanoindentacji.

Badania techniką kanałowania jonów, a także kinetyka powstawania defektów radiacyjnych z wykorzystaniem modelu „Multi-Step Damage Accumulation” wykazały różne mechanizmy przyrostu uszkodzeń radiacyjnych dla każdego zbadanego składu. Zauważono, że rozmiar i gęstość defektów radiacyjnych wpływają na kształt i intensywność uzyskanych widm RBS/C w zależności od składu, co jest związane z transformacją defektów radiacyjnych w bardziej złożone. Obrazy TEM wykazały znaczną degradację struktury przy zniszczeniach na poziomie 0.5 dpa, szczególnie dla Ni, a największe defekty zaobserwowano przy ok. 12 dpa. Na podstawie modelu MSDA zaobserwowaliśmy szybki wzrost liczby defektów do 0.5 dpa i wysoki wzrost poziomu dekanalizacji obserwowanego w zmierzonych widmach RBS/C dla wszystkich składów. Wykazano, że liczba defektów rozciągniętych utworzonych dla niskich fluencji jest znacznie niższa od wartości uzyskanych dla czystego Ni. Przy wyższym zdefektowaniu materiału, wynoszącym 1×10^{15} jon/cm² i 2×10^{15} jon/cm², zaobserwowaliśmy spadek koncentracji defektów, co sugeruje przekształcanie się małych pętli dyslokacji w większe i/lub tendencje do tworzenia skupisk defektów.

Analiza kinetyki powstawania defektów z wykorzystaniem modelu MSDA/ wykazała, że przekroje poprzeczne dla powstałych uszkodzeń radiacyjnych znacznie się zmniejszają dla Ni_{0.38}Fe_{0.62} i Ni_{0.62}Fe_{0.38} w porównaniu do czystego monokryształu Ni, co jest zgodne z wynikami RBS/C i TEM. Wyniki nanoindentacji pokazały, że stop Ni_{0.62}Fe_{0.38} posiada najwyższą twardość (2,96 GPa) wśród innych kompozycji w stanie pierwotnym. Aby zinterpretować ten wynik, zastosowano hybrydowe symulacje Monte Carlo/dynamiki molekularnej, aby sprawdzić obecność uporządkowanej fazy krystalicznej dla binarnych stopów Ni_xFe_{1-x}. Wyniki symulacji wykazały, że w zależności od zawartości żelaza mamy do czynienia z różnymi ilościami fazy FeNi₃ (L1₂). Dzięki dostrajaniu składu poprzez dodanie żelaza do Ni, wykazano, że dodatek żelaza powoduje zahamowanie procesu tworzenia się defektów radiacyjnych. Wynika to z tego, że Fe jest bardziej stabilny w stanie wzbudzonym niż Ni, co wynika z konfiguracji elektronowej obu pierwiastków, zatem im więcej jest żelaza w materiale, tym mniej defektów powstaje oraz ich rozmiar maleje.

5.3 Article C's description

W trzecim artykule przeprowadzono kompleksową analizę dynamiki powstawania defektów wywołanych defektowaniem strumieniem jonów, szczególnie w niskiej fluencji stopów Ni,

Ni_{0.88}Fe_{0.12} oraz Ni_{0.77}Fe_{0.23}. Wyniki uzyskano dzięki synergistycznemu podejściu łączącemu analizę mikroskopii elektronowej i spektrometrię rozpraszania wstecznego Rutherforda, uzupełnione eksperymentalnie kierowanymi symulacjami numerycznymi i modelem kinetyki uszkodzeń. W tej pracy zaprezentowano szczegółową charakterystykę pętli dyslokacji wywołanych defektowaniem w stopach Ni, Ni_{0.88}Fe_{0.12} i Ni_{0.77}Fe_{0.23}, stosując kombinację obrazowania z wykorzystaniem jasnego pola (BF) TEM w różnych warunkach dwuwiązkowych, symulacji dynamiki molekularnej (MD) i kodu MC McChasy opracowanego w NCBJ. W pracy dowiedziono, że w czystym Ni większość pętli dyslokacyjnych przy fluencjach 4×10^{13} i 2×10^{14} cm⁻² zidentyfikowano, jako pętle z uskokami, błędy ułożenia (SFT), pętle idealne i dyslokacje krawędziowe. Co ciekawe, przy wyższych fluencjach zaobserwowaliśmy pojawianie się bardziej złożonych pętli z tzw. uskokami, prawdopodobnie pętli Franka, z pewnymi przypadkami **nanofazy A15** przekształcającej się w pętle Franka. Obecność nanofazy A15 jest szczególnie ważna, ponieważ odgrywa ona kluczową rolę w formowaniu się i ewolucji defektów, potencjalnie wpływając na mechanizm utwardzania radiacyjnego. W Ni_{0.88}Fe_{0.12} i Ni_{0.77}Fe_{0.23}, zaobserwowano podobne trendy, z małymi pętlami idealnymi i SFT zlokalizowanymi w bliskim sąsiedztwie. Jednak przy wyższych fluencjach stopy te wykazywały więcej pętli z uskokami i skupisk defektów, co podkreśla złożoną interakcję między migracją defektów a składem stopu (potwierdzają to wykonane symulacje McChasy oparte na metodzie Monte Carlo). Identyfikacja nanofazy A15 podkreśla jej znaczenie w zrozumieniu wczesnych etapów powstawania defektów i jej wpływu na reakcję napromieniowania tych materiałów. Podsumowując, zastosowaliśmy szereg technik i symulacji, aby przeprowadzić ilościową i jakościową analizę defektów, zwłaszcza przy niskim poziomie fluencji. Zarówno wyniki symulacji, jak i zastosowanie modelu MSDA wykazały, że defekty punktowe dominują w strukturze stopów Ni i Ni_{0.88}Fe_{0.12}, co zostało również udowodnione poprzez analizę rozkładu losowo przemieszczonych atomów i defektów rozciągniętych obliczonych na podstawie eksperymentalnie uzyskanych widm RBS/C.

Wyniki przedstawione w niniejszej pracy, wnoszą istotne informacje na temat ewolucji defektów w monokryształach w szczególności w niskim zakresie dodatku żelaza do 23%at.

5.4 Article D's description

W przedostatnim artykule skupiono się na analizie eksperymentalnie uzyskanych widm RBS/C korzystając z nowej wersji kodu McChasy (nazywanej McChasy2), która daje możliwości symulacji eksperymentalnych widm dostarczanych przez spektrometrię rozpraszania

wstecznego Rutherforda w kierunku kanałowym (RBS/C), przy użyciu dużych struktur atomowych (ok. 108 atomów). W tej pracy przedstawiono najnowsze wyniki badań dotyczących symulacji rozciągniętych defektów strukturalnych (dyslokacji krawędziowych i pętli) rozwijających się w kierunkach typowo obserwowanych w układach fcc, które powstają wewnątrz monokrystalicznych stopów na bazie niklu. Modele defektów rozciągniętych zostały tworzone przy użyciu programu ATOMSK oraz dynamiki molekularnej (MD)-LAMMPS. Modele te są wykorzystywane do tworzenia wirtualnych próbek i dopasowywania eksperymentalnych widm RBS/C.

W artykule wykazano, że kod McChasy2 może być używany do symulacji RBS/C dużych struktur opracowanych przy użyciu aplikacji zewnętrznych. Przedstawione wyniki uzyskano przy użyciu sztucznie wytworzonych pętli dyslokacji o orientacji $\langle 110 \rangle$ i $\langle 112 \rangle$, leżących wzdłuż płaszczyzn $\{111\}$ i $\{-1-11\}$, które w rzeczywistych strukturach fcc pochodzą z rozszczepienia idealnej dyslokacji. Otrzymane rozkłady defektów dla rzeczywistego widma eksperymentalnego są zgodne z przewidywaniami kodu SRIM (warto wyjaśnić, że kod SRIM jest najczęściej używanym narzędziem przez inżynierów jądrowych służącym do symulacji np. poziomu zdefektowania). W pracy tej dowiedziono, że badania defektów radiacyjnych z wykorzystaniem symulacji MD i MC w połączeniu z eksperymentalnymi wynikami RBS/C w strukturach Ni mogą być użytecznym narzędziem do analizy pętli dyslokacji utworzonych w napromieniowanych materiałach.

5.5 Article E's description

Ostatnia praca dotyczy monokryształu Ni zdefektowanego strumieniem jonów w temperaturze ~ 800 K jonami Ar o energii 380 keV. Celem pracy było zbadanie ewolucji powstawania defektów radiacyjnych wywołanych w wysokiej temperaturze (ok. 520 °C) i zbadanie wpływu bąbli argonu na własności strukturalne i mechaniczne poprzez połączenie ze sobą technik eksperymentalnych i symulacji.

W celu określenia liczby defektów oraz profili głębokościowych wykorzystano najnowsze wersje kodów McChasy-1 i McChasy-2. Program LAMMPS w połączeniu z kodem McChasy-2 został wykorzystany do modelowania kształtu pętli dyslokacji (oraz modelowania pęcherzyków argonu) utworzonych wewnątrz zdefektowanego materiału. Pierwszym wynikiem analizy wykonanej przy użyciu McChasy-1 jest niski poziom krzywych nasycenia ze względu na znacznie większą ruchliwość defektów w wysokiej temperaturze, a zatem efektywne wyżarzanie dynamiczne, które występuje już podczas implantacji. Podczas analizy

kinetyki uszkodzeń zaobserwowano dodatkowy uskok widoczny dla najwyższej dawki (tj. 25 dpa), jako konsekwencja splątania dyslokacji i aglomeracji pęcherzyków gazu. Symulacje przeprowadzone przy użyciu drugiej generacji kodu McChasy'ego udowodniły, że wpływ pęcherzyków utworzonych wewnątrz materiału ma duże znaczenie i ich zignorowanie może wyolbrzymić analizę ilościową defektów w symulowanych widmach RBS. Badania nanomechaniczne wykazały, że w najbardziej uszkodzonych strukturach, to znaczy w tych, w których powstały pęcherzyki Ar, zmierzona twardość lokalnie i sukcesywnie spada na głębokości około 100–200 nm, gdzie występuje najwyższe stężenie pęcherzyków, a następnie wzrasta i utrzymuje się na podobnym poziomie. Obrazy TEM ujawniły, że w najniższym reżimie fluencji obecne są głównie pętle międzywęzłowe i małe błędy ułożenia zwane stacking fault tetrahedron (SFT) o rozmiarze 2–5 nm. W przypadku pośredniej fluencji jonów ($7 \times 10^{15} \text{ cm}^{-2}$) obserwujemy dodatkowo pęcherzyki Ar i wzrost rozmiaru SFT. W przypadku najwyższej dawki obserwujemy wzrost zarówno rozmiaru pęcherzyków (do 5–10 nm), jak i liczby SFT zorientowanych wzdłuż różnych kierunków krystalograficznych.

5.6 Summary

Podsumowując, wyniki zaprezentowane w pięciu artykułach potwierdzają słuszność stawianych tez badawczych:

“By tuning the chemical composition in Ni_xFe_{1-x} single crystals, it is possible to tailor the radiation tolerance of these materials”.

Oraz,

“By integration of structural techniques and simulations it is not only possible to make quantitative analysis of the radiation defects in the material but also predict their type and distribution”.

Article A:

*Tuning heterogeneous ion-radiation damage by
composition in Ni_xFe_{1-x} binary single crystals*

E. Wyszowska, C. Mieszczyński, Ł. Kurpaska, A. Azarov, I. Jóźwik, A. Kosińska, W. Chromiński, R. Diduszko, W.Y. Huo, I. Cieřlik, J. Jagielski,

Nanoscale, 15 (2023) 4870-4881, DOI: [10.1039/D2NR06178C](https://doi.org/10.1039/D2NR06178C)

IF: 8.3, Ministry points: 140

This article is licensed under a Creative Commons Attribution-NonCommercial 3.0 Unported Licence.

Published by Royal Society of Chemistry.

A.1 Abstract

Radiation-induced heterogeneous damage is the single largest source of failures seen in structural components in nuclear power reactors. Single crystal material, which is without grain boundaries, shows considerable promise for overcoming this problem. In this work, such heterogeneous damage was further overcome in Ni_xFe_{1-x} single crystal alloys via a simple strategy of fine tuning composition. [001] Ni_xFe_{1-x} (x=0, 0.38 and 0.62 at%) single crystals prepared using Bridgeman method were irradiated over a wide fluence range (4×10^{13} to 4×10^{15} ions/cm²). The irradiation-induced defect evolution was studied using Rutherford backscattering/channeling spectrometry, Monte Carlo simulations, transmission electron microscopy and nanoindentation. The results indicate an increased radiation tolerance of Ni_{0.38}Fe_{0.62} compared to pure Ni and Ni_{0.62}Fe_{0.38}. The structural analysis made by transmission electron microscopy revealed that defects tend to agglomerate at one place in Ni and Ni_{0.62}Fe_{0.38}, while in Ni_{0.38}Fe_{0.62} no defect accumulation zone (characteristic damage peak) has been captured either at low and high fluences. Moreover, we found that the hardness change with the increase of Fe content is due to different arrangements of Fe atoms in a crystal structure, which influences the obtained mechanical properties of Ni_xFe_{1-x} in a pristine state and after ion implantation.

Keywords: Nickel single crystals, Transmission Electron Microscopy, Rutherford Backscattering, Radiation effects, Nanoindentation

A.2 Introduction

The growing interest in the development of the nuclear industry worldwide is, among many others, a driving force to explore and investigate the new group of radiation resistance materials^{9–11,93}. Materials to be utilized as components of future fission and fusion reactors should be carefully selected due to harsh operational conditions^{1,2,13,31,52}. Therefore, while emerging as a new group of materials for such applications, special attention should be given to the high radiation tolerance, high thermal and phase stabilities, and elevated mechanical properties^{9,14}. Several papers and reports have described essential materials suggested for advanced fission reactors, especially Generation IV reactors^{2,10,13,15–17,94}. However, despite broad studies and advancements, multiple phenomena still require thorough investigation and explanation. Among many, one may name the swelling effect^{31,95–98}, embrittlement^{2,11,31}, or defect agglomeration zones, all induced by ion irradiation. As noted above, structural materials for the

next-generation fission reactors are prone to damage under irradiation. In particular, the formation of large vacancy clusters significantly deteriorates the performance of materials, as migrating and accumulating vacancies may lead to hardening and void swelling³¹. Therefore, controlling vacancy cluster migration and growth is crucial in selecting new advanced structural materials for nuclear applications^{9–11}. Modifying the compositional complexity of alloys has been considered a way to resolve the aforementioned challenges. Ni and Ni_xFe_{1-x} single crystal alloys are promising materials due to their extraordinary mechanical properties and high radiation tolerance¹¹. Unlike the novel, high entropy alloys or oxide-dispersion-strengthened (ODS) steels which face material processing challenges and show structural instability at elevated temperatures¹¹, single crystal alloys benefit from their simple structure^{9,10}. Due to the lack of grain boundaries within a single crystal, they are characterized by unique mechanical properties. Moreover, the possibility of modeling the development of defects using various techniques (e.g., ion channeling simulations, molecular dynamic simulations, etc.) is one of many advantages of choosing single crystals^{9–11}. Recent studies have shown that single-phase concentrated (binary and ternary) solid solution alloys exhibit outstanding mechanical and irradiation resistance properties in the Ni-based systems^{7,9–11,54}. Its properties rely on a well-ordered structure. Moreover, the processes, such as defect creation induced during ion irradiation or defect migration, can be easier to capture and understand than in amorphous materials.

It is common practice to manipulate chemical composition to achieve the desired material properties⁹⁹. For this reason, we developed a novel chemical composition of the material and compared its functional properties with pure counterparts and literature studies. In our research, pure Ni and Ni_xFe_{1-x} single crystal fcc alloys (with 0.38 and 0.62 at% of Fe element) were subjected to ion irradiation. The specimens for structural and nanomechanical investigation were irradiated with 1.5 MeV ⁵⁸Ni⁺ ions at room temperature with fluences of 4×10^{13} , 2×10^{14} , 5×10^{14} , and 4×10^{15} ions/cm². Afterward, the Rutherford backscattering spectrometry (RBS/C ion channeling) technique was used for qualitative and quantitative evaluation of radiation damage. The analysis was performed for fluences of 4×10^{13} , 2×10^{14} , 1×10^{15} , and 2×10^{15} ions/cm². In addition, the RBS/C spectra were fitted using a Monte Carlo (MC) simulation, which allowed us to determine the number of defects and their distribution within the single crystals. The RBS/C technique enabled us to identify the level of radiation damage for the considered compositions in various fluences. The obtained results are consistent with the Monte Carlo simulations. Subsequently, to confirm those findings, additional investigations using the

transmission electron microscopy (TEM) have been performed to verify types of radiation defects and their concentrations as a function of ion fluences. The results from both experiments provided comprehensive insight into the structural changes of the studied material.

A.3 Experiment and methods

A.3.1 Single crystal production and sample preparation

All single crystals considered in this work have been produced at the National Centre for Nuclear Research (NCBJ) in Otwock-Świerk, Poland ¹⁰⁰. Specimens were created using the vertical temperature gradient method (the Bridgman method ¹⁰¹). In this method, Ni and Fe metals characterized by high melting point temperatures were melted in an alundum crucible in which the heating element was a molybdenum wire. The crystallization process occurs due to the slow lowering of the crucible (from 1 to 2 cm/hour). Melting and crystallization took place in argon's inert gas protective atmosphere. The typical production time for one single crystal was 30 hours.

Samples for an ion irradiation experiment were cut along the [001] direction, grounded, and polished according to standard procedures. Mechanical grinding was performed on abrasive papers with grit sizes from 400 to 4000. In the next step, the samples were polished to a mirror-like surface finish using diamond pastes with grain sizes of 6 μm, 3 μm, and 0.5 μm. Subsequently, the samples were polished using electropolishing equipment (Struers LectroPol-5) with a mixture of 60% electrolytic perchloric acid and water to reduce stresses after mechanical polishing. The polishing time was set to 60 s, and the electric potential was 30 V.

A.3.2 Ion irradiation

The irradiations were carried out at room temperature with 1.5 MeV 58Ni⁺ ions using a 1 MV tandem accelerator (National Electrostatics Corporation, model 3SDH-2). The ion fluences ranged from 4×10^{13} ions/cm² to 4×10^{15} ions/cm². All implantations were performed at room temperature at 7 degrees off the normal direction to avoid channeling. The mean projected range of Ni ions in the Ni_xFe_{1-x} single crystal alloys was estimated using full cascade mode in the SRIM (Stopping Ion Range in Matter) program ⁶⁴.

A.3.3 RBS/C measurements and simulations

After implantation, the samples were measured by Rutherford backscattering spectrometry in channeling mode (RBS/C) using 1.6 MeV He⁺ ions in the [001] direction and backscattered into a detector placed at 165° relative to the incident beam direction.

The RBS/C spectra for pure Ni and Ni_xFe_{1-x} alloys implanted with different fluences were simulated using Monte Carlo (MC) McChasy code developed at NCBJ^{68,102}. A detailed description of the simulation procedures and the model of extended defects (Ext. Def.) used can be found in^{68,102,103}. The experimentally obtained spectra combined with the simulated spectra are shown in Figure 11 and Figure 12. The solid lines correspond to spectra in an aligned [001] direction obtained using MC simulations. The mean projected ranges of ions and induced defect distributions for Ni ions shown in Figure 11 and Figure 12 were estimated by SRIM simulations^{64,65,69}. The corresponding displacements per atom (dpa) profiles were predicted by the SRIM code under a displacement energy threshold of 40 eV for all elements using the full cascade mode. The SRIM-estimated damage peak is located at a depth of approximately 400 nm.

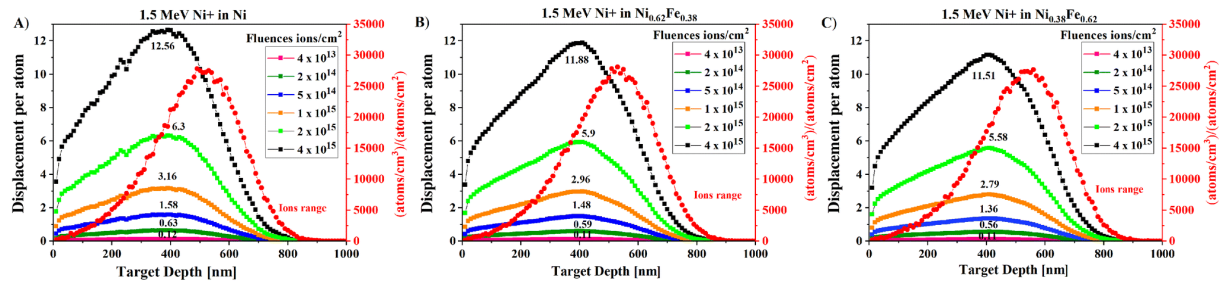


Figure 10. Damage profile of A) Ni and B) Ni_{0.62}Fe_{0.38} and C) Ni_{0.38}Fe_{0.62} irradiated with 1.5 MeV of Ni⁺ to the fluences of 4×10^{13} , 2×10^{14} , 5×10^{14} , 1×10^{15} , 2×10^{15} and 4×10^{15} ions/cm².

In Figure 10 the damage profiles of Ni (Figure 10 A), Ni_{0.62}Fe_{0.38} (Figure 10 B), and Ni_{0.38}Fe_{0.62} (Figure 10 C) irradiated with 1.5 MeV of Ni⁺ to fluences from 4×10^{13} ions/cm² to 4×10^{15} ions/cm² have been presented. The ion distribution was estimated from the RANGE.txt file. The corresponding dpa profiles were calculated using two files, VACANCY.txt and NOVAC.txt, under an assumed displacement energy threshold of 40 eV for all elements. The dpa profile is the sum of the vacancy concentrations using the column of "Knock-Ons" for Ni ions and the columns of "Vacancies" from target elements (the sum of Ni vacancies and Fe vacancies in the case of Ni_xFe_{1-x}) in VACANCY.txt, together with the replacement collisions in NOVAC.txt⁶⁷. Ion-induced damage in monoatomic and multi-elemental targets was predicted using full-cascade simulations^{68–71}.

A.3.4 Nanoindentation

Nanoindentation was performed utilizing the NanoTest Vantage system from Micro Materials Ltd. A Synton-MDP diamond Berkovich-shaped indenter was used in this study. The tests were conducted in multiple load cycles with increasing load from 0.5 mN up to 10 mN (in a total of ten cycles) using the load-controlled method. At least 16 indentations were made at each load with 50 μm spacing between the indents. Before the indentation campaign started, a Diamond Area Function (DAF) of the indenter tip was calculated. Calibration was performed using fused silica material over a wide load range to assess a reliable indenter shape for a given indentation depth. The described method allows hardness extraction from indentation load-displacement curves during one cycle of loading and unloading⁶³. Once the contact area is determined, the hardness is estimated from $H=P_{\text{max}}/A$, where P_{max} represents the maximum load, and A is the projected contact area at a specific peak load.

A.3.5 TEM defect characterization

TEM samples were prepared using the lift-out procedure and employing the focused ion beam system (Ga^+) installed in a Helios 5 UX (ThermoFisher Scientific) microscope. This allowed us to obtain thin lamellas with electron transparency. Final thinning of the lamellae was performed with 5 keV Ga^+ ions followed by a 2 keV Ga^+ gentle polishing. TEM observations were performed with a JEOL JEM1200EX II microscope. Observations were carried out under a diffraction vector of $g=200$ for bright-field imaging. Weak beam dark field $g\text{-}3g$ imaging was performed for the same diffraction vector. The two-beam convergent beam electron diffraction technique was used to determine the foil thickness (for dislocation density statistics)¹⁰⁴.

A.4 Results

A.4.1 RBS/C analysis and simulations

RBS/C analysis is an excellent tool for understanding the interaction between the injected ions and the structure in the surface region, which is usually less than 1 μm thick^{21,105}. The RBS/C spectra were fitted using McChasy, a Monte Carlo simulation package allowing the quantitative analysis of channeling spectra. According to the procedures developed in our group^{68,102}, the current investigations were performed mainly using the extended defect representation. The other parameters and simulation conditions (geometry etc.) were chosen carefully to match the

experimental data. It is worth mentioning that in the channeling mode, ion beam analysis reveals the crystal structure and therefore can be used as an alternative tool for crystallography, which is the domain of X-ray and neutron diffraction analysis. Using MeV He ions with wavelengths of 10^{-12} cm, the lattice is not viewed as a diffraction grating but rather as an actual crystal of rows and sheets of atoms that collimate and steer the beam. On the scale of lattice spacing, the MeV ion is a point probe weaving through the channels provided by the rows and planes of atoms²¹.

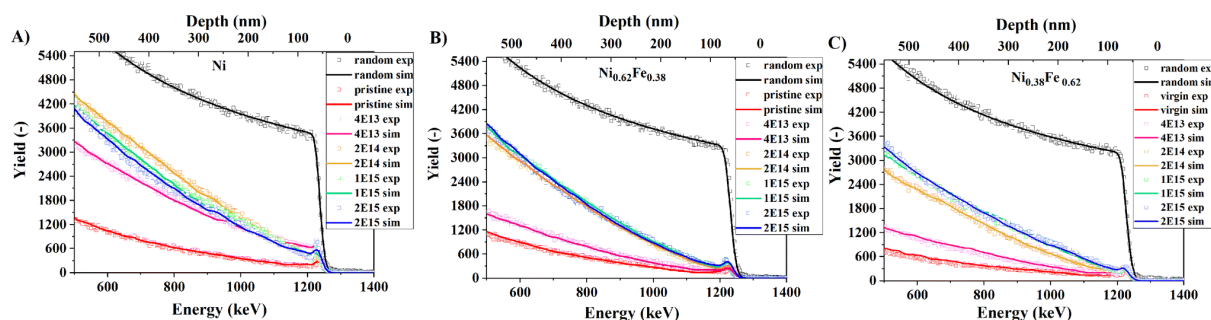


Figure 11. Ion channeling spectra of A) Ni, B) $\text{Ni}_{0.62}\text{Fe}_{0.38}$, C) $\text{Ni}_{0.38}\text{Fe}_{0.62}$ single crystals irradiated with the fluences from 4×10^{13} to 2×10^{15} ions/cm². Solid lines represent fits obtained using MC simulations. Virgin and random spectra are included as references.

Figure 11 shows the ion channeling spectra for pure Ni, $\text{Ni}_{0.62}\text{Fe}_{0.38}$, and $\text{Ni}_{0.38}\text{Fe}_{0.62}$ submitted to ion irradiation. One can observe that the random spectra attributed to the amorphous materials are considerably higher than the other spectra. In high-quality undamaged crystals, the backscattering yield is low (presented as the virgin level in Figure 11 A-C)^{11,21}. At the same time, fluence-dependent ion channeling spectra usually rise as a function of the damage. In other words, once the host atoms are displaced from their lattice sites, they can interact with the channeled beam, and an increase in the scattering yield is observed.

The most significant damage propagation (the highest backscattering yield) was observed for pure Ni, while the backscattering yield of Ni with 62 at% of Fe is the lowest (Figure 11 A-C) at each analyzed fluence. This effect suggests better radiation tolerance of the material with the addition of Fe. The addition of 38 at% Fe triggers an increase in radiation resistance to pure Ni. A drastic yield build-up for the low fluence of 4×10^{13} ions/cm² (approximately 0.1 dpa) is observed in Ni, while for the other compositions, the backscattering yield for this fluence is considerably lower. As the irradiation fluence increases up to 1×10^{15} and 2×10^{15} ions/cm² (damage levels of approximately 3 and 6 dpa, respectively), a visible drop in yield for pure Ni specimen can be noticed. The variation of backscattering yield depends strongly on the general lattice distortion after interaction of He ions with the lattice of the implanted material. Therefore, we observe an increased backscattering yield with increasing lattice distortion. Usually, in metals, most of the defects are mainly extended defects, e.g., dislocations or stacking

faults which lead to the dechanneling of incident He ions. Furthermore, in metals, we usually see the evolution of smaller defects occurring below the sample surface into larger, more complex defects at higher depths, as shown in the TEM images (Figure 16 A and B). Therefore, it can be assumed that lattice distortion could be related to defect size and density change since smaller defects cause smaller lattice distortion than complex defects (defect cluster, dislocation), hence, backscattering yield changes. In pure Ni, a saturation dose has been obtained at a fluence of 2×10^{14} ions/cm². The saturation and a small decrease in channeling yield may occur because the defect structure becomes more organized at high fluence, as reported here ⁹⁹. For example, point defects are transformed into more complex ones, such as dislocation loops, or small dislocation loops are changed into larger defect clusters that release strain induced by ion irradiation. Therefore, we observe a decrease in backscattering yield.

Moreover, one can noticed, different compositions reach saturation at different fluences. This means that the defect evolution is delayed by adding more Fe to Ni. This is related to both defect generation and defect growth. Usually, at higher irradiation fluence where more Ni ions are injected into the sample (causing a significant lattice distortion after an interaction of injected He ions), the generation of new defects and transformation from smaller to larger defects may occur. This transformation may also lead to stress release, affecting the backscattering yield. Moreover, adding Fe may effectively influence the energy transport during ion irradiation through electrons on the defect formation and distribution. Moreover, if the curves overlap like in Figure 11 B, we are most likely dealing with similar defect sizes and similar densities. Ni ions cause a significant lattice distortion at higher irradiation fluence, generating new defects and transforming from smaller to larger defects. This transformation may also lead to stress release, which further affects the backscattering yield.

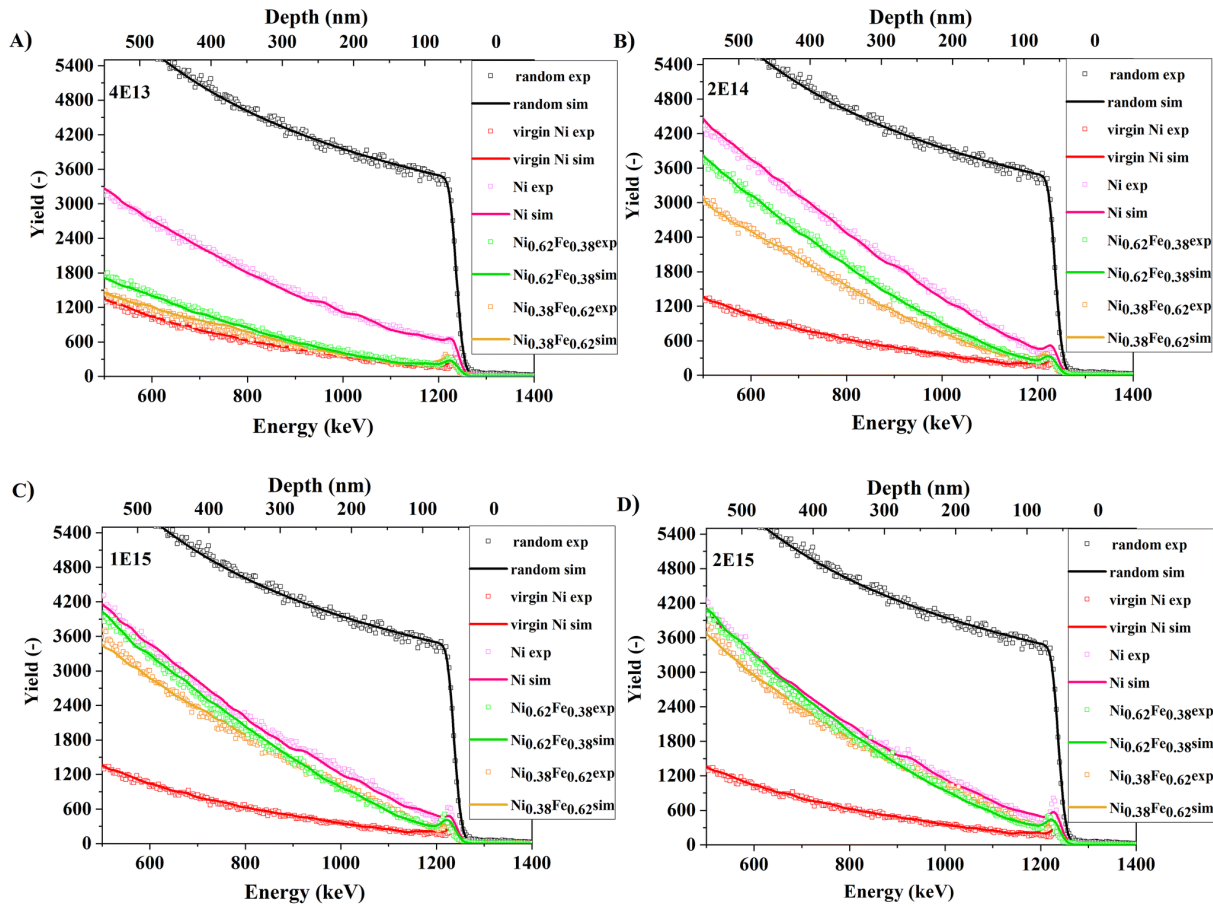


Figure 12. Recorded ion channeling spectra of Ni, $\text{Ni}_{0.62}\text{Fe}_{0.38}$ and $\text{Ni}_{0.38}\text{Fe}_{0.62}$. Specimens were irradiated with 1.5 MeV of Ni^{+} to the fluences of A) 4×10^{13} , B) 2×10^{14} , C) 1×10^{15} and D) 2×10^{15} ions/cm². The intensities of the spectra were normalized to the highest Ni-random spectrum.

Figure 12 A-D presents the different materials' responses to the ion fluences depending from the chemical composition tested. For low fluence irradiation such as 4×10^{13} ions/cm² (equivalent to 0.1 dpa), an increase in backscattering yield for pure Ni is noticeable compared to other compositions. For $\text{Ni}_{0.62}\text{Fe}_{0.38}$, the curves overlap, while in the case of $\text{Ni}_{0.38}\text{Fe}_{0.62}$, the yield remains the lowest. As the fluence rises to 2×10^{14} ions/cm² (damage level of approximately 0.5 dpa), a gradual decline in backscattering yield is observed with an increase in Fe content. In turn, for pure Ni we observe damage saturation starting at this fluence. This trend may suggest better radiation resistance and material stability than pure Ni and Ni with low Fe content. Somewhat miscellaneous behavior has been recorded for the higher dose of 1×10^{15} ions/cm² (approximately 3 dpa), where up to a depth of ~250 nm, the spectra of all materials overlap, and one may even observe an inverted intensity region. There might be two reasons for this: first, this can be related to the defect migration (a damage peak for these materials is approximately 400 nm), but they can concentrate at different depths^{8,11} second, the defects began to saturate at this dose. In most metallic materials, the fastest increase in degradation level occurs in the low fluence regime, usually up to 0.5 dpa. With a higher

irradiation dose, damage begins to saturate depending on the composition, which means the damage propagation (growth) stabilizes. In Figure 12 C and D, we already start to see a decrease in backscattering yield in pure Ni, but still, we observe the lowest yield for Ni_{0.38}Fe_{0.62} – that means Ni_{0.38}Fe_{0.62} still has room for damage increase. For a better understanding of this effect, in Table 2, we noted how each composition's maximum yield value (collected at 400 nm depth as maximum damage peak) changes with the irradiation fluence.

Table 2. Maximum backscattering yield (collected at 400 nm depth) of irradiated Ni, Ni_{0.62}Fe_{0.38}, and Ni_{0.38}Fe_{0.62} at fluences of 4×10^{13} , 2×10^{14} , 1×10^{15} and 2×10^{15} ions/cm².

Fluence/Material	Ni	Ni _{0.62} Fe _{0.38}	Ni _{0.38} Fe _{0.62}
4×10^{13}	2193	1088	877
2×10^{14}	3085	2359	1984
1×10^{15}	2707	2511	2321
2×10^{15}	2561	2388	2331

For Ni_{0.62}Fe_{0.38}, the backscattering yield constantly increases up to the fluence of 1×10^{15} ions/cm² and then decrease at 2×10^{15} ions/cm². In contrast, the backscattering yield in Ni_{0.38}Fe_{0.62} is lower than that in Ni_{0.62}Fe_{0.38} and increases gradually with fluence, which means that Ni_{0.38}Fe_{0.62} is the most resistant among the studied compositions. Damage reaches saturation in Ni at a fluence of 2×10^{14} ions/cm², while saturation in Ni_{0.62}Fe_{0.38} occurs above at 2×10^{15} ions/cm² and most probably for Ni_{0.38}Fe_{0.62} saturation begins above 2×10^{15} ions/cm². The best confirmation of this statement could be the TEM images presented in Figure 17, where the damage level decreases as the Fe content rises at low and high fluences. Moreover, we suppose that the better radiation tolerance with increasing Fe content is related to the physical nature of the iron atomic nucleus in its excited state compared to pure Ni. An iron atomic nucleus is more stable because it possesses only one orbital with unpaired electrons, while Ni has three. This means it is more vulnerable to electron movements and, thus, defect generation and mobility.

Finally, one must remember that many components used in the nuclear reactor operate only up to the time until they receive several dpa damages. After this time, they are replaced or as in the case of reactor pressure vessel RPV steel the whole unit is shut down. For this reason, it is of utmost importance to understand radiation damage build-up early in the defect accumulation stage.

A.4.2 Irradiation-induced hardening

The mechanical properties of Ni_xFe_{1-x} single crystal alloys have been evaluated using the nanoindentation technique. Pure Ni and Ni with different additions of Fe (0, 12, 23, 38, and 62 at%) in a pristine state were first investigated.

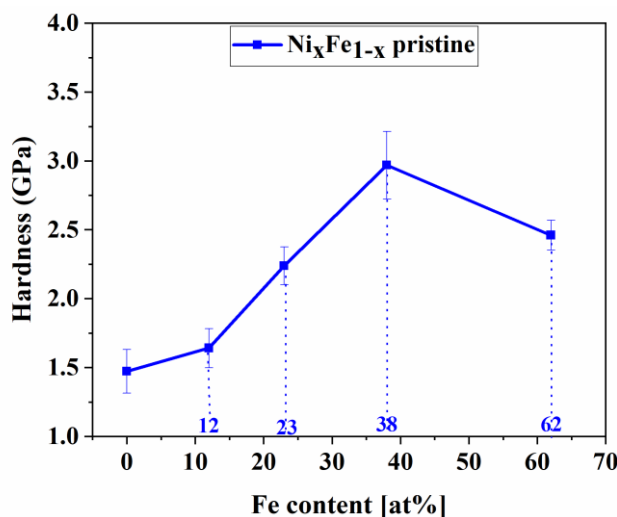


Figure 13. Nanoindentation hardness of the non-irradiated fcc Ni and Ni_xFe_{1-x} single crystal alloys as a function of Fe content.

In Figure 13 the hardness results as a function of Fe content are presented. From the pure nickel structure (0 at% Fe addition) to 38 at% of Fe, a gradual increase in hardness up to ~3 GPa was recorded. At 62 at% Fe, a substantial decline in hardness to 2.46 GPa has been recorded. One of the possible reasons for the hardness change with increasing Fe concentration during nanoindentation, as reported by Kurpaska et al.⁸¹, can be associated with extended distributions of formation and migration energies of vacancies and interstitials with alloying Fe with Ni. This may suggest that dislocation generation and propagation in pure Ni is easier than in Ni_xFe_{1-x}. They also explained that the combination of differences in the dislocation nucleation mechanisms during indentation and the defect sizes might lead to a hardness increase in the Ni_xFe_{1-x} samples with respect to pure Ni data. The mechanism of the formation of tetrahedral stacking faults from prismatic dislocation loops (PDL) in all studied Ni_xFe_{1-x} samples was also visible. The decreased mobility of PDLs and decreased size of dislocation loops with increasing Fe content have also been noticed. Therefore, it can be assumed that the main strengthening factors are associated with gradual dislocation diffusion, reduced defect sizes, and the nucleation of tetrahedral stacking faults⁸¹. Another possible reason for the hardness change over the various Fe compositions could be associated with a phase change of single crystals according to the phase diagram reported in⁴³. Based on this diagram, we can assume that in a

range of 10-29 at% of Fe, we are dealing with the FeNi_3 (L_{12}) phase. Next, between 29-47 at% of Fe, the FeNi (L_{10})+ FeNi_3 (L_{12}) phase occurs. This is a mixture of L_{10} and L_{12} structures where the Fe atoms occupy different positions in a crystal structure. Later, we can observe the presence of the FeNi (L_{10}) phase in a range between 48-54 at% of Fe. Finally, between 54-73 at% of Fe, we probably have a combination of the Fe_3Ni (L_{12}) + FeNi (L_{10}) phases. The different arrangements of Fe atoms in a crystal structure may influence hardness performance with increasing Fe content. However, more structural data are needed to prove the presence of those phases in the reported compositions.

It is known that nanoindentation is an exquisitely important technique that helps to evaluate the phenomenon of radiation hardening in materials modified by ions to several hundred nanometers¹⁰⁶. A series of multicycle indentations of the irradiated Ni and $\text{Ni}_x\text{Fe}_{1-x}$ alloys were performed to understand the mechanical behavior after ion irradiation. In Figure 14 A, the hardness as a function of irradiation fluence is presented for pure Ni and Ni with 38 and 62 at% Fe. It can be observed that the hardness growth with increasing ion fluence is visible for all of the tested materials, and this trend can be divided into two regimes. At first, a very rapid increase in hardness at a fluence of 4×10^{13} ions/cm² (approximately 0.1 dpa) is recorded. Afterward, the hardness change slows down at the level of 5×10^{14} ions/cm² (approximately 1.5 dpa). However, the trend remained. In Figure 14 B, the hardness difference based on the equation: $\Delta H = H_{\text{irradiated}} - H_{\text{pristine}}$ has been plotted. One can see that the most significant hardness change is visible in pure Ni, followed by $\text{Ni}_{0.62}\text{Fe}_{0.38}$ and then $\text{Ni}_{0.38}\text{Fe}_{0.62}$. The possible reason for that is the addition of Fe into the system, which slows down the aggregation of the interstitial-type dislocation loops, as observed in MD simulations⁸¹. This ultimately increases the radiation resistance of the material. Moreover, the disordered electronic structure essentially reduces the electron mean free path, so the effectiveness of the energy dissipation of a complex system decreases. This is visible in the case of radiation damage build-up. As we mentioned above, another reason for the different radiation responses of $\text{Ni}_x\text{Fe}_{1-x}$ could also be related to the different arrangements of Fe atoms in the crystal structure. Based on the phase diagram⁴³, we can assume that in a range of 29-47 at% of Fe, we deal with the FeNi (L_{10}) + FeNi_3 (L_{12}) phase combination while for 54-73 at% of Fe, we probably have a combination of Fe_3Ni (L_{12}) + FeNi (L_{10}) phases. The different arrangements of Fe atoms in a crystal structure may influence an irradiation-induced hardening mechanism in $\text{Ni}_x\text{Fe}_{1-x}$. This hypothesis will be verified in the future.

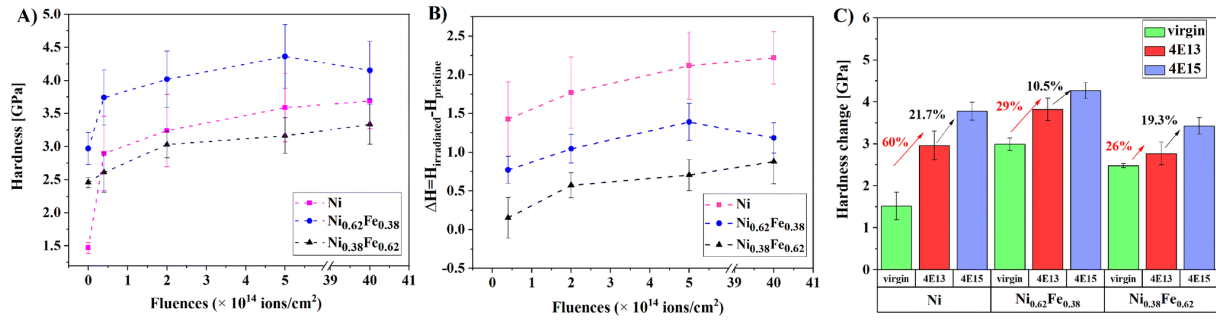


Figure 14. A) Nanoindentation hardness of fcc Ni, Ni_{0.62}Fe_{0.38}, and Ni_{0.38}Fe_{0.62} single crystal alloys as a function of irradiation fluence, B) hardness change according to the equation $\Delta H = H_{\text{irradiated}} - H_{\text{pristine}}$ and C) comparison of hardness change for pristine and irradiated samples of Ni, Ni_{0.62}Fe_{0.38} and Ni_{0.38}Fe_{0.62} between two fluences: 4×10^{13} and 4×10^{15} ions/cm².

In conclusion, the recorded data suggest that the Ni single crystal is the most sensitive material to ion irradiation. In comparison to the pristine sample Figure 14 C, an increase in hardness in pure Ni (for the highest fluence of 4×10^{15} ions/cm²) is approximately 60%. However, the hardness increase between the lowest and the highest dose was only ~21.7%. As the addition of Fe increases up to 62 at%, the irradiation-induced hardening phenomenon is the smallest among the studied samples, at approximately 26%. Then, the hardness increases by 19.3% between samples treated with the lowest and highest doses. To sum up, adding Fe to the Ni system effectively leads to an increase in radiation resistance, showing a lower level and increment of radiation hardening.

A.5 Discussion

In contrast to numerous studies on the radiation resistance of fcc Ni_xFe_{1-x} single crystals^{9–11}, in this article, we focused not only on the quantitative and qualitative analysis of damage: ~0.12, ~0.63, ~3.16, and ~6.3 dpa, but also on connecting the microstructure of the material with recorded mechanical (hardness) change. This comparison was made for damage levels of ~0.12, ~0.63, ~1.58, and ~12 dpa of new chemical compositions of fcc- type Ni_{0.62}Fe_{0.38} and Ni_{0.38}Fe_{0.62} single crystal alloys (recorded results were compared with pure Ni manufactured in the same way as studied monocrystals). The influence of Fe addition has been deeply studied and compared with the literature data, which revealed several interesting insights. Notably, both nanomechanical investigation and the obtained RBS/C spectra allowed us to obtain quantitative information about the radiation resistance response of the Ni, Ni_{0.62}Fe_{0.38}, and Ni_{0.38}Fe_{0.62} compositions.

The shape of the spectra reveals a continuous increase in the backscattering yield. This confirms our previous investigations⁶⁸ that the backscattering is mainly due to the dechanneling of the

analyzing beam and not due to a direct backscattering process, which is related to the occurrence of mainly extensive defects in the structure. It is worth mentioning that point defects can directly scatter a particle beyond the critical angle by a single collision. In contrast to localized point defects, dislocations provide an example of an extended defect in which the distortion around the defect causes dechanneling⁷¹. This is further confirmed by structural analysis in the following discussion. The dechanneling level of aligned spectra grows as a function of irradiation fluence, following the damage induced inside the investigated material. This is conspicuous, as a continuous increase in yield mainly proves the presence of complex defects. In turn, Jin et al.¹¹ recorded spectra with a "knee point," which confirms the presence of both simple and complex defects in the structure.

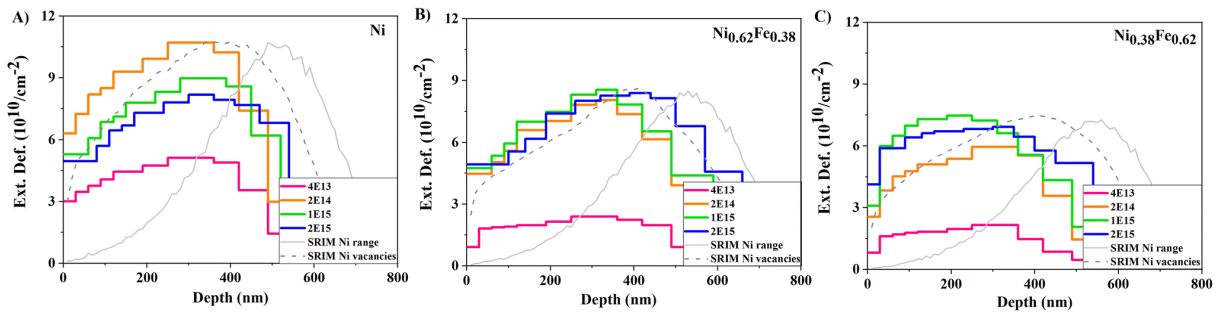


Figure 15. Damage distribution profiles obtained from the MC simulations performed for RBS/C experimentally obtained spectra. Normalized to the maximal value of Ext. Def., SRIM predicted profiles of vacancies and ion ranges are plotted in a.u. Total vacancies are used to calculate fluence-related dpa values.

In Figure 15, the damage distribution profiles of Ni (Figure 15 A), $\text{Ni}_{0.62}\text{Fe}_{0.38}$ (Figure 15 B), and $\text{Ni}_{0.38}\text{Fe}_{0.62}$ (Figure 15 C) obtained from the MC simulations are shown. The presented histograms demonstrate the quantitative values of the extensive defect concentration leading to the dechanneling of the beam that was used to obtain the best fits of the simulation curves to the experimentally obtained data. Moreover, the depths of simulated defect distributions are close to the SRIM predicted damage profiles (vacancies and ion distributions are also plotted with the damage distribution profiles in Figure 15 A-C). In the case of pure Ni, the damage saturates at a fluence of 2×10^{14} ions/cm² (~ 0.63 dpa), and the depth of defect penetration at the maximum peak shifts to the left side. The damage accumulation peak was captured at ~ 250 nm for 3.16 dpa and at 300 nm for 6.3 dpa. The defect concentration and distribution seem to look different for the $\text{Ni}_{0.62}\text{Fe}_{0.38}$ specimen. At 0.1 dpa, damage starts to accumulate at a depth of 250 nm. For the 0.59 and 2.96 dpa levels, one can observe defect accumulation at a depth of 300 nm, and finally, for the 5.9 dpa level, the damage peak moves further into the material to 380 nm depth. In the case of $\text{Ni}_{0.38}\text{Fe}_{0.62}$, the smallest increase in the number of defects to other compositions has been observed. Moreover, the number of defects in $\text{Ni}_{0.38}\text{Fe}_{0.62}$ is about twice

as small as that in pure Ni. Importantly, defect accumulation at various depths may suggest defect type and migration ability changes. It is worth noting that in fcc Ni_xFe_{1-x} alloys, interstitial-type defects could be dumbbell interstitials, as reported in the following works^{12,68,107,108}. These defects are made of split pairs of atoms centered around one atomic position and could bend the crystal lattice locally. When aligned with the ion beam, it may lead to dechanneling of the He⁺ ions (instead of direct scattering). A similar effect can be observed near dislocation loops^{12,68,107,108}.

TEM analysis was performed to confirm the conclusions related to defect migration and their type drawn from the experimental results (nanoindentation, RBS/C) and MC simulations. Since ion irradiation is a depth-dependent phenomenon, microstructural evaluation of the damage distribution below the sample surface induced by ion irradiation is crucial. In Figure 16, cross-sectional TEM images of the three compositions (Ni, Ni_{0.62}Fe_{0.38}, Ni_{0.38}Fe_{0.62}) irradiated to two fluences of 4×10^{13} ions/cm² (Figure 16 A) and 4×10^{15} ions/cm² (Figure 16 B) are presented. Black defect clusters were observed from the sample surface to the extended depth, migrating much further than SRIM calculations predicted for the highest fluence. For the low irradiation fluence in the case of the pure Ni specimen, large defect clusters are distributed away from the surface and start accumulating from 220 to ~550 nm depth. In Ni_{0.62}Fe_{0.38}, we observe that defects tend to concentrate mainly from 250 nm up to 400 nm. Furthermore, unlike to Ni and Ni_{0.38}Fe_{0.62}, disparate types of defects have been noticed in Ni_{0.62}Fe_{0.38}. One can see mainly longitudinal lines (edge dislocations) and small defect clusters, whereas, in Ni and Ni_{0.38}Fe_{0.62}, we observe defect clusters in the form of SFTs and dislocation loops. In the case of Ni_{0.38}Fe_{0.62}, the black defect clusters are visible and (almost) evenly distributed from the sample surface to the greater depths of the sample, where TEM analysis was performed. The defect range in all three compositions aligns with the SRIM estimations. However, the damage peak range shifts towards the surface when increasing the iron content up to 38 at%. For the highest fluence in the case of pure Ni, the defect clusters far exceeded the SRIM predicted depth (including the maximum defect range estimated at 800 nm), reaching 1000 nm of depth. Interestingly, we observe concentration of defects phenomenon at high irradiation fluence, similar to Ni_{0.62}Fe_{0.38} at low fluence.

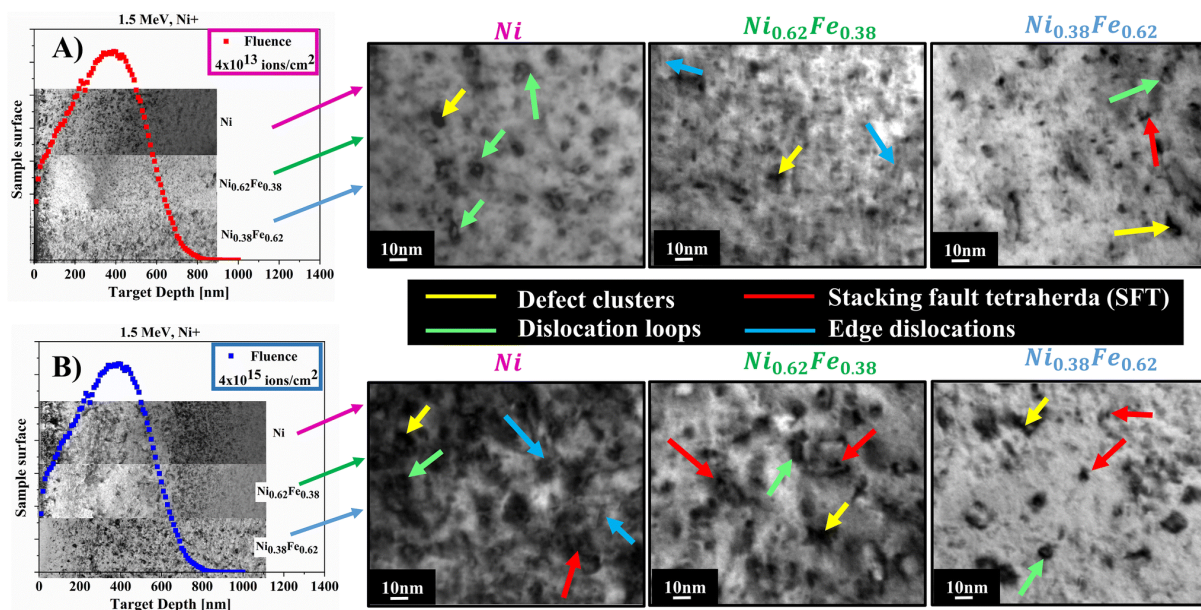


Figure 16. Cross-sectional TEM images of the Ni, $\text{Ni}_{0.62}\text{Fe}_{0.38}$, and $\text{Ni}_{0.38}\text{Fe}_{0.62}$ irradiated with various fluences A) 4×10^{13} ions/cm² and B) 4×10^{15} ions/cm² compared with SRIM calculations. In the bright-field images located on the right side, some typical defects like SFT (marked with red arrows), dislocation loops (marked with green arrows), edge dislocations (marked with blue arrows), and defect clusters (marked with yellow arrows) have been indicated.

With increasing Fe addition, the defect range decreases (Figure 16 B), for $\text{Ni}_{0.62}\text{Fe}_{0.38}$, reaching 800 nm. However, the defects aggregate in one place at around 700 nm. The reason why a damage peak shift was observed in $\text{Ni}_x\text{Fe}_{1-x}$ comparing to Ni is because the ion irradiation causes high mechanical stress, where the ions may propagate toward the bulk of the material. These stresses may drive the defects to migrate either toward the surface or further in the material bulk. As a result, we observe defect migration with an increased ion fluence as they generate a higher stress gradient due to the high amount of Ni ions implanted into the sample. The highest stress gradient is located at the center of the implanted layer (in our case, according to SRIM simulations, the damage peak was located at a depth of 400 nm). Moreover, the migration mechanism could result from a combination of processes such as defect recombination, production, cluster formation etc. as reported in ⁹⁹. In this study, we observed that Fe addition could influence energy transport during ion irradiation through electrons on the defect formation and distribution. Therefore, a damage peak in $\text{Ni}_x\text{Fe}_{1-x}$ is slightly shifted because Fe suppresses damage and stress induced by ion irradiation

Interestingly, in the case of $\text{Ni}_{0.38}\text{Fe}_{0.62}$, both for high and low fluences, we observe an even distribution of defects from the surface towards the material bulk (without a clear zone of defect accumulation). This phenomenon may undoubtedly suppress strain localization when material is being deformed. In the case of other compositions, where the area of defect accumulation is visible, material delamination or cracking in this region may occur.

TEM bright-field (BF) micrographs of irradiated samples are shown in Figure 16 A and B. Most defects visible for all the compositions are black clusters, dislocation loops, edge dislocations, and vacancy-type stacking fault tetrahedra (SFT). The BF images show that black dot defects agglomerate into larger dislocation loops and are further transformed into dislocation networks. This is in line with the RBS channeling spectra in which we observed decreasing backscattering yield for different fluences related to the reduction of lattice strain.

From the cross-sectional TEM images, several phenomena can be observed. It is clear that with increasing irradiation fluence, the range of defect distribution also increases and significantly exceeds the SRIM predicted range, which indicates that the defect migration mechanism changed due to a high level of mechanical stress induced by ion irradiation. As a result we observe defect migration towards the material bulk with an increased ion fluence because more Ni ions are implanted into sample. Moreover, migration mechanism may be a result of combination processes like defect recombination, production, cluster formation etc. which are especially visible at high fluence regime. Second, we observed that the addition of iron appreciably affects the distribution of defects in the material. It effectively stops the migration of defects. Similar behavior has also been reported in ¹¹. Moreover, this mechanism was explained as vacancies preferring migration through Fe atoms and interstitial migration through Ni atoms ⁵⁴. It was also reported that, in Ni_xFe_{1-x} binary systems, all sinks concentrate more Ni atoms, which influences the further interaction of mobile defects with voids and dislocations. Therefore, an increase in void size and the rise of dislocations are observed ⁵⁴.

Usually, the microstructural study of the irradiated alloy consists of three stages ¹⁰⁹. At a low ion irradiation regime (≤ 1 dpa), visible black dot defects could appear, and their density and average size increased with ion fluence. Meanwhile, the black dot defects also developed into larger ones, but their density decreased. The dislocation loops are formed at a higher ion irradiation regime (> 1 dpa) and grow into larger loops. With increasing irradiation dose, the loop diameter increases, and they may coalesce with each other to form larger dislocation networks ^{23,109}.

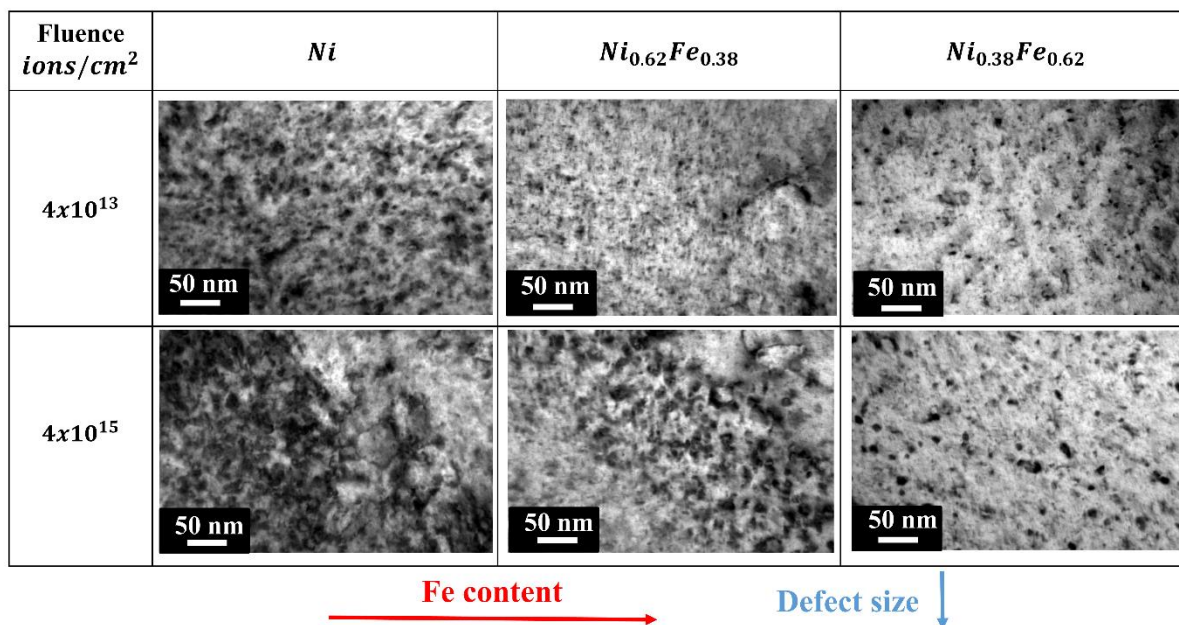


Figure 17. TEM images of A) Ni, $\text{Ni}_{0.62}\text{Fe}_{0.38}$, and $\text{Ni}_{0.38}\text{Fe}_{0.62}$ irradiated with the fluence of $4 \times 10^{13} \text{ ions}/\text{cm}^2$ and $4 \times 10^{15} \text{ ions}/\text{cm}^2$.

In the case of Ni and $\text{Ni}_x\text{Fe}_{1-x}$ single crystals ($\text{Ni}_{0.62}\text{Fe}_{0.38}$ and $\text{Ni}_{0.38}\text{Fe}_{0.62}$), slightly different dependencies related to the amount of Fe element were captured. In Figure 17, TEM images of the irradiated Ni, $\text{Ni}_{0.62}\text{Fe}_{0.38}$, and $\text{Ni}_{0.38}\text{Fe}_{0.62}$ with fluences of $4 \times 10^{13} \text{ ions}/\text{cm}^2$ and $4 \times 10^{15} \text{ ions}/\text{cm}^2$ are presented. All the images were taken from the peak damaged regions. Mostly large defect clusters and dislocation loops are observed for the low irradiation fluence in pure Ni. As the Fe content increases up to 38%, dislocation lines and vacancy type single stacking fault tetrahedra (SFT) with a size of a few nanometers become visible. In $\text{Ni}_{0.38}\text{Fe}_{0.62}$, small defect clusters and SFT defects are primarily observed. Moreover, an evident change in the defect size is visible with the addition of iron content. A calculation of defect size based on the TEM images was to confirm these findings. The analyses proved that the defect size decreases in alloys with higher Fe content (Figure 18 A), both at low and high fluence.

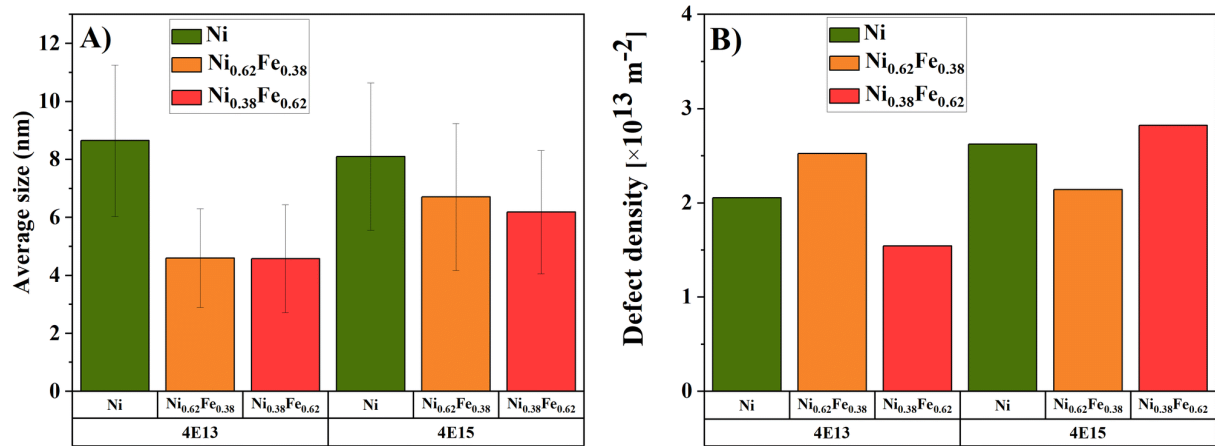


Figure 18. Average defect size calculated based on the TEM images, B) defect densities for the Ni, $\text{Ni}_{0.62}\text{Fe}_{0.38}$, and $\text{Ni}_{0.38}\text{Fe}_{0.62}$ irradiated to the fluence of 4×10^{13} ions/cm² and 4×10^{15} ions/cm².

Moreover, defect densities have been calculated to better understand the defect configuration for various binary compositions. Calculations have been made based on the TEM images taken at the peak damaged region. For this measurement, lamellae thickness has been measured in this region only. The densities were calculated by counting the number of defect sizes in a unit volume of crystalline material. Obtained defect density values (see Figure 18 B) show that for low fluencies, the defect density increases for pure Ni and $\text{Ni}_{0.62}\text{Fe}_{0.38}$. In the case of $\text{Ni}_{0.38}\text{Fe}_{0.62}$, this parameter decreases. One can see that the size of defects decreases with the addition of iron. For large damage levels, the defect density increases for $\text{Ni}_{0.38}\text{Fe}_{0.62}$, while for $\text{Ni}_{0.62}\text{Fe}_{0.38}$, the opposite trend has been recorded.

Usually, when irradiation damage increases, the dislocations disappear, and the density of the small interstitial-type loops or clusters increases¹¹⁰. Interestingly, the densities of network dislocations and dislocation loops number increased with the irradiation dose. For this reason, these defects could work as defect sinks that could absorb the black spot damage. Therefore, more black spots would dissolve in the sinks when the network of dislocations and dislocation loops increased. Moreover, a part of the enlarged neighboring black spots may coalesce into more prominent spots during irradiation, further decreasing their number^{110,111}.

The results distinguish the current strategy, i.e., finetuning composition in single crystal system, from conventional defect reinforcement strategies. It means that if single crystals are designed using a reasonable composition, the single crystals can have potentials for extreme radiation applications.

A.6 Conclusions

The results show that manipulation of the Fe content and leveraging the original Bridgman production method influence the overall radiation response of the Ni_xFe_{1-x} binary single crystals. The mechanical results indicate an increase in initial hardness with Fe content up to 38 at%. Then, above ~40 at% Fe, a decrease is visible. This may be due to the combination of differences in the dislocation nucleation mechanisms during indentation and the defect sizes. Interestingly, another possible way to explain the hardness change over the various Fe compositions could be associated with a phase change of single crystals because Ni_{0.62}Fe_{0.38} could be a mixture of the FeNi (L1₀)+FeNi₃ (L1₂) phase, and Ni_{0.38}Fe_{0.62} could be a combination of the Fe₃Ni (L1₂)+FeNi (L1₀) phase. The different arrangements of Fe atoms in a crystal structure may influence the hardness performance with increasing Fe content. However, more structural data are needed to prove those phases in the presented compositions. This also should be validated by numerical calculations. Importantly, these characteristics impact the irradiation hardening mechanism for ion-irradiated compositions. The reason for the better radiation resistance of Ni_xFe_{1-x} is most probably related to the physical nature of the iron atomic nucleus in its excited state (during irradiation), as it possesses only one orbital with unpaired electrons, while Ni has three orbitals. This means that Ni possesses more space for electron movements and, thus, defect generation and mobility. Therefore, Fe effectively suppresses damage and stress induced by ion irradiation. The different arrangement of Fe atoms in a crystal structure may also influence the obtained characteristics of Ni_xFe_{1-x} after ion implantation.

TEM analysis revealed no defect accumulation zone (characteristic damage peak) at either low or high fluences (0.1 dpa and ~12 dpa) in Ni_{0.38}Fe_{0.62}. The observed defects are evenly distributed toward the material bulk from the surface to greater depths. A uniform distribution of defects is an additional advantage of Ni_{0.38}Fe_{0.62} because it may suppress strain localization during deformation compared to Ni_{0.62}Fe_{0.38}.

Based on the obtained results, we propose performing a more detailed structural analysis and molecular dynamics simulations to prove the Fe atom arrangement change in a crystal lattice of fcc Ni_xFe_{1-x} single crystals. The results lay a solid foundation for developing advanced single crystals with strong radiation resistance.

Article B:

***The Fe addition as an effective treatment for improving
the radiation resistance of fcc Ni_xFe_{1-x} single-crystal alloys***

E. Wyszowska, C. Mieszczyński, Ł. Kurpaska, A. Azarov, W. Chromiński, I.
Jóźwik, A. Esfandiarpour, A. Kosińska, D. Kalita, R. Diduszko, J. Jagielski, S. T.
Nori, M. Alava,

Journal of Nuclear Materials, 584 (2023) 154565, DOI:

10.1016/j.jnucmat.2023.154565

IF: 3.55, Ministry Points: 100

This is an open access article distributed under the terms of the [Creative Commons CC-BY](#) license, which permits unrestricted use, distribution, and reproduction in any medium, provided the original work is properly cited.

Published by Elsevier B.V.

B.1 Abstract

In this work, five different compositions of *fcc* Ni and Ni_xFe_{1-x} single crystal alloys namely Ni, Ni_{0.88}Fe_{0.12}, Ni_{0.77}Fe_{0.23}, Ni_{0.62}Fe_{0.38}, Ni_{0.38}Fe_{0.62} were irradiated by 1.5 MeV ⁵⁸Ni ions at room temperature in a wide fluence range (4×10^{13} to 4×10^{15} ions/cm²). The role of Fe addition on the radiation resistance of the Ni_xFe_{1-x} single crystals was studied by hybrid Monte Carlo/ Molecular dynamics simulations combined with transmission electron microscopy (TEM), ion channeling technique (RBS/C) and nanoindentation techniques. The Multi-Step Damage Accumulation analysis revealed the cross-sections for damage formation significantly decreases for Ni_{0.38}Fe_{0.62} and Ni_{0.62}Fe_{0.38} as compared to that in pure Ni single crystal, which is consistent with RBS/C and TEM results. The results of nanoindentation show that Ni_{0.62}Fe_{0.38} alloy possesses the highest hardness (2.96 GPa) among the other compositions in a pristine state. To interpret this result, hybrid Monte Carlo/ Molecular dynamics simulations were used to check the presence of the ordered crystal phase structure for Ni_xFe_{1-x} binary alloys. The simulation results have shown that depending on the iron content, we deal with different amounts of FeNi₃ (L1₂) phase. This result revealed that in Ni_{0.62}Fe_{0.38} alloy, nanoprecipitate FeNi₃ (L1₂) phase (around 20%) is formed inside the disordered matrix, which could be one of the main reasons for the high hardness of this alloy before irradiation.

Additionally, we have found adding iron reduced the number and size of the defects (as a result of ion irradiation) in Ni_xFe_{1-x} because the Fe element is more stable than Ni, which results from the electron configuration of both elements in the excited state. Therefore, the more iron in the material, the fewer defects are created.

Keywords: Nanoindentation, fcc Ni_xFe_{1-x} single crystals, TEM, Ion channeling, MC/MD Simulations

B.2 Introduction

Structural materials for the next generation fission reactors must meet various requirements to ensure their safe operation. In particular, the radiation resistance of such materials is essential. Radiation damage in crystalline materials has been studied extensively for decades ⁴. This has been originally motivated to control neutron irradiation-induced degradation of fission reactor materials. The macroscopic material degradation is fundamentally a manifestation of the evolution of the radiation damage-induced defects. Three processes can describe the evolution of radiation-induced defect concentrations in metals across the primary and secondary damage

stages: (a) defect production from atomic collision cascades; (b) consecutive vacancy-interstitial recombination; and (c) point defect absorption by different types of sinks like dislocations and grain and phase boundaries⁷. The point defects that survive recombination and sink absorption may cause different effects. For example in the case of surrogate irradiation via heavy ions, defects may migrate both into the bulk material and to the surface at a high level of mechanical stress induced by ion irradiation. This can result in an extended damage region due to enhanced defect migration with increasing ion fluence. Thus, point defects can diffuse and subsequently generate dislocation loops⁸ and stacking fault tetrahedrons (SFT) under the stress gradient, depending on the material.

Additionally, the formation of large vacancy clusters significantly worsens the performance of materials, as vacancies may lead to void swelling. Therefore, controlling vacancy migration and effectively annihilating vacancies is crucial in selecting new advanced structural materials for nuclear applications^{9–11}. Thus, it is critical to understand the defect dynamics; however, research focused on enhancing defect recombination and controlling defect migration¹² in metallic alloys is meager. There is evidence that tuning the chemical composition of a single-phase alloy may significantly change the features of defect clusters⁸, which needs to be elaborated. Furthermore, the defect clusters may lead to macroscopically observable degradation effects, such as irradiation hardening, embrittlement, and irradiation-induced creep. These phenomena adversely affect materials used in advanced Generation IV fission and fusion reactors. This is because the materials are subjected to harsh operating conditions such as temperatures in excess of 600°C, high radiation fluences (around 50 displacements per atom (dpa)), high-mechanical stresses, and corrosive environments^{1,13,14}. Conventional metal alloys such as ferritic and austenitic stainless steel fail under such reactor conditions due to the effects mentioned above. Thus, the selection of new materials needs special attention for high radiation tolerance in a wide fluence range, high thermal and phase stabilities, and good mechanical properties⁹. Despite that materials for advanced reactors have been intensively studied during the past decade^{2,10,13,15–18}; there is still an emerging research field with great scope for exploration. Hence, in the present work, we focus on the investigation of novel metallic alloys for advanced nuclear reactor structural material applications and their assessment to understand defect dynamics and mechanical properties.

The new class of single-phase concentrated solid solution alloys (CSAs), including high entropy alloys (HEAs), exhibits remarkable mechanical, chemical, and magnetic properties, including high yield strength, fracture toughness, wear resistance, and corrosion resistance, compared to

conventional alloys^{4,36,38–40}. The Ni_xFe_{1-x} (x= atomic percentage of Ni) single crystal alloys are promising materials, which can withstand demanding environments, such as the structural materials for nuclear applications where high radiation tolerance is of primary concern^{9–11}. Understanding the irradiation response and material degradation level is still a great challenge especially the urgent analysis is necessary for initial damages up to 1 dpa and higher damages of the order of 10 or even 20 dpa^{1,14}. Initial studies of Ni_xFe_{1-x} alloys have demonstrated the formation of dislocation loops and stacking fault tetrahedral defects^{7–11,13,31}. Therefore, the proposed work would launch a state-of-the-art examination of Ni and Ni_xFe_{1-x} single crystal alloys. These are promising materials due to their extraordinary mechanical properties and high radiation tolerance related to simple structure, Fe element and lack of grain boundaries^{7–11,13,31}. In the present work, we use Rutherford backscattering/-channeling spectrometry (RBS/C) for qualitative evaluation of radiation damage or the Multi-Step Damage Accumulation (MSDA) analysis to reveal damage kinetics for each of the proposed compositions. The RBS/C technique allows for assessing the radiation damage level for different compositions in various fluences^{21,105}. In addition, the defect sizes and densities were studied with Transmission Electron Microscopy (TEM) in Ni_xFe_{1-x} single crystals. The nanoindentation technique was used to record mechanical properties such as hardness as a function of irradiation fluence and Fe concentration. Nanoindentation of irradiated materials is an emerging research avenue with inadequate understanding, and our research could contribute to its development. Moreover, the presence of the ordered crystal phase structure for Ni_xFe_{1-x} binary alloys by using atomistic simulation has been checked by performing hybrid Monte Carlo/ Molecular dynamics simulations.

In general in our research, we are conducting a parametric study individually for Fe addition, temperature, and irradiation dose. In the current work, we focus on Fe addition and irradiation dose; thus, the Fe implantation was conducted at room temperature. Moreover, since the defect density is relatively less and the defects are rather less mobile at room temperature, it provides an opportunity to understand the defect formation and evolution better via combining experimental and modeling efforts.

B.3 Material and Methods

B.3.1 Material Production and Sample Preparation

The *fcc* Ni and Ni_xFe_{1-x} single crystal alloys with different amounts of Fe (12, 23, 38 and 62 at%) were produced at NCBJ¹⁰⁰ using the vertical temperature gradient method (also called the Bridgman method¹⁰¹). In this method, metals with high melting temperatures, such as Ni and Fe, are melted and crystallized in an alundum crucible in an Ar gas protective atmosphere using a Mo wire heating element. The crystallization process utilized a slow lowering rate of ~1 to 2 cm/hour of the crucible, delivering one single crystal per ~30 hours. Samples were then cut along [001] direction, ground, and polished before ion irradiation. Firstly, mechanical grinding was performed using abrasive papers with grit sizes from 400 to 4000. Secondly, polishing to a mirror-like surface finish was achieved using diamond pastes with a grain size of 6 μm, 3 μm, and 0.5 μm and subsequent electro-polishing (Struers LectroPol-5) with 60% Perchloric acid electrolyte to reduce stresses generated by mechanical polishing. The electro-polishing time was set to 60 s and an electric potential of 30 V.

B.3.2 Ion Irradiation

All the specimens produced and prepared per the methodology mentioned in 2.1 were subjected to ion irradiation according to the parameters obtained by SRIM code⁶⁴ simulation (predicted damage depth, ions, energy). The irradiations were carried out at room temperature with 1.5 MeV ⁵⁸Ni⁺ ions using a 1 MV tandem accelerator (National Electrostatics Corporation, model 3SDH-2) in the University of Oslo. All ion irradiations were performed in a raster scanning mode. The beam current was kept constant at a relatively low value of ~50 nA/cm² corresponding to the ion flux of ~3e11 at/cm² s, to avoid sample heating during implantation. The Ni⁺ ions were chosen for irradiation because Ni is one of the major alloying elements in the Ni_xFe_{1-x} system. Therefore, there is no introduction of impurities during radiation damage buildup. Furthermore, in structural materials, there is an SIA cluster evolution bias due to their higher migration rate compared to vacancy clusters under irradiation. Self-ion implantation (Ni in this case) can further enhance this bias; however, the concentration of Ni ions implanted is insignificant compared to the SIAs created due to the radiation damage event. Thus, self-ion-induced defect evolution can emulate neutron irradiation effects albeit slower due to room

temperature effect. The irradiations were performed at an inclination of 7 degrees to the normal direction of the samples to avoid channeling.

The corresponding displacement per atom (dpa) profiles were predicted by the SRIM code for all elements using the full cascade mode. The dpa has been calculated based on the following equation according to recommendations of ^{66,69}.

$$dpa = [fluence (ions/cm^2) \times total\ vacancies/A-ion \times 10^8] / atomic\ density (atoms/cm^3) \quad (1)$$

The mean projected ranges of ions and induced defect distributions (estimated by SRIM simulations ^{66,68} for Ni and Ni_{0.38}Fe_{0.62} are shown in Figure 19 A and B.

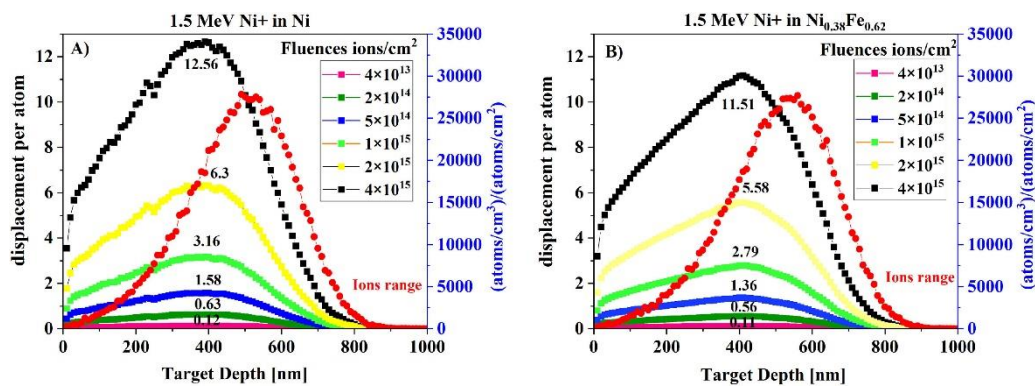


Figure 19. Damage profiles of (A) Ni and (B) Ni_{0.38}Fe_{0.62} irradiated with 1.5 MeV of Ni⁺ at fluences of 4×10^{13} , 2×10^{14} , 5×10^{14} , 1×10^{15} , 2×10^{15} , and 4×10^{15} ions/cm².

The ion distribution was estimated from the RANGE.txt file. The corresponding dpa profiles were calculated using two files, VACANCY.txt and NOVAC.txt, under an assumed displacement energy threshold of 40 eV for all elements. The dpa profile is the sum of the vacancy concentrations using the column of “Knock-Ons” for Ni ions and the columns of “Vacancies” from target elements (the sum of Ni vacancies and Fe vacancies in the case of Ni_xFe_{1-x}) in VACANCY.txt, together with the replacement collisions in NOVAC.txt. ⁶⁷. Ion-induced damage in monoatomic and multielemental targets was predicted using full-cascade simulations ^{66,68}. The SRIM-estimated damage peak is located at a depth of approximately 400 nm.

B.3.3 RBS/C (ion channeling) and MSDA model

After irradiation, the samples were examined by the RBS/C using 1.6 MeV He⁺ ions along the [001] direction and backscattered into a detector placed at 165° relative to the incident beam direction. RBS/C measurements were performed using 1 MV tandem accelerator (National Electrostatics Corporation, model 3SDH-2) in the University of Oslo. The RBS/C spectra for

pure Ni and Ni_xFe_{1-x} alloys irradiated with different fluences were simulated using the Monte Carlo McChasy code developed at the NCBJ^{66,103}. The energy of the backscattered particle can be directly related to the depth at which the close encounter scattering event occurred. The bulk scattering arises from particles that have been deflected atomic rows and have crossed over to another row, where they undergo a close-encounter event. To reveal the damage kinetics for investigated alloys the Multi-Step Damage Accumulation (MSDA) analysis was performed^{90,92}. This model is based on the equation assuming that the damage accumulation occurs through a series of structural transformations caused by the destabilization of the present crystal structure.

B.3.4 Hybrid MC/MD simulation

The possibility of formation of the ordered crystal phases was verified for Ni_xFe_{1-x} binary alloys by using hybrid Monte Carlo/ Molecular dynamics (MC/MD) atomistic simulation. We start the simulation with a random distribution of Ni and Fe atoms in the matrix for each Ni_xFe_{1-x} alloy. Such a random distribution cannot necessarily reproduce thermodynamically stable local atomic structure and hence, the simulations reveal an equilibrated stable system with the least potential energies. The hybrid MC/MD algorithm^{87,88} was employed to facilitate thermally induced kinetics and anneal each alloy system. To perform such a simulation, we utilized LAMMPS⁷⁴ and modified embedded atom method (MEAM) interatomic potential¹¹², which reproduced the phase diagrams of Ni_xFe_{1-x} binary alloys. For each composition, a simulation cell with *fcc* crystal and random distribution of constituent elements was created containing 32000 atoms. Periodic boundary conditions are applied in all three directions. After minimization of each system using the conjugate gradient algorithm, it is equilibrated at 300 K using the NPT ensemble. We used the following hybrid MC/MD steps⁸⁸:

- 1- Two different atom types (Fe and Ni) are selected randomly in the simulations and tried to swap the position so that the kinetic energy keeps constant by swapping.
- 2- Metropolis criterion is used and each swap attempt is accepted if $\epsilon < \frac{P_f}{P_i}$, where ϵ is a random number between [0,1] and $P_i = e^{-\beta U_i}$, where β is the inverse of $k_B T$ and U_i is the potential energy of the system. Swapping is tried 200 times.
- 3- To relax any local residual stress induced by swapping, 50 molecular dynamic time steps under constant pressure (NPT) conditions are performed.

We repeat these three steps until we reach reasonable convergence of the system's potential energy. The ordered crystal structures are analyzed using a polyhedral template matching algorithm⁸⁹ that is implemented in OVITO software⁸⁵.

B.3.5 Nanoindentation

Nanoindentation was performed utilizing the Micro Materials Ltd NanoTest Vantage system using a Synton-MDP diamond Berkovich-shaped indenter. The preliminary tests were conducted in multiple load cycles with increasing load from 0.5 mN up to 10 mN (in total ten cycles) using load controlled method. At least 16 indentations were made at each load with 50 μm spacing between the indents. Before starting the indentation campaign, a Diamond Area Function (DAF) of the indenter tip is calculated. The calibration is performed using Fused Silica material in a wide load range to assess a reliable indenter shape for a given indentation depth.

B.3.6 TEM Analysis

Suitable electron transparent lamellae were prepared from the area of interest of the samples via a focused ion beam/scanning electron microscope (FIB/SEM) for TEM microstructural studies. A lift-out procedure was utilized in FIB (Ga⁺) installed in Helios 5 UX (ThermoFisher Scientific) microscope at NCBJ. Final thinning of the lamellae was performed with 5 keV Ga⁺ ions followed by 2 keV Ga⁺ gentle polishing. TEM observations were performed with the JEOL JEM1200EX II microscope operated at 120 kV. Since ion irradiation is depth-dependent, evaluating the damage distribution below the sample surface induced by ion irradiation is crucial. All the lamellae have been cut perpendicularly to the ion irradiated surface to reveal the damage distribution into material up to the 2 μm depth. Afterward, images of the most degraded regions have been taken at 500k magnification to perform a detailed analysis of the type of the defects, sizes and calculate the defect densities. The two-beam convergent beam electron diffraction technique was used to determine lamellae thickness (for dislocation density statistics)¹⁰⁴. TEM bright-field (BF) micrographs of irradiated samples were obtained. The size of the defects and defect densities were calculated based on these TEM images, especially from the peak damaged regions. Observations were conducted under a diffraction vector of $g=200$ for BF and WBDF g -3 g imaging.

B.4 Results

B.4.1 RBS/C channeling

The RBS/C spectra were fitted using McChasy code, a Monte Carlo simulation package allowing the quantitative analysis of channeling spectra. A detailed description of RBS spectra analysis can be found in our previous study^{66,103}. The materials responses (Ni, Ni_{0.88}Fe_{0.12}, Ni_{0.77}Fe_{0.23}, Ni_{0.62}Fe_{0.38}, Ni_{0.38}Fe_{0.62}) to the fluence of 4×10^{13} ions/cm² (~0.1 dpa), 2×10^{14} (~0.5 dpa), 1×10^{15} (~3 dpa) and 2×10^{15} ions/cm² (~6 dpa) are shown in Figure 20 A, B, C and D respectively. To facilitate an interpretation of the results, the reference "virgin" and "random" spectra are marked in the graph. The virgin spectra reflects undamaged crystal (the backscattering yield is low) while the "random" spectra correspond to the amorphous material (with a high level of lattice distortion). When the irradiation damage in the material appears, the backscattering yield is increasing. The variation of backscattering yield depends on the general lattice distortions in the implanted material. Therefore, we observe an increased backscattering yield with increasing lattice disorder.

For the fluence of 4×10^{13} ions/cm² the highest backscattering yield is visible for pure Ni, indicating an efficient defects accumulation in this material. In turn, for the fluences of 2×10^{14} and 1×10^{15} ions/cm² the level of lattice distortion is growing for all the compositions (visible an increased backscattering yield), however, for Ni_{0.62}Fe_{0.38} and Ni_{0.38}Fe_{0.62} yield is the lowest. At 2×10^{15} ions/cm², the spectra of pure Ni, Ni_{0.77}Fe_{0.23} and Ni_{0.62}Fe_{0.38} overlap which means, damage saturation for these compositions has been achieved, while Ni_{0.38}Fe_{0.62} still remains the lowest. As we reported in our previous work⁷⁸ if the curves overlap, we are most likely dealing with similar defect sizes and similar densities. However, there are methods that can provide precise information on the size and density of defects, for example positron annihilation spectroscopy or doppler broadening spectroscopy. Detail description of these methods can be found here¹¹³. However, in our studies we provided only calculations based on TEM images as it also provide a reliable results. Moreover, it is worth emphasizing that Ni ions cause a significant lattice distortion at higher irradiation fluence (generating new defects and transforming from smaller to larger defects), which may lead to stress release and further affects the backscattering yield.

Interestingly, at the fluence of 1×10^{15} ions/cm² and 2×10^{15} ions/cm² an inverted intensity for Ni_{0.77}Fe_{0.23} has been recorded at the depth of 320 nm. Such tendency could be related to a

change in defect size. The shapes of the spectra up to the depth of 320 nm may indicate a predominance of point defects in Ni_{0.77}Fe_{0.23}. This also supported by TEM results (in section 4). Next, the spectra of Ni_{0.77}Fe_{0.23} and Ni_{0.62}Fe_{0.38} overlap each other for the fluence of 1×10^{15} ions/cm² while at 2×10^{15} ions/cm² an inversed intensity region is formed (backscattering yield of Ni_{0.77}Fe_{0.23} is lower than Ni_{0.62}Fe_{0.38}). This can be related to defects agglomeration into bigger dislocation loops, which are further transformed into dislocation networks.

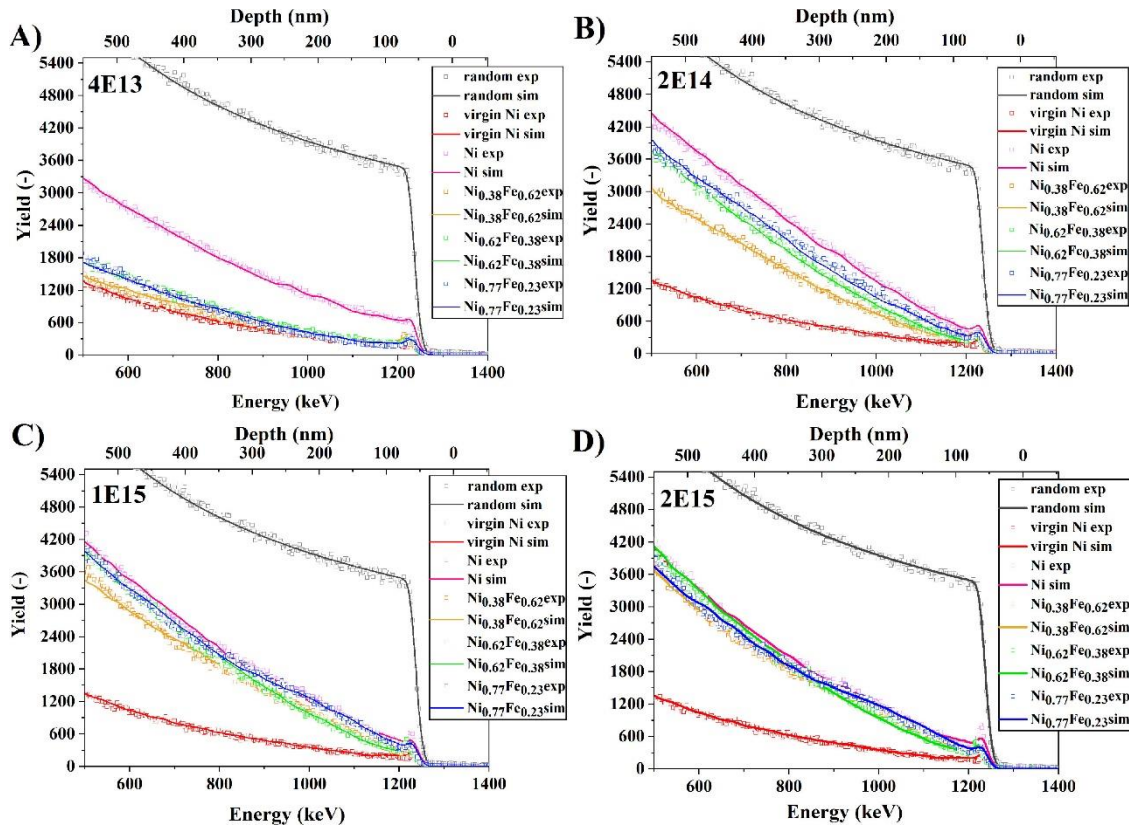


Figure 20. RBS/C spectra of Ni and Ni_xFe_{1-x} single crystal samples irradiated with 1,5 MeV of Ni⁺ to the fluences of A) 4×10^{13} , B) 1×10^{15} , C) 1×10^{15} and D) 2×10^{15} ions/cm². The intensities of the spectra were normalized to the highest Ni-random spectrum.

Figure 21 A-D shows the ion channeling spectra for pure Ni, Ni_{0.77}Fe_{0.23}, Ni_{0.62}Fe_{0.38}, and Ni_{0.38}Fe_{0.62} submitted to ion irradiation. For the fluence of 4×10^{13} ions/cm², a significant decrease in the yield was observed for the binary alloys suggesting a suppression of defects accumulation with increasing Fe content. Above the fluence of 2×10^{14} ions/cm² (about 0.63 dpa), for pure Ni, we observe full saturation with defects. For the higher fluences (1×10^{15} and 2×10^{15} ions/cm² (~3 to 6 dpa respectively)), the yield decreases, which means that the material is fully saturated. In the case of Ni_{0.77}Fe_{0.23} and Ni_{0.62}Fe_{0.38}, the saturation starts at the fluence of 1×10^{15} , while for Ni_{0.38}Fe_{0.62} we notice a gradual yield build-up with ion fluence, which suggests there is still a room for damage to increase.

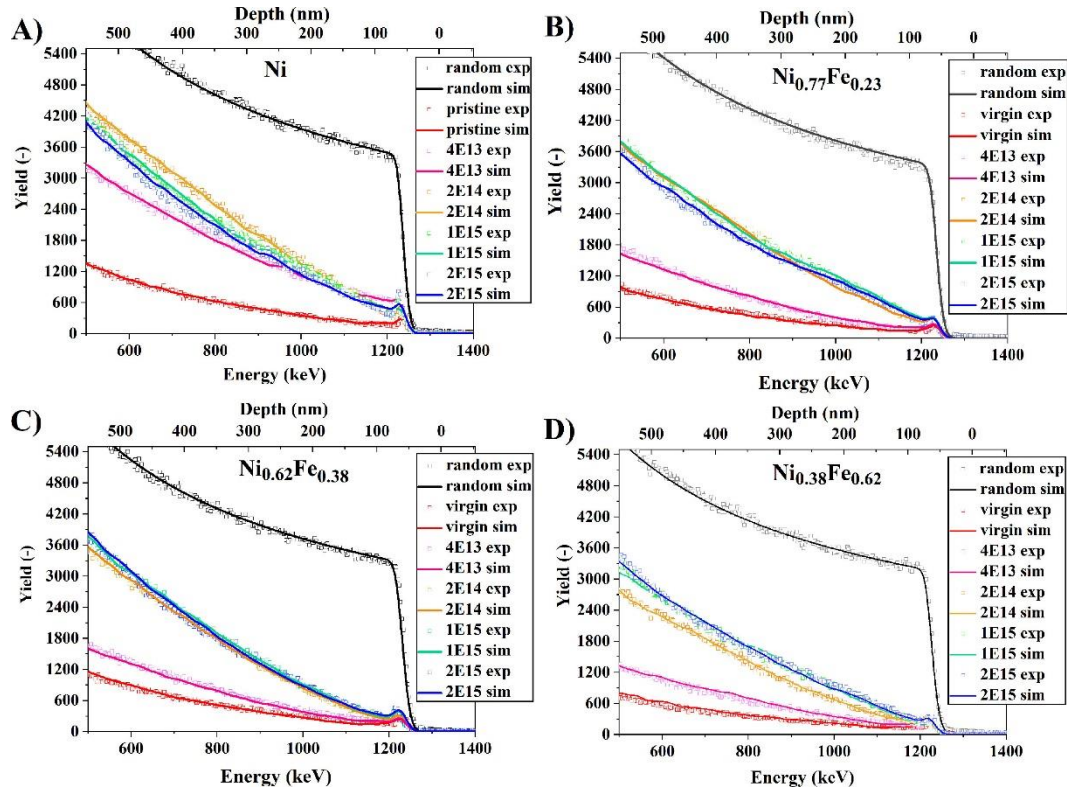


Figure 21. RBS/C spectra of A) Ni, B) Ni_{0.77}Fe_{0.23}, C) Ni_{0.62}Fe_{0.38}, D) Ni_{0.38}Fe_{0.62} single crystals irradiated with the fluences from 4×10^{13} to 4×10^{15} ions/cm². Solid lines represent fits obtained using MC simulations. Virgin and random spectra are included as references.

Usually, in metals, most of the defects are mainly extended defects, e.g., dislocations or stacking faults, which lead to the dechanneling of incident He ions²¹. It can be assumed that lattice distortion could be related to defect size and density change since smaller defects cause smaller lattice distortion than complex defects (defect cluster, dislocation), hence, backscattering yield changes. In pure Ni, a saturation dose has been obtained at a fluence of 2×10^{14} ions/cm². The saturation and a small decrease in channeling yield may occur because the defect structure becomes more organized at high fluence⁹⁹. For example, point defects are transformed into more complex structures, such as dislocation loops, or small dislocation loops are changed into larger defect clusters that release strain induced by ion irradiation. Therefore, we observe a decrease in backscattering yield. Moreover, one can notice different compositions reach saturation at different fluences. This means that the defect evolution is delayed by adding more Fe to Ni. This is related to both defect generation and defect growth. Usually, at higher irradiation fluence the generation of new defects and transformation from smaller to larger defects may occur. Moreover, adding Fe may effectively influence the energy transport during ion irradiation through electrons on the defect formation and distribution⁹⁹.

B.4.2 Damage kinetics

The MSDA analysis was performed to reveal damage kinetics for investigated materials; Ni, Ni_{0.77}Fe_{0.23}, Ni_{0.62}Fe_{0.38}, and Ni_{0.38}Fe_{0.62} and it is shown in Figure 22. Points in the figure are corresponding to maximal values of extended defects formed in irradiated materials. Solid lines are the fits made following the MSDA equation ^{66,90,92}:

$$f_d = \sum_{i=1}^n (f_{d,i}^{sat} - f_{d,i-1}^{sat}) G [1 - \exp(\sigma_i (\Phi - \Phi_{i-1}))] \quad (2)$$

where:

σ_i - cross-section for the formation of a given kind of defect

$f_{d,i}^{sat}$ - level of damage at saturation for i-th kind of defects

Φ_i - fluence threshold for triggering the formation of i-th kind of defects

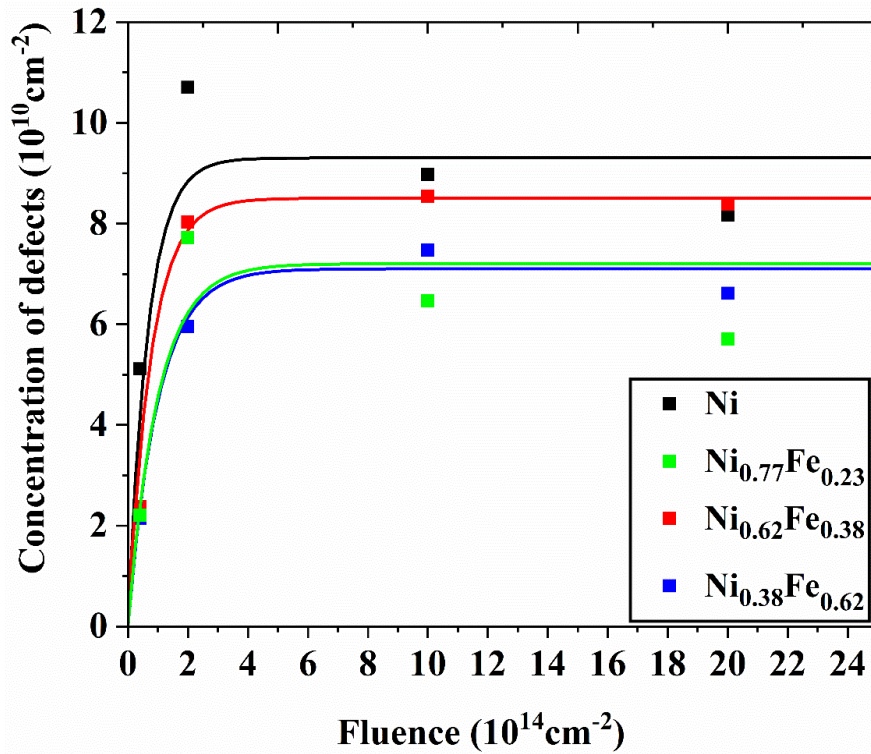


Figure 22. Damage kinetics for all investigated materials. Points represent the maximal values of extended defect distributions extracted from McChasy simulations, solid lines are fits to the experimental data using the MSDA model.

The decrease of cross-sections for defect formation for Ni_{0.38}Fe_{0.62} and Ni_{0.62}Fe_{0.38} alloys as compared to pure Ni single crystal is observed (see Table 3). The lower cross-section for damage formation Ni_{0.38}Fe_{0.62} alloys suggests the suppression of defect accumulation. Interestingly, Ni_{0.77}Fe_{0.23} shows a similar value of cross-section for defect formation as

Ni_{0.38}Fe_{0.62}. This is most likely related to the fact that for the MSDA model, we used the extended defects only. As we observed in Figure 20 B, C and Figure 21 B, the shape of the spectra indicated the occurrence of point defects in Ni_{0.77}Fe_{0.23} (up to the depth of 320 nm) in contrast to the rest of the tested compositions which is in line with MSDA calculations. As a result, the cross-section value for Ni_{0.77}Fe_{0.23} is lower (indicated in Table 3), since it consists of only extended defects and does not include the point defects contributing to the dechanneling level. Similar observation can be done for pure Ni structure. The consequence is a similar behavior of points in the MSDA model for Ni and Ni_{0.77}Fe_{0.23} alloy, which differs from the next two compositions.

Table 3. Cross-sections for defect formation extracted from the MSDA model

	$\sigma_I(10^{-14} \text{ cm}^2)$	$fd_I(10^{10} \text{ cm}^{-2})$
Ni	1.5	9.3
Ni _{0.77} Fe _{0.23}	1.0	7.2
Ni _{0.62} Fe _{0.38}	1.3	8.5
Ni _{0.38} Fe _{0.62}	1.0	7.1

A rapid increase in the number of defects at 0.5 dpa (see Figure 20 and Figure 21) has been noticed for all the compositions. The numbers of extended defects formed for low irradiation fluences are well below the values obtained for Ni. At higher irradiation fluences (1×10^{15} ions/cm² and 2×10^{15} ions/cm²) one can observe a decrease in defect concentration. This effect suggests a transformation of small loops into larger loops or defect clusters. A higher number of smaller defect structures leads to a more pronounced lattice distortion in their vicinity, as compared to one large dislocation loop containing the same number of defects and, hence, more efficient dechanneling of the analyzing beam.

Finally, we would like to point out, since the results for the Ni_{0.88}Fe_{0.12} composition practically coincided with Ni_{0.77}Fe_{0.23}, we did not include this composition in the RBS/C and MSDA studies to make the results more transparent.

B.4.3 Mechanical properties

Mechanical properties of Ni_xFe_{1-x} single crystal alloys have been evaluated using the nanoindentation technique. Indentation hardness as a function of contact depth for all the compositions is shown in Figure 23 A. It is seen that initial hardness is increasing up to 38 at% of Fe and then for 62 at% of Fe goes down below the hardness value of Ni_{0.62}Fe_{0.38} but it is

higher than Ni_{0.77}Fe_{0.23}. Moreover, one can notice the hardness values do not change with depth, which means we do not deal with the indentation size effect, therefore we can see almost flat curves. As we have already reported in our previous work ⁷⁸ the possible reason for hardness change with the addition of the Fe element could be related to the phase transformations. Depending on the temperature and atomic percentage of Fe (Ni), different phases such as a stable FeNi₃ (L1₂), metastable FeNi (L1₀), and unstable Fe₃Ni (L1₂) phase can be formed in the binary FeNi alloys ^{114,115}. Since it is hard to detect such phases with XRD, in this study we conducted some atomistic MC/MD simulations to see different ordered phases in Ni_xFe_{1-x} alloys (Section 3.4).

Mechanical response to ion irradiation has been recorded by performing a series of multicycle indentations of the irradiated Ni and Ni_xFe_{1-x} alloys. The results for individual fluences and compositions are presented as the average hardness value obtained in the load range of 0.5-10 mN. However, when considering the ion-irradiated specimens, we look at hardness values only from a depth between 40 nm to 150 nm. This methodology allows minimization of the impact of unmodified bulk material. However, it may be slightly misleading and provides unnaturally elevated hardness results as the damage profile changes over depth (it is graded). However, according to the author's experience, a much deeper damage profile (probably generated with energies around 8 MeV) should be done to capture the graded nature of the ion-irradiated later. Figure 23 B shows the hardness as a function of irradiation fluence for pure Ni and Ni with 12, 23, 38, and 62 at% of Fe. It can be seen that the hardness growth with increasing ion fluences is visible for all of the tested materials. At first, a very rapid increase in the hardness occurs at the fluence of 4×10^{13} ions/cm² (~ 0.1 dpa) and then gradually grows up to the fluence of 5×10^{14} ions/cm² (about 1.5 dpa). Afterward, the increment in hardness slightly decreases for all the alloys, however, the trend stays maintained. The smallest increase in hardness with fluence has been observed for Ni_{0.38}Fe_{0.62} and Ni_{0.62}Fe_{0.38} samples, while the most drastic increase has been observed for Ni, followed by Ni_{0.88}Fe_{0.12} and Ni_{0.77}Fe_{0.23}.

The Load-Displacement (L-D) curves obtained during multicycle indentation of irradiated *fcc* Ni, Ni_{0.88}Fe_{0.12}, Ni_{0.77}Fe_{0.23}, Ni_{0.62}Fe_{0.38}, and Ni_{0.38}Fe_{0.62} single crystal alloys at the fluences of 4×10^{13} ions/cm² and 4×10^{15} ions/cm² are presented in Figure 23 C and D, respectively. The hardness values in Figure 23 C-D originate from a depth of 100 nm. This probing depth allows for capturing relevant results, not distorted by artificial effects like, Indentation Size Effect (ISE) or indenter tip bluntness ^{116,117}. Therefore, to present the actual hardness values of the ion-implanted layer, taking into account the damage peak of about 400 nm (results estimated

from SRIM) and the ISE effect, the analysis of the area from this region is sufficient to describe the behavior of the irradiated material.

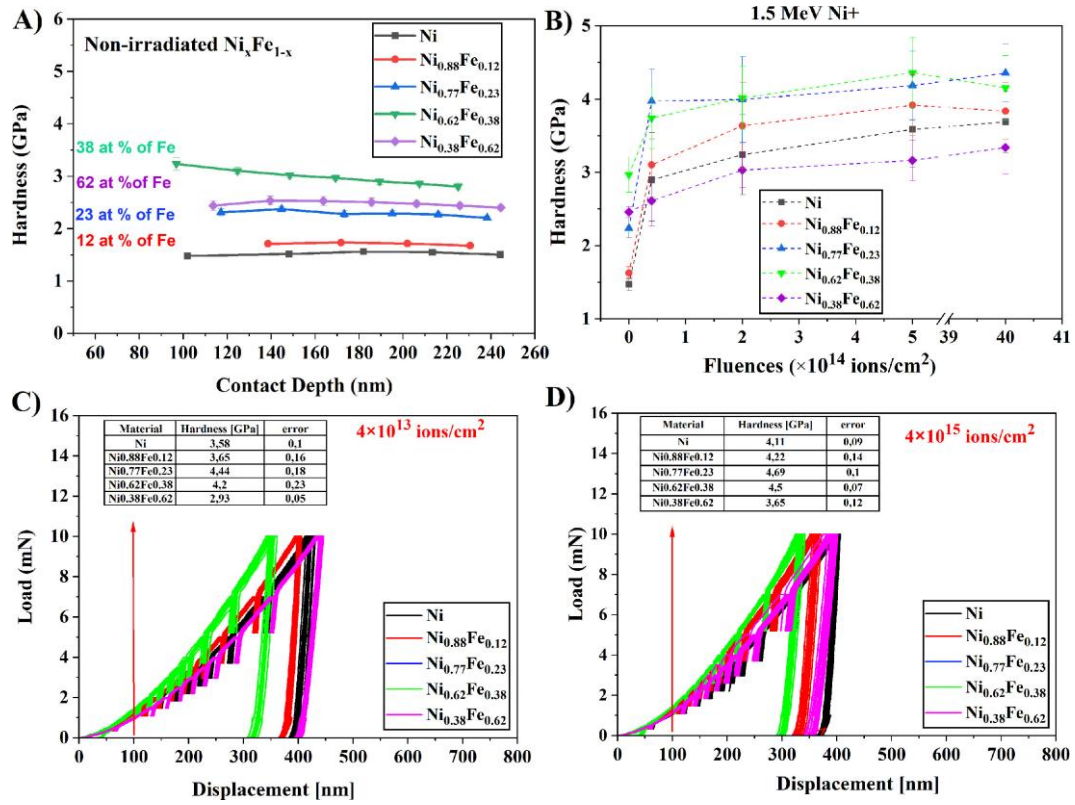


Figure 23. A) Nanoindentation hardness of pristine fcc Ni, $\text{Ni}_{0.88}\text{Fe}_{0.12}$, $\text{Ni}_{0.77}\text{Fe}_{0.23}$, $\text{Ni}_{0.62}\text{Fe}_{0.38}$ and $\text{Ni}_{0.38}\text{Fe}_{0.62}$ single crystal alloys as a function of contact depth, B) Nanoindentation hardness of irradiated fcc Ni, $\text{Ni}_{0.88}\text{Fe}_{0.12}$, $\text{Ni}_{0.77}\text{Fe}_{0.23}$, $\text{Ni}_{0.62}\text{Fe}_{0.38}$ and $\text{Ni}_{0.38}\text{Fe}_{0.62}$ single crystal alloys as a function of ion fluences, Load-Displacement curves obtained during multicyle indentation of the irradiated fcc Ni, $\text{Ni}_{0.88}\text{Fe}_{0.12}$, $\text{Ni}_{0.77}\text{Fe}_{0.23}$, $\text{Ni}_{0.62}\text{Fe}_{0.38}$ and $\text{Ni}_{0.38}\text{Fe}_{0.62}$ single crystal alloys with the fluences of C) 4×10^{13} ions/ cm^2 and D) 4×10^{15} ions/ cm^2 .

Obtained data show that pure Ni (Figure 23 C-D) is the most sensitive to ion radiation as compared to other compositions. According to the results shown in the tables (Figure 23 C), it can be seen that the hardness at the fluence of 4×10^{13} ions/ cm^2 (0.1 dpa) is increasing up to 23 at% of Fe element and then goes down for $\text{Ni}_{0.62}\text{Fe}_{0.38}$ and $\text{Ni}_{0.38}\text{Fe}_{0.62}$ respectively. The same trend appears for the fluence of 4×10^{15} ions/ cm^2 (Figure 23 D) (damage of ~ 12 dpa) with higher hardness values, which suggests that the Fe element effectively suppresses irradiation damage. Importantly, the L-D curves show a similar trend in terms of the hardness values presented in Figure 23 A and B. As we pointed out above, the reason for the different mechanical response of the alloys after irradiation might be related to different arrangements of Fe atoms in a crystal structure resulting from the presence of different phases.

B.4.4 Hybrid MC/MD simulation

Figure 24 A shows the potential energy per atom with respect to the random distribution of atoms in the alloys as a function of the number of swap attempts normalized by the total number of atoms. It is seen from Figure 24 A that for $\text{Ni}_{0.77}\text{Fe}_{0.23}$ there is the highest drop in potential energy before convergence while for $\text{Ni}_{0.38}\text{Fe}_{0.62}$ the drop of energy is the least. This means that thermodynamically the random distribution for $\text{Ni}_{0.77}\text{Fe}_{0.23}$ is unstable. We analyzed the L_{12} and L_{10} structures during this process. In $\text{Ni}_{0.88}\text{Fe}_{0.12}$ alloy all the Fe atoms belong to FeNi_3 (L_{12}) phase, which means the remaining Ni atoms are distributed in a form of clusters inside the matrix. As it is visible in Figure 24 B, after convergence of potential energy, for $\text{Ni}_{0.77}\text{Fe}_{0.23}$ most of the atoms (almost 70%) belong to the FeNi_3 (L_{12}) phase, for $\text{Ni}_{0.62}\text{Fe}_{0.38}$, 19.8% of atoms belong to FeNi_3 (L_{12}) phase, and for $\text{Ni}_{0.88}\text{Fe}_{0.12}$ 38% of atoms belong to FeNi_3 (L_{12}) phase. We didn't observe the Fe_3Ni L_{12} structure for $\text{Ni}_{0.38}\text{Fe}_{0.62}$ alloy. In all four compositions, 1-3% of atoms belong to the L_{10} structure.

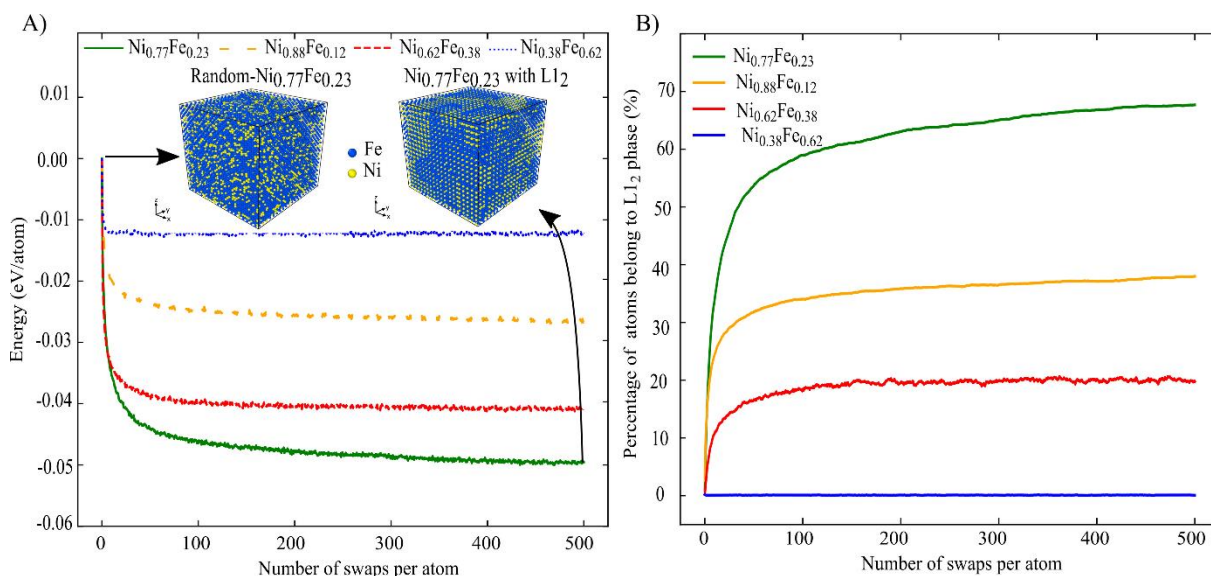


Figure 24. A) The potential energy per atom with respect to the random case vs the number of swap attempts normalized by the total number of atoms for three different $\text{Ni}_x\text{Fe}_{1-x}$ binary alloys. B) Percentage of atoms belonging to FeNi_3 (L_{12}) phase vs the number of swap attempts normalized by the total number of atoms for three different $\text{Ni}_x\text{Fe}_{1-x}$ binary alloys.

4.4 Discussion

To interpret the results based on atomistic simulations, we should notice that if nanoprecipitate with L_{12} phase is formed inside fcc alloys, the strength of the alloys will increase via the dislocation-bypass mechanism and dislocation-cutting mechanism¹¹⁸. This can be the main reason for the high hardness of $\text{Ni}_{0.62}\text{Fe}_{0.38}$ alloy, where around 20% of L_{12} atoms are formed in the disordered matrix. Although the L_{12} phase is also formed in $\text{Ni}_{0.77}\text{Fe}_{0.23}$ and $\text{Ni}_{0.88}\text{Fe}_{0.12}$

alloys, these two alloys showed less hardness before irradiation. For Ni_{0.77}Fe_{0.23}, most atoms are found in the L₁₂ phase while the remaining belong to the disordered phase. Specifically, the disordered regions with randomly distributed Fe and Ni atoms are dispersed within the ordered L₁₂ matrix. Consequently, the L₁₂ phase cannot act as a nanoprecipitate and provide nanoprecipitate hardening prior to irradiation. In Ni_{0.88}Fe_{0.12} alloy, all the Fe atoms belong to the FeNi₃ L₁₂ phase, which means the remaining Ni atoms are segregated inside the matrix. Before irradiation, the material's hardness is expected to be similar to pure Ni. However, irradiation can alter the distribution of Fe and Ni within the matrix, increasing hardness. Therefore, in the next study, the effect of irradiation in order-disorder phases will be investigated.

The irradiation-induced damage²³ can be categorized into two stages: primary and secondary. The primary damage occurs immediately after ion/neutron/electron impact by atomic collision processes far from thermodynamic equilibrium. The secondary damage is a long-timescale (nanoseconds to years) evolution caused by thermally activated processes⁶. During the secondary damage stage, the crystal defects evolve into more complicated microstructural features such as defect clusters, dislocation loops, and three-dimensional defects such as SFT⁶. Therefore, it is important to perform damage analysis at an early stage, e.g., 0.5 dpa and 12 dpa, to reveal defect evolution processes. For example, from hardness analysis, we have seen a drastic hardness increase in a low fluence regime up to 0.5 dpa. In turn, at higher fluences, the increase becomes less significant as the materials become saturated with defects. Therefore, in order to understand defect configurations in low and high fluence regimes, TEM analysis of each composition was conducted.

Figure 25 A shows cross-sectional TEM images of the Ni, Ni_{0.77}Fe_{0.23}, Ni_{0.62}Fe_{0.38} and Ni_{0.38}Fe_{0.62} irradiated with fluence of 2×10^{14} ions/cm² (damage level of 0.5 dpa), compared with SRIM calculations. The images were taken at a magnification of 150k in order to capture defects distribution below the sample surface. It should be emphasized, that all the lamellae have been cut perpendicularly to the ion-irradiated surface, to reveal the damage distribution into material up to the 2 μ m depth (in Figure 25 A, we show only the images up to 1100 nm). One can see that for Ni, Ni_{0.77}Fe_{0.23} and Ni_{0.62}Fe_{0.38} the damage zone reaches up to 600 nm (and it is in line with SRIM simulation where the damage peak is located at 400 nm), however, in Ni_{0.38}Fe_{0.62} defects are evenly distributed and slightly exceeds a damage zone. Figure 25 B compares the TEM images of Ni, Ni_{0.77}Fe_{0.23}, Ni_{0.62}Fe_{0.38} and Ni_{0.38}Fe_{0.62} taken in a low fluence regime at 4×10^{13} ions/cm². The images come from the regions where the peak damage occurs in each

alloy (taken at 500k magnification) to perform a detailed analysis of the defects and further to calculate the defect densities.

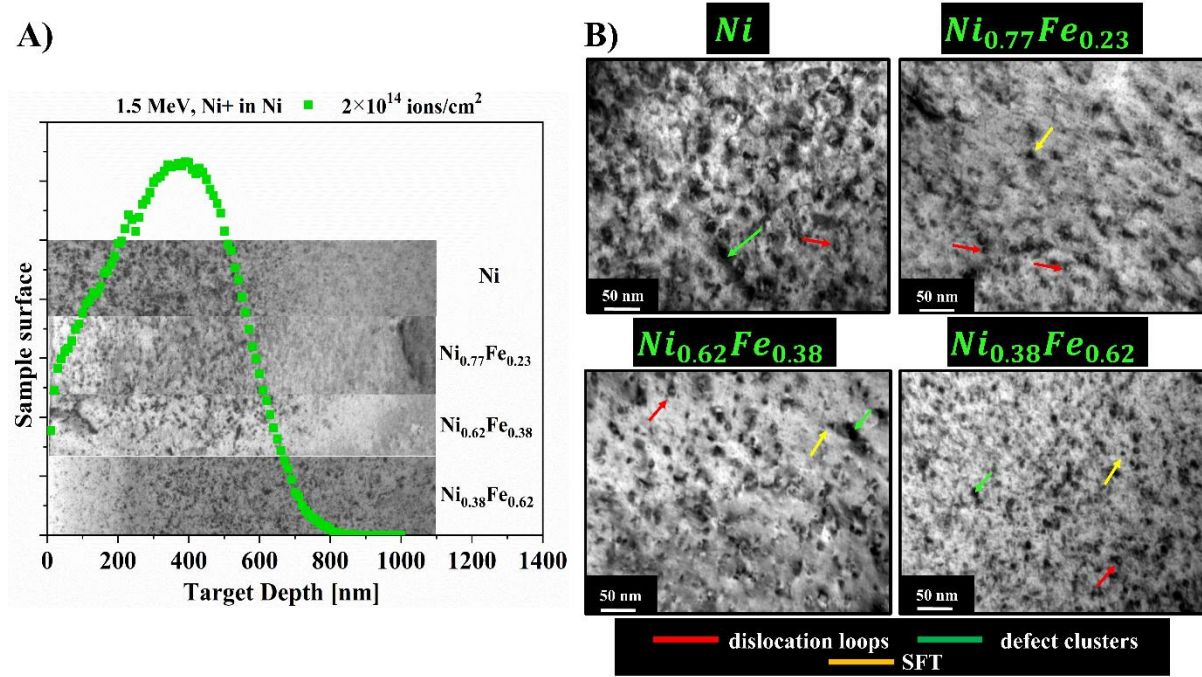


Figure 25. A) Cross-sectional TEM images of the Ni, Ni_{0.77}Fe_{0.23}, Ni_{0.62}Fe_{0.38} and Ni_{0.38}Fe_{0.62} irradiated with a fluence of 2×10^{14} ions/cm² compared with SRIM calculations. B) Bright-field images of Ni, Ni_{0.77}Fe_{0.23}, Ni_{0.62}Fe_{0.38} and Ni_{0.38}Fe_{0.62} irradiated with a fluence of 4×10^{15} ions/cm². The red arrow indicates dislocation loops, green – defect clusters and yellow – SFT.

One can notice that defect concentration decreases as the iron content rises. In pure Ni, large defect clusters and dislocation loops are the dominant defect types. In Ni_{0.77}Fe_{0.23}, SFTs, defect clusters (relatively smaller than in Ni) and dislocation loops are clearly visible. In Ni_{0.62}Fe_{0.38} and Ni_{0.38}Fe_{0.62} SFTs, dislocation loops and clusters are mainly dominant.

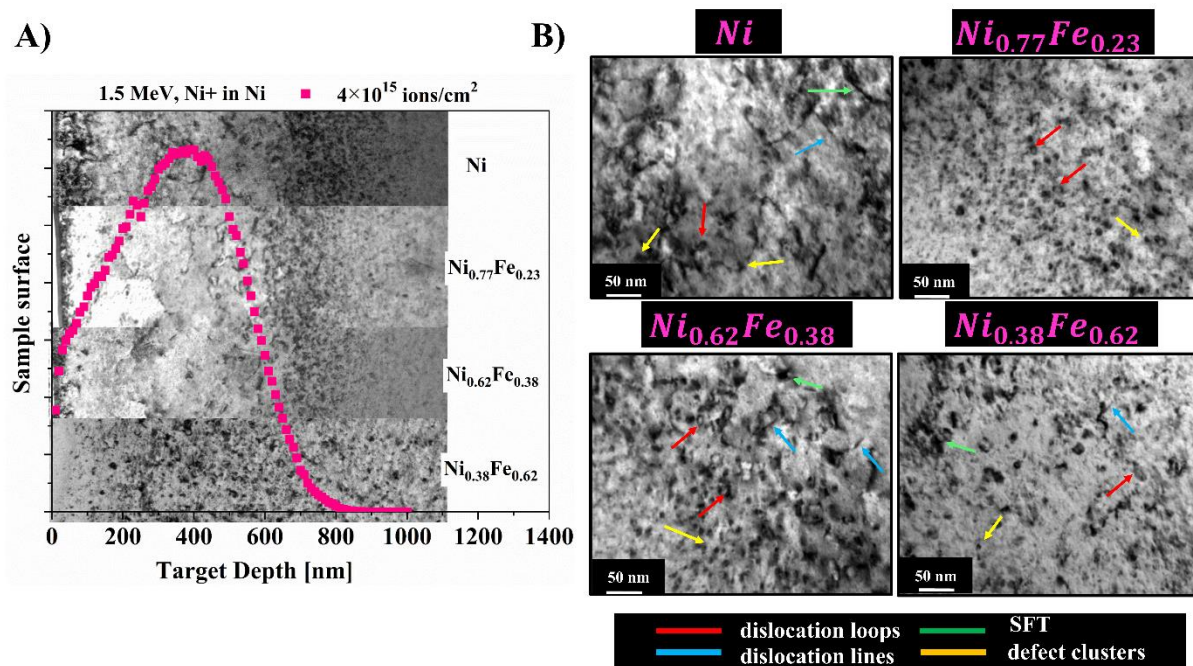


Figure 26. A) Cross-sectional TEM images of the Ni, $\text{Ni}_{0.77}\text{Fe}_{0.23}$, $\text{Ni}_{0.62}\text{Fe}_{0.38}$ and $\text{Ni}_{0.38}\text{Fe}_{0.62}$ irradiated with a fluence of $4 \times 10^{15} \text{ ions/cm}^2$ compared with SRIM calculations. B) Bright-field images of Ni, $\text{Ni}_{0.77}\text{Fe}_{0.23}$, $\text{Ni}_{0.62}\text{Fe}_{0.38}$ and $\text{Ni}_{0.38}\text{Fe}_{0.62}$ irradiated with a fluence of $4 \times 10^{15} \text{ ions/cm}^2$. The red arrow indicates dislocation loops, blue – dislocation lines, green – defect clusters and yellow – SFT.

Cross-sectional TEM images of the Ni, $\text{Ni}_{0.77}\text{Fe}_{0.23}$, $\text{Ni}_{0.62}\text{Fe}_{0.38}$ and $\text{Ni}_{0.38}\text{Fe}_{0.62}$ irradiated with a fluence of $4 \times 10^{15} \text{ ions/cm}^2$ are shown in Figure 26 A. In contrast to the low fluence, in this case we see that the defects have moved significantly into the material and are outside the damage peak, calculated in the SRIM program. Interestingly, in Ni, $\text{Ni}_{0.77}\text{Fe}_{0.23}$ and $\text{Ni}_{0.62}\text{Fe}_{0.38}$ damage concentration is located at 700 nm, while in $\text{Ni}_{0.38}\text{Fe}_{0.62}$, the defects are evenly distributed from the surface into the material, similar to what we observed at low damage level (0.5 dpa in Figure 25 A). This phenomenon has been already reported in our previous work ⁷⁸. It was reported that the reason why a damage peak shift was observed in $\text{Ni}_x\text{Fe}_{1-x}$ at high fluence is that the ion irradiation causes high mechanical stress, where the ions may propagate toward the bulk of the material. As a result, we observe defect migration with an increased ion fluence as they generate a higher stress gradient due to the high amount of Ni ions implanted into the sample. Moreover, the migration mechanism could result from a combination of processes such as defect recombination, production, cluster formation etc. as reported in ⁸.

In Figure 26 B, at the highest fluence (damage around 12 dpa), we can see the transformation of defect types in all the studied cases, which is consistent with RBS/C and MSDA analysis. For example, defects in Ni tend to form dislocation lines, SFTs, clusters, and dislocation loops while in $\text{Ni}_{0.77}\text{Fe}_{0.23}$ they form dislocation loops and STFs. In $\text{Ni}_{0.62}\text{Fe}_{0.38}$ and $\text{Ni}_{0.38}\text{Fe}_{0.62}$ we observe similar types of defects such as dislocation lines, many more SFTs, clusters and

dislocation loops. It is known that the defect evolution proceeds as follows, first at low fluence point defects are transformed into clusters then into dislocation loops and stacking faults^{54,119}. SFTs are known as the dominant type of defects in *fcc* NiFe single crystals having the shape of four equilateral vacancy-type stacking faults on {111} planes intersecting along <110> edges to form a perfect tetrahedron and are one of the most common vacancy-type defect clusters in metals of low stacking-fault energy¹²⁰. The vacancy-type SFTs can be produced in quenched metals or during irradiation by agglomeration of mobile vacancies at room and high temperatures⁸, which significantly affects mechanical properties.

In addition, based on the defect sizes calculations presented in Figure 27 A, we can observe that in pure Ni damage propagates very fast up to 0.5 dpa (we see the biggest changes in the structure among the rest of the compositions). However, at about 12 dpa defects are re-organized, we can see elongated defect clusters or dislocation lines rather than big dot-shaped clusters. As shown in RBS/C spectra in Figure 20 and Figure 21, we observed that in the case of pure Ni defect saturation occurs above the fluence of 2×10^{14} ions/cm² (about 0.5 dpa). In Ni_{0.77}Fe_{0.23}, defects become bigger at the highest fluence and they are more organized in one region. In contrast, in Ni_{0.62}Fe_{0.38} and Ni_{0.38}Fe_{0.62} defects are constantly growing with fluence, which again is in line with RBS/C analysis, where we could see the continuous growth of backscattering yield. Furthermore, it is worth mentioning that the most meaningful changes are visible at a damage level of 0.5 dpa in each case. Moreover, as the damage level increases the defect sizes become bigger. This can be validated by calculations for individual composition based on TEM images, as shown in Figure 27 A. The defect size has been calculated as an average size of defects on the image (taken at the highest magnification, 500k) of the most degraded region (where the damage peak occurs). Fifty random defects (visible as black clusters) have been chosen to obtain useful statistics. Interestingly, defect sizes decrease with an increase in Fe up to 38 at% and for 62 at% of Fe accrue, both at low and high fluences. Additionally, for the highest dose (~12 dpa) the sizes of defects rise.

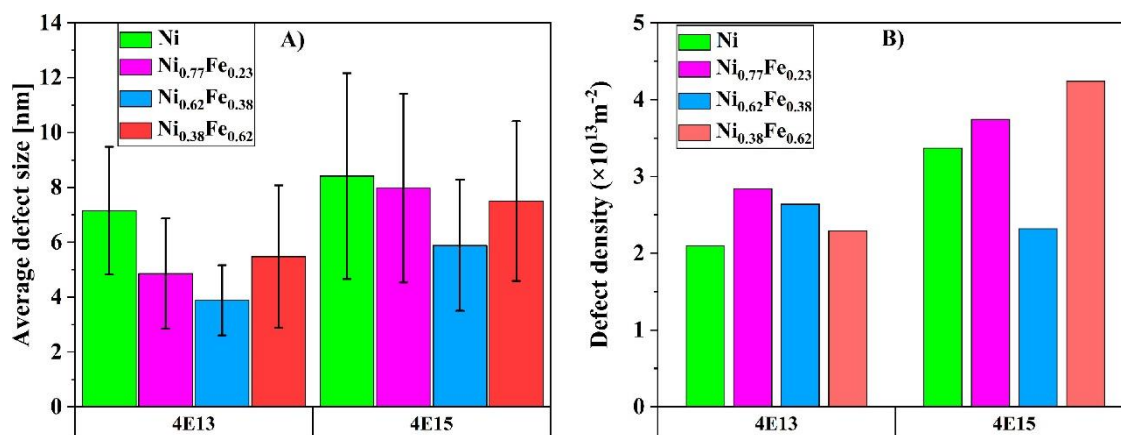


Figure 27. A) Defect sizes based on the TEM images calculated at the fluence of $4 \times 10^{13} \text{ ions/cm}^2$ and $4 \times 10^{15} \text{ ions/cm}^2$ and B) Average defect densities for the Ni, $\text{Ni}_{0.77}\text{Fe}_{0.23}$, $\text{Ni}_{0.62}\text{Fe}_{0.38}$ and $\text{Ni}_{0.38}\text{Fe}_{0.62}$ irradiated to the fluence of $4 \times 10^{13} \text{ ions/cm}^2$ and $4 \times 10^{15} \text{ ions/cm}^2$.

Moreover, in Figure 27 B defect densities have been calculated, to better understand the defect configuration for various compositions. Calculations were made based on the TEM images taken at the peak damaged region (at the highest magnification of 500k). For this measurement, lamellae thickness was also measured at the peak damage region only. The densities were calculated by counting the defect sizes in a unit volume of crystalline material (based on the same image where an average defect size was calculated and presented in Figure 26 A). As a result, we can observe that the defect density values are inversely proportional to the defect size results for the individual chemical compositions. It can be seen that the defect densities increase for pure Ni and $\text{Ni}_{0.77}\text{Fe}_{0.23}$, while decrease for $\text{Ni}_{0.62}\text{Fe}_{0.38}$ and $\text{Ni}_{0.38}\text{Fe}_{0.62}$ for low fluencies. One can see that the size of defects decreases with the addition of iron. Usually, when irradiation damage increases, the dislocations disappear, and the density of the small interstitial-type loops or clusters increases²⁴. Interestingly, the densities of network dislocations and dislocation loops increased with the irradiation dose. For this reason, these defects could work as defect sinks that could absorb the black spot damage. Therefore, more black spots would dissolve in the sinks when the network of dislocations and dislocation loops increased. Moreover, a part of the enlarged neighboring black spots may coalesce into more prominent spots during irradiation, further decreasing their number^{110,111}. While analyzing RBS/C spectra we have assumed that lattice distortion could be related to defect size and density change since smaller defects cause smaller lattice distortion as compared to complex defects (defect cluster, dislocation), hence, backscattering yield changes. In pure Ni, a saturation dose has been obtained at a fluence of $2 \times 10^{14} \text{ ions/cm}^2$. The saturation and a small decrease in channeling yield occur because the defect structure becomes more organized at higher fluences, as we can see in Figure 26 A. We see that point defects are transformed into more complex ones, such as dislocation lines and

larger defect clusters that release strain induced by ion irradiation. Therefore, we observe a decrease in backscattering yield. In order to better understand how the defect size would affect mechanical properties or RBS/C spectra we have introduced a detailed calculation of defect size up to around 20 nm at low and high fluence as shown in Figure 28 A and B. From the calculation, we can see that the smallest defects up to 5 nm occur in Ni_{0.77}Fe_{0.23} and Ni_{0.62}Fe_{0.38} in a low and high fluence regime. This is consistent with RBS/C results and MSDA analysis, which showed the existence of small defects (significantly more than the rest of the compositions) in the structure. It is clear that the size of defects increases at high fluence, which is in line with TEM images presented in Figure 26 A.

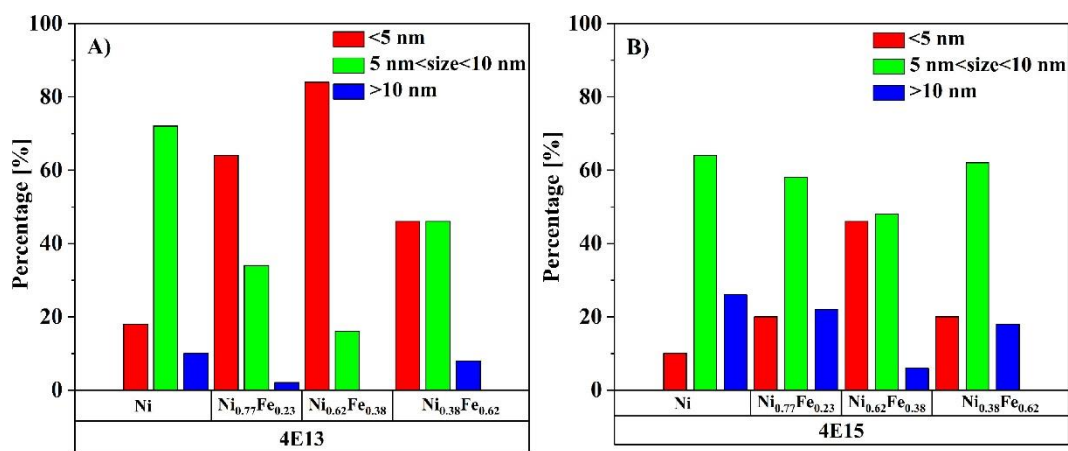


Figure 28. Percentage of defect size obtained for A) low 4×10^{13} ions/cm² and B) high 4×10^{15} ions/cm² fluence up to 10 nm.

At high fluence we observe an increase in defect size for all the compositions, while in Ni_{0.62}Fe_{0.38} defects are the smallest up to 10 nm. From MSDA analysis we assumed that in the case of high irradiation fluences such as 1×10^{15} ions/cm² and 2×10^{15} ions/cm² one can observe a decrease in defect concentration. This effect suggests a transformation in small loops into larger loops or defect clusters, which is visible in TEM images (Figure 26 A). We postulated that, the higher number of smaller defect structures leads to a more pronounced lattice distortion in their vicinity, as compared to one large dislocation loop containing the same number of defects hence more efficient dechanneling of the analyzing beam.

Furthermore, defect size and density could also affect the irradiation-induced hardening of the alloys. As we illustrate in Figure 23 B, the most prominent hardening occurred at low fluence regime in Ni_{0.77}Fe_{0.23} where we deal with a significant transformation from small defects into bigger ones. Based on the results in Figure 27 B, we see that the average defect size decreases and the defect density increases. In contrast, Ni_{0.62}Fe_{0.38} and Ni_{0.38}Fe_{0.62} showed the lowest level of hardening among all the alloys. The reason behind such differences is most probably related

to the physical nature of the iron atomic nucleus in its excited state (during irradiation), as it possesses only one orbital with unpaired electrons, while Ni has three orbitals. This could be explained, as Ni possesses more space for electron movements and, thus, defect generation and mobility⁷⁸. Therefore, Fe effectively suppresses damage and stress induced by ion irradiation. The different arrangement of Fe atoms in a crystal structure may also influence the obtained characteristics of Ni_xFe_{1-x} after ion implantation, therefore, this should be validated by performing additional hybrid MC/MD simulation. In Figure 23 we observed that the hardness of virgin materials is changing with the percentage of iron content. The preliminary results of MC/MD simulations (of virgin materials) have shown that depending on the iron content we achieved different structures. In Ni_{0.77}Fe_{0.23}, 70% of FeNi₃ (L₁₂) phase is observed, while in Ni_{0.62}Fe_{0.38} around 20%. Ni_{0.38}Fe_{0.62} is characterized by disorder *fcc* structure. Moreover, simulations revealed that in each composition 1-3% of the L₁₀ phase occurs. It is worth empathizing that, if the nanoparticulate FeNi₃ with L₁₂ phase is distributed in the random *fcc* structure, the strength of the material increase^{114,115}. It means that the material becomes harder. Therefore, in Ni_{0.62}Fe_{0.38} we observe the maximum hardness in a pristine sample and then the hardness decrease in Ni_{0.38}Fe_{0.62} where we deal with *fcc* phase and little amount of L₁₀ phase (1-3%) according to simulations.

B.5 Conclusions

Comprehensive studies of *fcc* Ni_xFe_{1-x} single crystals were performed using a combination of various techniques to understand defect evolution and radiation response of each investigated composition. Ion channeling studies as well as damage kinetics demonstrated various responses of damage build-up mechanisms for each individual composition. We have noticed that the defect size and density influence the shape and intensity of the obtained RBS/C spectra depending on the composition. TEM images revealed a significant degradation of the structure at 0.5 dpa, especially for Ni and, the largest defects are observed at 12 dpa. From MSDA we observed a rapid increase in the number of defects at 0.5 dpa and a high increase in the dechanneling level observed in measured RBS/C spectra, for all the compositions. The numbers of extended defects formed for low irradiation fluences are well below the values obtained for Ni. At higher irradiation fluence of 1×10^{15} ions/cm² and 2×10^{15} ions/cm² we observed a decrease in defect concentration, which suggests a transformation of small loops into larger loops or defect clusters.

The atomistic simulations allowed to obtain insightful results related to hardening of $\text{Ni}_x\text{Fe}_{1-x}$ in a pristine state. The main reason for the highest hardness of $\text{Ni}_{0.62}\text{Fe}_{0.38}$ alloy before irradiation could be related to the presence of nanoprecipitate FeNi_3 (L1_2) phase (around 20%), which is formed inside the disordered matrix. It was found that a combination of atomistic simulations together with experimental studies may help to better understand mechanisms such as hardening or phase distribution within various $\text{Ni}_x\text{Fe}_{1-x}$ single crystals. Interestingly, irradiation can change the distribution of the atoms and increase the disordered phase, since irradiation may spread the Fe atoms inside Ni atoms and the hardness will increase. Therefore, as a next step, investigation of the hardening effect and verification of L1_2 phase presence after irradiation in order-disorder phases should be performed. We postulate that the existence of the L1_2 phase influences the irradiation response of $\text{Ni}_x\text{Fe}_{1-x}$ single crystals.

Article C:

*Nanoscale Defect Formation in fcc Ni and low Fe
content Ni_xFe_{1-x} Single Crystals Under Self-Ion Irradiation*

***E. Wyszowska**, C. Mieszczyński, A. Aligayev, A. Azarov, W. Chromiński, D.
Kalita, A. Kosińska, F. J. Dominguez-Gutierrez, Ł. Kurpaska, I. Jóźwik, J.
Jagielski,*

Nanoscale (2025) Accepted manuscript,

<https://doi.org/10.1039/D5NR00117J>

IF:5.8, Ministry points:140

Published by Royal Society of Chemistry.

C.1 Abstract

Fcc Ni_xFe_{1-x} single crystal alloys serve as model systems to study defect evolution under self-ion irradiation at room temperature across fluences from 4×10^{13} to 2×10^{15} cm⁻². Defect characterization was performed using Rutherford backscattering spectrometry/ channeling (RBS/C) and transmission electron microscopy (TEM) to distinguish defect types and calculate damage kinetics via a Multi-Step Damage Accumulation Model. Complementary molecular dynamics simulations of overlapping collision cascades revealed defect formation mechanisms at low irradiation doses. The simulations indicated that an A15 Frank-Kasper phase forms within the {111} plane in pure Ni, Ni_{0.88}Fe_{0.12}, and Ni_{0.77}Fe_{0.23} up to a fluence of 2×10^{14} cm⁻², which underlies Frank loop nucleation. This provided insight into the role of Fe atoms in influencing dislocation nucleation and evolution. The combination of TEM observations, and RBS/C analysis using Monte Carlo-based McChasy simulations revealed that point defects - interstitials, dumbbells, vacancies, and A15 phase - dominate in all compositions up to 2×10^{14} cm⁻². At higher fluences of 2×10^{15} cm⁻², these defects transform into complex structures such as dislocation loops and stacking fault tetrahedra. Notably, in Ni_{0.77}Fe_{0.23}, compact 3D precipitates form but remain too small to evolve into Frank loops, despite significant Fe decoration.

Keywords: Point defects, A15 nano-phase, Nanoindentation, MD simulations, MC simulations

C.2 Introduction

Ni-based fcc concentrated solid solution alloys (CSAs) comprising 3d transition metals are known for their exceptional fracture toughness and damage tolerance under mechanical loading^{4,7–11,25,28,31,37,71,78,79,121–126}. Their superior radiation resistance is largely due to atomic-level heterogeneity, which impedes dislocation motion and suppresses defect cluster growth^{25,44}. Neutron irradiation typically induces defects ranging from a few to several nanometres in size, which can degrade mechanical and structural properties^{31,49,78,79,107,116,126,127}. Recent advances in numerical simulations¹²⁴ and experimental techniques have driven substantial progress in understanding the fundamental mechanisms of radiation-induced damage^{37,124}. This insight into defect formation mechanisms is critical for designing materials with improved radiation tolerance, particularly for extreme operating conditions^{1,13,14}. For instance, Aidhy *et al.*⁵¹ utilized molecular dynamics simulations to examine point defect evolution in pure Ni, Ni_{0.5}Fe_{0.5}, and Ni_{0.8}Cr_{0.2}, finding that irradiation-induced interstitials form $1/3 \langle 111 \rangle$ {111}

- type faulted dislocation loops. Their results also indicated that defect diffusion was slower in the alloys compared to pure Ni, delaying defect cluster formation. Similarly, Lu *et al.*²⁷ investigated migration behaviours in pure Ni and Ni-Fe alloys (1–35% Fe) under irradiation at 773 K, reporting that higher iron content slowed dislocation loop evolution, thereby influencing interstitial cluster migration and complex defect nucleation mechanisms.

The increased resistance to void swelling and delayed dislocation evolution in more concentrated Ni-Fe alloys was attributed to the shortening of the mean free path of defect clusters, which becomes 3-D dominant at around 20% Fe. Further studies on temperature effects and defect evolution in Ni and Ni-Fe alloys are described in the following works^{86,121,128–130}. Moreover, early-stage defect evolution in CSAs has been extensively described by Zhang *et al.*³⁷. Molecular dynamics simulations revealed that in pure Ni, interstitials form 1/3 $\langle 111 \rangle$ Frank loops, and vacancies form stacking fault tetrahedra (SFT). In NiFe and Ni_{0.8}Cr_{0.2}, defect clusters were also observed, but their kinetics were significantly slower compared to pure Ni. This slower kinetics was attributed to the chemical complexity and the associated sluggish diffusion. Additionally, the diffusion coefficient increases with higher Fe concentration, with the maximum sluggish effect observed in vacancy diffusion at approximately 20 at. % Fe. Goryaeva *et al.*¹³¹ have recently contributed to this area of research. Their atomistic simulations and experiments revealed that, before the formation of dislocation loops, interstitial atoms in FCC metals like Al, Cu, and Ni accumulate into compact 3D inclusions of the A15 Frank-Kasper phase^{132–134}. The study explained that the FK Z phase, along with the A15 phases, is a fundamental structure that serves as building blocks for all FK phases. In addition, Chartier *et al.*¹³⁵ used atomistic simulations to study the formation of self-interstitial atom clusters in BCC Fe under irradiation. They discovered that C15 clusters appear at the very early stages of microstructural evolution in irradiated iron, preceding the formation of any dislocation loops. Both $\frac{1}{2}\langle 111 \rangle$ and $\langle 100 \rangle$ loops can nucleate directly from these C15 clusters. Additionally, the three-dimensional C15 clusters were found to form before the production of loops under irradiation¹³⁵.

While significant advances have been made in understanding radiation-induced defect formation in pure Ni and NiFe alloys, the early-stage mechanisms governing the transition from isolated point defects to extended structures, such as dislocation loops and stacking fault tetrahedra, are still under investigation, particularly under low-fluence, room-temperature irradiation. This gap is especially relevant for CSAs, where local chemical complexity is expected to influence defect stability, migration, and interaction. The current study addresses

this gap by focusing on Ni and Ni_xFe_{1-x} single crystals (with up to 23 at. % Fe), serving as model systems to investigate defect evolution at the atomic scale. Our central hypothesis is that Fe incorporation alters the defect formation pathway and promotes distinct defect structures compared to pure Ni. In particular, the identification of a metastable A15 Frank-Kasper phase^{131–134} from MD simulations suggests a possible precursor to Frank loop nucleation. Although the A15 phase is not directly observed via TEM due to resolution limitations and its transient nature, the formation of faulted loops at matching fluences provides indirect experimental support. This synergistic approach—linking MD simulations, RBS/channeling analysis, TEM imaging, and Monte Carlo-based McChasy modelling—offers a unique contribution by bridging the atomistic-scale mechanisms with experimentally observed defect features. The study not only proposes a new interpretation of defect nucleation pathways in fcc NiFe systems but also provides a quantitative framework for understanding damage accumulation in CSAs under irradiation.

C.3 Experiments and Methods

C.3.1 Ion Irradiation and SRIM Calculations

The *fcc* Ni and Ni_xFe_{1-x} single crystal alloys with different amounts of Fe (0, 12, 23 at%) were irradiated at room temperature with 1.5 MeV ⁵⁸Ni⁺ ions using a 1 MV tandem accelerator (National Electrostatics Corporation, model 3SDH-2) in the University of Oslo. All ion irradiations were performed in a raster scanning mode. The beam current was kept constant at a relatively low value of ~50 nA/cm², corresponding to the ion flux of ~3×10¹¹ at/cm²s, to avoid sample heating during implantation. The Ni⁺ ions were chosen for irradiation because Ni is one of the major alloying elements in the Ni_xFe_{1-x} system. Therefore, there is no introduction of impurities during radiation damage buildup. The irradiations were performed at an inclination of 7 degrees to the normal direction of the samples to avoid channeling. Detailed information regarding sample preparation can be found in our previous works^{78,79}.

The corresponding displacement-per-atom (dpa) profiles were predicted by the Stopping and Range of Ions in Matter (SRIM) code⁶⁴, which is based on the binary collision approximation method, for all elements using the full cascade mode. The mean projected ranges of implanted ions and distributions of primary defects as predicted by SRIM code^{49,69} simulations for Ni, Ni_{0.88}Fe_{0.12}, and Ni_{0.77}Fe_{0.23} are shown in Figure 29.

The dpa has been calculated based on the following equation⁶⁹:

$$dpa = \frac{\text{fluence } \text{cm}^{-2} \times \frac{\text{total vacancies}}{A_{\text{ion}}} \times 10^8}{\text{atomic density } \frac{\text{atoms}}{\text{cm}^3}} \quad (1)$$

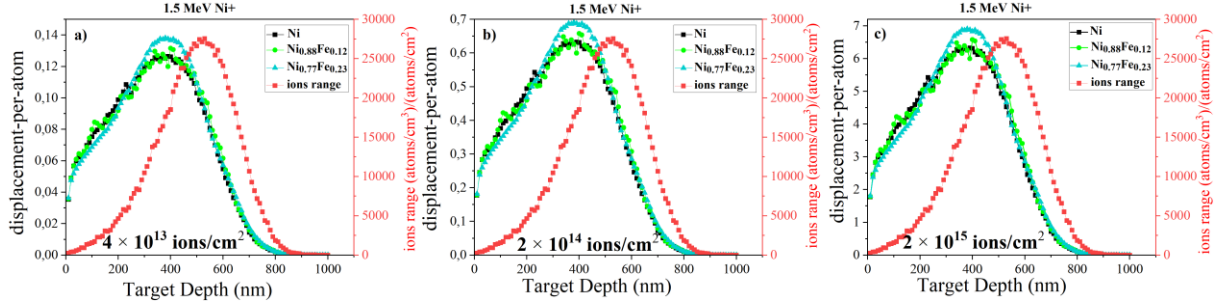


Figure 29. Damage profiles of Ni, $\text{Ni}_{0.88}\text{Fe}_{0.12}$, and $\text{Ni}_{0.77}\text{Fe}_{0.23}$ irradiated with 1.5 MeV of Ni^+ at fluences of a) 4×10^{13} , b) 2×10^{14} , and c) $2 \times 10^{15} \text{ cm}^{-2}$.

The ion distribution was estimated from the RANGE.txt file. The corresponding dpa profiles were calculated using two files, VACANCY.txt and NOVAC.txt, under an assumed displacement energy threshold of 40 eV for all elements. The dpa profile is the sum of the vacancy concentrations using the column of “Knock-Ons” for Ni ions and the columns of “Vacancies” from target elements (the sum of Ni vacancies and Fe vacancies in the case of $\text{Ni}_x\text{Fe}_{1-x}$ in VACANCY.txt, together with the replacement collisions in NOVAC.txt.⁶⁷ Ion-induced damage in monoatomic and multi-elemental targets was predicted using full-cascade simulations⁶⁸. The SRIM-estimated damage peak is located at a depth of approximately 400 nm.

C.3.2 Computational modeling

In order to study the formation and evolution of dislocation and voids at different irradiation doses, we conduct a series of Molecular Dynamics (MD) simulations with the Large-scale Atomic/Molecular Massively Parallel Simulator (LAMMPS) software⁶, renowned for its versatility in studying material behavior under various conditions. We utilize interatomic potentials developed by Bonny *et al.*^{74,75}, which are based on the Embedded Atom Method (EAM) with Ziegler-Biersack-Littmark (ZBL) corrections to account for short-range interactions⁷⁶. Thus, we began by defining the *fcc* Ni sample with a dimension of (10.23, 10.58, 10.94) nm³ and 107 880 atoms along the [001] orientation, followed by optimizing the system's energy using The FIRE (Fast Inertial Relaxation Engine) 2.0 protocol⁷⁷. This optimization continued until achieving a homogeneous temperature and pressure profile at a density of 8.88 g/cm³^{78,79} aligning well with experimental values. Subsequently, the prepared sample underwent a relaxation step for 10 ps to dissipate any artificial heat. To create the *fcc* $\text{Ni}_x\text{Fe}_{1-x}$

alloys, randomness was introduced by substituting 12% and 23% of Ni atoms Fe, following experimental results ^{76,80}. The optimization process focused on reaching the nearest local minimum of the energy structure, with criteria ensuring minimal change in energy between iterations and maintaining a global force vector length of all atoms below 10^{-8} eV/Å. The subsequent steps mirrored those of the pristine case, considering a series of MC simulations to search for each possible metastable configuration at room temperature ^{76,80}.

To model the generation of defects at low irradiation doses, MD simulations are widely employed to capture the mechanisms of point defect formation resulting from primary knock-on atoms (PKAs) with recoil energies typically ranging from 1 to 100 keV ^{81,82}. These simulations effectively describe the early stages of defect evolution, including the formation of isolated vacancies and interstitials. As irradiation proceeds, these defects can aggregate into clusters and eventually form extended structures such as dislocation networks, dislocation loops, and stacking fault tetrahedra (SFT). However, a limitation of MD is the extremely high damage rate (dpa/s) inherent to the simulations, which significantly exceeds that of real experimental conditions. As a result, while the simulated fluence may match the experimental values, the rapid defect accumulation and lack of long-term diffusion or recovery processes can lead to discrepancies between the predicted and observed microstructures. This inherent difference in damage kinetics makes direct quantitative comparison challenging and highlights the importance of interpreting MD results as qualitative insights into defect formation mechanisms rather than direct analogies to experimental outcomes.

Thus, the Ni, Ni_{0.88}Fe_{0.12}, and Ni_{0.77}Fe_{0.23} alloys are irradiated using cumulative overlapping collision cascade simulations at 5 keV recoils with temperature of 300 K. The dpa dose is calculated as $(n/N) (0.8E_{\text{PKA}}/2E_d)$ ^{83,84} with n as the number of cascades, $N = 107880$ as the total number of atoms in the numerical cell, E_{PKA} is the impact energy, and E_d is the threshold energy set at 40 eV for Ni ⁸⁵. Requiring a number of $n = 215$ and 1080 consecutive recoil MD simulations to obtain dpa values of 0.1 and 0.5, respectively ^{84,86}, which correspond to fluences in the range of 10^{13} - 10^{14} ions/cm². In the process, we ensure that heat spikes generated by the recoils were fully developed within the cell and that periodic boundary conditions did not influence the final outcomes. Established simulation techniques for irradiation effects were employed, including adaptive time step algorithms, border cooling, electronic stopping power considerations, and the use of an EAM interatomic potential tailored for repulsion and defect properties ^{76,83,85}. To mitigate cascade-induced shock waves, border cooling, and damping were implemented by applying a thermostat on a 5 Å thick shell around the periodic borders of the

cell^{76,86}. Each recoil event was simulated for 20 ps, followed by an additional 10 ps under the NPT ensemble to allow for stress release and swelling. Random shifts of the simulation cell were applied between each recoil to ensure homogeneous irradiation. Each set of N-recoils was repeated three times, utilizing different seed numbers in the random number generator and different initial random cells. This extensive approach aimed to demonstrate that the results were not influenced by stochastic anomalies. To comprehend the nucleation of defects in irradiated *fcc* Ni and Ni_xFe_{1-x} single crystals, we conduct MD simulations of overlap collision cascades, tracing dislocation nucleation across various dpa doses using the DXA method implemented in OVITO⁸⁵.

C.3.3 RBS/C (ion channeling) and Multi-step damage accumulation (MSDA) model

After irradiation, the samples were examined by the RBS/C using 1.6 MeV He⁺ ions along the [001] direction and backscattered into a detector placed at 165° relative to the incident beam direction. The RBS/C spectra for pure Ni and Ni_xFe_{1-x} alloys irradiated with different fluences were simulated using the MC-based McChasy code developed at the NCBJ^{122,123}. The energy of the backscattered particle can be directly related to the depth at which the close encounter scattering event occurred. The bulk scattering arises from particles that have been deflected atomic rows and have crossed over to another row, where they undergo a close-encounter event. To reveal the damage kinetics for investigated alloys the Multi-Step Damage Accumulation (MSDA) analysis was performed^{90,92}. This model is based on the equation assuming that the damage accumulation occurs through a series of structural transformations caused by the destabilization of the present crystal structure. The type of defect, which is associated with a given step is determined by the lowest free energy of this specific atomic configuration⁹². MSDA can be described as follows:

$$f_d = \sum_{i=1}^n (f_{d,i}^{sat} - f_{d,i-1}^{sat}) G [1 - \exp(\sigma_i (\Phi - \Phi_{i-1}))] \quad (2)$$

where,

σ_i - cross-section for the formation of a given kind of defect

$f_{d,i}^{sat}$ - level of damage at saturation for i-th kind of defects

Φ_i - fluence threshold for triggering the formation of i-th kind of defects

C.3.4 TEM analysis

The TEM observations were conducted with two main objectives: first, to compare the distribution and density of radiation-induced defects across all specimens, and second, to perform a detailed analysis of dislocation types for comparison with computer simulations. To achieve these goals, all samples were prepared with a [110] orientation along the viewing direction, ensuring that the same types of defects were visible under consistent viewing conditions. Electron-transparent lamellae for TEM microstructural studies were prepared from the regions of interest using a focused ion beam (FIB) technique. Initially, the samples were carefully oriented to maintain the desired lamella orientation during cutting. The lift-out procedure was conducted using a dual-beam scanning electron microscope (SEM) (Helios 5 UX, ThermoFisher Scientific). Final polishing of the lamellae was performed with 5 keV Ga⁺ ions, followed by a 2 keV Ga⁺ ion treatment to remove Ga-induced defects formed during thinning. Samples were examined with a JEOL F200 transmission electron microscope operated at 200kV. The distribution and density of defects across the irradiated zones were determined from images taken under two-beam conditions with $g=002$ in bright field mode. Dislocation density was calculated using the line intercept method, accounting for the thin foil's thickness, which was determined using the Kossel-Möllenstedt approach with convergent beam electron diffraction under two-beam conditions¹⁰⁴. The samples were first precisely tilted to the closest [110] zone axis, followed by a series of incremental tilts. Special care was taken to use the smallest tilt angles necessary to achieve proper two-beam conditions, minimizing geometrical distortions in the images. Images from each region of interest were captured with excited diffraction vectors of 002, -111, 1-1-1 and -220. The observed defects were then compared to the results from molecular dynamics simulations.

C.4 Results

C.4.1 Computational modeling

The experimental pure Ni and Ni_xFe_{1-x} samples were irradiated with Ni ions with energies of 1.5 MeV, resulting in the formation of dense cascades within the material. These cascades produced damage similar to that caused by neutron recoils in nuclear reactors. The energy recoil of the recoiling atoms ranged from 1 to 100 keV⁶. Thus, the atomistic modeling can be based on overlap collision cascades by performing a series of MD simulations at room temperature.

In order to analyze of results, we compute the dislocation density (ρ) as $\rho = l/V$, where V represents the volume of the numerical cell, and l denotes the length of each type of dislocation, including Shockley with a Burgers vector of $1/6\langle 112 \rangle$, stair-rod with $1/6\langle 110 \rangle$, Frank with $1/3\langle 111 \rangle$, Hirth with $1/3\langle 001 \rangle$, and Perfect $1/2\langle 110 \rangle$. To align our calculations closely with experimental data, we sum the densities of each dislocation type to obtain the total dislocation density. Since TEM lacks the resolution to detect single nanometer-scale defect clusters typically present within MD simulation cells of limited size, a direct comparison of experimental and simulated cluster size distributions is not feasible in this study. However, as TEM effectively identifies larger defect structures (formed as a result of defect evolution), we find that simulation results on larger defect clusters are most suitable for comparison with experimental observations. In Figure 30, we showcase snapshots of selected MD simulations illustrating the formation of Prismatic and $1/3\langle 111 \rangle$ Frank loops. Additionally, we identify voids and single vacancies as semi-transparent grey volumes using the tessellation method implemented in OVITO⁸⁵. Furthermore, we highlight the presence of the A15 nano-phase with yellow spheres, identified through the polyhedral template matching tool known to serve as a source of prismatic or faulted dislocation loops. Such defects in Ni and Ni_xFe_{1-x} alloys arise readily due to $\langle 100 \rangle$ dumbbells surrounding the interstitial atom, depicted as black dots which were identified by considering thermal motion. These dumbbells initially form at the centers of the faces of the fcc unit cell, arranging around an interstitial atom to create a distorted icosahedral configuration. This structure represents a metastable defect state resulting from the immediate aftermath of collision cascades. However, due to the continuous overlapping of cascades inherent to the simulation conditions, these small defect clusters are progressively destabilized. As damage accumulates, the system undergoes structural relaxation and reorganization, leading to the transformation of point defects into more energetically favorable extended defects. In particular, the aggregation of SIAs along close-packed $\langle 110 \rangle$ directions can result in the formation of prismatic dislocation loops, as mainly observed in Ni, these loops often adopt a faulted configuration (Frank loops), lying in the $\{111\}$ habitat planes. The tendency for these faulted loops to form is associated with the low stacking fault energy of Ni, which stabilizes the insertion of a partial dislocation bounding a stacking fault¹³⁶. Simultaneously, the collapse of vacancy-rich regions—formed by the aggregation of multiple vacancies generated in the core of cascades—can give rise to stacking fault tetrahedra (SFTs). These are three-dimensional vacancy-type defects bounded by $\{111\}$ planes. Their formation is energetically favorable in fcc materials under irradiation due to the inherent symmetry and

crystallography, allowing vacancy clusters to reorganize into tetrahedral configurations to minimize strain^{29,77}. The interaction and accumulation of these 1D and 3D defects contribute to the emergence of a dislocation network and complex defect structures at higher fluences. This progression is particularly evident in pure Ni samples, where the defect evolution dynamics lead to a higher density of Frank loops and SFTs, consistent with experimental observations and prior literature reports.

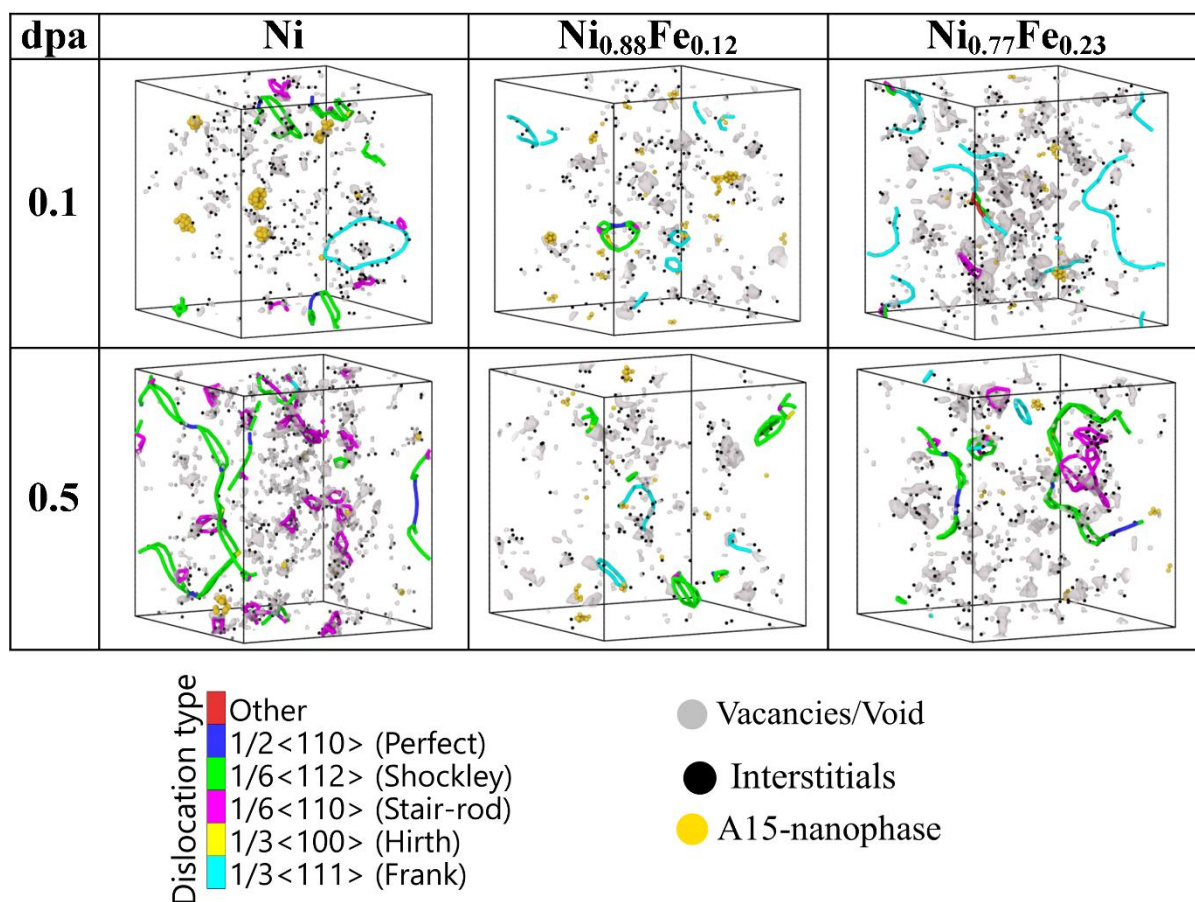


Figure 30. Snapshots of the selected frames of MD simulations for dislocation networks and defect clusters in Ni and $\text{Ni}_x\text{Fe}_{1-x}$, at the doses of ~ 0.1 and 0.5 dpa. The lines of different colours represent dislocations with different Burgers vectors, where green is a Shockley, purple a stair-rod, light blue a Frank, and blue on is perfect. Voids are depicted as semi-transparent grey volumes, while point defects are coloured by black dots for SIA and yellow spheres for A15 type. Detailed information (videos) are available at the Supporting Information section as Video S1a, Video S1b, and Video S1c.

C.4.2 The Multi-step damage accumulation (MSDA) model

The damage accumulation in irradiated single crystals occurs through a series of structural transformations triggered by the destabilization of the current structure of crystals⁹⁰. This process can be described by the MSDA model, where each step is characterized by a dominant type of defect. In Figure 31 damage kinetics calculated for Ni, $\text{Ni}_{0.88}\text{Fe}_{0.12}$, and $\text{Ni}_{0.77}\text{Fe}_{0.23}$ is

presented. It is clear that for all the studied compositions, the fastest increase in defects occurs in the fluence up to $2 \times 10^{14} \text{ cm}^{-2}$ and then it decreases gradually with the higher fluence level.

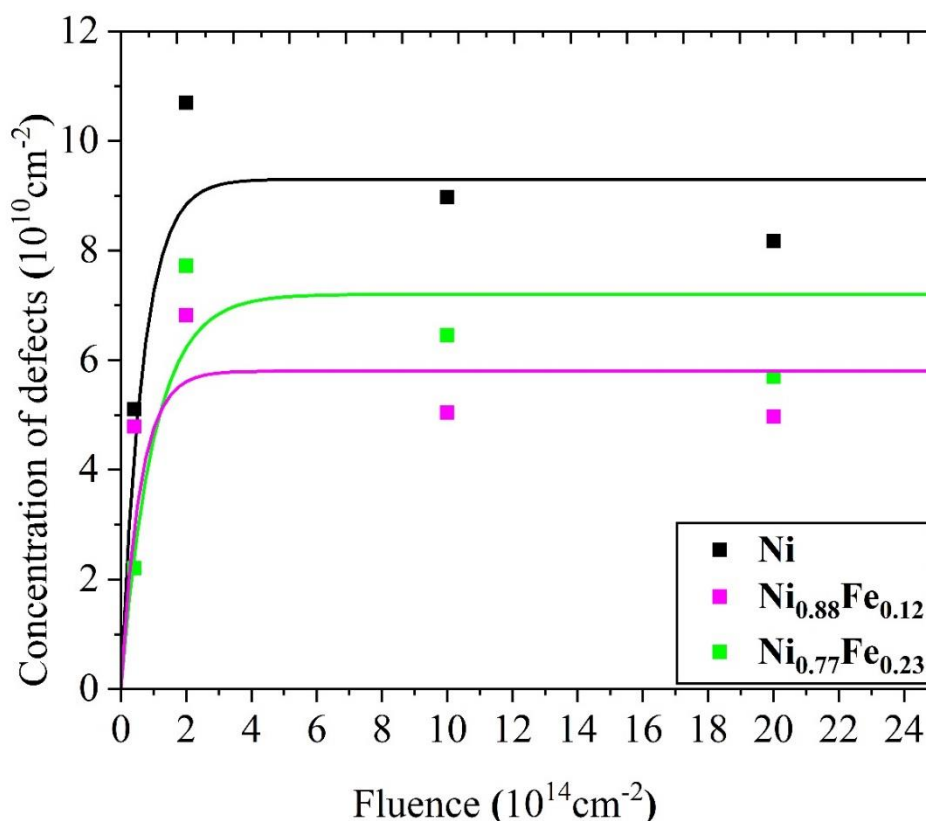


Figure 31. Damage kinetics calculated for Ni, Ni_{0.88}Fe_{0.12}, and Ni_{0.77}Fe_{0.23}. Points represent the maximal values of extended defect distributions extracted from McChasy simulations, solid lines are fits to the experimental data using the MSDA model.

The process of damage accumulation within alloys can be characterized by distinct stages, each marked by specific phenomena, as reported by Jagielski *et al.*⁹². Firstly, at low fluences, there is a generation of small defect clusters, leading to a rapid increase in strain. This effect is supported by simulations (Figure 30), as we identify voids and single vacancies as semi-transparent gray volumes at low damage level. Additionally, we noticed the presence of the A15 nano-phase with yellow spheres, which serve as a source of prismatic or faulted dislocation loops. Next, these defects tend to decrease over time, giving way to the rise of more complex defects such as SFT, which increasingly populate all samples. Secondly, at intermediate fluences, an immediate relaxation of the strain is observed following the formation of prismatic and faulted dislocation loops. Lastly, at high fluences, regions experiencing heightened stress witness the proliferation and clustering of edge dislocations, particularly within specific planes. In Figure 31 it is shown that the numbers of extended defects formed for low and high irradiation fluences for Ni_{0.88}Fe_{0.12} and Ni_{0.77}Fe_{0.23} are significantly below the values obtained for Ni. Interestingly, at higher irradiation fluences ($1 \times 10^{15} \text{ cm}^{-2}$ and $2 \times 10^{15} \text{ cm}^{-2}$) one can

observe a decrease in defect concentration, which is related to strain release due to the transformation of small loops into larger loops or defect clusters.

In Table 4, the cross-section values for defect formation for pure Ni, Ni_{0.88}Fe_{0.12}, and Ni_{0.77}Fe_{0.23} is presented. Ni_{0.88}Fe_{0.12} shows a similar value of cross-section to the pure Ni. However, at the same time, the saturation level of the extended defects is the lowest. The reason for this is, that in Ni_{0.88}Fe_{0.12} point defects such as single vacancies, self-interstitials, and the presence of A15 nano-phase predominate in this composition, as it was shown clearly in Figure 30. Since the MSDA model considers the existence of extended defects only, therefore the fd_I value for Ni_{0.88}Fe_{0.12} is the lowest (because there are more point defects and less extended defects). The cross-section values for Ni_{0.77}Fe_{0.23} are the lowest, which suggests the suppression of defect accumulation. However, we observed that compositions with lower iron content exhibit a higher density of point defects compared to compositions with higher iron content^{78,79}.

Table 4 Cross-sections for defect formation derived from the Modified Stopping and Range of Ions in Matter (MSDA) model. The uncertainties in these values account for the cumulative effects of several sources of error, including experimental inaccuracies in the Rutherford Backscattering/Channeling (RBS/C) technique, statistical uncertainties inherent to Monte Carlo simulations, and deviations introduced during the curve-fitting process applied to the MSDA model.

	$\sigma_I(10^{-14}cm^2)$	$fd_I(10^{10}cm^{-2})$
Ni	1.5	9.3
Ni _{0.88} Fe _{0.12}	1.6	5.8
Ni _{0.77} Fe _{0.23}	1.0	7.2

C.4.3 TEM analysis

TEM images taken at the fluence of $4 \times 10^{13} \text{ cm}^{-2}$ are presented in Figure 32. The images reveal that in pure Ni (Figure 32a), there is a high density of extended defects, primarily Frank and perfect dislocation loops, stacking fault tetrahedra (SFT), and defect clusters. This observation aligns well with the results from MSDA calculations and MD simulations. The main types of point defects, which we found during irradiation MD simulations in pure Ni are single vacancies, voids, self-interstitial atoms (SIAs), dumbbells, crowdions, and A15 nano-phase. This A15 nano-phase in Ni has also been reported and deeply studied by A. Goryaeva *et al.*¹³¹. In contrast to pure Ni, in Ni_{0.88}Fe_{0.12} (Figure 32b) we mainly see small defect clusters, which again confirm our findings based on the MSDA model analysis. Similarly to pure Ni, we also observe the effects of the formation of A15 nano-phase in the Ni_{0.88}Fe_{0.12} alloy. Moreover, we found single extended defects such as small SFT and dislocation loops. Whereas, in Ni_{0.77}Fe_{0.23} (Figure 32c) defect clusters are significantly smaller and we mostly see single extended defects

like SFT. As reported by Zhang *et al.*³⁷, in complex CSAs, the coupled electronic and atomic-level properties contribute to suppressing defect evolution and damage accumulation. At the atomic level, lattice distortion and a complex aperiodic energy landscape hinder defect migration and inhibit the growth of extended defects. A more disordered energy landscape results in smaller fault clusters, which create more localized, stressed regions within the lattice. Consequently, in complex CSAs, damage initiation and cluster formation mechanisms are influenced by local heat dissipation and enhanced defect annihilation, due to stronger electron-phonon coupling. This leads to fewer defects and more dispersed small clusters.

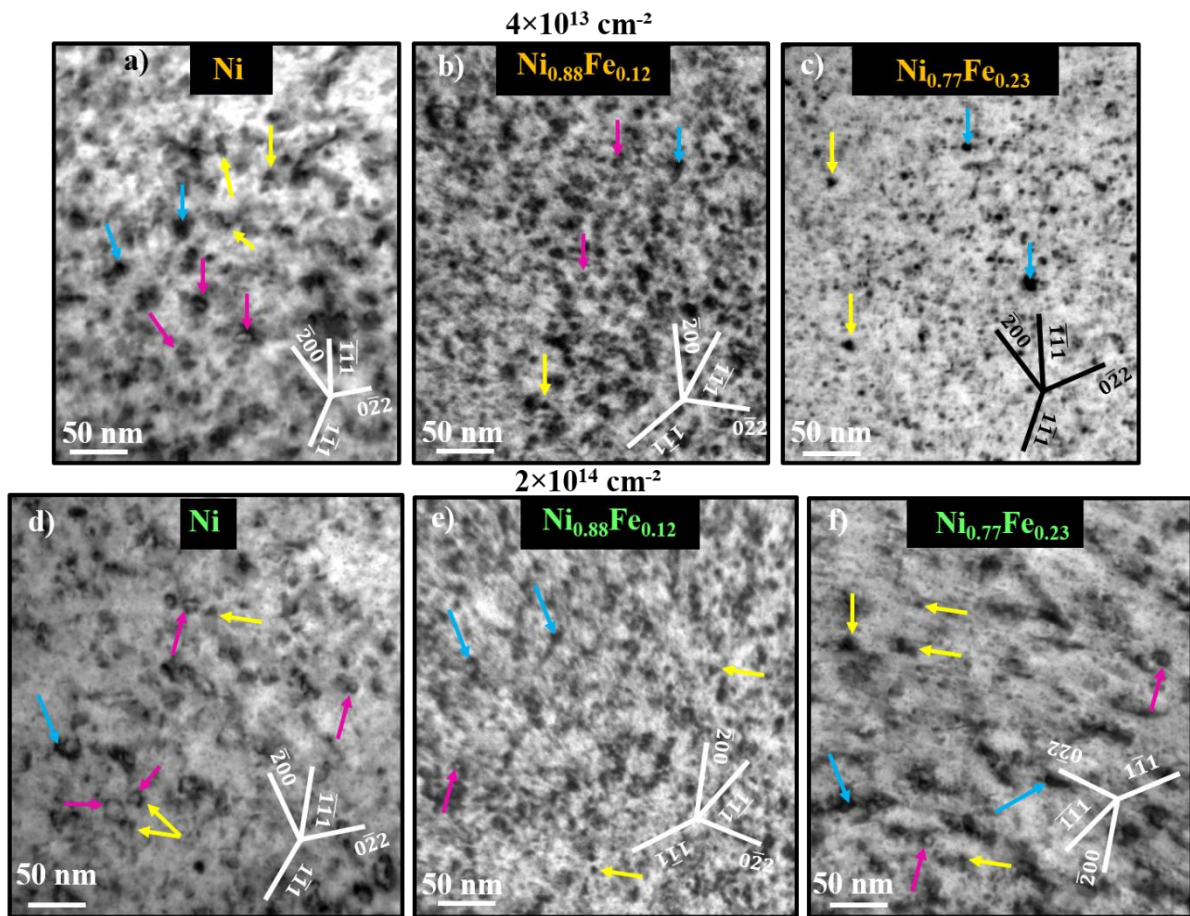


Figure 32. Bright field TEM images of a) Ni, b) Ni_{0.88}Fe_{0.12} and c) Ni_{0.77}Fe_{0.23} irradiated to the fluence of $4 \times 10^{13} \text{ cm}^{-2}$ and c) Ni, d) Ni_{0.88}Fe_{0.12}, f) Ni_{0.77}Fe_{0.23} irradiated to the fluence of $2 \times 10^{14} \text{ cm}^{-2}$. Pink arrows indicate dislocation loops, yellow SFT and blue, defect clusters.

TEM BF images of Ni, Ni_{0.88}Fe_{0.12}, and Ni_{0.77}Fe_{0.23} irradiated to the fluence of $2 \times 10^{14} \text{ cm}^{-2}$ are presented in Figure 32d, e and f. In Figure 32d, one can observe an increase in both the size and quantity of dislocation loops. Additionally, we can see SFT and small defect clusters are present, which suggest a decrease in the number of point defects. Interestingly, Figure 32d clearly shows that SFT are located at the borders of dislocation loops (see areas marked with pink arrows). This effect was also captured and described by Li *et al.*¹³⁷ during in-situ TEM

observation of irradiation-induced Frank loops and SFT in Pd. SFT were nucleated within the dislocation loops and they were also visible in the upper and lower regions of the loop plane. The same phenomenon is observed in pure Ni at the fluence of $2 \times 10^{14} \text{ cm}^{-2}$. SFT tends to be distributed within or near the Perfect loops¹³⁷. In Ni_{0.88}Fe_{0.12} (Figure 32e), we observe that the structure is dominated by defect clusters, suggesting the presence of a large number of point defects. Additionally, we can distinguish some SFT and small dislocation loops. In Ni_{0.77}Fe_{0.23} (Figure 32f) we spotted more extended defects than in Ni_{0.88}Fe_{0.12} and fewer point defect clusters which is in line with MD simulations (Figure 30) and MSDA analysis. The observation of more extended defects in Ni_{0.77}Fe_{0.23} is attributed to the defect migration phenomenon. As reported by Lu *et al.*⁸, point defects and defect clusters migrate much slower in SP-CSAs than in pure nickel. In pure Ni and Ni_{0.88}Fe_{0.12}, at higher fluences where mechanical stress is decreased, defect propagation in the bulk material may occur perpendicular to the sample surface. This could lead to an extended damage range with enhanced defect migration as ion fluence increases⁸. Consequently, in Ni_{0.77}Fe_{0.23}, we observe more densely packed defects (larger defect clusters) at the damage peak region, while in pure Ni and Ni_{0.88}Fe_{0.12}, defects may disperse into deeper regions of the sample. It is also noteworthy that although defect clusters form in both pure Ni and NiFe alloys, the kinetics of defect formation are significantly slower in NiFe than in pure Ni³⁷.

In order to quantitatively compare types and amount of defects in the irradiated Ni and Ni_xFe_{1-x} alloys up to the fluence of $2 \times 10^{14} \text{ cm}^{-2}$, we performed a comparative analysis based on the TEM experimental results and MD simulations (see Table 5) To measure dislocation size from MD simulations, we applied the DXA method to the samples, calculating the length of the dislocation loops in all cases. The average loop diameter was determined using the formula $d = \text{length} / \pi$. For SFT, the size was calculated based on the defect height, considering its pyramidal shape. For the calculation from the experiment we selected 20 defects in each composition and fluence and the total number of SFT was calculated as the sum of 20 defects with a size based on the height of the pyramidal shape and for dislocations we took into account its length.

Table 5. Quantitative comparison of stacking fault tetrahedra and dislocation loops based on TEM experiments and MD simulations. A good agreement was observed between the experimental measurements and MD simulations, showing that the presence of Fe in the Ni matrix reduces the number of SFT and dislocations, while an increase in fluence leads to an increase in their quantities.

Total length (sum) of SFT (nm)						
4×10 ¹³ cm ⁻²				2×10 ¹⁴ cm ⁻²		
	Ni	Ni _{0.88} Fe _{0.12}	Ni _{0.77} Fe _{0.23}	Ni	Ni _{0.88} Fe _{0.12}	Ni _{0.77} Fe _{0.23}
Experiment	46.02	46.81	42.47	62.98	54.97	50.37
Simulations	0.97	-	0.86	1.42	-	0.92
Total length (sum) of dislocations (nm)						
Experiment	82.69	53.78	52.94	110.41	55.24	80.68
Simulations	3.88	1.66	1.45	6.89	1.89	5.12

The comparison between simulation and experimental results reveals a consistent trend: the total length of stacking fault tetrahedra (SFT) decreases with increasing Fe content at both fluence levels. At a fluence of 4×10¹³ cm⁻², the SFT count remains comparable across different Fe concentrations. As ion fluence increases, we observe an overall increase in the number of SFT, indicating their growth. A similar trend is observed for dislocation loops. While the SFT count decreases with increasing Fe content at 4×10¹³ cm⁻² in both simulations and experiments, at the higher fluence of 2×10¹⁴ cm⁻², a decrease in the number of dislocations is observed in Ni_{0.88}Fe_{0.12} compared to pure Ni and Ni_{0.77}Fe_{0.23}.

C.5 Discussion

C.5.1 Defects evolution under irradiation

In order to validate the results obtained from MD simulations (see Figure 30) regarding point defects in Ni, Ni_{0.88}Fe_{0.12}, and Ni_{0.77}Fe_{0.23}, in Figure 33a-c we present results of experimentally obtained RBS/C spectra. Initially, the RBS/C data shows a decrease in backscattering yield with increasing Fe content, suggesting a reduction in the quantity of extended defects, mainly for Ni_{0.77}Fe_{0.23}. This is in line with other findings ³⁷, which shows that defect production and recombination are closely dependent on the alloy complexity.

In Figure 34 we see the percentage of randomly displaced atoms (RDA) obtained from the experimentally obtained spectra. In the RDA model, we assume that within a given depth range a certain percentage of atoms are randomly displaced, which generates direct scattering for the analyzing beam ^{78,79}. In Figure 34a, randomly displaced atoms in Ni are presented. From the figure, it is clear that in pure Ni, point defects are mostly concentrated near the surface up to the depth of 320 nm. However, the highest percentage of point defects is calculated at the

fluence of $4 \times 10^{13} \text{ cm}^{-2}$ (suggesting accumulation of small defects and their partials, which later coalescence), then the amount of point defects decreases with increasing ion fluence, which confirms that point defects start to transform to extended defects at fluence of $2 \times 10^{14} \text{ cm}^{-2}$.

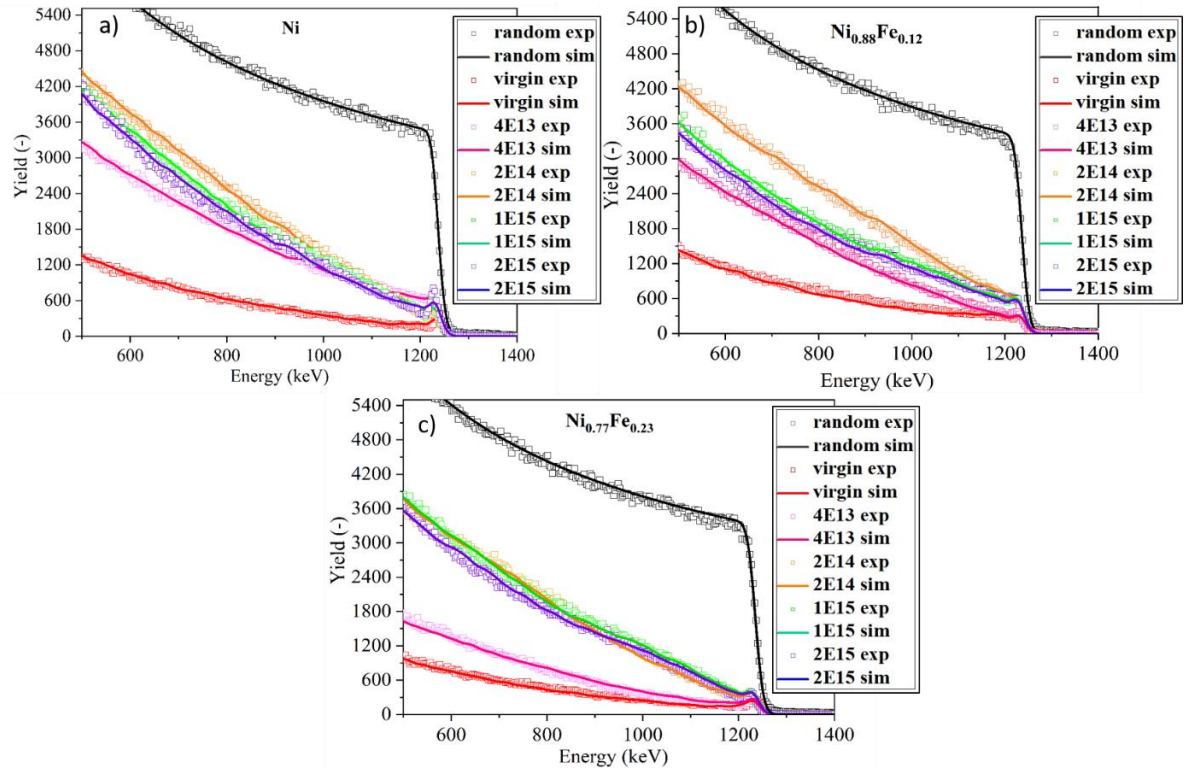


Figure 33. RBS/C spectra of a) Ni, b) $\text{Ni}_{0.88}\text{Fe}_{0.12}$, and c) $\text{Ni}_{0.77}\text{Fe}_{0.23}$ single crystals irradiated with the fluences from 4×10^{13} to $4 \times 10^{15} \text{ cm}^{-2}$. Solid lines represent fits obtained using MC simulations. Virgin and random spectra are included as references.

These experimentally obtained results are in line with MD simulations. Next, we can see the percentage difference between the amounts of RDA in $\text{Ni}_{0.88}\text{Fe}_{0.12}$ (Figure 34b) and in $\text{Ni}_{0.77}\text{Fe}_{0.23}$ (Figure 34c). The number of RDA in $\text{Ni}_{0.88}\text{Fe}_{0.12}$ increases up to fluence of $2 \times 10^{14} \text{ cm}^{-2}$ and then it decreases, which again is in line with our simulations, MSDA model and TEM analysis. In addition, point defects are distributed from the surface, deep into the material up to 500 nm at the fluence of $2 \times 10^{14} \text{ cm}^{-2}$. For the higher fluences, we observe less displaced atoms and their location is concentrated near the surface.

Notably, the most significant differences in defect distributions, both in terms of shape and quantity, are observed at relatively low doses. As fluence increases, we observe a trend toward normalization and saturation, resulting in similar distributions at higher doses. This indicates a shift in the types of defects with increasing dose in the tested materials. Additionally, this mechanism is different for pure nickel and the $\text{Ni}_{0.88}\text{Fe}_{0.12}$ alloy compared to the $\text{Ni}_{0.77}\text{Fe}_{0.23}$ alloy. In the first case, there is a decrease in the number of point defects correlated with an increase in extended defects, as reported in Figure 34a, and b). For the $\text{Ni}_{0.77}\text{Fe}_{0.23}$ alloy,

however we observe an increase and sort of segregation of point defects as a function of the dose. This is clearly visible in the RBS/C spectra (Figure 33c), where, at higher fluences, a bulge (damage peak) originating from point defects begins to appear after reaching saturation with defects. Our proposed mechanism for alloys with lower iron content and pure nickel is the transition from A15-type defect clusters to dislocation loops observed in MD and reported elsewhere¹³¹ (for pure nickel only).

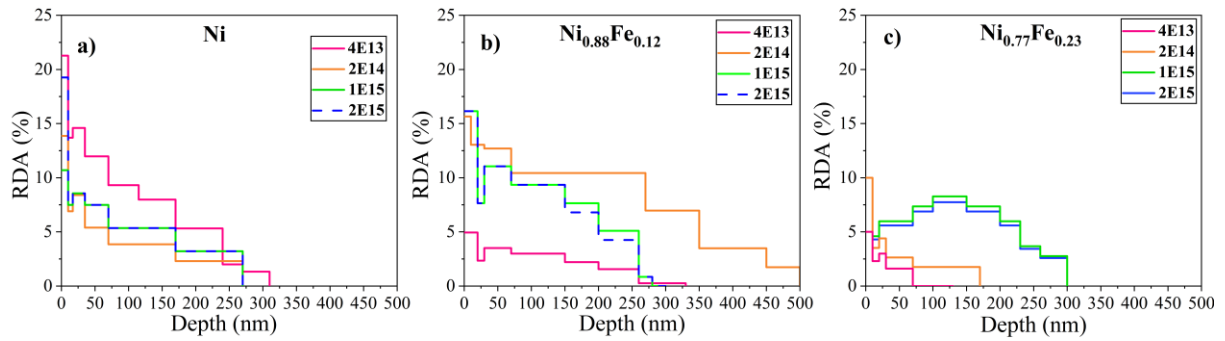


Figure 34. The depth profiles of randomly displaced atoms in a) Ni, b) Ni_{0.88}Fe_{0.12}, and in b) Ni_{0.77}Fe_{0.23} as a function of ion dose as indicated in the corresponding legends.

In contrast to Ni_{0.88}Fe_{0.12} in Ni_{0.77}Fe_{0.23} the number of point defects is significantly lower for low fluences up to $2 \times 10^{14} \text{ cm}^{-2}$. For these doses, displaced atoms are mainly concentrated near the surface unlike Ni_{0.88}Fe_{0.12}, where point defects extend into the material. We also see that for the higher fluences ($1 \times 10^{15} \text{ cm}^{-2}$) the total amount of point defects is significantly less in Ni_{0.77}Fe_{0.23} than in Ni_{0.88}Fe_{0.12}; however, their range of concentration is similar. The differences resulting from the depth of defect penetration between these two compositions are probably due to the fact that in pure Ni the defects have greater mobility than in alloys, which has been confirmed in several works^{8,9,78}. Therefore, the more Ni in the alloy, the greater mobility of defects in the material.

To quantitatively analyze defect structures, Figure 35 presents the concentration profiles of extended defects in Ni, Ni_{0.88}Fe_{0.12}, and Ni_{0.77}Fe_{0.23}, as derived from MC McChasy simulations. The model applied in this study is grounded in the Peierls-Nabarro framework for edge dislocations, where atomic displacements follow an arctan function, with the bending angle diminishing asymptotically as the distance from the dislocation core increases. Detailed descriptions of the simulation procedures and the underlying model can be found in previous studies^{78,103,121,138}.

It is clear that the number of extended defects is half as large for alloys as for pure Ni (Figure 35a). The number of defects increases up to $2 \times 10^{14} \text{ cm}^{-2}$ in Ni and then decreases with the fluence, which suggests fast defect saturation. The same trend is visible in Figure 35b and c,

which means that the saturation level at fluence of $2 \times 10^{14} \text{ cm}^{-2}$ is the same regardless of the chemical compositions. However, in Figure 35b, we see that the maximal values of the extended defects are the highest for Ni and comparable for alloys $\text{Ni}_{0.88}\text{Fe}_{0.12}$ and $\text{Ni}_{0.77}\text{Fe}_{0.23}$. The direct comparison between the investigated alloys reveals that the maximal number of extended defects for the highest fluences in $\text{Ni}_{0.88}\text{Fe}_{0.12}$ is lower compared to $\text{Ni}_{0.77}\text{Fe}_{0.23}$ which again confirms MD results (Figure 30) and MSDA analysis (Figure 31). Moreover, we noticed that for the higher fluences, defects migrate deeper into the material, which could result from a combination of processes such as defect recombination, production, cluster formation etc., as reported in ⁹⁹. According to Zhang *et al.* ³⁷ during modelling of Ni-Fe random alloys they noticed that chemically biased sluggish diffusion can be reinforced by increasing Fe content. The more sluggish defect diffusion, the higher possibility that vacancies and interstitials will interact and recombine, thus suppressing radiation damage accumulation. Defect recombination has also been visible in Figure 30. We can see that, for example, pure Ni point defects (interstitial, single vacancies, dumbbell) transform quickly into extended defects like Frank loops or SFT mainly formed by stair-rod dislocations. According to a recent study of irradiated fcc metals ⁹⁹ vacancy clusters rearrange directly to form SFT due to compressive stress fields induced by interstitial Frank loops.

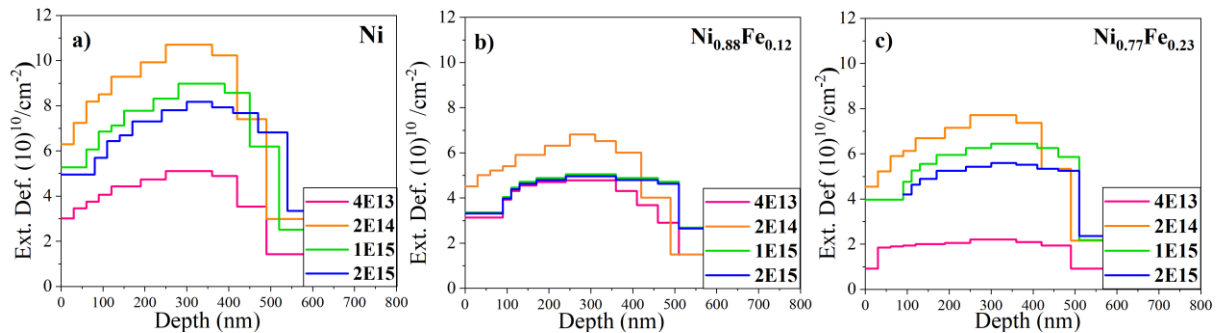


Figure 35. Damage distribution profiles for a) Ni, b) $\text{Ni}_{0.88}\text{Fe}_{0.12}$, and c) $\text{Ni}_{0.77}\text{Fe}_{0.23}$ obtained from the MC simulations performed for RBS/C experimentally obtained spectra and normalized to the maximal value of Ext. Def.

What is interesting, SFT acquires growth by clustering of vacancies, while the growth of Frank dislocation loops occurs through the absorption of interstitial atoms. It is worth mentioning that in the alloys, the defect formation and distribution can be influenced by Fe content because of the different electron configurations of Fe compared to Ni. In alloys with elements having large differences in valence electrons, perturbations can significantly impact energy dissipation through interatomic electron rearrangement and charge transfer. This phenomenon has been described in detailed by Zhang *et al.* ³⁷. It is explained the interstitial tend to migrate by exchange with Ni atoms, and vacancies in $\text{Ni}_x\text{Fe}_{1-x}$ prefer to migrate by exchange with Fe atoms.

The presence and origin of slow vacancy-based diffusion is attributed to differences in the energy barriers between the alloying elements and the vacancies. The diffusion barrier, which represents the obstacle between a vacancy and a neighbouring atom, varies for Fe and Ni vacancies (i.e., the vacancy's exchange with nearby Fe or Ni atoms). This variation suggests that Fe vacancies are more mobile compared to Ni vacancies. When a Fe atom is adjacent to a vacancy, the vacancy can repeatedly swap places with the Fe atom (primarily exchanging with the Fe atom), moving back and forth. This repeated exchange can slow down the overall diffusion process. Since there is a lower chance of the vacancy exchanging with a Ni atom, the diffusion path will only progress if the vacancy encounters another Fe atom to exchange with. In dilute alloys, the number of such interactions (or traps) is minimal. However, as the Fe concentration approaches around 20%, which is near the site percolation threshold, more traps become available, significantly increasing the chances of delayed vacancy diffusion. Once this threshold is exceeded, the probability of forming connections between vacancies and surrounding Fe atoms rises. Consequently, the diffusion coefficient increases with higher Fe concentration, with the maximum observed sluggish effect under the vacancy diffusion mechanism occurring at approximately 20 atomic percent of Fe ³⁷.

C.5.2 Defect formation mechanisms

We observe the presence of A15 nano-phase clusters in Ni and Ni_{0.88}Fe_{0.12}, and occasionally in Ni_{0.77}Fe_{0.23} samples for low fluences during modeling. According to literature ⁸⁶ small A15 clusters are formed via the accumulation of non-parallel <100> dumbbells around the interstitial atom at the octahedral site ⁸⁶. Bigger A15 clusters can be formed by agglomeration of interstitial atoms in *fcc* octahedral sites around the A15 icosahedron, followed, by accumulation of dumbbells that built icosahedral structures. The formation process of A15 in the *fcc* matrix occurs through the progressive accumulation of interstitial atoms at *fcc* octahedral sites. This effect occurs at low doses of irradiation or very low dpa levels (0.05-0.1 dpa). As irradiation of the Ni-based samples continues, the A15 nano-phase, comprising more than 10 atoms, promotes the formation of Frank loops within their native {111} plane; according to the atomistic modeling. This mechanism is observed in pure Ni, consistent with previously reported results ^{86,131} as well as in Ni_{0.88}Fe_{0.12} and Ni_{0.77}Fe_{0.23} alloy. However, for concentrations exceeding 20% of Fe in the Ni matrix, although A15 nano-phases are formed, their small size prevents them from evolving into Frank loops, despite being highly Fe decorated. Therefore, we postulate that this phase can be partially responsible for the most prominent hardening in Ni, Ni_{0.88}Fe_{0.12},

compared to Ni_{0.77}Fe_{0.23} where there was the least amount of this phase (see supplementary materials). To understand the nature of the irradiation-induced dislocation loops in Ni, Ni_{0.88}Fe_{0.12}, Ni_{0.77}Fe_{0.23}, we have performed a detailed study based on conventional TEM imaging under the two-beam conditions^{139–141}. As a first step of the observation, samples were tilted to the closest [011], low-index zone axis. Then, a series of bright BF images in various two-beam conditions were taken from the same area. As a result it was possible to compare dislocation appearance under different imaging conditions. Figure 36 presents BF TEM two-beam condition images near the [011] zone axis of pure Ni sample at a fluence of 4×10^{13} and 2×10^{14} cm⁻² using various g vector. We added results obtained from MD simulations to guide the identification of faulted loops and SFT for g -vectors of (002), (-111), (-11-1) and (-220). Most of the dislocation loops in pure Ni for both fluences are the faulted loops, SFT, perfect loops and edge dislocations, which were clearly visible under g -vector of (-220).

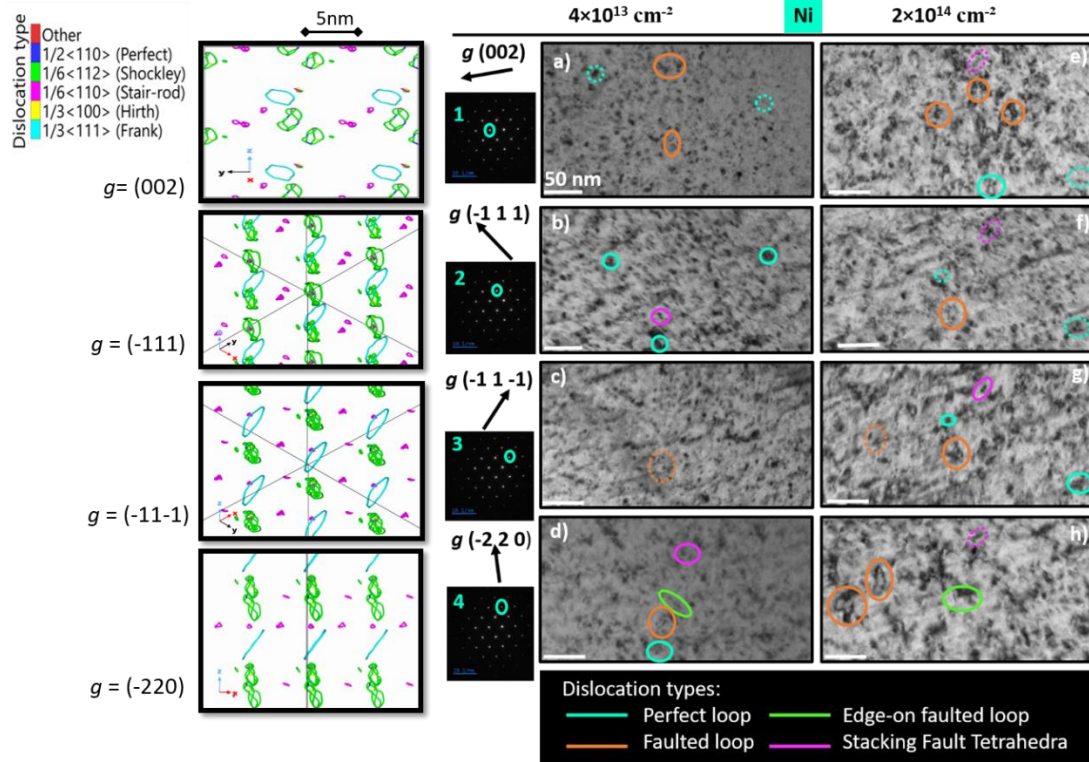


Figure 36. BF TEM two-beam condition images near the [011] zone axis of pure Ni sample at a fluence of 4×10^{13} and 2×10^{14} cm⁻² using different g vector by identifying perfect and faulted loops, as well as stacking faults guided by MD simulations results.

In Figure 36(b,d,g) we report that SFT typically appear in pairs and are closely aligned. At a fluence of 2×10^{14} cm⁻², we observe more complex faulted loops, which MD simulations identify as Frank loops (see Figure 30). Additionally, there is evidence of the transformation of the A15 nano-phase into Frank loops (see videos of MD simulations in supplementary material). At a

fluence of $4 \times 10^{13} \text{ cm}^{-2}$, perfect loops are visible under the $[-111]$ g-vector. These loops are small (approximately 2-3 nm) and are not detectable with other g-vectors. At higher fluences, perfect loops are also observed under the $[002]$ and $[-11-1]$ g-vectors, and are positioned closely together. In the Ni_{0.88}Fe_{0.12} alloy (Figure 37), at lower fluences, small perfect loops are similarly observed near each other under the $[002]$ g-vector, analogous to pure Ni. Faulted loops are present under all imaging conditions and fluences. SFT, similar to those in pure Ni, are observed in proximity under the $[-11-1]$ and $[-220]$ g-vectors. At higher fluences, the predominant features are faulted loops and small defect clusters, which appear as dark regions in the images. Edge-on faulted loops are visible under the $[-111]$ and $[-11-1]$ g-vectors. Finally, for the Ni_{0.77}Fe_{0.23} alloy (Figure 38), small SFT are visible at lower fluences under the $[002]$, $[-111]$, and $[-11-1]$ g-vectors, arranged similarly to those in Ni and Ni_{0.88}Fe_{0.12}. Perfect loops are seen under the $[-111]$ g-vector at low fluences and under the $[-220]$ g-vector at both fluences, though they are not observed at a fluence of $2 \times 10^{14} \text{ cm}^{-2}$ under the $[-11-1]$ g-vector. At higher fluences, there is a notable increase in faulted loops and edge-on dislocations under the $[-11-1]$ and $[-220]$ g-vectors.

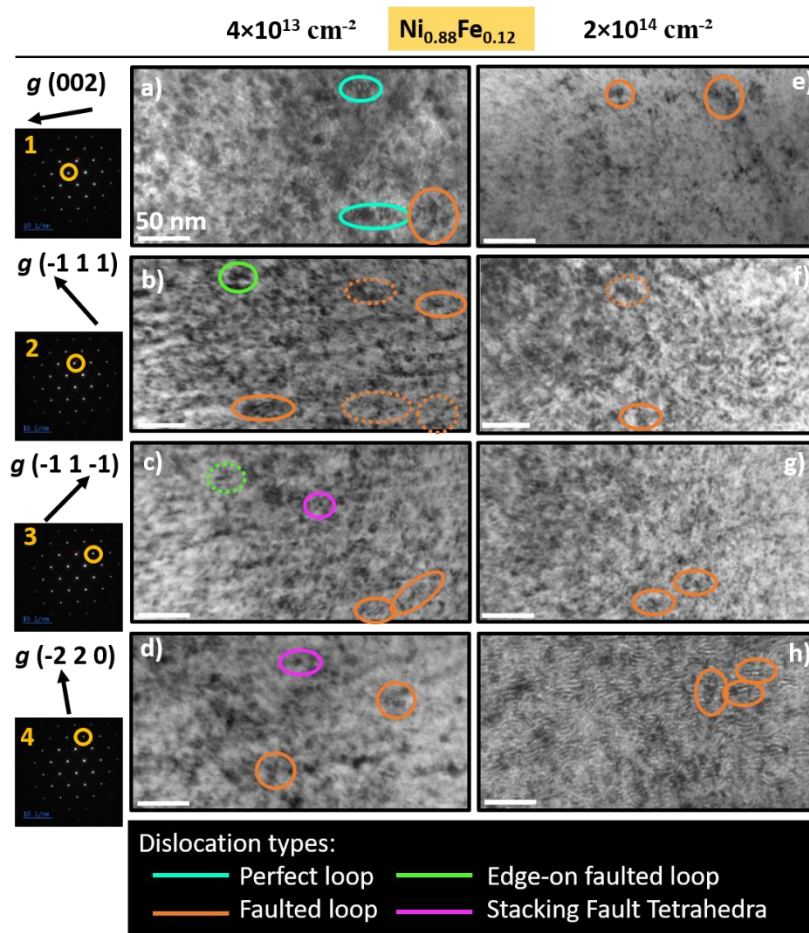


Figure 37. BF TEM two-beam condition images near the $[011]$ zone axis of Ni_{0.88}Fe_{0.12} sample at a fluence of 4×10^{13} and $2 \times 10^{14} \text{ cm}^{-2}$ using different g vector by identifying perfect and faulted loops, as well as stacking faults.

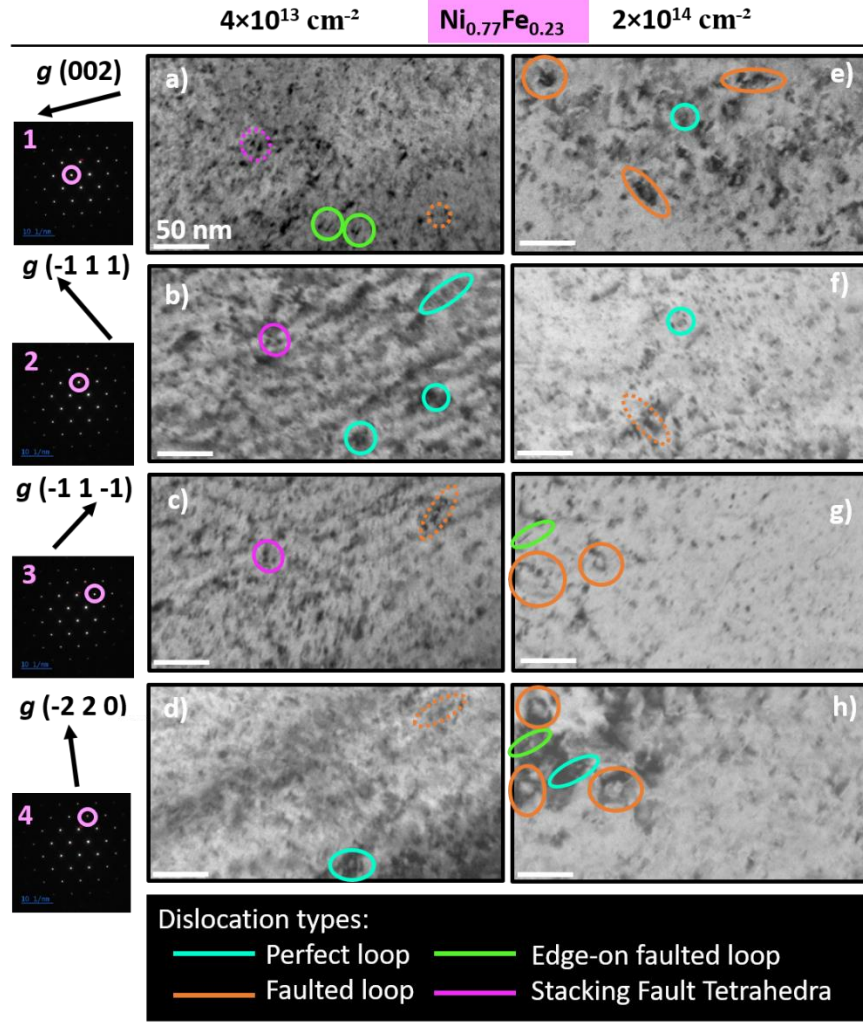


Figure 38. BF TEM two-beam condition images near the $[011]$ zone axis of $\text{Ni}_{0.77}\text{Fe}_{0.23}$ sample at a fluence of 4×10^{13} and $2 \times 10^{14} \text{ cm}^{-2}$ using different g vector by identifying perfect and faulted loops, as well as stacking faults.

Moreover, we evaluate defect size and density changes during irradiation. Specifically, an average defect size and defect density for the Ni, $\text{Ni}_{0.88}\text{Fe}_{0.12}$, and $\text{Ni}_{0.77}\text{Fe}_{0.23}$ at fluences of 4×10^{13} and $2 \times 10^{14} \text{ cm}^{-2}$ are shown in Table 6. A noticeable difference is that the size of the defects decreases with increasing iron content and increases with the dose for a particular composition. Similar effects have been observed for the compositions with higher content of Fe (38, 50, 62 at. %) ^{11,78,79}. Interestingly, D.S. Aidhy *et al.* ⁵¹ have reported that the addition of Fe to Ni has a larger effect on the cluster sizes due to the modification of migration energies and extended defect formation energies. Moreover, they demonstrated that point defect diffusion followed by clustering kinetics is slower in NiFe and NiCr leading to slower cluster formation. These findings are in line with our experimental and simulation results.

In Table 6, we present the averages from three series of MD simulations at fluences of 4×10^{13} and $2 \times 10^{14} \text{ cm}^{-2}$ alongside a comparison with experimental results obtained from TEM images. Both experimental data and MD simulations reveal that dislocation density across all samples

escalates with increasing dpa levels, particularly evident in pure Ni where the dislocation density markedly rises. This phenomenon arises from the presence of Fe atoms in the Ni matrix, which diminishes dislocation mobility. Additionally, this trend is reflected in the size of dislocation loops, although there may be discrepancies in absolute values between MD simulations and experiments due to differences in length and time scales.

Table 6. Dislocation density and defect size of Ni, Ni_{0.88}Fe_{0.12}, and Ni_{0.77}Fe_{0.23} at 0.1 and 0.5 dpa. Comparison between MD, in bold, and experimental, in italic, data.

	$\rho(10^{13}m^{-2})$		Defect size (nm)	
	0.1 dpa	0.5 dpa	0.1 dpa	0.5 dpa
Ni	1.25 <i>2.00</i>	2.88 <i>7.00</i>	3.45 ± 1.5 <i>7.0 ± 2.5</i>	8.65 ± 0.75 <i>8.0 ± 4.0</i>
Ni _{0.88} Fe _{0.12}	0.98 <i>2.00</i>	1.00 <i>2.00</i>	0.98 ± 0.15 <i>5.5 ± 2.5</i>	2.85 ± 1.15 <i>6.0 ± 2.5</i>
Ni _{0.77} Fe _{0.23}	0.78 <i>3.50</i>	1.18 <i>4.50</i>	1.12 ± 0.15 <i>5.0 ± 2.5</i>	3.30 ± 1.15 <i>6.0 ± 2.5</i>

Simulations are confined to short timescales (up to a few nanoseconds) and small system sizes, which limit the extent of dislocation evolution and interactions that can be captured. Moreover, the modelling presented in this study focuses on the early stages of damage formation, particularly overlapping collision cascades, whereas experimental irradiation involves longer-term effects such as defect migration, clustering, and interactions with microstructural features. These cumulative effects can significantly increase the dislocation density in real materials. Additionally, experimental dislocation densities were estimated from TEM images using the line-intercept method, which may account for both extended and sub-threshold defect features not readily resolved in atomistic simulations. Conversely, the dislocation densities in simulations are calculated from atomic configurations using precise identification algorithms that may exclude incipient or highly diffuse structures. These factors collectively explain the observed discrepancies. Notwithstanding, the observed trend remains consistent; defect sizes augment with rising dpa levels for each sample, albeit mitigated by the inclusion of Fe in the Ni matrices, leading to a reduction in defect sizes.

In Figure 39, we present the evolution of dislocation density as a function of displacement per atom (dpa) from MD simulations. At the earliest stages of irradiation, collision cascades lead to the formation of Frenkel pairs—SIAs and vacancies—which rapidly coalesce into small Shockley partial dislocation loops on {111} planes, driven by the low stacking fault energy of

fcc Ni and NiFe alloys^{29,77}. As damage accumulates through overlapping cascades, these small loops undergo mutual interaction, leading to complex defect reactions. Shockley loops can transform into faulted Frank loops via the addition of SIAs along $\langle 111 \rangle$ directions. In parallel, Lomer–Cottrell-type stair-rod dislocations form as sessile junctions where multiple Shockley partials intersect, particularly at high dislocation densities. Our simulations (Figure 39a–b) demonstrate that the density of stair-rod dislocations increases progressively with dose, consistent with the increased prevalence of stacking fault tetrahedra (SFTs), which are vacancy-stabilized extended defects enclosed by $\{111\}$ planes. Conversely, Frank loops, once nucleated, tend to grow by absorbing mobile SIAs or smaller loops. Notably, our simulations show cases where larger Shockley chains can absorb pre-existing Frank loops, leading to loop coalescence and size distribution evolution—particularly evident at fluences on the order of $4 \times 10^{13} \text{ cm}^{-2}$ in both pure Ni and Ni_{0.77}Fe_{0.23}. This asymmetry in loop evolution behavior is supported by Barashev et al.⁵⁴, who demonstrated that Ni-rich sinks have a higher affinity for interstitial atoms than for vacancies, promoting growth of SIA-type dislocation loops under irradiation. In Figure 39c, we illustrate a representative Frank loop and adjacent SFT formed in the MD simulations, along with an A15 nano-phase cluster composed of 13 atoms. These snapshots, validated by the crystallographic configurations and Burgers vector analysis, serve as guides for interpreting extended defects in TEM images. Supplementary videos provide full temporal visualizations of the defect evolution—including point defects, loop formation, SFT nucleation, and A15-phase clustering—as a function of dose for all compositions.

Our atomistic simulations, further corroborated by TEM observations, reveal that dislocation loops predominantly form and glide along $\{111\}$ planes. Frank loops, bounded by sessile $\langle 111 \rangle$ partials, act as potent obstacles to mobile dislocations due to their high line energy and lack of mobility. These loops contribute directly to irradiation-induced hardening by impeding dislocation motion. The interaction mechanisms between mobile dislocations and three-dimensional SFTs are more nuanced. When the glide plane of a moving dislocation intersects the habit plane of an SFT, several outcomes are possible, depending on the geometric and energetic configuration. If the vertical distance between the SFT and the glide plane exceeds the SFT height, no interaction occurs. However, if the glide plane intersects the SFT volume, the dislocation may (1) shear through and incorporate the SFT into its line, or (2) truncate the SFT, potentially fragmenting it into smaller tetrahedra. These interaction modes are particularly prevalent in the NiFe alloys, where higher defect complexity arises due to compositional effects on defect mobility and binding energies. Overall, the nucleation, growth, and interaction of

dislocation loops and SFTs constitute a major source of irradiation hardening. These extended defects act as strong barriers to dislocation motion by altering the local stress field and introducing strain incompatibility across slip planes. The corresponding hardness trends, linked to defect density and type, are discussed in the Supplementary Materials.

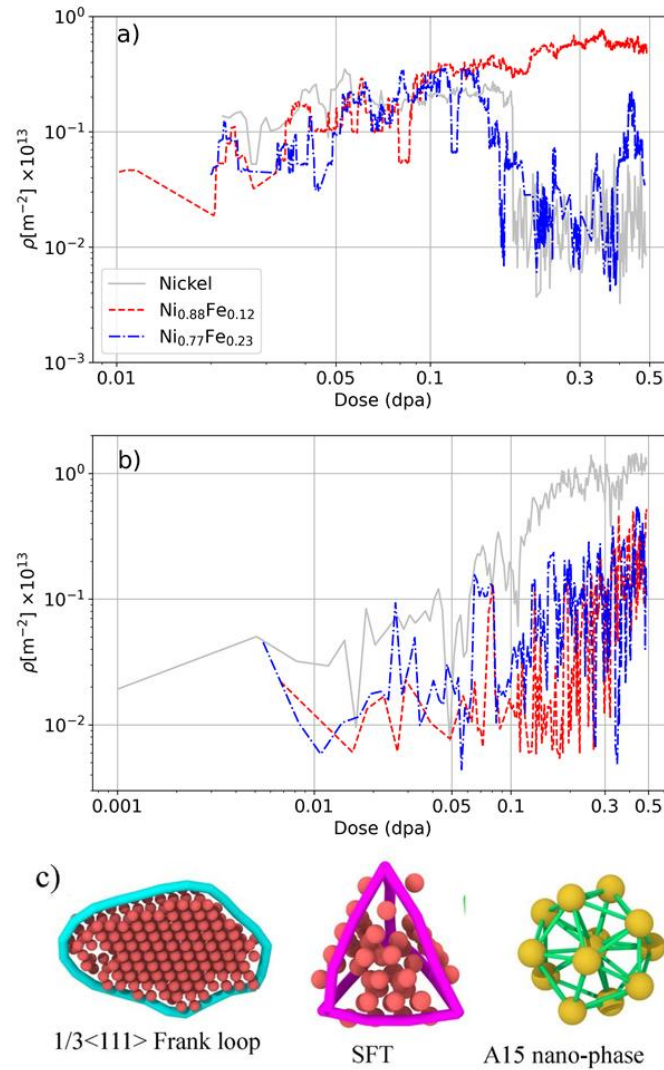


Figure 39. Dislocation density as a function of the dpa for (a) Frank loops and (b) Stair-rod dislocations for Ni and NiFe CSAs. (c) The defects formed in the MD simulations with a $1/3\langle 111 \rangle$ Frank loop with 2 stacking fault planes, and SFT mainly formed by stair rod dislocation, and an A15 nano-phase formed by 13 atoms.

C.6 Conclusions

Our study represents a comprehensive demonstration of the formation and dynamics of irradiation induced defects, especially, within the low irradiation fluence for pure Ni, $\text{Ni}_{0.88}\text{Fe}_{0.12}$, and $\text{Ni}_{0.77}\text{Fe}_{0.23}$ alloys. This insight was achieved through a synergistic approach combining electron microscopy analysis and Rutherford backscattering spectrometry, complemented by experimentally guided atomistic simulations and a damage kinetics model.

A detailed characterization of irradiation-induced dislocation loops in Ni, Ni_{0.88}Fe_{0.12}, and Ni_{0.77}Fe_{0.23} alloys, employing a combination of bright field (BF) TEM imaging under various two-beam conditions, molecular dynamics (MD) simulations, and the MC McChasy code developed in NCBJ was presented. In pure Ni, most dislocation loops at fluences of 4×10^{13} and 2×10^{14} cm⁻² were identified as faulted loops, stacking fault tetrahedra (SFT), perfect loops, and edge dislocations. Notably, at higher fluences, we observed the emergence of more complex faulted loops, likely Frank loops, with some instances of A15 nano-phase transforming into Frank loops. The presence of the A15 nano-phase is particularly important, as it plays a crucial role in defect formation and evolution, potentially influencing the irradiation-hardening mechanism. In Ni_{0.88}Fe_{0.12} and Ni_{0.77}Fe_{0.23}, we observed similar trends, with small perfect loops and SFT located in close proximity. However, at higher fluences, these alloys exhibited more faulted loops and defect clusters, highlighting the complex interplay between defect migration and alloy composition, as supported by our Monte Carlo-based McChasy simulations. The identification of the A15 nano-phase underscores its significance in understanding the early stages of defect formation and its impact on the irradiation response of these materials.

To sum up, we used a number of techniques and simulations to perform a quantitative and qualitative analysis of the defects, especially at a low fluence level. Both the simulation results and the use of the MSDA model showed that point defects dominate in the structure of Ni and Ni_{0.88}Fe_{0.12} alloys, which was also proven by analyzing the distribution of randomly displaced atoms and extended defects calculated from experimentally obtained RBS/C spectra. Our findings are pivotal for the design of structural materials for nuclear applications, providing valuable insights into material behavior under specific conditions. Looking ahead, future research endeavors should extend to high-temperature implantation testing to comprehensively assess the utility of these materials and evaluate the evolution of point defects at elevated temperatures.

Supplementary materials:

Description Video S1a:

Visualization of defect formation during irradiation for a pure Ni sample reveals the formation of the A15 nano-phase at low dpa values, progressing to Frank loops. At higher dpa values, the formation of stacking fault tetrahedra is observed.

Description Video S1b:

Defect formation as a function of dpa dose in the low Fe content Ni_{0.88}Fe_{0.12} alloy exhibits a similar mechanism, with the A15 nanophase evolving into Frank loops, akin to observations in pure Ni.

Description Video S1c:

The inclusion of Fe in the Ni_{0.77}Fe_{0.23} alloy leads to an increase in dislocation density, coupled with a reduction in the size of extended defects such as dislocation loops and stacking fault tetrahedra (SFTs) during irradiation, as shown by MD simulations.

Article D:

*Combining MD-LAMMPS and MC-McChasy2 codes for
dislocation simulations of Ni single crystal structure*

*Cyprian Mieszczyński, Przemysław Józwik, Kazimierz Skrobias, Kamila
Stefańska-Skrobias, Renata Ratajczak, Jacek Jagielski, Frederico Garrido,
Edyta Wyszowska, Alexander Azarov, Katharina Lorenz, Eduardo Alves,
**Nuclear Instruments and Methods in Physics Research Section B: Beam
Interactions with materials and Atoms, 540 (2023) 38-44,***

DOI: 10.1016/j.nimb.2023.04.010

IF: 1.377, Ministry points: 70

D.1 Abstract

The unique capability of the new version of the McChasy code (called McChasy2) is to provide the possibility to simulate experimental energy spectra delivered by Rutherford Backscattering Spectrometry in channeling direction (RBS/C) using large atomic structures (ca. 10^8 atoms). Ni-based alloys are nowadays one of the most studied and promising materials that can be used in the power generation sector and in general for high-temperature applications because of their radiation resistance and proof against harsh environmental conditions.

In this work, we present recent results of investigations regarding simulations of extended structural defects (edge dislocations and loops) developed in the directions typically observed in the *fcc* systems that are formed inside nickel-based single-crystal alloys. The extended defect models are created using ATOMSK and the Molecular Dynamics (MD)-LAMMPS thermalization process. The models are then used to create virtual samples and fit experimental RBS/C spectra.

Keywords: Rutherford backscattering, Ion channeling, Monte Carlo simulations, Molecular Dynamics simulations, Dislocation loops.

D.2 Introduction

The constant increase in electricity consumption forces the dynamic development of a new generation of nuclear and thermonuclear reactors and hence, new materials resistant to specific operating conditions (radiation, high temperature, corrosive environment). In fact, one of the most significant factors that have the biggest impact on the materials (fuel, cladding, etc.) considered for nuclear power plants is the resistance to defect creation (both point and extended defects) caused by irradiation and fission product incorporation.

Radiation-induced defects formed in nuclear materials have been extensively studied by many groups over the past decades. For the analysis of structural properties for damaged single crystals, the Rutherford Backscattering Spectrometry in channeling mode (RBS/C) can be used as a standard method^{142–145}. However, due to the complexity of the scattering process in the presence of defects and the limited availability of computational software dedicated to the analysis of ion channeling data, the correct and unambiguous interpretation of the RBS/C spectra is challenging. Analytical models are usually applied to extract depth profiles from channeling data for the case of randomly displaced lattice atoms. By applying the discontinuous model of dechanneling, depth distributions can be also obtained in case of extended defects

^{146,147}. At the National Centre for Nuclear Research (NCBJ) in Poland, the McChasy code (called McChasy1) ^{73,102,103,148}, has been developed with the main purpose to find an alternative way and to improve the quantitative analysis of defects. Using Monte Carlo (MC) algorithms the code can reproduce RBS/C experimental spectra by simulating He-ions traveling inside a single unit cell (surrounded by neighboring atoms) of a considered crystalline structure and calculate the probability of the backscattering process that is eventually converted to an RBS/C energy spectrum.

Because of the huge potential of atomistic and molecular simulations, the use of more realistic models of complex defects in large structures is envisaged in the new (v.2.1) version of the McChasy code that has been recently developed at NCBJ. The code can simulate channeling spectra in large structures containing up to $\sim 10^8$ atoms (with the possibility to increase this number, if needed). It is important to mention that the new code can operate with different file formats and it is compatible with almost every program providing atomic positions of the material under investigation as an output. In terms of capabilities, the McChasy2 code can be compared to the similar, existing (under development) RBSADEC code ^{149–151}. The main assumption implemented in the McChasy2 code is the possibility of cutting, multiplying, and propagating a particular, selected type of defect (according to a given depth distribution) and then studying the relationships between the parameters of the chosen defect (e.g., its size, position, orientation, etc.) and the RBS/C spectra.

In this work, we use the McChasy2 code for structures produced in two alternative ways: (i) using a built-in application that works based on crystallographic data and (ii) using an open-source Large-scale Atomic/Molecular Massively Parallel Simulator Molecular Dynamic (LAMMPS) code ¹⁵². The huge potential of an early version of the code has already been presented elsewhere ^{92,153}. The reported simulations performed for magnesium aluminate spinel (MgAl₂O₄) result in a very good agreement with experimental RBS/C spectra as well as with the previous generation of the code (i.e., McChasy1). The spinel structure was chosen previously as a test case material with randomly displaced single atoms being the dominant type of radiation-induced damage. For that reason, simulations involve only one model of defects that is required to reproduce RBS/C experimental spectra and provide better unambiguity, which is necessary to fairly compare experimental results with those obtained via a computational approach. The good agreement with the previous version of the code proves that defects modeled as randomly displaced atoms (RDA) are applied in a similar manner using both programs. It should be pointed out that the models of defects are easier to be implemented

in the second version of the code and the implementation itself in large structures gives much more possibilities. The new version of the code (v.2.1) is compatible with almost every program giving a file containing atomic positions as output. Moreover, it can work with other computer applications that provide crystallographic structures containing analytically added defects.

In this paper, we focus on simulations performed with the McChasy2 code for a crystalline structure of (001) Ni containing dislocation loops that were created by complementary use of two programs designed for materials modeling: ATOMSK software¹⁵⁴ and LAMMPS code. Specifically, ATOMSK software provides an analytical algorithm to create a selected defect in a structure of interest, while the LAMMPS code uses Molecular Dynamics simulations that give a possibility to thermalize analytically developed defects (and the whole structure itself) and allows using of peripheral add-ons to reproduce spectra of several structural techniques like TEM or XRD^{155,156}. Thanks to this, one can obtain the full structural overview of a modeled sample.

The current status of an early testing phase of the code and recent simulation results with special emphasis placed on the difficulties related to the MD–MC interface of the code is discussed and presented in the paper using the example of a monocrystalline Ni structure. Because of its resistant response to harsh environmental conditions^{44,68,157} and the potential applications for the power generation sector, the studies of radiation resistance and defect formations especially the evolution of formed dislocation loops¹⁴¹ in Ni-alloys are of high importance.

D.3 Methods

The LAMMPS simulations provide models of defected Ni crystal structures at a temperature of 300 K and pressure of 10 atm. For each case, well-thermalized atom positions were obtained after 20,000 steps, which correspond to 20 ps of real-time, the step interval was set equal to 1 fs; as a gauge of a final thermalization, the fluctuation of total energy less than 1% was assumed. Both temperature and pressure were controlled by Nosé–Hoover algorithm (100), which emulates the NPT ensemble, where N corresponds to the constant number of atoms, P - constant pressure, and T - constant temperature. To avoid spurious surface effects, calculations were done under periodic boundary conditions, which create virtual infinite crystals. The final 250 steps of the simulation were recorded and next averaged to produce atomic positions close to free of thermal motion. Interactions between atoms during ongoing MD simulations are approximated by potential energy functions. In this case, the Embedded Atom Model (EAM) potential with parameters given by Foiles was used¹⁵⁸.

The self-ion irradiation was carried out at room temperature with 1.5 MeV $^{58}\text{Ni}^+$ ions using a 1 MV NEC tandem accelerator. The ion fluence was set to $2 \times 10^{14} \text{ cm}^{-2}$. To avoid channeling, the implantation was performed with a tilt of 7 degrees off the normal $\langle 100 \rangle$ direction. The virgin and implanted samples were characterized by RBS/C using 1.6 MeV He^+ ions. The backscattering yield was measured by a detector placed at 165° relative to the incident beam direction.

The mean projected ranges of Ni ions and depth distributions of defects induced by bombarding Ni ion beams were estimated using Stopping and Range of Ions in Matter (SRIM) simulations^{65,69}. The corresponding displacements per atom (DPA) profiles were predicted by SRIM code under a displacement energy threshold of 40 eV for all elements using the full cascade mode. The maximum damage profile estimated by SRIM is located at the depth of about 500 nm for beam energy used (1.5 MeV $^{58}\text{Ni}^+$). MC simulations were performed using the most recent version of the McChasy2 code. Considering the shape of experimentally obtained channeling spectra and based on the results of RBS/C simulations of single-phase concentrated solid solution alloys (SP-CSAs)⁶⁸, the current investigations were done using mainly the representation of extended, dislocation-like defects (with no RDA taken into account). The model of dislocations developed for McChasy1 is based on the Peierls-Nabarro approach^{159–161} and requires geometrical parameters of the defect to be determined for every structure^{73,103}. In the second version of the code, the user can create defects using external codes, e.g., ATOMSK. Hence, dislocation loops of different sizes and orientations can be easily prepared for further simulations using the McChasy2 code. In the present study, we used $\langle 110 \rangle$ and $\langle 112 \rangle$ oriented dislocation loops along $\{111\}$ and $\{-1-11\}$ planes. Such defects in *fcc* structures usually exist as Shockley partials coming from the splitting of the $a/2 \langle 110 \rangle \{111\}$ edge dislocation, which is energetically favorable and in the end leads to the formation of a Stacking Fault (SF)^{81,162}. The other parameters and simulation conditions were chosen carefully to match the experimental ones. A detailed description of the MC channeling simulation procedures can be found elsewhere^{68,102,103}.

To avoid the issue related to discrete positions of extended defects reported in our previous papers^{138,153}, in the newest version of McChasy2 instead of using a single sample for each concentration, dozens of virtual samples with different distributions of the loops were created. The obtained spectra were simultaneously averaged during ongoing simulations. In fact, due to a compromise between the number of samples produced, computer capabilities, and computation time, this solution does not fully help to deal with the spectrum roughness. In

McChasy1 this problem was not observed because the positions of dislocations are randomly chosen during the simulation, so the statistics are related directly to the number of probing projectiles used for simulations and not to the number of samples created (like in the case of McChasy2, which uses, in fact, certain numbers of both structures and probing projectiles).

For graphical interpretation and 3D visualization of atomistic data obtained from MD or MC simulations, the custom applications combined with Origin, Gnuplot and Open Visualization Tool (OVITO) software were used ⁸⁵.

D.4 Results and Discussion

D.4.1 Atomic Positions Given by External Codes

The most important capability that is required to simulate RBS/C experimental spectra recorded for ion-bombarded crystalline materials is the possibility to create structures containing complex defects according to given depth distributions depending on the parameters of the bombarding ion beam (e.g. nature, energy, fluence). Such structures can be prepared for use in the McChasy2 code using custom merging procedures. Dislocation loops or any other structural defects can be cut off, multiplied, and merged with bulk material to create large (hundreds nm long) structures. The typical dimensions of a single cell are about (30x30x500) nm³. The cubature, of course, can be adjusted to meet the appropriate conditions. Such samples typically contain from millions up to a few hundred million atoms. The developed structures can be later used for MC simulations.

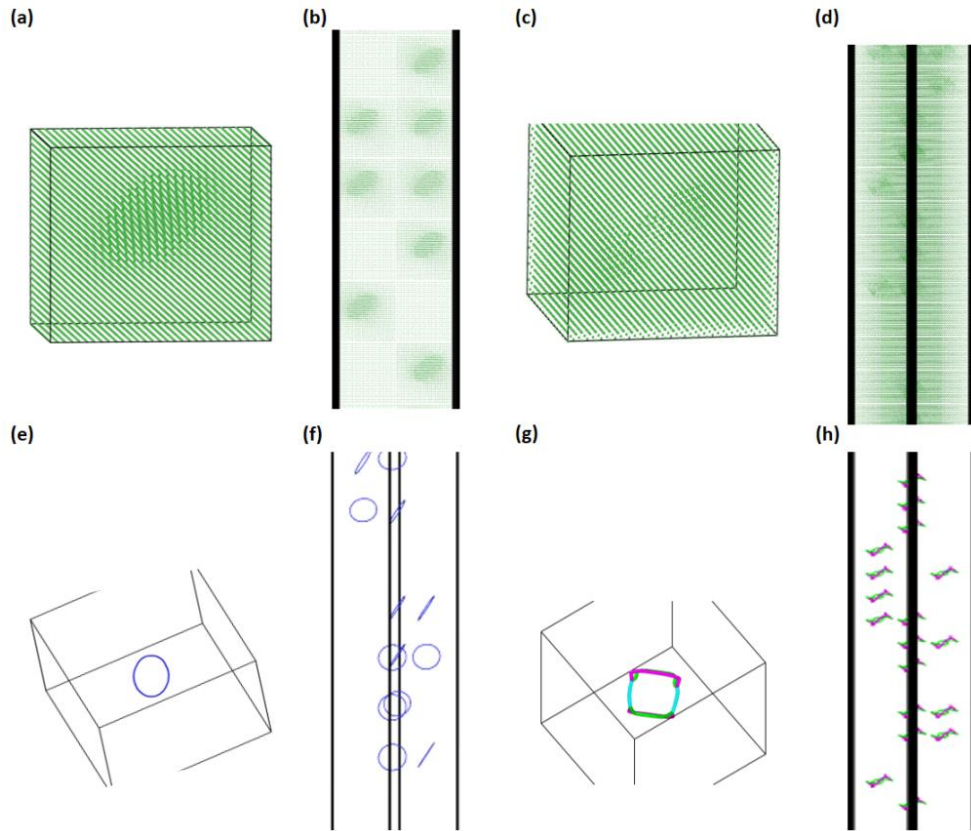


Figure 40. An example of how to develop an extended defect distribution along $\{111\}$ plane inside a large structure using ATOMSK code (a,b,e,f) and MD-relaxed structure (c,d,g,h). Dislocation loops of the 3 nm size are randomly distributed using merging procedures implemented in McChasy2 (b) and (d). Corresponding visualizations of pure defects after DXA analysis with atoms removed are shown in (e) to (h).

For this purpose, firstly we developed a single pristine MD cell and then removed two atomic planes of a diagonal of ~ 3 nm (a typical size of observed dislocation loops in the *fcc* metallic structures^{163,164}) in the middle of it. Ni possesses a cubic (*fcc*) structure, so the atoms are situated on two distinct, parallel planes (the cube base and the parallel plane crossing the center of the cube). Simply getting rid of only one of the planes to create the loop may not preserve the long-range crystal symmetry and could create unsymmetrical defects and clustering. After the defect was formed, the LAMMPS relaxation procedure was running for the next few ps to stabilize the system. Next, the cells were aligned to (001) direction and the created extended defect was cut and merged with bulk cells to create a large sample.

Another possibility to implement dislocations is to use the model of loops corresponding to the displacement field that comes from the elastic theory of dislocations^{154,165}. A similar methodology as for MD-created samples was applied for the loops created using the ATOMSK code, except for the relaxation procedure. Because of that, the dislocation loops are of perfect circular shape but the atomic positions are not optimized. For the presented study, the radius of

the developed loop is about 3 nm (using MD procedures) and exactly 3 nm using the ATOMSK code. Both defects are recognized by OVITO ⁸⁵ mode for dislocation analysis (DXA) as partial dislocation loops lying along {111} planes.

Figure 40(a) shows the atoms of a Ni cell with a dislocation loop implemented in the middle of it using the ATOMSK code. A corresponding large structure created by the McChasy's merging procedure with randomly distributed cells containing the developed defect mixed with cells of pristine structure is present in Figure 40(b). Figure 40(c) and (d) are created in the same manner as the two before but with the defect developed from the MD-relaxed structure. Figure 40(e - h) refer to the corresponding visualization after the DXA analysis (only recognized defects are shown).

D.4.2 Challenges – Atomic Positions from MD-Relaxed Structure

As it turned out, dealing with the atomic positions obtained from the LAMMPS code is extremely challenging. In the McChasy code, the interaction between a probing ion and an oriented/aligned monocrystalline structure is reproduced at every atomic layer orthogonal to the channeling direction by calculation of the probability of the projectile-atom collision with the impact parameter small enough that the projectile is backscattered ¹⁶⁶. Due to the atomic thermal vibrations, this probability has a Gaussian-like distribution around the atomic location ¹⁶⁷. Sampling plane by plane and tracking the changes that occurred due to the projectile-atoms interactions allows the reproduction of the depth-sensitive channeling spectra.

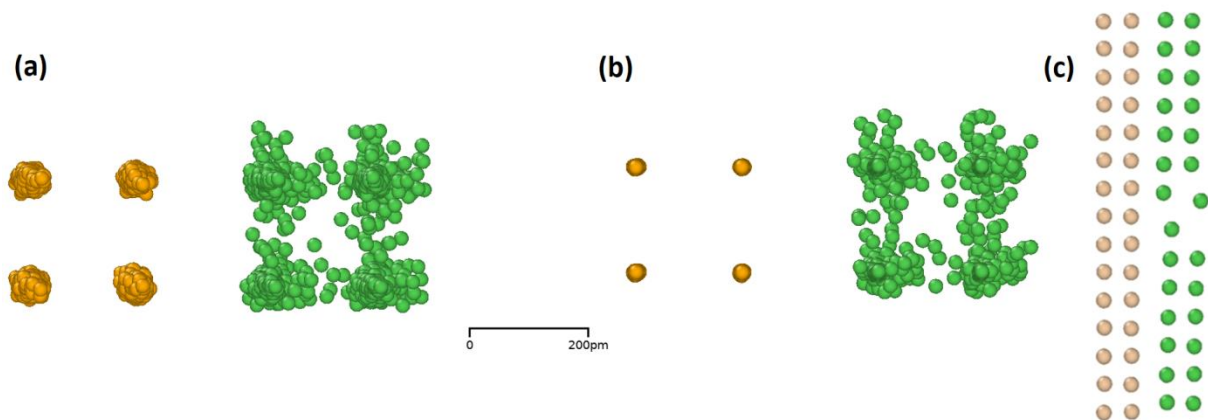


Figure 41. Comparison of row fluctuations in Ni obtained for (a) single MD frame and (b) averaged atomic positions after 250 frames for pristine (brown) and close-to-edge dislocation (green) structures. (a), and (b) show the projected view of atomic rows on an orthogonal plane while (c) is a view along the rows.

What was unexpected, for several reasons (boundary conditions, phonons, faultiness of used potential), single atomic row fluctuations (extracted from a particular point/frame in the MD simulation) can reach even half of the width between the atomic rows. This is demonstrated in Figure 41(a) and (b) which presents a comparison between the projections of four rows taken from the MD cells. Figure 41(c) shows two rows drawn from pristine material and also two rows close to a single edge dislocation that was incorporated inside the MD cell to observe changes that occurred to atomic rows in close surroundings of the defect.

The amplitude of thermal vibrations for a single Ni row is about 50 pm for undamaged, pristine material and even more for the structure with the defect incorporated inside (Figure 41(a)). The values are almost an order of magnitude larger than expected. Such fluctuations along atomic rows would dechannel an analyzing He⁴ beam resulting in a non-realistic level of backscattering yield of simulated spectra. Because of that, the final structure used for MC simulations was additionally analyzed by an internal code calculating the average/equilibrium atomic position. In the nearest future, another approach to test statistical sampling, in which deviations from equilibrium positions may be determined by molecular dynamics, will be tested. Unfortunately, most probably, it will require much longer simulations and another interference in the MC code that allows to turn off the Gaussian distribution of thermal vibrations.

D.4.3 Challenges – MERGING Procedure

Another issue related to the creation of a large sample out of smaller boxes must be considered in discussing the RBS/C spectra. One may pay attention to the possible interface contribution. To clarify the real contribution of interfaces between smaller components of a larger sample to an RBS/C spectrum, two samples having identical nickel structures were considered: one was made as a large, solid structure and another one was developed out of dozens of boxes (Figure 42). As shown there is no considerable difference between the two spectra obtained for solid and merged pristine structures.

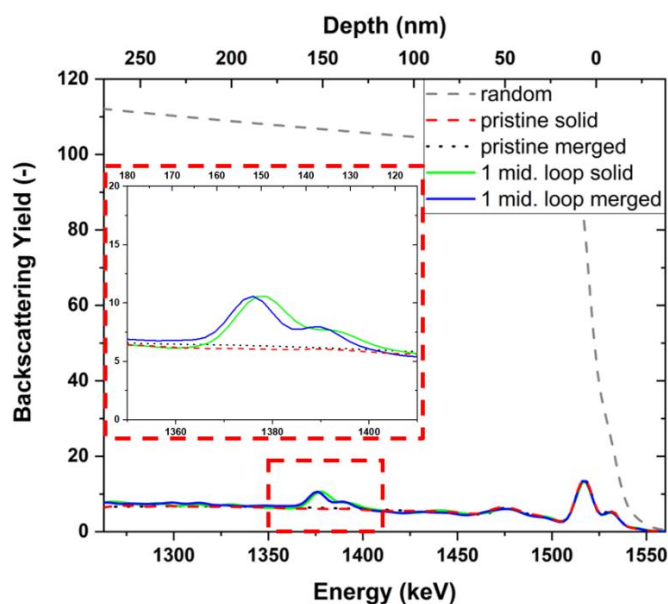


Figure 42. Axial RBS/C spectra simulated using two differently created structures. One with a single loop that was created in the middle of the solid (green) and merged sample (blue). For the comparison, the simulated spectra for pristine and randomly oriented structures are also presented. The enlarged peak occurring region is shown as an inset image.

To check the situation when we deal with additional distortion produced by extended defects and, hence, possible merged cells interface problem, a similar comparison of the defected structure was performed. Two structures were created in two different ways with a single dislocation loop located in the middle of the developed corridor (at 150 nm). The loops were exactly the same regarding their size and orientation. The resulting influence of constructed models on simulated channeling spectra is shown in Figure 42. As presented, no sufficient difference is observed. There is a small shift (less than 5 nm) between the maximal position of the dislocation contribution observed at the depth of 150 nm (around 1375 keV).

Most probably, it is due to the uncertainty of the merging procedure. It seems that the procedure should be improved regarding the possibility to control the gap between the merged boxes. The most important outcome is that the hypothetical interfaces that could cause supernumerary backscattering and dechanneling resulting in additional peaks visible in a channeling spectrum and an increased level of backscattering yield are not present.

D.4.4 Monte Carlo Simulations

The first attempts of MC simulations using the McChasy2 code concerning the possibility of specifying a defined defect distribution were performed for dislocation loops created in the ATOMSK program. To test whether different types of developed defects can be mixed in one virtual sample, we created two loops of the same size but lying on two perpendicular planes.

Due to their mutual relation, they should be well distinguished in a large structure after the MERGING procedure. An additional aspect that required testing was the accuracy of the defect density determination. Therefore, in the first step, we created a homogeneous distribution with a mixture of loops and then compared it with a more complicated distribution, whose average value of the dislocation density was in agreement with the homogeneous distribution. The red and blue lines presented as patterns for distributions in Figure 43(a) correspond to dislocation loops of different orientations.

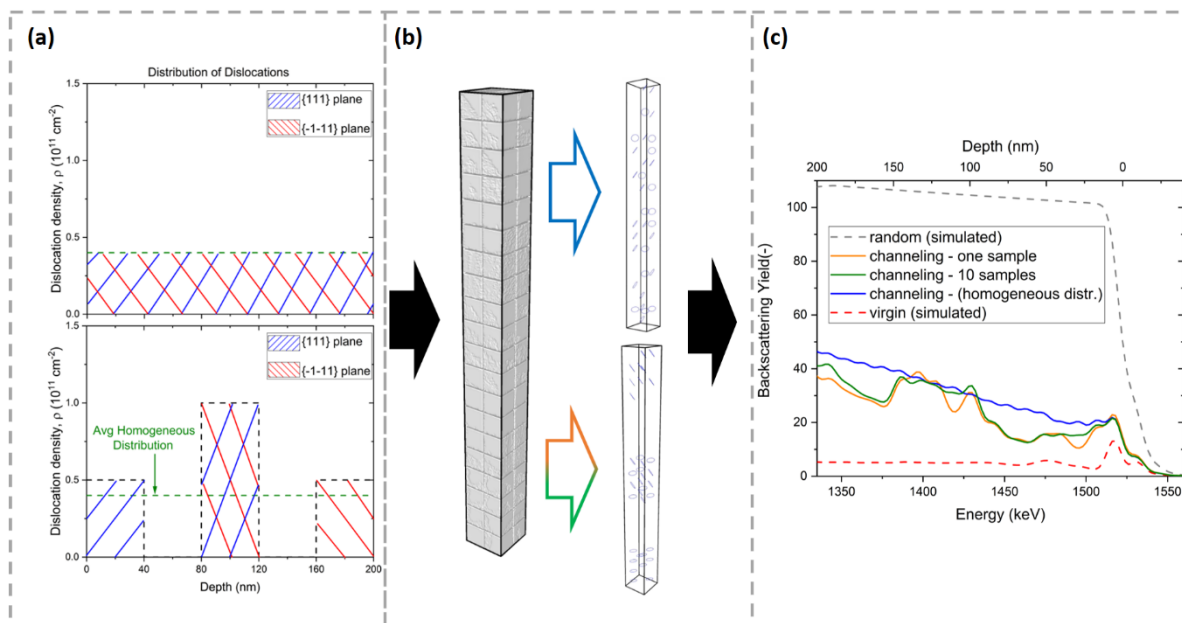


Figure 43. Dislocation loops of the 3 nm size (radius) are selected randomly from those lying on the {111} and {-1-11} planes (a). The loops are distributed homogenously and according to the given distribution by merging procedures (b). The average dislocation density of the presented complex distribution is the same as the value used for homogenous distribution (c).

The MC simulation procedures were tested for one and several structures created, covering a wide variety of defect distributions. A blue curve plotted for simulations of homogenous distribution was obtained after averaging outcoming spectra from calculations of 25 large structures. As presented, the statistic is good enough to see an almost smooth spectrum but it could be additionally improved by increasing the number of investigated structures to get rid of small fluctuations that are still visible. The same conclusion can be made regarding the tested complex distributions. We can see the improvement in the smoothness of the obtained spectrum by comparing simulations performed for 1 and 10 samples. The thing that should be pointed out is that the dechanneling levels for homogenous and complex distributions are similar.

The simulations performed for the homogenous distributions of the loops (blue line in Figure 43(c)) as well as for its complex distribution with an average density corresponding to the homogenous one (orange and green lines in Figure 43(c)) show that the McChasy2 code is

sensitive to the local loop concentration and can be used to determine the defect depth-distribution.

Having already tested the possibility of arranging the defects according to the given distribution, the final investigations were focused on the simulation procedures of the real experimental spectrum. For this purpose, the RBS/C spectra acquired for the implanted Ni single crystals were considered. The cross-sectional view of the MD-created loop and its distribution used for MC simulations are shown in Figure 44(a) and (b). The experimental spectra and the simulated fits made using the McChasy2 code are shown in Figure 44(c).

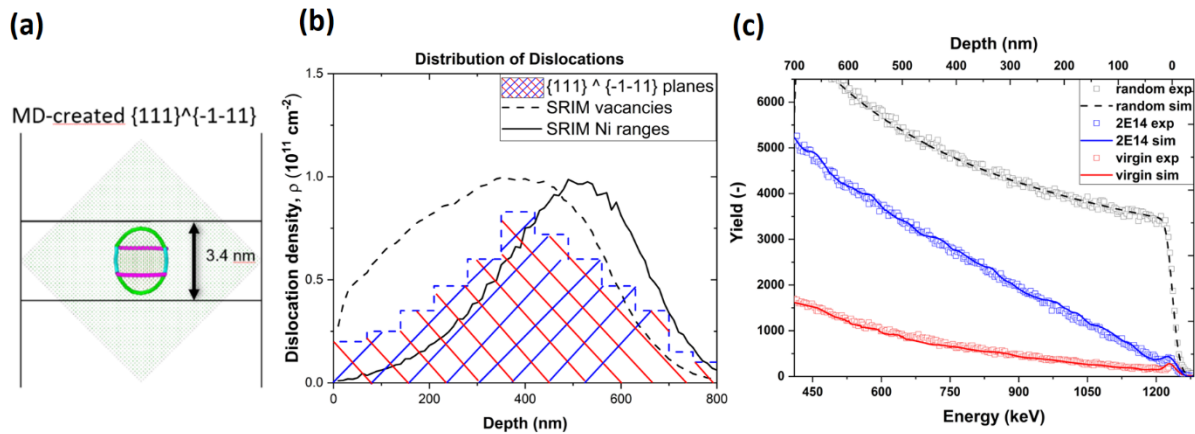


Figure 44. (a) MD-created dislocation loop, (b) depth distributions of dislocation loops used for the simulations performed for RBS/C experimental spectra shown in (c) together with the fits made by the McChasy2 code. Also shown in (b) is the range of 1.5 MeV Ni ions in Ni crystal as well as the vacancy profile, as predicted by the SRIM code, both normalized for easy comparison with the McChasy2 defect profile [26].

We came to the same observations and conclusion during MC simulations of real spectra as for the tested structures. The roughness of the simulated spectra is not related to the number of ions used in simulations but to the fixed positions of defects in a single atomic structure. To obtain a relatively smooth spectrum, the simulation was carried out for nearly one hundred samples with overall distributions presented in Figure 44(b). The created damage profiles are in good agreement with the distributions of displaced atoms obtained using the SRIM calculations.

D.5 Conclusions

The current state of the McChasy2 testing phase and the recent results regarding dislocation loops formed using the ATOMSK and the MD-LAMMPS procedures are presented and discussed. We demonstrate that the McChasy2 code already works and can be used for RBS/C simulations of large structures developed using external applications. The presented results were obtained using artificially produced $\langle 110 \rangle$ and $\langle 112 \rangle$ -oriented dislocation loops lying

along {111} and {-1-11} planes that in real *fcc* structures come from the splitting of the perfect dislocation. Worth mentioning is that for McChasy2, good statistics can only be built with a mixture of the number of both particles and virtual samples used in the simulation. The resulting distributions of the defects obtained for the real experimental spectrum are in good agreement with the SRIM code predictions. However, to receive more accurate results more complex defect structures with loops of different sizes and orientations should be used. Moreover, the merge of MD and MC simulations should also be performed for other models e.g. dumbbells formed inside Ni single crystals that were reported elsewhere^{42,68,108}. The next step would be to perform a similar analysis on more complex Ni-based alloys. Thus, our studies on the MD and MC simulations combined with experimental RBS/C results of radiation defects in Ni structures could be a useful tool for the analysis of dislocation loops created in irradiated materials.

Article E:
***Damage Kinetics in High-Temperature Irradiated Ni
Crystals***

C. Mieszczyński, **E. Wyszowska**, P. Jóźwik, K. Skrobas, K. Stefanska-Skrobas,
M. Barlak, R. Ratajczak, A. Kosińska, W. Chromiński, K. Lorenz

Journal of Applied Surface Science, 676 (2024) 160991,

<https://doi.org/10.1016/j.apsusc.2024.160991>

IF: 6.3, Ministry points: 140

This is an open access article distributed under the terms of the Creative Commons CC-BY license, which permits unrestricted use, distribution, and reproduction in any medium, provided the original work is properly cited.

Published by Elsevier B.V.

E.1 Abstract

High-temperature (~ 800 K) ion irradiation with 380 keV Ar ions was used to modify the surface of Ni single crystals in order to generate radiation defects and mimic the effect of neutrons avoiding sample activation. The modified 800 nm thick layer was analyzed regarding structural and mechanical properties utilizing a combination of experimental and simulation techniques. The ion implantation fluence ranged from $1 \times 10^{14} \text{ cm}^{-2}$ up to $1 \times 10^{16} \text{ cm}^{-2}$, which corresponds to values of displacements per atom from 0.25 to 25, respectively. The structural characterization was performed by Rutherford Spectroscopy in Channeling mode (RBS/C) associated with scanning (SEM) and transmission electron microscopy (TEM). The experimental results were supported by Monte Carlo (McChasy) and Molecular Dynamics (MD-LAMMPS) simulations. The simulations performed using the second generation of the McChasy code show that the influence of bubbles formed inside the material is not negligible and affects the quantitative analysis of defects in the simulated spectra. A second step in damage kinetics was revealed for the highest dose (i.e., 25 dpa) as a consequence of the entanglement of dislocations and agglomeration of noble gas bubbles, which was confirmed by TEM analysis. Moreover, nanomechanical results confirm that Ar bubbles deteriorate mechanical properties such as hardness.

Keywords: High-temperature Implantation, Ion channeling, Monte Carlo simulations, Molecular Dynamics simulations.

E.2 Introduction

One of the major challenges that have recently faced engineers and material scientists is studies of materials that can be used for high-temperature (HT) applications, e.g., in new generations of nuclear power plants. However, these materials must meet a number of essential criteria such as resistance to harsh environmental conditions, especially high temperatures, corrosive environments, and radiation. Therefore, in order to understand the influence of the above-mentioned factors, it is critical to examine the radiation effects, defect creation, and configuration and to understand the material's behavior at elevated temperatures.

Irradiation-induced degradation, e.g., swelling and hardening, is influenced by many factors related to material design and manufacturing processes, including major elements, solute additions, grain boundaries, or precipitates³¹. In addition, among the factors that influence the formation of radiation damage (e.g., particle energy, dose, and dose rate), irradiation

temperature can significantly influence the formation, migration, and evolution of defects¹²². Single crystals are good candidates to meet these requirements, due to the absence of grain boundaries, which gives a decrease in yield strength and the amount of creep, which is critical for high-temperature applications. Moreover, recent studies have shown, that this group of materials is characterized by high radiation tolerance and extraordinary mechanical properties^{11,31,78,79}. E. Levo *et al.*¹⁶⁸ investigated temperature effect by means of simulations of implanted Ni and Ni-based EAMC-alloys at temperatures varying from 138 to 800 K. They have demonstrated that, with an increased temperature, the saturation level of accumulated point defects is lowered. Pure Ni has about twice the difference between the highest and lowest saturation temperatures, while alloys have a difference of a factor three. They also reported that the amount of interstitial-type clusters smaller than 20 nm is reduced as a function of temperature, opposite to the larger clusters. In the case of vacancy type clusters, the sizes are increasing with the temperature. In turn, Z. Fan *et al.*¹²² made analysis of pure Ni and NiFe irradiated at temperatures varying from 150 to 500 K. They found that post-irradiation annealing at 500 K causes defect evolution and its effect is different compare to 150 K and 300 K. Annealing at 150 K causes defect migration to shallower depth. Moreover, the onset temperature for vacancy cluster dissociation has been found to be between 500 K and 700 K. Shi *et al.*¹⁶⁹ demonstrated that the size of the defects increase as a function of dose for in-situ ion irradiation using Kr ions that were implanted at 773 K in Ni and Ni-based alloys. In our previous work⁶⁸, we studied effects of 500 keV Ar and 550 keV Si in-situ irradiations with a fluences ranging from 2×10^{13} up to $1 \times 10^{16} \text{ cm}^{-2}$ on pure Ni crystal and two equiatomic NiFe and NiFeCoCr alloys. The samples were irradiated at 16 K and room temperature (RT, i.e., $\sim 300 \text{ K}$). We found that in the case of RT, the damage level measured for complex alloys at the highest irradiation fluence of $2 \times 10^{15} \text{ cm}^{-2}$ ($\sim 3 \text{ dpa}$) was higher than that obtained for pure nickel samples and suggesting two-step damage accumulation process with a defect transformation taking place at the fluence of about $1.5 \times 10^{15} \text{ cm}^{-2}$. Moreover, with increasing degree of chemical complexity and high solid-solution strengthening effects from Ni to NiFe and to NiFeCoCr, the enhanced lattice stiffness resists to randomization of atomic configurations and inhibits the growth of extended defects.

Despite such a wide characteristic, the structural and mechanical stability of these materials at elevated temperatures requires thorough understanding. Therefore, in this work, monocrystalline Ni structures implanted at 800 K with 380 keV Ar ions were used as the case study to analyze the formation of defects upon ion bombardment.

For the structural analysis of radiation-induced defects we utilized the Rutherford Backscattering Spectrometry in channeling mode (RBS/C) combined with transmission (TEM) and scanning electron microscopies (SEM). The experimental techniques are accompanied by Monte Carlo (MC) and Molecular Dynamics (MD) simulations. The MC simulations were performed using two generations of McChasy codes^{103,170} and Stopping and Range of Ions in Matter (SRIM)⁶⁵.

The studies of defect formation that pay attention to the evolution of dislocations and dislocation loops formed in Ni-based alloys seem to be very important¹⁴¹, mainly because of their potential applications for the power generation sector^{33,68,171}. In addition, the purpose of this study was to test the latest version of the McChasy-2 program, in which we added the ability to interpret gas bubbles in the material and examine their influence on the obtained RBS/C spectra.

E.3 Material and methods

E.3.1 Sample preparation

The Ni single crystal samples (1×1 cm²) were manufactured by MaTecK GmbH Company. However, low crystallinity of the samples was revealed by preliminary SEM and RBS/C measurements (cf. Figure 45(a) and (d)). An unexpectedly high channeling spectrum recorded for the pristine sample is the evidence of the presence of defects probably due to the method of sample manufacturing and the mechanical polishing (MP) used. For this reason, the samples were additionally pretreated in two ways before the originally planned modification by ion implantation. The reference sample was electro-polished (EP) using Struers LectroPol- with 60% Perchloric acid electrolyte to reduce stress generated by MP. The electro-polishing time was set to 40 s, the electric potential to 30 V, and the temperature to 5°C. The remaining samples were treated with a high-voltage electron beam gun (EG), which allows the generation of low-energy, high-current electron beams (LEHCEB) of a large diameter of ~10 cm. The major LEHCEB parameters are as follows: electron energy up to 30 keV, pulse duration of 2.5 μs, and energy density from 1 to 5 Jcm⁻². The parameters of the beam were chosen carefully to deposit enough energy per cm² (between 4 and 5 Jcm⁻²) to allow recrystallization of the surface of the investigated material. The details regarding the method can be found elsewhere^{172 173}.

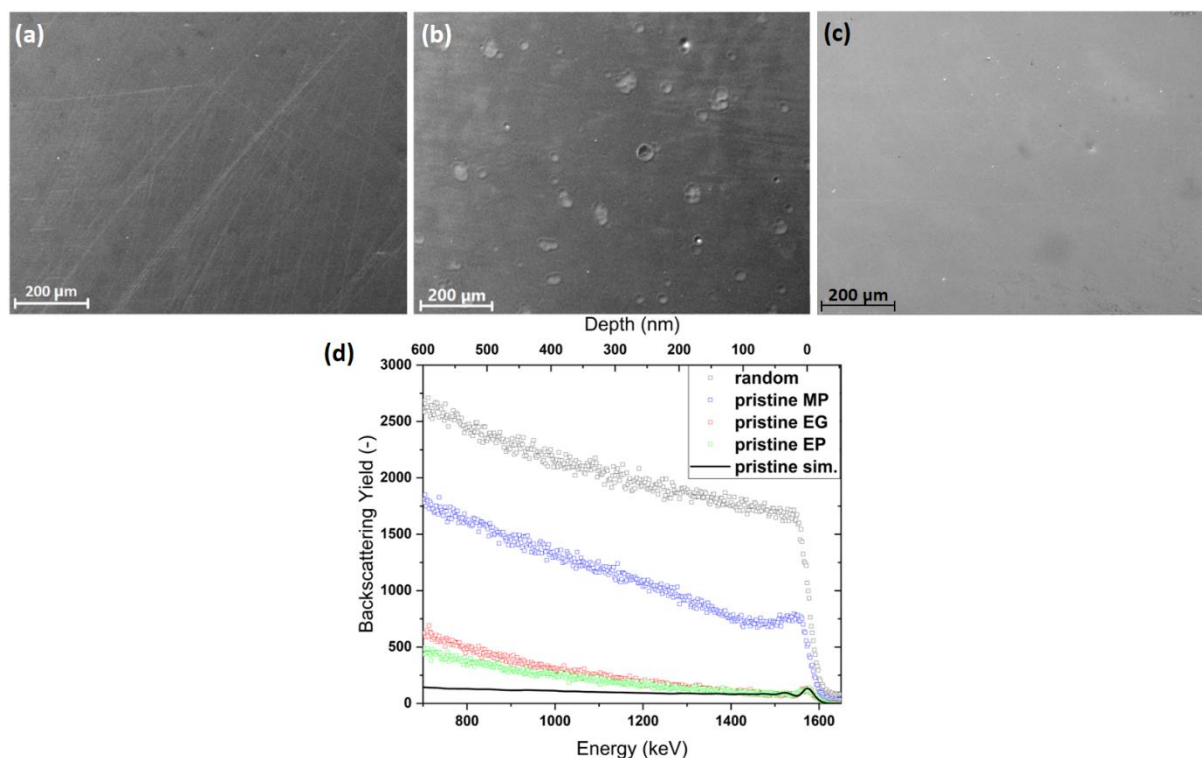


Figure 45. SEM images captured before (a) and after (b) EG and (c) EP treatment as well as (d) RBS/C results obtained for pristine material before and after sample preparation (MP – mechanical polishing, EG – electron gun, EP – electro-polishing). Also shown in (d) is the aligned, pristine spectrum (orange solid line) as predicted by MC simulations in McChasy code (pristine MC sim.). (For interpretation of the references to color in this figure legend, the reader is referred to the web version of this article.)

Figure 45(a), (b), and (c) show the comparison of SEM images collected before and after the EG and EP treatment. Figure 45(d) also shows RBS/C spectra of the pristine material prepared using both preparation techniques. From the comparison of the SEM pictures, one can see that all the visible scratches created by MP were removed. However, new structures, noticeable on the surface, appear after treating the sample with the electron gun. The observed craters are the natural elements of the surface microstructure of materials melted using electron¹⁷⁴, ion⁵⁹, plasma⁵⁸, or laser beams¹⁷⁵. The authors of Ref.¹⁷⁴ suggest that the most probable mechanisms of crater formation during electron annealing are selective melting and subsequent erosion of individual surface areas due to differences in the melting temperature of phase components. Although the electron annealed surface of the single crystal is not ideal do not affect the channeling spectra, as can be seen in Figure 45(d).

The minimum yield of the RBS/C spectra, i.e., (aligned yield)/(random yield) calculated for the energy at 1400 keV decreased after using EG or EP methodology of sample preparation from 44% (MP) to 5% (EG and EP). It means that the quality of the material was significantly improved. The resulting quality is close to the perfect, undamaged one. For comparison, the simulation of the pristine material using only Ni thermal vibrations with the amplitude of their

Gaussian distribution¹⁷⁶ and no structural defects was performed (orange solid line in Figure 45(d)). The higher dechanneling intensities visible in lower energy range for EG and EP compared to the perfect one suggest that even in the pristine materials some defects remain.

E.3.2 Experimental techniques

The surface microstructure of the samples before the ion implantation was examined with the use of a Zeiss EVO® (Oberkochen, Germany) MA10 scanning electron microscope. The measurements were performed using the secondary electron detector.

The samples were ion-bombarded at Laboratório de Aceleradores e Tecnologias da Radiação (LATR)¹⁷⁷ at HT (~800 K) with 380 keV Ar⁺ ions with a tilt of ~7° off the normal $\langle 100 \rangle$ direction to avoid channeled implantation. The implantation parameters were selected carefully to avoid interference between the surface and the conceivable damage peak (indicating point defects and small defect clusters) as well as to minimize ambiguities due to the straggling and dispersion of the probing ion beam that could arise if the damage peak was created in deeper region upon high energy implantation. Moreover, the chosen implantation temperature, 800 K, is assumed to be the main steam temperature obtained during High Temperature Gas Cooled Reactor (HTGR) operation^{178,179}. The ion fluence ranged from $1 \times 10^{14} \text{ cm}^{-2}$ to $1 \times 10^{16} \text{ cm}^{-2}$, which corresponds to values of displacements per atom (dpa) from 0.25 to 25, respectively. The dpa corresponds to low and moderate damage levels (1–50 dpa). These values are the displacement damage dose regimes for structural materials that are used in current Gen II fission reactors, Very High Temperature and High Temperature Gas Cooled Reactor (VHTR/HTGR), Super Critical Water Reactor (SCWR) and ITER fusion reactor^{14,57,180}. RBS/C random and aligned energy spectra were recorded using a 2.0 MeV He⁺ ion beam and a silicon pin-diode detector located at a 140 backscattering angle.

Suitable electron transparent lamellae were prepared from the area of interest of the samples via FIB/SEM for TEM microstructural studies. A lift-out procedure was utilized in FIB (Ga⁺) installed in Helios 5 UX (ThermoFisher Scientific) microscope at NCBJ. Final thinning of the lamellae was performed with 5 keV Ga⁺ ions followed by 2 keV Ga⁺ gentle polishing. TEM observations were performed with the JEOL F200 transmission electron microscope operated at 200 kV. Since ion irradiation is depth-dependent, evaluating the damage distribution below the sample surface induced by ion irradiation is crucial. All the lamellae were cut perpendicularly to the ion-irradiated surface to reveal the damage distribution into material up to the 2 μm depth. Afterward, images of the most degraded regions were taken to perform a

detailed analysis of the defect types, size and to calculate the defect densities. The two-beam convergent beam electron diffraction technique was used to determine lamellae thickness (for dislocation density statistics) ¹⁰⁴.

Nanoindentation was performed utilizing the Micro Materials Ltd. NanoTest Vantage system using a Synton-MDP diamond Berkovich-shaped indenter. Before starting the measurements, a Diamond Area Function (DAF) of the indenter tip was calculated using Fused Silica material in a wide load range to assess a reliable indenter shape for a given indentation depth. The hardness tests were conducted in multiple load cycles with increasing load from 0.1 mN up to 6 mN (in total 12 cycles) using load controlled method. These correspond to the depth from around 15 nm to 400 nm, depending on the irradiation fluence. Ten indentations were made at each load with 30 μ m spacing between the indents. The hardness value for each material was calculated as an average value obtained from multicycle indentation.

E.3.3 Simulation methods

The mean projected range of the implanted Ar ions and depth distributions of defects induced by the Ar ion bombardment were estimated using Stopping and Range of Ions in Matter (SRIM) calculation package ^{65,104}. The corresponding dpa were estimated using two produced files, VACANCY.txt and NOVAC.txt under an assumed displacement energy threshold of 40 eV using the full cascade mode. The maximum damage profile estimated by SRIM is located at the depth of about 120 nm for the Ar beam energy of 380 keV.

The virtual Ni structures were created using ATOMSK software ¹⁵⁴ and then they were transferred to MD-based LAMMPS code for further processing. Interactions between atoms were approximated by the Embedded Atom Model (EAM) potential with parameters given by Foiles ¹⁵⁸. To avoid surface effects, simulations were performed under periodic boundary conditions. Temperature and pressure were controlled by Nosé–Hoover algorithm ¹⁸¹. The step interval was set to 1 fs. The positions of atoms were obtained after 20,000 steps, which correspond to 20 ps. The fluctuation of total energy lower than 1% was used as the indicator of the final thermalization. To obtain a structure close to the case of no thermal motion, the atomic positions over the final 250 steps of the simulation were averaged.

MC simulations were performed using the most recent versions of two simultaneously developed versions of the McChasy software, namely McChasy-1 v.65 and McChasy-2 v.2.2. In McChasy-1 ^{73,102,148} the structures are created by internal software based on crystallographic

data. Thermal vibrations and desired defects are applied from built-in procedures during ongoing simulations. In McChasy-2, the structures are generated using an open-source Large-scale Atomic/Molecular Massively Parallel Simulator Molecular Dynamic code (LAMMPS)¹⁵². The potential of early versions of the code has already been presented elsewhere^{92,138,153}.

The model of edge dislocations and dislocation loops developed for McChasy-1 is based on the Peierls-Nabarro approach^{159–161} and requires geometrical parameters of the defect to be determined for every structure independently^{73,103,182}. To have a possibility to compare the results with part of the results previously obtained for single-phase concentrated solid-solution alloys (SP-CSAs), in this study we used the mixture of $\langle 1\ 0\ 0 \rangle$ and $\langle 0\ 1\ 0 \rangle$ -oriented edge dislocations (same as in Ref.⁶⁸).

In the McChasy-2, the $\langle 1\ 1\ 0 \rangle$ and $\langle 1\ 1\ 2 \rangle$ -oriented dislocation loops were developed along $\{1\ 1\ 1\}$ and planes. In reality, the developed defects originate as Shockley partials coming from the splitting of the $a/2\ \langle 1\ 1\ 0 \rangle\ \{1\ 1\ 1\}$ edge dislocations^{81,162}. The more detailed description of the channeling simulation procedures in both McChasy codes (1 and 2) can be found elsewhere^{68,102,103,138}. The custom software combined with Gnuplot and Open Visualization Tool (OVITO) code⁸⁵, as well as the Origin application, were used for graphical visualization.

To reveal the damage kinetics for the investigated structure, the Multi-Step Damage Accumulation (MSDA) analysis was performed^{90,92}. This model is based on the equation assuming that the damage accumulation occurs through a series of structural transformations caused by the destabilization of the present crystal structure:

$$f_d = \sum_{i=1}^n (f_{d,i}^{sat} - f_{d,i-1}^{sat}) G [1 - \exp(\sigma_i (\Phi - \Phi_{i-1}))] \quad (1)$$

where: σ_i is the cross-section for the formation of a given kind of defect, $f_{d,i}^{sat}$ is the level of damage at saturation for i-th kind of defects, and Φ_i is the fluence threshold for triggering the formation of i-th kind of defects.

E.4 Results and Discussion

E.4.1 TEM results

TEM analysis was performed to recognize defect types and distribution at different damage levels in investigated ion-bombarded samples. Figure 46(a) shows cross-sectional TEM images of the samples bombarded with Ar ions to fluences of 7×10^{14} , 7×10^{15} , and $1 \times 10^{16} \text{ cm}^{-2}$. The images clearly show that in pure Ni at the lowest fluence of Ar ions, defects are evenly distributed over the depth from the surface up to deeper regions in the material, which is in line with SRIM simulations. With increasing ion fluence, defects tend to accumulate between 100 and 160 nm, and what is interesting, we do see some bubbles in contrast to the low fluences. At the highest fluence of $1 \times 10^{16} \text{ cm}^{-2}$, defects migrate towards the surface and locate at a depth of 30 to 60 nm. Moreover, much bigger bubbles are formed.

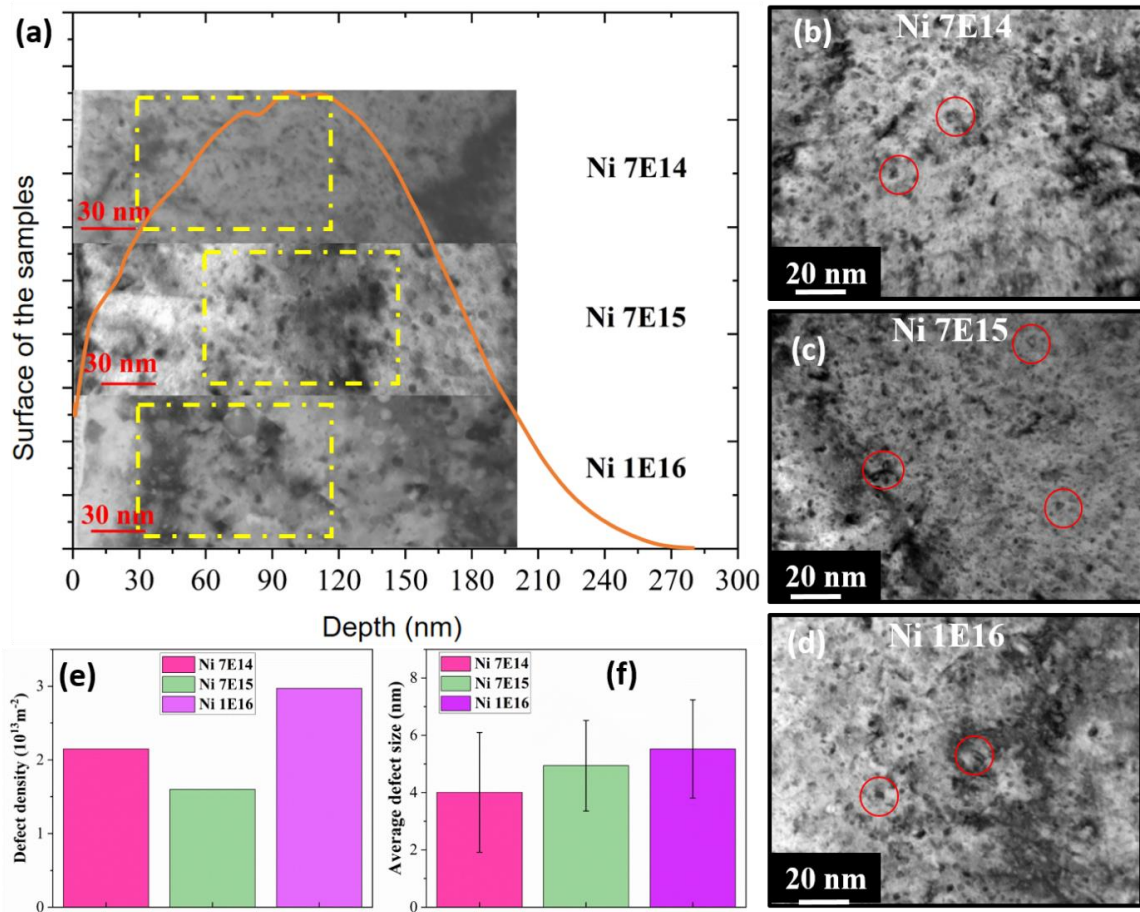


Figure 46. TEM images of the Ni crystals bombarded with Ar ions to fluences of 7×10^{14} , 7×10^{15} , and $1 \times 10^{16} \text{ cm}^{-2}$, denoted by Ni 7E14, Ni 7E15, and Ni 1E16, respectively: (a) cross-sectional images (orange curve represents the damage distribution profile obtained using SRIM), (b-d) bright-field images (red circles indicate dislocation loops), corresponding defect densities (e) and defect sizes (f), calculated based on the TEM images taken at the damage peak region.

In Figure 46(b), (c), and (d), one can see that the defect size increases with the fluence, which is confirmed by performing calculations of the defect size (Figure 46(f)) and density (Figure 46(e)), based on the TEM images. Defect densities were calculated based on the TEM images taken at the peak damage region. For this measurement, lamellae thickness was measured at the peak damage region only. The surface area for all the materials was calculated as $1.08 \times 10^{-13} \text{ m}^2$. The densities were calculated by counting the number of defects in a unit volume of the crystalline material (volume = surface area / lamella thickness). The lamella thicknesses were as follows: 60, 108, and 65 nm, which corresponds to the fluence of 7×10^{14} , 7×10^{15} , and $1 \times 10^{16} \text{ cm}^{-2}$, respectively.

One may note a slight decrease in defect density for the fluence equal to $7 \times 10^{15} \text{ cm}^{-2}$. This result may be directly related to the noble gas bubbles reported by TEM measurements for the mentioned fluence. The bubbles formed at the fluence of $7 \times 10^{15} \text{ cm}^{-2}$ and $1 \times 10^{16} \text{ cm}^{-2}$ are shown in Figure 47(a) and (b), respectively. The reduction of defect density can be due to interactions between loops and noble gas cavities that may lead to loop punching¹⁸³, pinning, or annihilation^{184,185} during the bubble growth process as a result of kinetic competition between inert gas, vacancy, and the self-interstitial atoms, especially at elevated temperatures¹⁸⁶. For the higher fluence, i.e., $1 \times 10^{16} \text{ cm}^{-2}$, the amount and size of Ar bubbles increases and argon-vacancy complexes may act as nucleation sites for the loops, and therefore the defect density increases (Figure 46(e)). In order to quantitatively assess the number of bubbles in the structure, we calculated bubble density and their size (Figure 47(c) and (d)). What is interesting, in the lowest fluence we observed mainly an interstitial loops and small 2–5 nm size Stacking Fault Tetrahedrons (SFT). For the intermediate ion fluence ($7 \times 10^{15} \text{ cm}^{-2}$), we additionally observe bubbles and an increase of the size of the SFTs. For the highest dose, we observe an increase in both the size of the bubbles (up to 5–10 nm) and the number of SFTs that are oriented along different crystallographic directions. It is worth noting that when a material is irradiated with gas ions, e.g., Ar^+ or He^+ , at elevated temperatures, one can expect bubbles to be visible in the structure, which may affect the mechanical properties of the material¹⁸⁷. On the other hand, if it is implanted with metal ions at high temperatures, one can expect visible voids that increase with the ion fluence. Such studies are presented and described in Refs.^{28,31}. For example, Lu *et al.*²⁸ explained that voids are the result of the three-dimensional agglomeration of vacancies, while dislocation loops and network dislocations are formed due to the agglomeration of interstitials. In this work, we postulate that the temperature-dependent

increase in bubble size is due to the mobility of vacancies, Ar atoms, and clusters, which facilitate the growth of bubbles ¹⁸⁸.

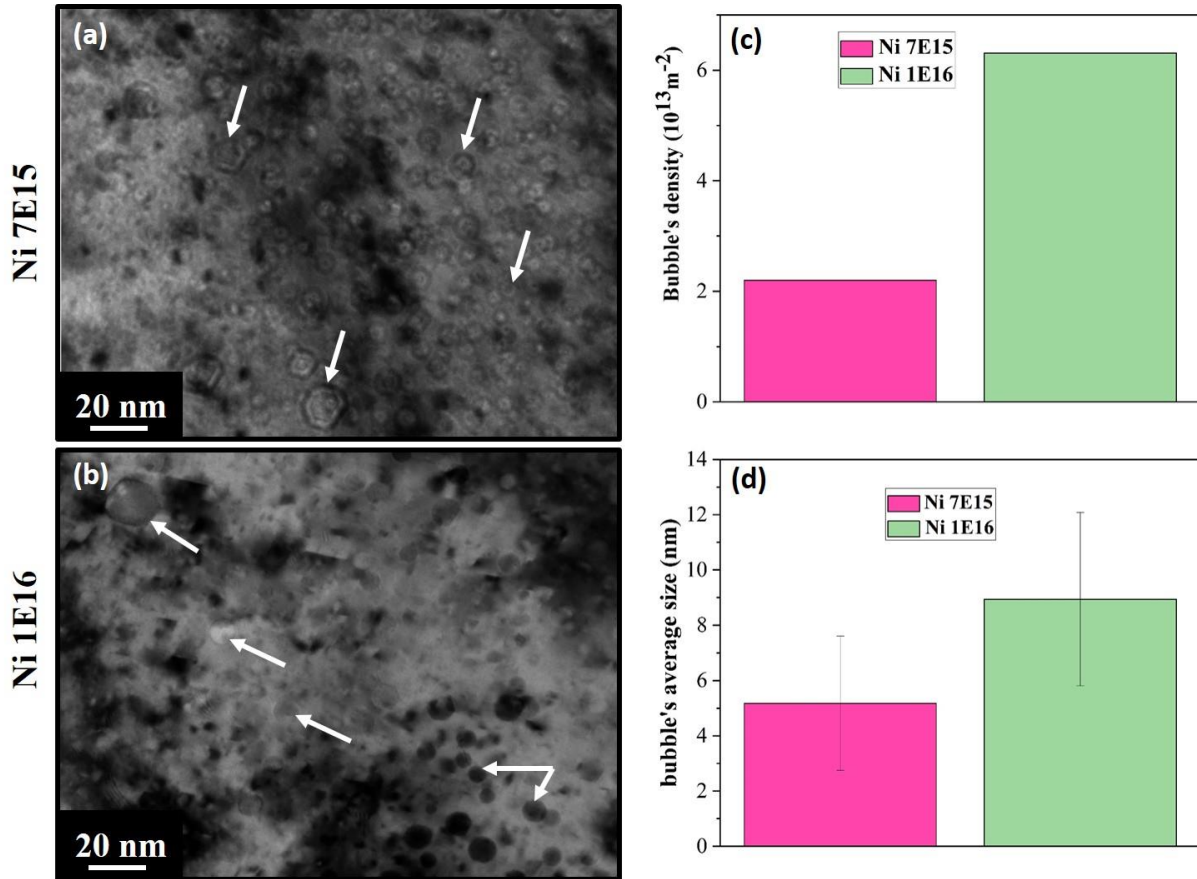


Figure 47. (a-b) Bright-field images of bubbles in Ni bombarded samples with the fluences of $7 \times 10^{15} \text{ cm}^{-2}$ and $1 \times 10^{16} \text{ cm}^{-2}$, denoted by Ni 7E15 and Ni 1E16 respectively, (c) Ar bubble density, and (d) average bubble size.

E.4.2 Nanomechanical results

It is well known, that in both fission and fusion materials, where the inert gas such as He or Ar is used, a high density of nanoscale bubbles is formed ¹⁸⁸. These bubbles have a serious impact on the mechanical and physical properties of the material. In this work, we aim to understand the combined impact of defects formed and Ar noble gas accumulation on the hardness behavior in Ni. As shown in Figure 48, we see that the greatest hardening for all doses occurs at a depth of 50 nm, which is consistent with the SRIM calculations, where the damage peak is located at a depth of 90–150 nm. It should be emphasize, that the plastic zone developed below the indenter tip during indentation is around five times bigger, than the given indentation depth, therefore, in order to read an appropriate hardness value, the indentation depth should be

carefully chosen. It is worth mentioning, that we were unable to measure hardness at shallower depths (up to 20 nm) because surface effects interfered with correct hardness readings.

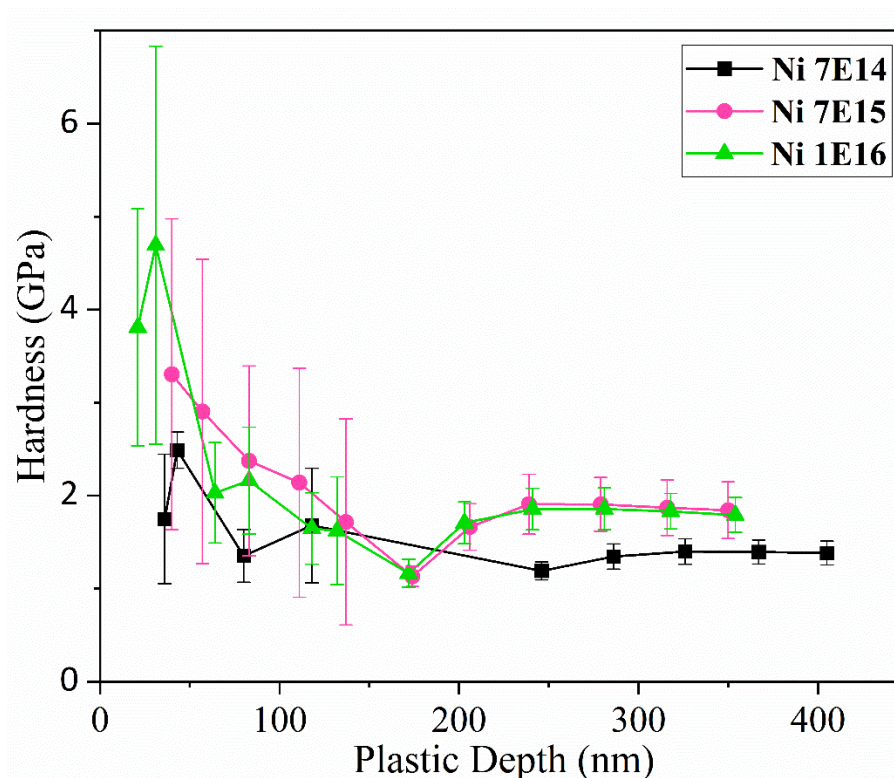


Figure 48. Nanoindentation hardness of Ni samples irradiated up to the fluence of $1 \times 10^{16} \text{ cm}^{-2}$.

The most pronounced hardening was observed for the highest ion fluence. Interestingly, according to the TEM analysis, for the fluence $1 \times 10^{16} \text{ cm}^{-2}$, defects are shifted to the surface of the sample, at a depth between 30 nm and 100 nm, which could also affect the highest hardness reading in this range. For example, for NiFe irradiated with 1.5 MeV Ni⁺ to fluences ranging from 4×10^{13} to $3 \times 10^{16} \text{ cm}^{-2}$ (~ 0.08 – 63.5 dpa) at 150 K, coalescence and growth of small defects can substantially reduce the irradiation-induced lattice strain and mechanical stress, which can cause the retraction of defects to a shallower depth¹²². Moreover, one can see that in the most damaged structures, in which argon bubbles were formed, i.e., for the doses $7 \times 10^{15} \text{ cm}^{-2}$ and $1 \times 10^{16} \text{ cm}^{-2}$, the hardness locally decreases successively at a depth of approximately 100–200 nm, where the highest concentration of the bubbles is present, and then increases and remains at a similar level.

Above 200 nm, the bubble concentration decreases, and the hardening rises, ultimately reaching a higher hardening level than the lowest dose of $7 \times 10^{14} \text{ cm}^{-2}$, where the number and size of defects are smaller.

E.4.3 RBS/c simulations and MSDA using McChasy-1

The main idea behind the chosen implantation parameters was to observe how radiation defects behave under conditions comparable to those in the HT reactor. It seems logical that due to the different mobility of defects, one should observe different defect kinetics for similar fluences implanted at low temperature (LT), RT, and HT. The results obtained in this research are compared with the LT and RT investigations with relatively similar (except for the temperature) irradiation conditions (Ni:Ar 500 keV at 16 K and Ni:Si 550 keV at 300 K) published elsewhere⁶⁸.

RBS/C spectra collected for the Ni single crystals with different fluences of Ar ions implanted at ~ 800 K and corresponding MC simulations are shown in Figure 49(a). As expected for materials that mainly form dislocations upon ion irradiation, no apparent damage peak (centered at about the maximum ion range) was formed. However, the dechanneling level of aligned spectra increases as a function of Ar fluence, following the damage induced inside the investigated material.

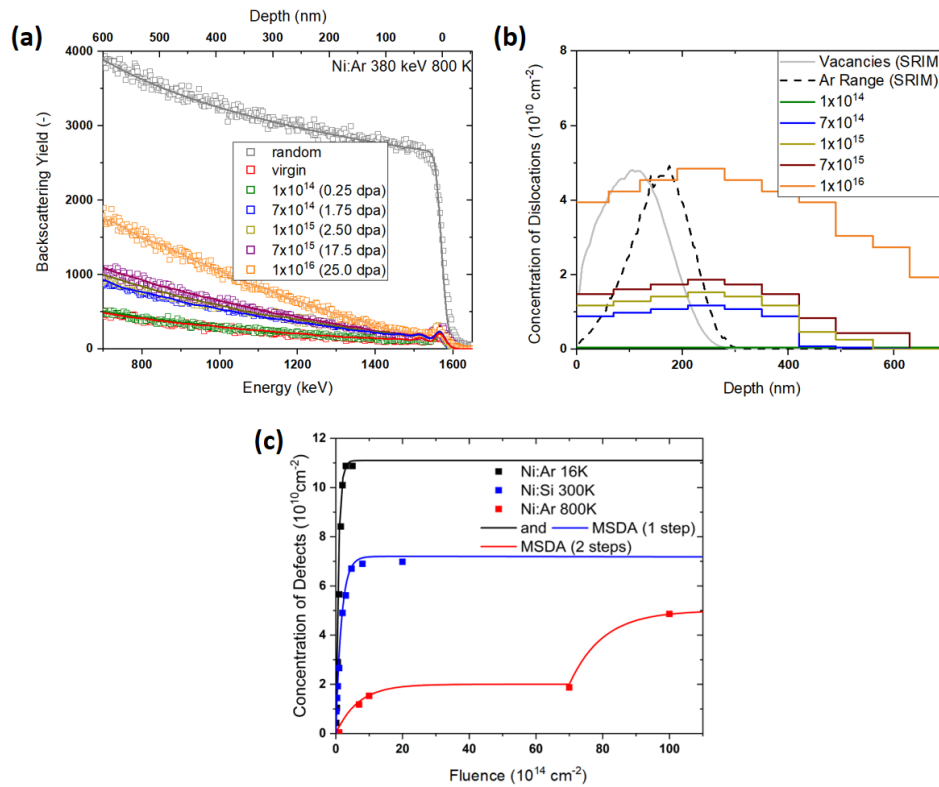


Figure 49. (a) Ni RBS/C spectra recorded along $\langle 001 \rangle$ direction (squares) with fits obtained using McChasy-1 simulations (solid lines of corresponding colors). Pristine and random spectra are included as references. (b) Damage distribution profiles and Ni ion range obtained from McChasy-1 simulations and SRIM calculations. (c) Damage kinetics for different bombardment conditions of Ni single crystals: full squares represent the maximal values of extended defect distributions extracted from the McChasy simulations while solid lines are the fits to the experimental data using the MSDA model; red color corresponds to the HT results described in this research while black corresponds to LT and blue to RT studies described in Ref.⁶⁸.

The obtained damage profiles confirm that the concentration of point defects or amorphous-like damage domains inside HT-implanted samples is low. Defect profiles are shifted into the

depth of the samples (at around 200 nm), compared to the results obtained from SRIM simulations, where the damage peak is located at around 100 nm (see Figure 49(b)). This so-called ‘long-range’ effect was already studied in several monocrystalline materials and it was shown that it is more pronounced in *fcc* than in *hcp/bcc* structures, as the stress for dislocation propagation is generally smaller in *fcc* metals^{107,122}. This effect is also visible in the TEM cross-sectional images and the nanoindentation results. However, as already mentioned, also the shift toward the surface of the sample for the highest dose was observed. This is not the case for RBS/C analysis. Here, starting from the lower dose, the shape of the damage profiles is relatively similar.

Points in the MSDA graph (Figure 49(c)) correspond to the maximal values of the extended defects profiles formed in the irradiated materials. Solid lines are the fits made using the MSDA equation. The first clear outcome of the analysis is a significantly lower level of saturation curves in samples irradiated at high temperatures when compared to RT and LT experiments. The cross-sections for the damage formation (Table 7) in the case of HT implantation are also lower compared to the RT and LT ones.

Table 7. Cross-sections for defect formation extracted from the MSDA model.

	$\sigma_1(10^{-14}\text{cm}^2)$	$fd_1(10^{10}\text{cm}^{-2})$	$\sigma_2(10^{-14}\text{cm}^2)$	$fd_2(10^{10}\text{cm}^{-2})$	$\Phi_2(10^{14}\text{cm}^{-2})$
Ni:Ar LT	1.3	11.1	-	-	-
Ni:Si RT	0.6	7.2	-	-	-
Ni:Ar HT	0.2	2.0	0.1	5.0	70.0

It seems that the irradiation temperature plays a significant role in the defect accumulation. This is likely an effect of the increased mobility of defects at HT that leads to more efficient annihilation. The irradiation temperature is already in the peak swelling regime¹⁸⁹, hence the void swelling and cluster-dislocation interactions that are observed for the higher fluence in the 5th recovery stage ($\sim 0.3 T_m$)¹⁹⁰ should take place. It may suggest also that most of the point defects and/or clusters formed during the implantations are annealed due to the temperature of the process. What is interesting, in the case of HT irradiation another step for the higher fluence is visible, which was observed also for SP-CSA alloys⁶⁸. It is worthwhile to note that this step is created for the high dose (~ 25 dpa). The height of the spectrum and the additional level in The MSDA are most likely a combination of two effects. Firstly, in this regime, the growth and collapse of dislocation loops to dislocation tangles for pure metallic structures were reported¹⁹¹ and secondly, this is an effect related to the agglomeration of implanted Ar in the form of bubbles visible in TEM pictures (Figure 47).

E.4.4 RBS/C simulations using McChasy-2

To test how the results for more realistic finite dislocation loop models look like the experimental spectra were simulated using the McChasy-2 code. The tests were performed for pristine, random, and the most damaged (i.e. $1 \times 10^{16} \text{ cm}^{-2}$) experimental RBS/C spectra. Usually, a distribution of the loop sizes is observed in Ni-like fcc metallic structures. It seems that the general agreement is that during RT implantation, the size of the formed loops varies between 1 to 10 nm¹⁸⁶. Many authors have commonly claimed that the size of the loops formed in fcc metals is around 3–6 nm^{163,192}. This statement is somehow proved by our TEM measurements ((Figure 46(f). For the current MD investigations, the loops were developed by removing two circle-shaped layers of atoms of a diagonal of 3, 4, and 5 nm in the middle of the pristine cell along the {111} plane. After cutting out, the LAMMPS relaxation procedure was run for the next few ps to stabilize the system and create the targeted defects. The outcoming cells with the defects formed are shown in Figure 50. One can observe that during the relaxation procedures, the resulting sizes of the defects (recognized as partial dislocation loops using dislocation analysis (DXA) by OVITO software) are broader than the given ones.

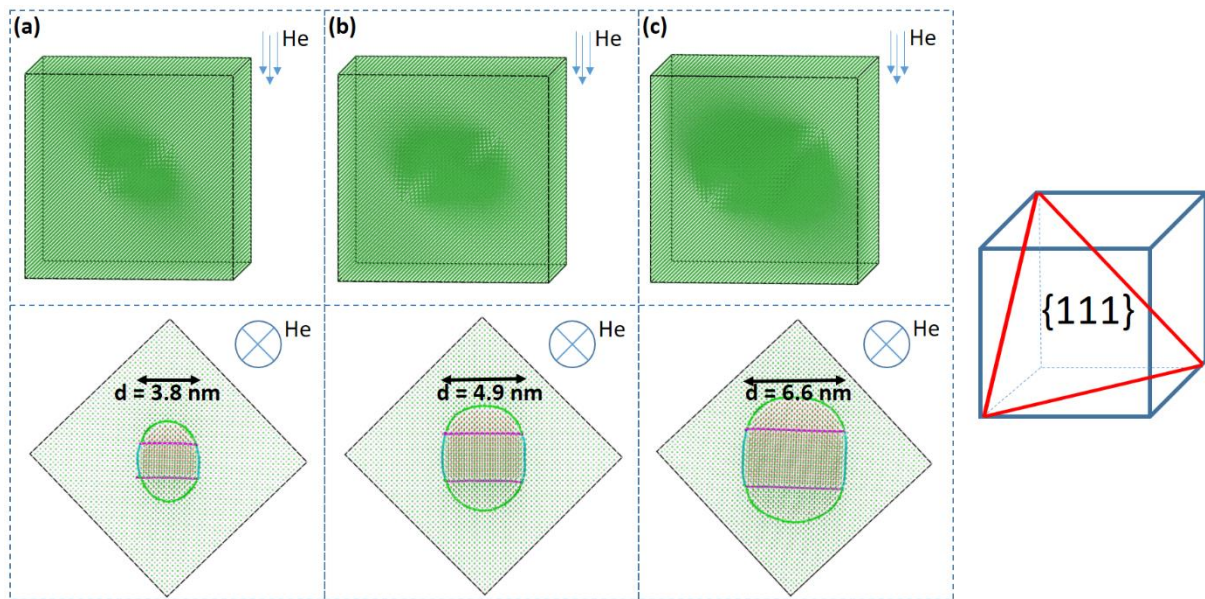


Figure 50. Dislocation loops along {111} plane developed using MD-LAMMPS after relaxation. Obtained cells with loops of different sizes and corresponding top views (bottom row) of cells with defect visualizations after DXA analysis (colors corresponding to the differently oriented parts of the loops) are shown.

Next, the developed defects are cut off, multiplied, and merged for the use in the McChasy-2 code, as shown in Figure 51(a). The code randomizes the arrangement of cubes taking into account the introduced distribution. In order to create more realistic defects (different orientations), a similar set of loops was created along the plane in the virtual sample. The distributions of the created loops

used for the MC simulations combined with the results of the SRIM calculations are shown in Figure 51(d). The experimental spectra and the simulated fits made using the second generation of the McChasy are shown in Figure 51(c). Due to the observation of a high concentration of Ar bubbles in the implanted material, in the new version of the code we tried to investigate their impact on the RBS/C spectra. For this purpose, we developed a model of such bubbles in the investigated structure Figure 51(b). In a sphere of approximately 5 nm in size, we replaced 90 % of the Ni atoms with Ar atoms and distributed them randomly inside the sphere. Since the density of bubbles in the modified layer is comparable (or higher) to the density of defects (Figure 46(e) and (c)), we distributed them homogeneously so that their density was at the level of the maximum density of defects (without taking into account the bubbles themselves – Figure 51(d). To obtain a relatively smooth spectrum, the simulations were carried out for 20 samples with overall distributions presented in Figure 51(d).

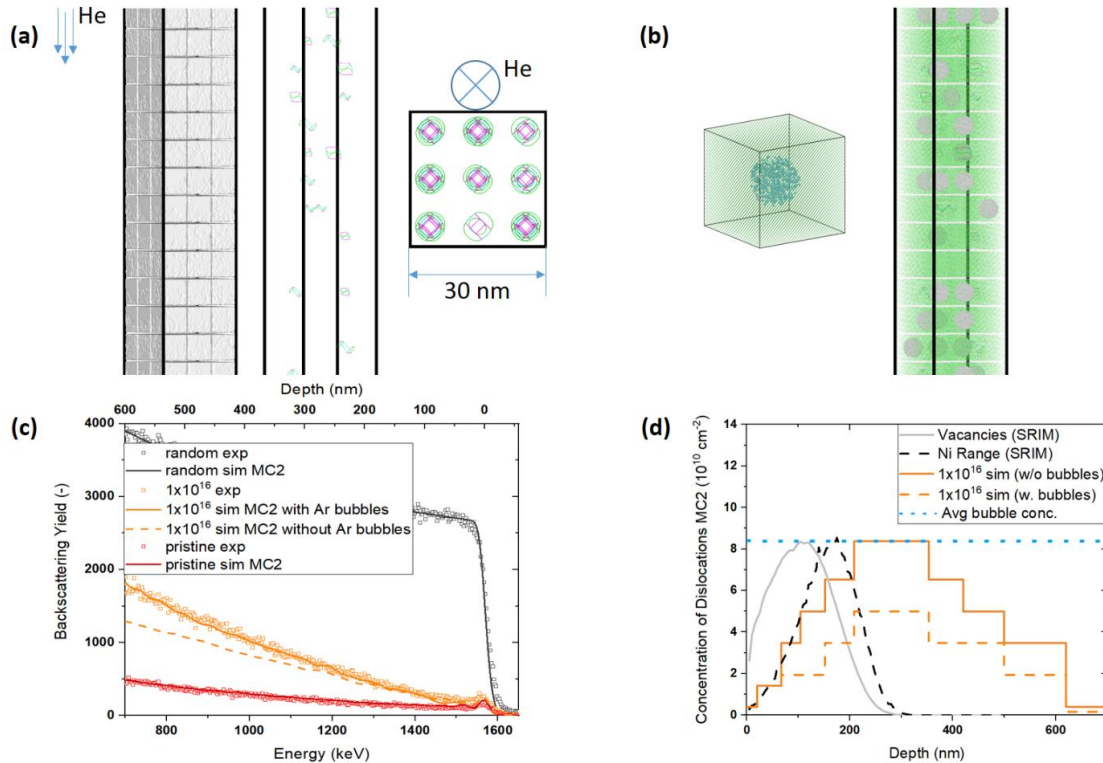


Figure 51. (a) Example of an MD/McChasy-created large structure. Surrounding atoms were removed from the structure to highlight defects inside the virtual sample. The resulting dislocation loops, marked by DXA analysis, were left (inset–top view along $\langle 100 \rangle$ direction). (b) Same structure with homogeneously distributed Ar bubbles. (c) Experimental and simulated RBS/C spectra obtained using depth distributions of defects shown in (d).

The average loop density received from the second generation of the code was estimated from equation, where V is the volume of the virtual sample and D is the average diameter of all dislocation-like defects and bubbles (same as for TEM investigations). The average loop density calculated in this way is equal to $4.86 \times 10^{10} \text{ cm}^{-2}$ and $2.91 \times 10^{10} \text{ cm}^{-2}$ for 25 dpa without

and with the bubbles considered, respectively. The value is in the range of reported experimental values^{141,193}. The negligible difference regarding the absolute value of the dislocation densities, which can be observed by comparing the results obtained from the different generations of the code, is due to the different models of extended defects used for the simulations. In McChasy-2, the finite loops are placed along *diagonal* planes, which affects fewer trajectories of channeling ions compared to perpendicular, infinite edges used in McChasy-1. What should be highlighted is that the relative disorder difference between different values of dpa or fluences obtained using both generations of the code remains the same. However, the influence of the bubbles in the simulations is clearly visible. By not having the ability to simulate them in Ni in the first generation of the code, we may unjustifiably exaggerate the number of defects in the simulated distributions.

E.5 Conclusions

In the article, we present and discuss the recent results of the combination of several experimental and simulation techniques performed to investigate defects formed inside Ni single crystals implanted at HT with 380 keV Ar ions. The newest versions of the McChasy-1 and McChasy-2 codes were successfully implemented to quantify the number of defects and determine the depth profiles. LAMMPS combined with the McChasy-2 code was utilized to model the shape of dislocation loops (and for the latter, argon bubbles) formed inside the irradiated material.

The first outcome of the analysis performed using McChasy-1 is a low level of saturation curves due to much higher mobility of defects at HT and hence, the efficient dynamic annealing that occurs already during the implantation. The resulting distributions of the defects obtained for the real experimental spectrum are in good agreement with the SRIM code predictions. A second step in damage kinetics is visible for the highest dose (i.e., 25 dpa) as a consequence of the entanglement of dislocations and agglomeration of noble gas bubbles. The simulations performed using the second generation of the McChasy code proved that the impact of the bubbles formed inside the material is not negligible and disregarding them may exaggerate the quantitative analysis of defects in the simulated spectra. A comparison of the simulations performed using two generations of the McChasy code leads to the conclusion that the obtained shapes of the distributions are very similar. A small difference was observed regarding the absolute values of dislocation densities due to the different models of dislocations used in both

codes (infinite edge dislocations for McChasy-1 oriented along channeling axis and finite loops for McChasy-2).

Nanomechanical tests revealed that in the most damaged structures, i.e., in those where the Ar bubbles were formed, the measured hardness decreases locally and successively at the depth of approximately 100–200 nm, where the highest concentration of the bubbles is present, and then increases and remains at a similar level. TEM images disclosed that, in the lowest fluence regime, mainly interstitial loops and small 2–5 nm size SFTs are present. For the intermediate ion fluence ($7 \times 10^{15} \text{ cm}^{-2}$), we additionally observe bubbles and an increase of the size of the SFTs. For the highest dose, we observe an increase in both the size of the bubbles (up to 5–10 nm) and the number of SFTs that are oriented along different crystallographic directions.

Chapter 6

Conclusions

This chapter concludes the thesis by summarizing the obtained results, verifying the hypotheses and identifying directions for further work.

6.1 Summary of obtained results

Ion irradiation is a powerful technique that can be successfully used, in particular, at the stage of designing new materials and testing their potential for nuclear applications. Unlike highly costly, lengthy, and complicated neutron irradiation, ion irradiation has been widely adopted due to its low costs, short irradiation times, and controllable irradiation conditions. However, ion irradiation has some drawbacks, such as a limited penetration depth (several micrometers), which makes it quite challenging to characterize, for example, the mechanical properties of ion-irradiated materials via conventional mechanical tests. To overcome this obstacle, in this work, state-of-the-art experimental techniques such as RBS/C ion channeling, TEM, nanoindentation, together with MC/MD simulations, were successfully used to study irradiation-induced defects in a thin irradiated layer of Ni and Ni_xFe_{1-x} single crystals.

The work aimed to understand the impact of various levels of Fe addition ranging from 0% to 62% on the response of fcc single crystals of Ni_xFe_{1-x} alloys following Ni⁺ irradiation in the range of 4×10^{13} to 4×10^{15} cm⁻², which corresponds to radiation damage levels from 0.1 to 12.5 dpa, respectively. The study of defect identification, distribution, and evolution focused on microscopic examinations using TEM and RBS/C techniques. Through TEM and RBS/C, the work aims to track defect dynamics changes with Fe additions and ion fluences. Furthermore, the RBS/C spectra were fitted using a Monte Carlo (MC) simulation based on the latest McChasy codes developed at NCBJ, which allowed determining the number of defects, their kinetic (based on MSDA model) and distribution within the single crystals. Molecular dynamics (MD) simulations have helped interpret the evolution of defects from single atoms to more complex extended defects and to calculate defect size and density. Next, the studies aimed to measure the materials' hardness as a function of Fe addition and ion fluences. The research aims to compare the measurements between pristine and irradiated materials. The

measurements were correlated to depth-dependent Ni⁺ irradiation-induced defect aggregates. As a last attempt, the effect of high-temperature irradiation (~ 800 K) was studied in pure single-crystal Ni using 380 keV Ar ions to modify the surface and to generate radiation defects. The ion implantation fluence ranged from 1×10^{14} cm⁻² up to 1×10^{16} cm⁻², corresponding to displacements per atom (dpa) values from 0.25 to 25, respectively. The structural characterization was performed by RBS/C associated with SEM and TEM. The experimental results were supported by Monte Carlo (McChasy) and Molecular Dynamics (MD-LAMMPS) simulations, and mechanical properties were assessed using the nanoindentation technique.

To fulfill the dissertation's objectives and to support the pertinence of the hypotheses, five scientific papers have been published and presented in chapters A to E.

In "Article A", three compositions, namely fcc Ni, Ni_{0.62}Fe_{0.38} and Ni_{0.38}Fe_{0.62} were first examined after irradiation. The results indicated an increased radiation tolerance of Ni_{0.38}Fe_{0.62} compared to pure Ni and Ni_{0.62}Fe_{0.38}. Damage distribution profiles obtained from the MC simulations have shown that the number of defects in Ni_{0.38}Fe_{0.62} is about twice as small as that in pure Ni. The structural analysis performed using transmission electron microscopy revealed that defects tend to concentrate in a specific region in Ni and Ni_{0.62}Fe_{0.38} at both low and high irradiation fluences. In contrast, in Ni_{0.38}Fe_{0.62}, nanoscale defects (of a size between 2 – 10 nm) are evenly distributed from the surface into the material (both at low and high fluence), which improves the overall mechanical performance. The mechanical results obtained on the samples in a virgin state indicate an increase in initial hardness with Fe content up to 38 at%. Then, above ~ 40 at% Fe, a decrease has been observed. This is most likely due to the different arrangement of Fe atoms in a crystal structure influencing the obtained mechanical properties of Ni_xFe_{1-x} in a virgin state and after ion irradiation. Irradiation-induced hardening has been observed for all the compositions. However, better radiation resistance of Ni_xFe_{1-x} (with increasing Fe content) than in pure Ni has been reported. This phenomenon is most probably related to the physical nature of the iron atomic nucleus in its excited state (during irradiation), as it possesses only one orbital with unpaired electrons, while Ni has three. This means that Ni possesses more space for electron movements and, thus, defect generation and mobility. Therefore, Fe effectively suppresses damage and stress induced by ion irradiation.

"Article B" was devoted to the analysis of five different compositions, fcc Ni and Ni_xFe_{1-x} single crystal alloys, namely Ni, Ni_{0.88}Fe_{0.12}, Ni_{0.77}Fe_{0.23}, Ni_{0.62}Fe_{0.38}, Ni_{0.38}Fe_{0.62} irradiated by 1.5 MeV ⁵⁸Ni ions at room temperature in a wide fluence range (4×10^{13} to 4×10^{15} ions/cm²). This work aim at studying the role of Fe addition on the radiation resistance of the Ni_xFe_{1-x} single crystals,

by performing hybrid Monte Carlo/Molecular dynamics simulations combined with TEM, RBS/C, and nanoindentation techniques. Ion channeling studies, as well as the damage kinetics, demonstrated various responses of damage build-up mechanisms for each individual composition. It has been noticed that the defect type, size and density influence the shape and intensity of the obtained RBS/C spectra depending on the composition. The TEM images revealed a significant degradation of the structure at 0.5 dpa, especially for Ni. The Multi-Step Damage Accumulation analysis revealed that the cross-sections for damage formation significantly decrease in the case of $\text{Ni}_{0.38}\text{Fe}_{0.62}$ and $\text{Ni}_{0.62}\text{Fe}_{0.38}$ compared to pure Ni single crystal, which is consistent with the RBS/C and TEM results.

The atomistic simulations enabled the obtaining of insightful results related to the hardening of $\text{Ni}_x\text{Fe}_{1-x}$ in its pristine state. The main reason for the highest hardness of $\text{Ni}_{0.62}\text{Fe}_{0.38}$ alloy before irradiation could be related to the presence of nanoprecipitate FeNi_3 (L_{12}) phase (around 20%), which is formed inside the disordered matrix. Moreover, we observed the smallest increase in hardness with fluence for $\text{Ni}_{0.38}\text{Fe}_{0.62}$ and $\text{Ni}_{0.62}\text{Fe}_{0.38}$ samples, while the most drastic increase is observed for Ni, followed by $\text{Ni}_{0.88}\text{Fe}_{0.12}$ and $\text{Ni}_{0.77}\text{Fe}_{0.23}$. Additionally, it has been noticed that the addition of iron reduced the number and size of the defects in $\text{Ni}_x\text{Fe}_{1-x}$.

The next step (“Article C”) encompassed investigations of defect evolution of three compositions: Ni, $\text{Ni}_{0.88}\text{Fe}_{0.12}$ and $\text{Ni}_{0.77}\text{Fe}_{0.23}$ single crystals. This work addresses the gaps in the understanding of three-dimensional defect formation, considering the presence of the A15 nano-phase, in both pure Ni and $\text{Ni}_x\text{Fe}_{1-x}$ single crystals. A detailed investigation, combining experimental and computational methods, to elucidate the mechanisms of defect formation, distribution, and kinetics in Ni and $\text{Ni}_x\text{Fe}_{1-x}$ single crystals with up to 23% iron content under low ion fluences has been conducted. Notably, it has been observed for the first time that the A15 nano-phase forms not only in pure Ni but also in $\text{Ni}_{0.88}\text{Fe}_{0.12}$ and $\text{Ni}_{0.77}\text{Fe}_{0.23}$ single crystals. The simulations revealed the formation of the A15 Frank-Kasper phase in pure Ni, $\text{Ni}_{0.88}\text{Fe}_{0.12}$, and $\text{Ni}_{0.77}\text{Fe}_{0.23}$ up to the fluence of 2×10^{14} ions/cm² as a responsible mechanism for Frank loop nucleation within their native {111} plane, which is observed in pure Ni as well as in $\text{Ni}_{0.88}\text{Fe}_{0.12}$ and $\text{Ni}_{0.77}\text{Fe}_{0.23}$. This enables the investigation of the impact of Fe atoms on dislocation nucleation and evolution. Moreover, atomistic simulations, RBS/C, and Monte Carlo McChasy simulations indicate that point defects (mainly; interstitial, dumbbell, single vacancies, and A15 phase as well as voids) dominate in pure Ni, $\text{Ni}_{0.88}\text{Fe}_{0.12}$, and $\text{Ni}_{0.77}\text{Fe}_{0.23}$ samples up to the fluence of 2×10^{14} ions/cm² and they are transformed into more complex defects, such as dislocation loops or stacking fault tetrahedra at the fluence of 2×10^{15} ions/cm². However, in

Ni_{0.77}Fe_{0.23}, although A15 phases are formed, their small size prevents them from evolving into Frank loops, despite being highly Fe-decorated. The presented study represents a comprehensive demonstration of the formation and dynamics of irradiation-induced defects, especially within the low irradiation fluence for pure Ni, Ni_{0.88}Fe_{0.12}, and Ni_{0.77}Fe_{0.23} alloys. This insight was achieved through a synergistic approach combining electron microscopy analysis and Rutherford backscattering spectrometry, complemented by experimentally guided atomistic simulations and a damage kinetics model.

Further research (“Article D”) presents dislocation modeling capabilities using the latest code of the McChasy2 developed at NCBJ, which utilizes the ATOMSK and the MD-LAMMPS procedures. The dislocation modeling was performed on a Ni single crystal after ion implantation. The McChasy2 was used to analyze experimentally obtained RBS/C spectra using large atomic structures (ca. 10⁸ atoms). The models helped create virtual samples using artificially produced <110> and <112>-oriented dislocation loops lying along {111} and {-1-11} planes, which fit experimentally obtained spectra in real fcc structures. This approach is highly necessary because it provides the opportunity for a detailed analysis of the type of dislocations, their distributions, and dynamics, which would not be possible with the analysis of purely experimental spectra without the aid of numerical tools.

The final step of this study (“Article E”) evaluated the impact of temperature on the evolution and distribution of defects during high-temperature (~800 K) ion irradiation with 380 keV Ar ions in a Ni single crystal. The ion implantation fluence ranged from 1×10¹⁴ cm⁻² up to 1 × 10¹⁶ cm⁻², which corresponds to values of displacements per atom from 0.25 to 25, respectively. In this work, a combination of several experimental and simulation techniques to unravel and explain the effects that occur in the high-temperature ion-modified surface of a Ni single crystal at a depth of approximately 800 nm has been presented. For this reason, RBS experimental techniques in channeling mode, TEM, SEM, and nanoindentation techniques have been utilized to reveal the structural and mechanical changes. Afterwards, the RBS/C experimental results were supported using the latest two generations of the McChasy code, utilizing different extended defects (edge dislocations or loops). The damage models were developed using internal McChasy procedures and by the Molecular Dynamics (MD)-LAMMPS code. It has been found that most point defects and/or clusters were annealed during the high-temperature implantation process. The TEM combined with nanoindentation results revealed that the size of the noble gas bubbles increases with the ion fluence influencing the hardening effect. In the case of the HT irradiation of Ni, another step in damage kinetics is visible for the highest dose

(i.e., 25 dpa) as a consequence of the entanglement of dislocations and agglomeration of noble gas bubbles. The simulations performed using the second generation of the McChasy code demonstrated that the impact of bubbles formed within the material is not negligible and disregarding them may exaggerate the quantitative analysis of defects in the simulated spectra. The obtained results can be utilized for designing structural materials for nuclear applications, as well as predicting their behavior under harsh conditions such as the simultaneous impact of irradiation and high temperature.

The resulting distributions of the defects obtained for the real experimental spectrum were in good agreement with the SRIM code predictions. This approach was also employed in other presented works and yielded several advantages (e.g., detecting specific types of radiation defects) in the interpretation of the RBS/C results.

6.2 Thesis verification

The conducted research delivered significant information on the evolution of defects and mechanical properties of $\text{Ni}_x\text{Fe}_{1-x}$ single crystals after irradiation and in high-temperature conditions. The results presented in this dissertation prove that, depending on the chemical composition and radiation dose, the evolution of defects has a variable character and depends on the amount of Fe addition. It is because the addition of Fe effectively influences energy transport during defect formation by ion flow through electrons during defect formation and distribution. The research results presented in the series of articles indicate an increased radiation tolerance of the $\text{Ni}_{0.38}\text{Fe}_{0.62}$ and $\text{Ni}_{0.62}\text{Fe}_{0.38}$ compositions. This information is fundamental, as it may suggest future direction for designing more complex HEA alloys intended for nuclear application. Therefore, the conducted research proved the validity of the first proposed research hypothesis: *“by tuning the chemical composition in $\text{Ni}_x\text{Fe}_{1-x}$ single crystals, it is possible to tailor the radiation tolerance of these materials”*.

Next, experimental studies supported by numerical simulations helped to understand the behavior of the studied materials under harsh operational conditions such as temperature and radiation. Specifically, the models used to calculate the damage kinetics of defect formation, MC and MD simulations, and the usage of the latest McChasy code, allowed obtaining detailed information on the specific defect types, their distributions, and the rate of defect formation at specific radiation damages. The collected information can be regarded as key for the qualification of these materials for applications in the nuclear or space industry. It also confirms the validity of the second hypothesis: *“the integration of structural characterization techniques*

with computational simulations enables not only quantitative analysis of radiation-induced defects in materials, but also allows for prediction of their type and distribution”.

In conclusion, the presented data included in this thesis allowed for a successful confirmation of the research hypotheses and fulfillment of the dissertation objectives stated in chapter 3.

6.3 Future works

Despite extensive characterization of $\text{Ni}_x\text{Fe}_{1-x}$ single crystals, there is still a need to perform detailed study of the L_{12} phase existence in $\text{Ni}_x\text{Fe}_{1-x}$ by performing Atom Probe Tomography (APT) analysis or Synchrotron X-ray Diffraction (XRD) at the virgin state and after irradiation. Irradiation can change the distribution of the atoms and increase the disordered phase, since irradiation may spread the Fe atoms inside the Ni matrix, resulting in an increase in hardness. This should be verified by a combination of atomistic simulations together with experimental studies, which may help to better understand mechanisms such as hardening and phase distribution within various $\text{Ni}_x\text{Fe}_{1-x}$ single crystals. Therefore, as a next step, investigation of the hardening effect and verification of the L_{12} phase presence after irradiation in the order-disorder phases should be performed. This is particularly important as recent studies conducted by Han et al. ¹⁹⁴ published in the Nature journal suggest that the L_{12} phase has a very favorable impact on the mechanical properties (ductility and yield strength), hence an optimal Ni:Fe balance has been found which will motivate future studies devoted to this alloy development.

Looking ahead, future research endeavors should be extended towards high-temperature irradiation testing, in order to comprehensively assess the utility of these materials, assessing the evolution of defects at elevated temperatures at various dpa levels up to 50-100 dpa (mimicking operational conditions of the Gen IV nuclear reactors). Both metal (heavy) and gas (light) ion irradiation should be performed in order to evaluate simultaneous effects of voids and bubbles formation on the structural and mechanical properties of $\text{Ni}_x\text{Fe}_{1-x}$ single crystals.

Finally, selected $\text{Ni}_x\text{Fe}_{1-x}$ single crystal compositions should then be fabricated using various techniques such as 3D printing, casting or spark plasma sintering to establish the optimal manufacturing techniques for this class of alloys. Also, corrosion resistance improvement by adding additional elements could be regarded as another avenue of this research.

To obtain more accurate results during simulations, it is recommended to use more complex defect structures with loops of varying sizes and orientations. Moreover, the merge of MD and MC simulations should also be performed for other models e.g. dumbbells formed inside Ni

single crystals. The next step would be to perform a similar analysis on more complex Ni-based alloys. Thus, the studies on MD and MC simulations combined with experimental RBS/C results of radiation defects in Ni structures could be a useful tool for analyzing of dislocation loops created in irradiated materials.

References

1. Zinkle SJ, Was GS. Materials challenges in nuclear energy. *Acta Mater.* 2013;61(3):735-758. doi:10.1016/j.actamat.2012.11.004
2. Frelek-Kozak M, Kurpaska L, Lesniak M, Jozwik I, Jagielski J. Mechanical and structural properties of ODS RAF steels submitted to low-energy ions irradiation. *Fusion Eng Des.* 2018;127:54-59. doi:10.1016/j.fusengdes.2017.12.006
3. Bollen G, Baek I, Blideanu V, et al. Rare isotope accelerator—conceptual design of target areas. *Nucl Instruments Methods Phys Res Sect A Accel Spectrometers, Detect Assoc Equip.* 2006;562(2):915-920. doi:10.1016/j.nima.2006.02.106
4. Simos N, Kirk HG, Thieberger P, et al. Irradiation damage studies of high power accelerator materials. *J Nucl Mater.* 2008;377(1):41-51. doi:10.1016/j.jnucmat.2008.02.074
5. Pellemoine F. High power density targets. *Nucl Instruments Methods Phys Res Sect B Beam Interact with Mater Atoms.* 2013;317:369-372. doi:10.1016/j.nimb.2013.06.038
6. Nordlund K, Zinkle SJ, Sand AE, et al. Primary radiation damage: A review of current understanding and models. *J Nucl Mater.* 2018;512:450-479. doi:10.1016/j.jnucmat.2018.10.027
7. Anento N, Serra A, Osetsyky Y. Effect of nickel on point defects diffusion in Fe – Ni alloys. *Acta Mater.* 2017;132:367-373. doi:10.1016/j.actamat.2017.05.010
8. Lu C, Jin K, Béland LK, et al. Direct Observation of Defect Range and Evolution in Ion-Irradiated Single Crystalline Ni and Ni Binary Alloys. *Sci Rep.* 2016;6(1):19994. doi:10.1038/srep19994
9. Jin K, Bei H, Zhang Y. Ion irradiation induced defect evolution in Ni and Ni-based FCC equiatomic binary alloys. *J Nucl Mater.* 2016;471:193-199. doi:10.1016/j.jnucmat.2015.09.009
10. Ullah MW, Aidhy DS, Zhang Y, Weber WJ. Damage accumulation in ion-irradiated Ni-based concentrated solid-solution alloys. *Acta Mater.* 2016;109:17-22. doi:10.1016/j.actamat.2016.02.048
11. Jin K, Guo W, Lu C, et al. Effects of Fe concentration on the ion-irradiation induced defect evolution and hardening in Ni-Fe solid solution alloys. *Acta Mater.* 2016;121:365-373. doi:10.1016/j.actamat.2016.09.025
12. Middleburgh SC, King DM, Lumpkin GR, Cortie M, Edwards L. Segregation and migration of species in the CrCoFeNi high entropy alloy. *J Alloys Compd.* 2014;599:179-182. doi:10.1016/j.jallcom.2014.01.135
13. Rowcliffe AF, Mansur LK, Hoelzer DT, Nanstad RK. Perspectives on radiation effects in nickel-base alloys for applications in advanced reactors. *J Nucl Mater.* 2009;392(2):341-352. doi:10.1016/j.jnucmat.2009.03.023
14. Zinkle SJ, Busby JT. Structural materials for fission & fusion energy. *Mater Today.* 2009;12(11):12-19. doi:10.1016/S1369-7021(09)70294-9
15. Vörtler K, Juslin N, Bonny G, Malerba L, Nordlund K. The effect of prolonged irradiation on defect production and ordering in Fe–Cr and Fe–Ni alloys. *J Phys Condens Matter.* 2011;23(35):355007. doi:10.1088/0953-8984/23/35/355007
16. Wilam R. Corwin, Timothy D. Burchell, William G. Halsey, et al. *The Gas Cooled Fast Reactor (GFR) Survey of Materials Experience and R&D Needs to Assess Viability. Report ORNL/TM2004/99.*; 2005.
17. R.E. Stoller, L.K. Mansur. *Modeling and Microstructural Analysis: Needs and Requirements for Generation IV Fission Reactors. Tennessee: Oak Ridge National Laboratory. Report ORNL/TM-2003/242.*; 2004.
18. G.O. Hayner et. al. *Next Generation Nuclear Plant Materials Selection and Qualification Program Plan. Report INEEL/EXT-03-001128.*; 2003.
19. Odette GR, Yamamoto T, Rathbun HJ, He MY, Hribernik ML, Rensman JW. Cleavage fracture and irradiation embrittlement of fusion reactor alloys: mechanisms, multiscale models, toughness measurements and implications to structural integrity assessment. *J Nucl Mater.* 2003;323(2-3):313-340. doi:10.1016/j.jnucmat.2003.08.023
20. Cabet C, Jang J, Konys J, Tortorelli PF. Environmental Degradation of Materials in Advanced Reactors. *MRS Bull.* 2009;34(1):35-39. doi:10.1557/mrs2009.10
21. Leonard C. Feldman, James W. Mayer, S. Thomas Picraux. *MATERIALS ANALYSIS BY ION CHANNELING. Submicron Crystallography.* Academic Press; 1982.
22. Perez A, Coussement R, eds. *Site Characterization and Aggregation of Implanted Atoms in Materials.* Springer US; 1980. doi:10.1007/978-1-4684-1015-0
23. Gary S. Was. *Fundamentals of Radiation Materials Science. Metals and Alloys.* Springer; 2007.
24. Aidhy DS, Lu C, Jin K, et al. Formation and growth of stacking fault tetrahedra in Ni via vacancy aggregation mechanism. *Scr Mater.* 2016;114:137-141. doi:10.1016/j.scriptamat.2015.12.020
25. Zhao S, Osetsyky Y, Stocks GM, Zhang Y. Local-environment dependence of stacking fault energies in concentrated solid-solution alloys. *npj Comput Mater.* 2019;5(1):13. doi:10.1038/s41524-019-0150-y

26. Loretto MH, Phillips PJ, Mills MJ. Stacking fault tetrahedra in metals. *Scr Mater.* 2015;94:1-4. doi:10.1016/j.scriptamat.2014.07.020
27. Lu C, Yang T, Niu L, et al. Interstitial migration behavior and defect evolution in ion irradiated pure nickel and Ni-xFe binary alloys. *J Nucl Mater.* 2018;509:237-244. doi:10.1016/j.jnucmat.2018.07.006
28. Lu C, Niu L, Chen N, et al. Enhancing radiation tolerance by controlling defect mobility and migration pathways in multicomponent single-phase alloys. *Nat Commun.* 2016;7(1):13564. doi:10.1038/ncomms13564
29. Ustrzycka A, Dominguez-Gutierrez FJ, Chromiński W. Atomistic analysis of the mechanisms underlying irradiation-hardening in Fe–Ni–Cr alloys. *Int J Plast.* 2024;182:104118. doi:10.1016/j.ijplas.2024.104118
30. GE D. *Mechanical Metallurgy*. McGraw-Hill; 1976.
31. Jin K, Lu C, Wang LM, et al. Effects of compositional complexity on the ion-irradiation induced swelling and hardening in Ni-containing equiatomic alloys. *Scr Mater.* 2016;119:65-70. doi:10.1016/j.scriptamat.2016.03.030
32. Jin K, Sales BC, Stocks GM, et al. Tailoring the physical properties of Ni-based single-phase equiatomic alloys by modifying the chemical complexity. *Sci Rep.* 2016;6(1):20159. doi:10.1038/srep20159
33. Zhang Y, Jin K, Xue H, et al. Influence of chemical disorder on energy dissipation and defect evolution in advanced alloys. *J Mater Res.* 2016;31(16):2363-2375. doi:10.1557/jmr.2016.269
34. Zhang Y, Egami T, Weber WJ. Dissipation of radiation energy in concentrated solid-solution alloys: Unique defect properties and microstructural evolution. *MRS Bull.* 2019;44(10):798-811. doi:10.1557/mrs.2019.233
35. Yeh J -W., Chen S -K., Lin S -J., et al. Nanostructured High-Entropy Alloys with Multiple Principal Elements: Novel Alloy Design Concepts and Outcomes. *Adv Eng Mater.* 2004;6(5):299-303. doi:10.1002/adem.200300567
36. Chuang MH, Tsai MH, Wang WR, Lin SJ, Yeh JW. Microstructure and wear behavior of Al_xCo_{1.5}CrFeNi_{1.5}Ti_y high-entropy alloys. *Acta Mater.* 2011;59(16):6308-6317. doi:10.1016/j.actamat.2011.06.041
37. Zhang Y, Osetsky YN, Weber WJ. Tunable Chemical Disorder in Concentrated Alloys: Defect Physics and Radiation Performance. *Chem Rev.* 2022;122(1):789-829. doi:10.1021/acs.chemrev.1c00387
38. Senkov ON, Wilks GB, Miracle DB, Chuang CP, Liaw PK. Refractory high-entropy alloys. *Intermetallics.* 2010;18(9):1758-1765. doi:10.1016/j.intermet.2010.05.014
39. Wu Z, Bei H, Otto F, Pharr GM, George EP. Recovery, recrystallization, grain growth and phase stability of a family of FCC-structured multi-component equiatomic solid solution alloys. *Intermetallics.* 2014;46:131-140. doi:10.1016/j.intermet.2013.10.024
40. Ma SG, Zhang Y. Effect of Nb addition on the microstructure and properties of AlCoCrFeNi high-entropy alloy. *Mater Sci Eng A.* 2012;532:480-486. doi:10.1016/j.msea.2011.10.110
41. Egami T, Guo W, Rack PD, Nagase T. Irradiation Resistance of Multicomponent Alloys. *Metall Mater Trans A.* 2014;45(1):180-183. doi:10.1007/s11661-013-1994-2
42. Osetsky Y, Barashev A V., Béland LK, Yao Z, Ferasat K, Zhang Y. Tunable chemical complexity to control atomic diffusion in alloys. *npj Comput Mater.* 2020;6(1):38. doi:10.1038/s41524-020-0306-9
43. Vernyhora I V., Tatarenko VA, Bokoch SM. Thermodynamics of f.c.c.-Ni–Fe Alloys in a Static Applied Magnetic Field. *ISRN Thermodyn.* 2012;2012:1-11. doi:10.5402/2012/917836
44. Zhang Y, Stocks GM, Jin K, et al. Influence of chemical disorder on energy dissipation and defect evolution in concentrated solid solution alloys. *Nat Commun.* 2015;6(1):8736. doi:10.1038/ncomms9736
45. Swihart JC, Butler WH, Stocks GM, Nicholson DM, Ward RC. First-Principles Calculation of the Residual Electrical Resistivity of Random Alloys. *Phys Rev Lett.* 1986;57(9):1181-1184. doi:10.1103/PhysRevLett.57.1181
46. Mu S, Wimmer S, Mankovsky S, Ebert H, Stocks GM. Influence of local lattice distortions on electrical transport of refractory high entropy alloys. *Scr Mater.* 2019;170:189-194. doi:10.1016/j.scriptamat.2019.05.032
47. Zhao S, Egami T, Stocks GM, Zhang Y. Effect of d electrons on defect properties in equiatomic NiCoCr and NiCoFeCr concentrated solid solution alloys. *Phys Rev Mater.* 2018;2(1):013602. doi:10.1103/PhysRevMaterials.2.013602
48. Osetsky YN, Béland LK, Barashev A V., Zhang Y. On the existence and origin of sluggish diffusion in chemically disordered concentrated alloys. *Curr Opin Solid State Mater Sci.* 2018;22(3):65-74. doi:10.1016/j.cossms.2018.05.003
49. Zhao S, Stocks GM, Zhang Y. Defect energetics of concentrated solid-solution alloys from ab initio calculations: Ni_{0.5}Co_{0.5}, Ni_{0.5}Fe_{0.5}, Ni_{0.8}Fe_{0.2} and Ni_{0.8}Cr_{0.2}. *Phys Chem Chem Phys.* 2016;18(34):24043-24056. doi:10.1039/C6CP05161H
50. Stoller RE, Tamm A, Béland LK, et al. Impact of Short-Range Forces on Defect Production from High-Energy Collisions. *J Chem Theory Comput.* 2016;12(6):2871-2879. doi:10.1021/acs.jctc.5b01194

51. Aidhy DS, Lu C, Jin K, et al. Point defect evolution in Ni, NiFe and NiCr alloys from atomistic simulations and irradiation experiments. *Acta Mater.* 2015;99:69-76. doi:10.1016/j.actamat.2015.08.007
52. He MR, Wang S, Shi S, et al. Mechanisms of radiation-induced segregation in CrFeCoNi-based single-phase concentrated solid solution alloys. *Acta Mater.* 2017;126:182-193. doi:10.1016/j.actamat.2016.12.046
53. Schuler T, Trinkle DR, Bellon P, Averback R. Design principles for radiation-resistant solid solutions. *Phys Rev B.* 2017;95(17):174102. doi:10.1103/PhysRevB.95.174102
54. Barashev A, Osetsky Y, Bei H, Lu C, Wang L, Zhang Y. Chemically-biased diffusion and segregation impede void growth in irradiated Ni-Fe alloys. *Curr Opin Solid State Mater Sci.* 2019;23(2):92-100. doi:10.1016/j.cossms.2018.12.001
55. Oh HS, Kim SJ, Odbadrakh K, et al. Engineering atomic-level complexity in high-entropy and complex concentrated alloys. *Nat Commun.* 2019;10(1):2090. doi:10.1038/s41467-019-10012-7
56. P.K. Chu GSW. *Surface Modification of Magnesium and Its Alloys for Biomedical Applications.* Elsevier; 2015. doi:10.1016/C2013-0-16447-1
57. Gao J, Lv S, Zhao Y, Chen D, Li Z. Simulation of primary knock-on atom distribution in HTGR graphite under neutron and ion irradiation. *Nucl Instruments Methods Phys Res Sect B Beam Interact with Mater Atoms.* 2021;492:15-22. doi:10.1016/j.nimb.2021.01.013
58. Piekoszewski J, Werner Z, Langner J, Jakubowski L, Pochrybniak C, Harasiewicz A. Pulse implantation doping - concentration profiles and surface morphology. *Nucl Instruments Methods Phys Res.* 1983;209-210:477-482. doi:10.1016/0167-5087(83)90841-4
59. Zhu XP, Lei MK, Dong ZH, Miao SM, Ma TC. Crater formation on the surface of titanium irradiated by a high-intensity pulsed ion beam. *Surf Coatings Technol.* 2003;173(1):105-110. doi:10.1016/S0257-8972(03)00321-9
60. Barlak Marek, Jacek W. Effect of noble gases ion implantation on the life time of WC-Co tools used in wood-based material machining. *Ann WULS - SGGW, For Wood Technol.* 2023;24:77-84.
61. Przemysław J. *Zastosowanie Kanałowania Jonów w Analizie Deformacji w Kryształach.* 2017.
62. Levchenko E V., Dappe YJ, Ori G, eds. *Theory and Simulation in Physics for Materials Applications.* Vol 296. Springer International Publishing; 2020. doi:10.1007/978-3-030-37790-8
63. Oliver WC, Pharr GM. Measurement of hardness and elastic modulus by instrumented indentation: Advances in understanding and refinements to methodology. *J Mater Res.* 2004;19(1):3-20. doi:10.1557/jmr.2004.19.1.3
64. James Ziegler. www.srim.org.
65. Ziegler JF, Ziegler MD, Biersack JP. SRIM – The stopping and range of ions in matter (2010). *Nucl Instruments Methods Phys Res Sect B Beam Interact with Mater Atoms.* 2010;268(11-12):1818-1823. doi:10.1016/j.nimb.2010.02.091
66. Stoller RE, Toloczko MB, Was GS, Certain AG, Dwaraknath S, Garner FA. On the use of SRIM for computing radiation damage exposure. *Nucl Instruments Methods Phys Res Sect B Beam Interact with Mater Atoms.* 2013;310:75-80. doi:10.1016/j.nimb.2013.05.008
67. Zhang Y, Lian J, Zhu Z, et al. Response of strontium titanate to ion and electron irradiation. *J Nucl Mater.* 2009;389(2):303-310. doi:10.1016/j.jnucmat.2009.02.014
68. Mieszczynski C, Ratajczak R, Jagielski J, et al. Defect evolution in Ni and solid-solution alloys of NiFe and NiFeCoCr under ion irradiation at 16 and 300 K. *J Nucl Mater.* 2020;534:152138. doi:10.1016/j.jnucmat.2020.152138
69. Weber WJ, Zhang Y. Predicting damage production in monoatomic and multi-elemental targets using stopping and range of ions in matter code: Challenges and recommendations. *Curr Opin Solid State Mater Sci.* 2019;23(4):100757. doi:10.1016/j.cossms.2019.06.001
70. Crocombette JP, Van Wambeke C. Quick calculation of damage for ion irradiation: implementation in Iradina and comparisons to SRIM. *EPJ Nucl Sci Technol.* 2019;5:7. doi:10.1051/epjn/2019003
71. Béland LK, Lu C, Osetskiy YN, et al. Features of primary damage by high energy displacement cascades in concentrated Ni-based alloys. *J Appl Phys.* 2016;119(8). doi:10.1063/1.4942533
72. Barrett JH. Monte Carlo Channeling Calculations. *Phys Rev B.* 1971;3(5):1527-1547. doi:10.1103/PhysRevB.3.1527
73. Jozwik P, Nowicki L, Ratajczak R, et al. Advanced Monte Carlo Simulations for Ion-Channeling Studies of Complex Defects in Crystals. In: Elena V. Levchenko YJDGO, ed. ; 2020:133-160. doi:10.1007/978-3-030-37790-8_8
74. Thompson AP, Aktulga HM, Berger R, et al. LAMMPS - a flexible simulation tool for particle-based materials modeling at the atomic, meso, and continuum scales. *Comput Phys Commun.* 2022;271:108171. doi:10.1016/j.cpc.2021.108171
75. Bonny G, Bakaev A, Olsson P, Domain C, Zhurkin EE, Posselt M. Interatomic potential to study the formation of NiCr clusters in high Cr ferritic steels. *J Nucl Mater.* 2017;484:42-50.

- doi:10.1016/j.jnucmat.2016.11.017
76. Bonny G, Castin N, Terentyev D. Interatomic potential for studying ageing under irradiation in stainless steels: the FeNiCr model alloy. *Model Simul Mater Sci Eng.* 2013;21(8):085004. doi:10.1088/0965-0393/21/8/085004
77. Aligayev A, Landeiro Dos Reis M, Chartier A, Jabbarli U, Domínguez-Gutiérrez FJ, Huang Q. Irradiation-induced defect evolution in concentrated solid-solution alloys: a molecular dynamics perspective. *Plasma Phys Control Fusion.* 2025;67(5):055020. doi:10.1088/1361-6587/adcd2b
78. Wyszkowska E, Mieszczynski C, Kurpaska Ł, et al. Tuning heterogeneous ion-radiation damage by composition in NixFe1-x binary single crystals. *Nanoscale.* 2023;15(10):4870-4881. doi:10.1039/D2NR06178C
79. Wyszkowska E, Mieszczynski C, Kurpaska Ł, et al. The Fe addition as an effective treatment for improving the radiation resistance of fcc NixFe1-x single-crystal alloys. *J Nucl Mater.* 2023;584:154565. doi:10.1016/j.jnucmat.2023.154565
80. Guénolé J, Nöhring WG, Vaid A, et al. Assessment and optimization of the fast inertial relaxation engine (fire) for energy minimization in atomistic simulations and its implementation in lammmps. *Comput Mater Sci.* 2020;175:109584. doi:10.1016/j.commatsci.2020.109584
81. Kurpaska Ł, Dominguez-Gutierrez FJ, Zhang Y, et al. Effects of Fe atoms on hardening of a nickel matrix: Nanoindentation experiments and atom-scale numerical modeling. *Mater Des.* 2022;217:110639. doi:10.1016/j.matdes.2022.110639
82. Boleininger M, Mason DR, Sand AE, Dudarev SL. Microstructure of a heavily irradiated metal exposed to a spectrum of atomic recoils. *Sci Rep.* 2023;13(1):1684. doi:10.1038/s41598-022-27087-w
83. Granberg F, Nordlund K, Ullah MW, et al. Mechanism of Radiation Damage Reduction in Equiatomic Multicomponent Single Phase Alloys. *Phys Rev Lett.* 2016;116(13):135504. doi:10.1103/PhysRevLett.116.135504
84. Domínguez-Gutiérrez FJ, Byggmästar J, Nordlund K, Djurabekova F, von Toussaint U. Computational study of crystal defect formation in Mo by a machine learning molecular dynamics potential. *Model Simul Mater Sci Eng.* 2021;29(5):055001. doi:10.1088/1361-651X/abf152
85. Stukowski A. Visualization and analysis of atomistic simulation data with OVITO—the Open Visualization Tool. *Model Simul Mater Sci Eng.* 2010;18(1):015012. doi:10.1088/0965-0393/18/1/015012
86. Levo E, Granberg F, Fridlund C, Nordlund K, Djurabekova F. Radiation damage buildup and dislocation evolution in Ni and equiatomic multicomponent Ni-based alloys. *J Nucl Mater.* 2017;490:323-332. doi:10.1016/j.jnucmat.2017.04.023
87. Sadigh B, Erhart P, Stukowski A, Caro A, Martinez E, Zepeda-Ruiz L. Scalable parallel Monte Carlo algorithm for atomistic simulations of precipitation in alloys. *Phys Rev B.* 2012;85(18):184203. doi:10.1103/PhysRevB.85.184203
88. Esfandiarpour A, Alvarez-Donado R, Papanikolaou S, Alava M. Atomistic simulations of dislocation plasticity in concentrated VCoNi medium entropy alloys: Effects of lattice distortion and short range order. *Front Mater.* 2022;9. doi:10.3389/fmats.2022.1046291
89. Larsen PM, Schmidt S, Schiøtz J. Robust structural identification via polyhedral template matching. *Model Simul Mater Sci Eng.* 2016;24(5):055007. doi:10.1088/0965-0393/24/5/055007
90. Jagielski J, Thomé L. Multi-step damage accumulation in irradiated crystals. *Appl Phys A.* 2009;97(1):147-155. doi:10.1007/s00339-009-5294-z
91. Karolina D. *Procesy Defektowania i Termicznie Aktywowane Transformacje Defektowe w Implantowanych Warstwach Epitaksjalnych AlxGa1-XN.* Narodowe Centrum Badań Jądrowych; 2012.
92. Jagielski J, Thomé L, Chartier A, Dorosh O, Mieszczynski C, Jozwik I. Damage accumulation studies in ion-irradiated oxides: Current status and new perspectives. *Nucl Instruments Methods Phys Res Sect B Beam Interact with Mater Atoms.* 2018;435:2-7. doi:10.1016/j.nimb.2017.11.015
93. Yu HQ, Wang SL, Zhang YF, et al. Response of nanoclusters to heavy-ion irradiation in an Fe-12Cr ODS steel. *Fusion Eng Des.* 2021;172:112759. doi:10.1016/j.fusengdes.2021.112759
94. Huo W, Wang S, Fang F, et al. Microstructure and corrosion resistance of highly <111> oriented electrodeposited CoNiFe medium-entropy alloy films. *J Mater Res Technol.* 2022;20:1677-1684. doi:10.1016/j.jmrt.2022.07.175
95. Lee M, Kim G, Jung Y, Ahn S. Radiation-induced swelling and precipitation in Fe++ ion-irradiated ferritic/martensitic steels. *J Nucl Mater.* 2021;555:153137. doi:10.1016/j.jnucmat.2021.153137
96. Ryabikovskaya E, French A, Gabriel A, et al. Irradiation-induced swelling of pure chromium with 5 MeV Fe ions in the temperature range 450–650 °C. *J Nucl Mater.* 2021;543:152585. doi:10.1016/j.jnucmat.2020.152585
97. Luu VN, Murakami K, Samouh H, et al. Swelling of alpha-quartz induced by MeV ions irradiation: Critical dose and swelling mechanism. *J Nucl Mater.* 2020;539:152266. doi:10.1016/j.jnucmat.2020.152266
98. Zhang SJ, Li DH, Chen HC, et al. Ion irradiation-induced swelling and hardening effect of Hastelloy

- N alloy. *J Nucl Mater.* 2017;489:180-186. doi:10.1016/j.jnucmat.2017.03.036
99. Ding Q, Zhang Y, Chen X, et al. Tuning element distribution, structure and properties by composition in high-entropy alloys. *Nature.* 2019;574(7777):223-227. doi:10.1038/s41586-019-1617-1
100. Antonii Modrzejewski. *Monokryształy Metali.* Wydawnictwo Naukowo-Techniczne; 1960.
101. Saranraj A, Murugan R, Dhas SSJ, Jose M, Dhas SAMB. Indigenously developed vertical semi transparent Bridgman setup for the growth of single crystals. *Mater Today Commun.* 2017;13:386-390. doi:10.1016/j.mtcomm.2017.11.003
102. Nowicki L, Turos A, Ratajczak R, Stonert A, Garrido F. Modern analysis of ion channeling data by Monte Carlo simulations. *Nucl Instruments Methods Phys Res Sect B Beam Interact with Mater Atoms.* 2005;240(1-2):277-282. doi:10.1016/j.nimb.2005.06.129
103. Jozwik P, Nowicki L, Ratajczak R, et al. Monte Carlo simulations of ion channeling in crystals containing dislocations and randomly displaced atoms. *J Appl Phys.* 2019;126(19). doi:10.1063/1.5111619
104. David B. Williams, C. Barry Carter. Transmission Electron Microscopy. A Textbook for Materials Science. In: ; 2009:352.
105. Zhang Y, Debelle A, Boulle A, Kluth P, Tuomisto F. Advanced techniques for characterization of ion beam modified materials. *Curr Opin Solid State Mater Sci.* 2015;19(1):19-28. doi:10.1016/j.cossms.2014.09.007
106. Nix WD, Gao H. Indentation size effects in crystalline materials: A law for strain gradient plasticity. *J Mech Phys Solids.* 1998;46(3):411-425. doi:10.1016/S0022-5096(97)00086-0
107. Friedland E, Fletcher M. Structure dependence of radiation damage depths after ion implantation. *Nucl Instruments Methods Phys Res Sect B Beam Interact with Mater Atoms.* 1992;64(1-4):242-245. doi:10.1016/0168-583X(92)95473-5
108. Zhao S, Osetsky Y, Zhang Y. Diffusion of point defects in ordered and disordered Ni–Fe alloys. *J Alloys Compd.* 2019;805:1175-1183. doi:10.1016/j.jallcom.2019.07.142
109. Liu J, Huang H, Gao J, Zhu Z, Li Y. Defects evolution and hardening in the Hastelloy N alloy by subsequent Xe and He ions irradiation. *J Nucl Mater.* 2019;517:328-336. doi:10.1016/j.jnucmat.2019.02.022
110. Chen HC, Li DH, Lui RD, et al. Ion irradiation induced disappearance of dislocations in a nickel-based alloy. *Nucl Instruments Methods Phys Res Sect B Beam Interact with Mater Atoms.* 2016;377:94-98. doi:10.1016/j.nimb.2016.04.030
111. Jin SX, Guo LP, Yang Z, et al. Microstructural evolution in nickel alloy C-276 after Ar⁺ ion irradiation. *Nucl Instruments Methods Phys Res Sect B Beam Interact with Mater Atoms.* 2011;269(3):209-215. doi:10.1016/j.nimb.2010.12.004
112. Wu C, Lee BJ, Su X. Modified embedded-atom interatomic potential for Fe-Ni, Cr-Ni and Fe-Cr-Ni systems. *Calphad.* 2017;57:98-106. doi:10.1016/j.calphad.2017.03.007
113. Selim FA. Positron annihilation spectroscopy of defects in nuclear and irradiated materials- a review. *Mater Charact.* 2021;174:110952. doi:10.1016/j.matchar.2021.110952
114. Cacciamani G, De Keyser J, Ferro R, Klotz UE, Lacaze J, Wollants P. Critical evaluation of the Fe–Ni, Fe–Ti and Fe–Ni–Ti alloy systems. *Intermetallics.* 2006;14(10-11):1312-1325. doi:10.1016/j.intermet.2005.11.028
115. Cacciamani G, Dinsdale A, Palumbo M, Pasturel A. The Fe–Ni system: Thermodynamic modelling assisted by atomistic calculations. *Intermetallics.* 2010;18(6):1148-1162. doi:10.1016/j.intermet.2010.02.026
116. Sharkeev Y., Kozlov E. The long-range effect in ion implanted metallic materials: dislocation structures, properties, stresses, mechanisms. *Surf Coatings Technol.* 2002;158-159:219-224. doi:10.1016/S0257-8972(02)00212-8
117. Wyszowska E, Kurpaska L, Frelek-Kozak M, Jozwik I, Perkowski K, Jagielski J. Investigation of the mechanical properties of ODS steels at high temperatures using nanoindentation technique. *Nucl Instruments Methods Phys Res Sect B Beam Interact with Mater Atoms.* 2019;444:107-111. doi:10.1016/j.nimb.2019.02.021
118. Liu L, Zhang Y, Han J, et al. Nanoprecipitate-Strengthened High-Entropy Alloys. *Adv Sci.* 2021;8(23). doi:10.1002/advs.202100870
119. Li J, Yang X, Wang P, An Q. Healing stacking fault tetrahedron in NiFe solid solution alloys through grain boundary migration. *J Nucl Mater.* 2022;565:153738. doi:10.1016/j.jnucmat.2022.153738
120. Nordlund K, Gao F. Formation of stacking-fault tetrahedra in collision cascades. *Appl Phys Lett.* 1999;74(18):2720-2722. doi:10.1063/1.123948
121. Veliša G, Granberg F, Levo E, et al. Recent progress on understanding the temperature-dependent irradiation resistance ranking among NiFe, NiCoCr, and NiCoFeCr alloys: A review. *J Mater Res.* 2023;38(6):1510-1526. doi:10.1557/s43578-023-00922-0
122. Fan Z, Veliša G, Jin K, et al. Temperature-dependent defect accumulation and evolution in Ni-irradiated

- NiFe concentrated solid-solution alloy. *J Nucl Mater.* 2019;519:1-9. doi:10.1016/j.jnucmat.2019.03.031
123. Zhou Y, Veliša G, San S, et al. Role of chemical disorder on radiation-induced defect production and damage evolution in NiFeCoCr. *J Nucl Mater.* 2022;565:153689. doi:10.1016/j.jnucmat.2022.153689
124. Gilbert MR, Arakawa K, Bergstrom Z, et al. Perspectives on multiscale modelling and experiments to accelerate materials development for fusion. *J Nucl Mater.* 2021;554:153113. doi:10.1016/j.jnucmat.2021.153113
125. Veliša G, Jin K, Fan Z, et al. Multi-axial and multi-energy channeling study of disorder evolution in ion-irradiated nickel. *J Nucl Mater.* 2019;525:92-101. doi:10.1016/j.jnucmat.2019.07.025
126. Matijasevic M, Van Renterghem W, Almazouzi A. Characterization of irradiated single crystals of Fe and Fe–15Cr. *Acta Mater.* 2009;57(5):1577-1585. doi:10.1016/j.actamat.2008.11.042
127. Zhao S, Velisa G, Xue H, Bei H, Weber WJ, Zhang Y. Suppression of vacancy cluster growth in concentrated solid solution alloys. *Acta Mater.* 2017;125:231-237. doi:10.1016/j.actamat.2016.11.050
128. Osetsky Y, Barashev A V., Zhang Y. Sluggish, chemical bias and percolation phenomena in atomic transport by vacancy and interstitial diffusion in Ni Fe alloys. *Curr Opin Solid State Mater Sci.* 2021;25(6):100961. doi:10.1016/j.cossms.2021.100961
129. Ma K, Décamps B, Huang L, et al. Impact of micro-alloying in ion-irradiated nickel: From the inhibition of point-defect cluster diffusion by thermal segregation to the change of dislocation loop nature. *Acta Mater.* 2023;246:118656. doi:10.1016/j.actamat.2022.118656
130. Ma K, Décamps B, Fraczkiewicz A, Prima F, Loyer-Prost M. Drastic influence of micro-alloying on Frank loop nature in Ni and Ni-based model alloys. *Mater Res Lett.* 2020;8(5):201-207. doi:10.1080/21663831.2020.1741042
131. Goryaeva AM, Domain C, Chartier A, et al. Compact A15 Frank-Kasper nano-phases at the origin of dislocation loops in face-centred cubic metals. *Nat Commun.* 2023;14(1):3003. doi:10.1038/s41467-023-38729-6
132. Frank FC, Kasper JS. Complex alloy structures regarded as sphere packings. II. Analysis and classification of representative structures. *Acta Crystallogr.* 1959;12(7):483-499. doi:10.1107/S0365110X59001499
133. Mosseri R, Sadoc JF. Frustration and defects in non-periodic solids. *Comptes Rendus Phys.* 2014;15(1):90-99. doi:10.1016/j.crhy.2013.09.006
134. Su Z, Hsu CH, Gong Z, et al. Identification of a Frank–Kasper Z phase from shape amphiphile self-assembly. *Nat Chem.* 2019;11(10):899-905. doi:10.1038/s41557-019-0330-x
135. Chartier A, Marinica MC. Rearrangement of interstitial defects in alpha-Fe under extreme condition. *Acta Mater.* 2019;180:141-148. doi:10.1016/j.actamat.2019.09.007
136. Ma K, Guo L, Dartois A, et al. Decoding the interstitial/vacancy nature of dislocation loops with their morphological fingerprints in face-centered cubic structure. *Sci Adv.* 2025;11(15). doi:10.1126/sciadv.adq4070
137. Li Y, Lin Y, Cui D, Deng H, Ran G. Direct formation of novel Frank loop and stacking-fault tetrahedron complex. *Acta Mater.* 2023;257:119145. doi:10.1016/j.actamat.2023.119145
138. Mieszczynski C, Nowicki L, Skrobias K, Jozwik P, Jagielski J. Edge dislocations in Ni monocrystalline structure studied by McChasy 2.0 Monte Carlo code. *J Phys Conf Ser.* 2022;2326(1):012014. doi:10.1088/1742-6596/2326/1/012014
139. Xiu P, Bei H, Zhang Y, Wang L, Field KG. STEM Characterization of Dislocation Loops in Irradiated FCC Alloys. *J Nucl Mater.* 2021;544:152658. doi:10.1016/j.jnucmat.2020.152658
140. Cui LJ, Yang HL, Du YF, Shi QQ, Kano S, Abe H. TEM characterization of irradiation-induced dislocation loops and voids in ion-irradiated pure chromium. *J Nucl Mater.* 2022;569:153920. doi:10.1016/j.jnucmat.2022.153920
141. Xiu P, Osetsky YN, Jiang L, et al. Dislocation loop evolution and radiation hardening in nickel-based concentrated solid solution alloys. *J Nucl Mater.* 2020;538:152247. doi:10.1016/j.jnucmat.2020.152247
142. Bøgh E. Defect studies in crystals by means of channeling. *Can J Phys.* 1968;46(6):653-662. doi:10.1139/p68-081
143. Vantomme A. 50 years of ion channeling in materials science. *Nucl Instruments Methods Phys Res Sect B Beam Interact with Mater Atoms.* 2016;371:12-26. doi:10.1016/j.nimb.2015.11.035
144. Veliša G, Wendler E, Zhao S, et al. Delayed damage accumulation by athermal suppression of defect production in concentrated solid solution alloys. *Mater Res Lett.* 2018;6(2):136-141. doi:10.1080/21663831.2017.1410863
145. Ratajczak R, Mieszczynski C, Prucnal S, et al. Correlations between the structural transformations and concentration quenching effect for RE-implanted ZnO systems. *Appl Surf Sci.* 2020;521:146421. doi:10.1016/j.apsusc.2020.146421
146. Gärtner K, Uguzzoni A. Energy dependence of dechanneling due to dislocation loops. *Nucl Instruments Methods Phys Res Sect B Beam Interact with Mater Atoms.* 1992;67(1-4):189-193. doi:10.1016/0168-583X(92)95799-W

147. Gärtner K. Modified master equation approach of axial dechanneling in perfect compound crystals. *Nucl Instruments Methods Phys Res Sect B Beam Interact with Mater Atoms*. 2005;227(4):522-530. doi:10.1016/j.nimb.2004.10.087
148. Dygo A, Turos A. Surface studies of AIIIBV compound semiconductors by ion channeling. *Phys Rev B*. 1989;40(11):7704-7713. doi:10.1103/PhysRevB.40.7704
149. Zhang S, Nordlund K, Djurabekova F, Zhang Y, Velisa G, Wang TS. Simulation of Rutherford backscattering spectrometry from arbitrary atom structures. *Phys Rev E*. 2016;94(4):043319. doi:10.1103/PhysRevE.94.043319
150. Sequeira MC, Mattei JG, Vazquez H, et al. Unravelling the secrets of the resistance of GaN to strongly ionising radiation. *Commun Phys*. 2021;4(1):51. doi:10.1038/s42005-021-00550-2
151. Jin X, Crocombette JP, Djurabekova F, et al. New developments in the simulation of Rutherford backscattering spectrometry in channeling mode using arbitrary atom structures. *Model Simul Mater Sci Eng*. 2020;28(7):075005. doi:10.1088/1361-651X/ab81a9
152. Plimpton S. Fast Parallel Algorithms for Short-Range Molecular Dynamics. *J Comput Phys*. 1995;117(1):1-19. doi:10.1006/jcph.1995.1039
153. Nowicki L, Jagielski J, Mieszczyński C, Skrobas K, Jóźwik P, Dorosh O. McChasy2: New Monte Carlo RBS/C simulation code designed for use with large crystalline structures. *Nucl Instruments Methods Phys Res Sect B Beam Interact with Mater Atoms*. 2021;498:9-14. doi:10.1016/j.nimb.2021.04.004
154. Hirel P. Atomsk: A tool for manipulating and converting atomic data files. *Comput Phys Commun*. 2015;197:212-219. doi:10.1016/j.cpc.2015.07.012
155. Skrobas K, Stelmakh S, Gierlotka S, Palosz BF. IUCr, NanoPDF64: software package for theoretical calculation and quantitative real-space analysis of powder diffraction data of nanocrystals. *J Appl Crystallogr*. 2017;50(6):1821-1829. doi:10.1107/S1600576717013152
156. Stelmakh S, Skrobas K, Gierlotka S, Palosz B. Effect of the surface on the internal structure of CdSe crystal lattice based on molecular dynamics simulations. *J Nanoparticle Res*. 2017;19(5):170. doi:10.1007/s11051-017-3852-4
157. T.S. Srivatsan CYHLRAVMG. Beyond Nickel-Base Superalloys. Processing and Fabrication of Advanced Materials XIII. In: Stallion Press; 2005:563-574.
158. Foiles SM, Baskes MI, Daw MS. Embedded-atom-method functions for the fcc metals Cu, Ag, Au, Ni, Pd, Pt, and their alloys. *Phys Rev B*. 1986;33(12):7983-7991. doi:10.1103/PhysRevB.33.7983
159. Nabarro FRN. Fifty-year study of the Peierls-Nabarro stress. *Mater Sci Eng A*. 1997;234-236:67-76. doi:10.1016/S0921-5093(97)00184-6
160. Peierls R. The size of a dislocation. *Proc Phys Soc*. 1940;52(1):34-37. doi:10.1088/0959-5309/52/1/305
161. Xiang Y, Wei H, Ming P, E W. A generalized Peierls–Nabarro model for curved dislocations and core structures of dislocation loops in Al and Cu. *Acta Mater*. 2008;56(7):1447-1460. doi:10.1016/j.actamat.2007.11.033
162. Zhao S, Osetsky YN, Zhang Y. Atomic-scale dynamics of edge dislocations in Ni and concentrated solid solution NiFe alloys. *J Alloys Compd*. 2017;701:1003-1008. doi:10.1016/j.jallcom.2017.01.165
163. Erel C, Po G, Crosby T, Ghoniem N. Generation and interaction mechanisms of prismatic dislocation loops in FCC metals. *Comput Mater Sci*. 2017;140:32-46. doi:10.1016/j.commatsci.2017.07.043
164. H.C. Chen RDLCLRFHJLGLHLDXWXWQHDHLLYXTZ. Evolution of dislocation loops in He ion irradiated nickel under different temperature. *J Appl Phys*. 2016;120:125303.
165. Elizabeth H. Mann. An elastic theory of dislocations. *Proc R Soc London Ser A Math Phys Sci*. 1949;199(1058):376-394. doi:10.1098/rspa.1949.0144
166. Barrett JH. Monte Carlo Channeling Calculations. *Phys Rev B*. 1971;3(5):1527-1547. doi:10.1103/PhysRevB.3.1527
167. B. T. M. Willis, A. W. Pryor. *Thermal Vibrations in Crystallography: Crystals -- Thermal Properties*. Cambridge University Press; 1975.
168. Levo E, Granberg F, Nordlund K, Djurabekova F. Temperature effect on irradiation damage in equiatomic multi-component alloys. *Comput Mater Sci*. 2021;197:110571. doi:10.1016/j.commatsci.2021.110571
169. Shi S, He MR, Jin K, Bei H, Robertson IM. Evolution of ion damage at 773K in Ni- containing concentrated solid-solution alloys. *J Nucl Mater*. 2018;501:132-142. doi:10.1016/j.jnucmat.2018.01.015
170. Mieszczyński C, Jozwik P, Skrobas K, et al. Combining MD-LAMMPS and MC-McChasy2 codes for dislocation simulations of Ni single crystal structure. *Nucl Instruments Methods Phys Res Sect B Beam Interact with Mater Atoms*. 2023;540:38-44. doi:10.1016/j.nimb.2023.04.010
171. M. Gupta, T.S. Srivatsan, C.Y.H. Lim RAV (Eds. . Beyond Nickel-Base Superalloys. *Process Fabr Adv Mater XIII*,. Published online 2005:563-574.
172. Werner Z, Barlak M, Dłużewski P, et al. Crystallographic changes in electron pulse annealing of Ti-implanted GaP. *Radiat Eff Defects Solids*. 2020;175(7-8):719-729. doi:10.1080/10420150.2020.1756814
173. Werner Z, Barlak M, Ratajczak R, et al. The recovery effects of electron beam pulse treatment in Sn

- implanted Ge. *Radiat Eff Defects Solids*. 2022;177(9-10):1088-1102. doi:10.1080/10420150.2022.2113076
174. Teryaev DA. The effect of crater creation on the surface of steel targets under irradiated of high-current pulsed electron beams. *J Phys Conf Ser*. 2020;1713(1):012046. doi:10.1088/1742-6596/1713/1/012046
175. Guan Y, Zhou W, Li Z, Zheng H. Boiling effect in crater development on magnesium surface induced by laser melting. *Surf Coatings Technol*. 2014;252:168-172. doi:10.1016/j.surfcoat.2014.05.002
176. Khidirov I, Rakhmanov SD, Makhmudov SA. Root-Mean-Square Amplitude of Zero-Point Vibrations in a Crystal. *Russ Phys J*. 2021;64(7):1225-1231. doi:10.1007/s11182-021-02448-6
177. Alves E, Lorenz K, Catarino N, et al. An insider view of the Portuguese ion beam laboratory. *Eur Phys J Plus*. 2021;136(6):684. doi:10.1140/epjp/s13360-021-01629-z
178. Wright R. *Structural Alloys for HTGR and VHTR Systems*, NRC HTGR.(2019).
179. Skrzypek E, Muszyński D, Skrzypek M, et al. Pre-Conceptual Design of the Research High-Temperature Gas-Cooled Reactor TeResa for Non-Electrical Applications. *Energies*. 2022;15(6):2084. doi:10.3390/en15062084
180. Iwamoto Y, Meigo S, Ichiro, Hashimoto S. Estimation of reliable displacements-per-atom based on athermal-recombination-corrected model in radiation environments at nuclear fission, fusion, and accelerator facilities. *J Nucl Mater*. 2020;538:152261. doi:10.1016/j.jnucmat.2020.152261
181. Hoover WG. Canonical dynamics: Equilibrium phase-space distributions. *Phys Rev A*. 1985;31(3):1695-1697. doi:10.1103/PhysRevA.31.1695
182. Jóźwik P, Caçador A, Lorenz K, Ratajczak R, Mieszczyński C. Monte Carlo simulations of ion channeling in the presence of dislocation loops: New development in the McChasy code. *Nucl Instruments Methods Phys Res Sect B Beam Interact with Mater Atoms*. 2023;538:198-204. doi:10.1016/j.nimb.2023.03.002
183. Jin M, Gao Y, Zhang Y, Jiang C, Gan J. Dissociated prismatic loop punching by bubble growth in FCC metals. *Sci Rep*. 2021;11(1):12839. doi:10.1038/s41598-021-92219-7
184. Wei Y, Gao N, Shen Z, Chen C, Xie Z, Guo L. Interactions between hydrogen bubbles and prismatic interstitial dislocation loops in BCC iron. *Comput Mater Sci*. 2020;180:109724. doi:10.1016/j.commatsci.2020.109724
185. Ono K, Sakamoto R, Muroga T, Yoshida N. Dynamical process of defects clustering in nickel under low energy hydrogen ion irradiation. *J Nucl Mater*. 1996;233-237:1040-1044. doi:10.1016/S0022-3115(96)00117-1
186. Chen HC, Lui RD, Ren CL, et al. Evolution of dislocation loops in He ion irradiated nickel under different temperature. *J Appl Phys*. 2016;120(12). doi:10.1063/1.4963344
187. Griffiths M, Boothby R. Radiation Effects in Nickel-Based Alloys. In: *Comprehensive Nuclear Materials*. Elsevier; 2020:334-371. doi:10.1016/B978-0-12-803581-8.11705-9
188. Sprouster DJ, Sun C, Zhang Y, Chodankar SN, Gan J, Ecker LE. Irradiation-Dependent Helium Gas Bubble Superlattice in Tungsten. *Sci Rep*. 2019;9(1):2277. doi:10.1038/s41598-019-39053-0
189. Budylkin NI, Mironova EG, Chernov VM, Krasnoselov VA, Porollo SI, Garner FA. Neutron-induced swelling and embrittlement of pure iron and pure nickel irradiated in the BN-350 and BOR-60 fast reactors. *J Nucl Mater*. 2008;375(3):359-364. doi:10.1016/j.jnucmat.2008.01.015
190. Golubov S., Singh B., Trinkaus H. Defect accumulation in fcc and bcc metals and alloys under cascade damage conditions – Towards a generalisation of the production bias model. *J Nucl Mater*. 2000;276(1-3):78-89. doi:10.1016/S0022-3115(99)00171-3
191. Singh BN, Zinkle SJ. Defect accumulation in pure fcc metals in the transient regime: a review. *J Nucl Mater*. 1993;206(2-3):212-229. doi:10.1016/0022-3115(93)90125-I
192. Tippelt B, Breitschneider J, Hähner P. The Dislocation Microstructure of Cyclically Deformed Nickel Single Crystals at Different Temperatures. *Phys status solidi*. 1997;163(1):11-26. doi:10.1002/1521-396X(199709)163:1<11::AID-PSSA11>3.0.CO;2-X
193. Breidi A, Dudarev SL. Dislocation dynamics simulation of thermal annealing of a dislocation loop microstructure. *J Nucl Mater*. 2022;562:153552. doi:10.1016/j.jnucmat.2022.153552
194. Han L, Maccari F, Souza Filho IR, et al. A mechanically strong and ductile soft magnet with extremely low coercivity. *Nature*. 2022;608(7922):310-316. doi:10.1038/s41586-022-04935-3

Lists of figures

Figure 1. Structure degradation during irradiation of Ni and Ni _x Fe _{1-x} single crystal, radiation-induced defects.	18
Figure 2. Operating temperatures and displacement damage dose regimes for structural materials in current (generation II) and proposed future (Generation IV) fission and fusion energy systems ¹⁴	21
Figure 3. Schematic representation of several irradiation induced-defects (vacancy, interstitial, dislocation loop, precipitate, void).	23
Figure 4. The effect of bulk nickel concentration on swelling resulting from irradiation with different particles: neutrons, nickel ions and protons ²³	26
Figure 5. HRTEM image of bubbles in Ni bombarded samples with the fluences of $1 \times 10^{16} \text{ cm}^{-2}$ at temperature $\sim 800 \text{ K}$ with 380 keV Ar ⁺ ions.	26
Figure 6. Experimentally obtained “metastable” phase diagram of Ni–Fe alloys taken from ⁴³ a). Face-Centered Cubic (fcc) unit cell b).	33
Figure 7. Diagram of an ion implanter without mass separation (left) and with mass separation (right).	46
Figure 8. Flowchart of a typical RBS experiment.	47
Figure 9. A schematic representation of nanoindentation experiment and generated load-displacement curve	50
Figure 10. Damage profile of A) Ni and B) Ni _{0.62} Fe _{0.38} and C) Ni _{0.38} Fe _{0.62} irradiated with 1.5 MeV of Ni +	67
Figure 11. Ion channeling spectra of A) Ni, B) Ni _{0.62} Fe _{0.38} , C) Ni _{0.38} Fe _{0.62} single crystals irradiated with the fluences from 4×10^{13} to $2 \times 10^{15} \text{ ions/cm}^2$	69
Figure 12. Recorded ion channeling spectra of Ni, Ni _{0.62} Fe _{0.38} and Ni _{0.38} Fe _{0.62}	71
Figure 13. Nanoindentation hardness of the non-irradiated fcc Ni and Ni _x Fe _{1-x} single crystal alloys as a function of Fe content.	73
Figure 14. A) Nanoindentation hardness of fcc Ni, Ni _{0.62} Fe _{0.38} , and Ni _{0.38} Fe _{0.62} single crystal alloys as a function of irradiation fluence.	75
Figure 15. Damage distribution profiles obtained from the MC simulations performed for RBS/C experimentally obtained spectra.	76
Figure 16. Cross-sectional TEM images of the Ni, Ni _{0.62} Fe _{0.38} , and Ni _{0.38} Fe _{0.62} irradiated with various fluences.	78
Figure 17. TEM images of A) Ni, Ni _{0.62} Fe _{0.38} , and Ni _{0.38} Fe _{0.62} irradiated with fluence of 4×10^{13} and $4 \times 10^{15} \text{ ions/cm}^2$	80
Figure 18. Average defect size calculated based on the TEM images, B) defect densities for the Ni, Ni _{0.62} Fe _{0.38} , and Ni _{0.38} Fe _{0.62}	81
Figure 19. Damage profiles of (A) Ni and (B) Ni _{0.38} Fe _{0.62} irradiated with 1.5 MeV of Ni ⁺ at fluences of 4×10^{13} , 2×10^{14} , 5×10^{14} , 1×10^{15} , 2×10^{15} , and $4 \times 10^{15} \text{ ions/cm}^2$	88
Figure 20. RBS/C spectra of Ni and Ni _x Fe _{1-x} single crystal samples irradiated with 1,5 MeV of Ni ⁺ to the fluences of A) 4×10^{13} , B) 1×10^{15} , C) 1×10^{15} and D) $2 \times 10^{15} \text{ ions/cm}^2$	92
Figure 21. RBS/C spectra of A) Ni, B) Ni _{0.77} Fe _{0.23} , C) Ni _{0.62} Fe _{0.38} , D) Ni _{0.38} Fe _{0.62} single crystals.	93
Figure 22. Damage kinetics for all investigated materials.	94
Figure 23. A) Nanoindentation hardness of pristine fcc Ni, Ni _{0.88} Fe _{0.12} , Ni _{0.77} Fe _{0.23} , Ni _{0.62} Fe _{0.38} and Ni _{0.38} Fe _{0.62} single crystal alloys as a function of contact depth.	97
Figure 24. A) The potential energy per atom with respect to the random case vs the number of swap attempts normalized by the total number of atoms for three different Ni _x Fe _{1-x} binary alloys.	98
Figure 25. A) Cross-sectional TEM images of the Ni, Ni _{0.77} Fe _{0.23} , Ni _{0.62} Fe _{0.38} and Ni _{0.38} Fe _{0.62} irradiated with a fluence of $2 \times 10^{14} \text{ ions/cm}^2$ compared with SRIM calculations.	100
Figure 26. A) Cross-sectional TEM images of the Ni, Ni _{0.77} Fe _{0.23} , Ni _{0.62} Fe _{0.38} and Ni _{0.38} Fe _{0.62} irradiated with a fluence of $4 \times 10^{15} \text{ ions/cm}^2$ compared with SRIM calculations.	101
Figure 27. A) Defect sizes based on the TEM images calculated at the fluence of $4 \times 10^{13} \text{ ions/cm}^2$ and $4 \times 10^{15} \text{ ions/cm}^2$ and B) Average defect densities for the Ni, Ni _{0.77} Fe _{0.23} , Ni _{0.62} Fe _{0.38} and Ni _{0.38} Fe _{0.62}	103
Figure 28. Percentage of defect size obtained for A) low $4 \times 10^{13} \text{ ions/cm}^2$ and B) high $4 \times 10^{15} \text{ ions/cm}^2$ fluence.	104
Figure 29. Damage profiles of Ni, Ni _{0.88} Fe _{0.12} , and Ni _{0.77} Fe _{0.23} irradiated with 1.5 MeV of Ni ⁺ at fluences of a) 4×10^{13} , b) 2×10^{14} , and c) $2 \times 10^{15} \text{ cm}^{-2}$	111

Figure 30. Snapshots of the selected frames of MD simulations for dislocation networks and defect clusters in Ni and Ni _x Fe _{1-x} , at the doses of ~0.1 and 0.5 dpa..	116
Figure 31. Damage kinetics calculated for Ni, Ni _{0.88} Fe _{0.12} , and Ni _{0.77} Fe _{0.23} .	117
Figure 32. Bright field TEM images of a) Ni, b) Ni _{0.88} Fe _{0.12} and c) Ni _{0.77} Fe _{0.23} irradiated to the fluence of 4×10^{13} cm ⁻² and c) Ni, d) Ni _{0.88} Fe _{0.12} , f) Ni _{0.77} Fe _{0.23} irradiated to the fluence of 2×10^{14} cm ⁻² .	119
Figure 33. RBS/C spectra of a) Ni, b) Ni _{0.88} Fe _{0.12} , and c) Ni _{0.77} Fe _{0.23} single crystals irradiated with the fluences from 4×10^{13} to 4×10^{15} cm ⁻² .	122
Figure 34. The depth profiles of randomly displaced atoms in a) Ni, b) Ni _{0.88} Fe _{0.12} , and in b) Ni _{0.77} Fe _{0.23} as a function of ion dose as indicated in the corresponding legends.	123
Figure 35. Damage distribution profiles for a) Ni, b) Ni _{0.88} Fe _{0.12} , and c) Ni _{0.77} Fe _{0.23} obtained from the MC simulations performed for RBS/C experimentally obtained spectra.	124
Figure 36. BF TEM two-beam condition images near the [011] zone axis of pure Ni sample at a fluence of 4×10^{13} and 2×10^{14} cm ⁻² using different g vector.	126
Figure 37. BF TEM two-beam condition images near the [011] zone axis of Ni _{0.88} Fe _{0.12} sample at a fluence of 4×10^{13} and 2×10^{14} cm ⁻² using different g vector.	127
Figure 38. BF TEM two-beam condition images near the [011] zone axis of Ni _{0.77} Fe _{0.23} sample at a fluence of 4×10^{13} and 2×10^{14} cm ⁻² using different g vector.	128
Figure 39. Dislocation density as a function of the dpa for (a) Frank loops and (b) Stair-rod dislocations	131
Figure 40. An example of how to develop an extended defect distribution along {111} plane	141
Figure 41. Comparison of row fluctuations in Ni obtained for (a) single MD frame and (b) averaged atomic positions after 250 frames for pristine and close-to-edge dislocation.	142
Figure 42. Axial RBS/C spectra simulated using two differently created structures.	144
Figure 43. Dislocation loops of the 3 nm size are selected randomly from the {111} and {-1-11} planes (a).	145
Figure 44. (a) MD-created dislocation loop, (b) depth distributions of dislocation loops used for the simulations performed for RBS/C experimental spectra shown in (c) together with the fits made by the McChasy2 code.	146
Figure 45. SEM images captured before (a) and after (b) EG and (c) EP treatments (sim.).	153
Figure 46. TEM images of the Ni crystals bombarded with Ar ions to fluences of 7×10^{14} , 7×10^{15} , and 1×10^{16} cm ⁻² , denoted by Ni 7E14, Ni 7E15, and Ni 1E16.	157
Figure 47. (a-b) Bright-field images of bubbles in Ni bombarded samples with the fluences of 7×10^{15} cm ⁻² and 1×10^{16} cm ⁻² , denoted by Ni 7E15 and Ni 1E16 respectively.	159
Figure 48. Hardness of Ni samples irradiated up to the fluence of 1×10^{16} cm ⁻² .	160
Figure 49. (a) Ni RBS/C spectra recorded along $\langle 001 \rangle$ direction (squares) with fits obtained using McChasy-1 simulations (solid lines of corresponding colors).	161
Figure 50. Dislocation loops along {111} plane developed using MD-LAMMPS after relaxation.	163
Figure 51. (a) Example of an MD/McChasy-created large structure. Surrounding atoms were removed from the structure to highlight defects inside the virtual sample.	164

Lists of tables

Table 1. Maximum backscattering yield (collected at 400 nm depth) of irradiated Ni, Ni _{0.62} Fe _{0.38} , and Ni _{0.38} Fe _{0.62} at fluences of 4×10^{13} , 2×10^{14} , 1×10^{15} and 2×10^{15} ions/cm ² .	72
Table 2. Cross-sections for defect formation extracted from the MSDA model	95
Table 3 Cross-sections for defect formation derived from the Modified Stopping and Range of Ions in Matter (MSDA) model.	118
Table 4. Quantitative comparison of stacking fault tetrahedra and dislocation loops based on TEM experiments and MD simulations.	121
Table 5. Dislocation density and defect size of Ni, Ni _{0.88} Fe _{0.12} , and Ni _{0.77} Fe _{0.23} at 0.1 and 0.5 dpa. Comparison between MD, in bold, and experimental, in italic, data.	129
Table 6. Cross-sections for defect formation extracted from the MSDA model.	162

Acknowledgments

This thesis is the result of an amazing journey that started for me almost nine years ago, when I joined the National Centre for Nuclear Research (NCBJ). This is the appropriate place to thank all the people who kept me on the right track and helped me bring this work to fruition.

First, I would like to express my gratitude to my supervisor **Lukasz Kurpaska** for giving me the opportunity to conduct my PhD research and to develop as a researcher in his group. Thank you for your trust in my skills and for all the support provided to me throughout all the years of my research. I appreciate your patience, understanding, motivation and constant readiness to help. I am especially grateful for the opportunity to participate in numerous scientific conferences, workshops and international projects, which undoubtedly broadened my professional experience. You are not only a great supervisor but also a reliable friend. I would also like to express my immense thanks to my second supervisor **Cyprian Mieszczyński** for great cooperation, mutual motivation and for being a great example of a reliable and honest scientist, good parent and a true friend. I would like to thank **professor Jacek Jagielski** for involving me in the topic of Nickel alloys, as well as for numerous consultations, help in analyzing the results and involvement in interesting research projects, thanks to which I could develop my knowledge and meet outstanding scientists.

I would like to acknowledge all the scientists who supported me in conducting the experiments and simulations, as well as those who provided valuable advices and constructive criticism throughout my PhD endeavors: Iwona Jóźwik, Iwona Cieślik, Witold Chromiński, Amin Esfandiarpour, Ryszard Didusko, Anna Kosińska, Alexander Azarov, Aneta Ustrzycka, Sri Tapaswi Nori, Marcin Chmielewski, Amil Aligayev, Damian Kalita, Przemysław Jóźwik, Renata Ratajczak, Kazimierz Skrobias, Armand Budzianowski, Marek Barlak, Katarzyna Nowakowska-Langier. I would like to especially thank **Javier Dominguez** for sharing his optimism and passion for science with me – I admire your extraordinary diligence and appreciate your continuous willingness to help. I would like to thank everyone who contributed directly or indirectly to the creation of my doctoral thesis, in particular to all the employees of the Materials Research Laboratory, Nomaten Centre of Excellence and the Department of Materials Physics at the NCBJ.

Last, but not the least, I would like to thank my parents and parents-in-law **Krystyna Krzyżak, Lesław Krzyżak** and **Krystyna Wyszowska, Stanisław Wyszowski** for their support, understanding, love, encouragement, and kindness. Most importantly, I would like to thank my beloved husband **Przemysław Wyszowski**, who inspired me with his passion for learning and exploring the world. Your patience, empathy, support and belief in me have been extremely helpful and motivating – all this led me to where I am now. Finally, I would like to thank my beloved daughter **Jagoda Wyszowska** for her incredible wisdom, maturity, patience and understanding, although being only 5 years old now. Your presence and love give me wings every day and make me able to fly to the right places.

Scientific achievements

Scientometric data

Lp.	Data type	Points
1.	Hirsch index	11
2.	Citations	299
3.	Number of publications included in the doctoral dissertation	5
5.	Number of publications unrelated to the topic of the doctoral dissertation	25

Lists of scientific publications constituting the subject of the doctoral dissertation:

1. **E. Wyszowska**, C. Mieszczyński, Ł. Kurpaska, A. Azarov, I. Jóźwik, A. Kosińska, W. Chromiński, R. Diduszek, W. Huo, I. Cieřlik, J. Jagielski, *Tuning heterogeneous ion-radiation damage by composition in Ni_xFe_{1-x} binary single crystals*, **Nanoscale**, **15** (2023) 4870-4881, (IF:8.3), Ministry points: **140**, <https://doi.org/10.1039/D2NR06178C>
2. **E. Wyszowska**, C. Mieszczyński, Ł. Kurpaska, A. Azarov, W. Chromiński, I. Jóźwik, A. Esfandiarpour, A. Kosińska, D. Kalita, R. Diduszek, J. Jagielski, S. T. Nori, M. Alava, *The Fe addition as an effective treatment of improving the radiation resistance properties in fcc Ni_xFe_{1-x} single-crystal alloys*, **J. Nucl. Mater.** 584 (2023) 154565 (IF:3.55), Ministry points: **100**, <https://doi.org/10.1016/j.jnucmat.2023.154565>
3. **E. Wyszowska**, C. Mieszczyński, A. Aligayev, A. Azarov, W. Chromiński, D. Kalita, A. Kosińska, F. J. Dominguez-Gutierrez, Ł. Kurpaska, I. Jóźwik, J. Jagielski, *Defect Formation in fcc Ni and low Fe content Ni_xFe_{1-x} Single Crystals Under Self-Ion Irradiation*, **Nanoscale (2025) Ref.: NR-ART-01-2025-000117 Accepted for publication**, (IF:5.8), Ministry points: **140**
4. C. Mieszczyński, P. Jóźwik, K. Skrobas, K. Stefańska-Skrobas, R. Ratajczak, J. Jagielski, F. Garrido, **E. Wyszowska**, A. Azarov, K. Lorenz, E. Alves, *Combining MD-LAMMPS and MC-McChasy 2.0 codes for dislocation simulations of Ni-based alloys*, **Nucl. Instr. Meth. B**, 540 (2023) 38-44, (IF:1.377), Ministry points: **70**, <https://doi.org/10.1016/j.nimb.2023.04.010>
5. C. Mieszczyński, **E. Wyszowska**, P. Jóźwik, K. Skrobas, K. Stefańska-Skrobas, M. Barlak, R. Ratajczak, K. Lorenz, *Damage Kinetics in High-Temperature Irradiated Ni Crystals*, **Appl. Surf. Sci.**, 676 (2024) 160991, (IF:6.3), Ministry points: **140**, DOI: /10.1016/j.apsusc.2024.160991

Scientific publications not included in the scope of the doctoral dissertation:

6. **E. Wyszowska**, M. Leśniak, Ł. Kurpaska, R. Prokopowicz, I. Jozwik, M. Sitarz, J. Jagielski, *Functional properties of poly(tetrafluoroethylene) (PTFE) gasket working in nuclear reactor conditions*, **J. Mol. Struct.**, 1157 (2018) 306-311, (IF: 3.4) Ministry points: **70**, <https://doi.org/10.1016/j.molstruc.2017.12.070>
7. **E. Wyszowska**, Ł. Kurpaska, M. Frelek-Kozak, I. Jozwik, K. Perkowski, J. Jagielski, *„Investigation of the mechanical properties of ODS steels at high temperatures using nanoindentation technique”*, **Nucl. Instr. Meth. B.**, 444 (2019) 107-111, (IF:1.377) Ministry points: **70**, <https://doi.org/10.1016/j.nimb.2019.02.021>
8. A. Zaborowska, Ł. Kurpaska, Mj. Zieliński, Q. Xu, **E. Wyszowska**, J. O’Connell, J.H. Neethling, F. DiFonzo, M. Frelek-Kozak, S. Papanikolaou, R. Diduszek, J. Jagielski *High-temperature behavior of amorphous alumina coatings: Insights from in-situ nanoindentation and X-ray diffraction studies*, **Ceram. Int.**, 51 (10) (2025) 12918-12931, (IF: 5.1) Ministry points: **100**, <https://doi.org/10.1016/j.ceramint.2025.01.134>

9. R. Babilas, J. Bicz, A. Radoń, M. Kądziołka-Gaweł, D. Łukowiec, K. Matus, **E. Wyszowska**, Ł. Kurpaska, D. Rudomilova, K. Młynarek-Żak, *Structure, corrosion resistance and nanomechanical properties of CoCrFeNiX (X=Nb,Mo,B,Si) high entropy alloys*, ***Electrochim. Acta*** (2025) 145933, (IF: 5.5), Ministry points: 100, <https://doi.org/10.1016/j.electacta.2025.145933>
10. J. Lorkiewicz, M. Barlak, **E. Wyszowska**, S. Okrasa, A. Kosińska, M. Wilczopolska, P. Marchlewski, K. Nowakowska-Langier, *The influence of initial lead implantation into niobium substrate on the adhesion of Pb layers obtained in cathodic arc and by magnetron sputtering*, ***J. Adhesion*** (2025) 1-26, (IF: 2.9), Ministry points: 100, <https://doi.org/10.1080/00218464.2025.2478991>
11. R. Psiuk, J. Chrzanowska-Giżyńska, P. Denis, **E. Wyszowska**, M. Wiśniewska, M. Lipińska, E. Wojtiuk, Ł. Kurpaska, J. Smolik, T. Mościcki, *Microstructural and properties investigations of tantalum-doped tungsten diboride ceramic coatings via HiPIMS and RF magnetron sputtering*, ***Arch. Civ. Mech. Eng.***, 24 (2024) 239, (IF: 4.4), Ministry points: 140 <https://doi.org/10.1007/s43452-024-01050-0>
12. L. Kurpaska, M. Clozel, J. H. O'Connell, I. Jóźwik, **E. Wyszowska**, W. Y. Huo, W. Chrominski, F. Fang, J. Jagielski, J. H. Neethling, *Nanoindentation responses of Fe-Cr alloys from room temperature to 600°C*, ***Mater. Sci. Eng. A.***, 902 (2024) 146590 (IF:6.4) Ministry points: 140, <https://doi.org/10.1016/j.msea.2024.146590>
13. Agata Strojny-Nędza; Katarzyna Pietrzak; Iwona Jóźwik; Bartosz Bucholc; **Edyta Wyszowska**; Łukasz Kurpaska; Agnieszka Grabias; Agnieszka Malinowska; Marcin Chmielewski, *Effect of Nitrogen Atmosphere Annealing of Alloyed Powders on the Microstructure and Properties of ODS Ferritic Steels*, ***Materials***, 17 (2024) 1743, (IF:3.4) Ministry points: 140, <https://doi.org/10.3390/ma17081743>
14. A. Olejarz, W. Huo, D. Kalita, M.M. Zieliński, **E. Wyszowska**, W. Chromiński, R. Diduszko, M. Chmielewski, I. Jóźwik, Ł. Kurpaska, *Cr-rich structure evolution and enhanced mechanical properties of CoCrFeNi high entropy alloys by mechanical alloying*, ***J. Mater. Res. Technol.***, 30 (2024) 1490, (IF:5.039) Ministry points: 100, <https://doi.org/10.1016/j.jmrt.2024.03.116>
15. F. J. Dominguez-Gutierrez, M. Landeiro Dos Reis, **E. Wyszowska**, W. Y. Huo, A. Olejarz, D. Kalita, I. Jozwik, L. Kurpaska, S. Papanikolaou, M. J. Alava, and K. Muszka, *Atomistic-Level Analysis of Nanoindentation-Induced Plasticity in Arc-Melted NiFeCrCo Alloys: The role of stacking faults*, ***J. Appl. Phys.***, 135 (2024) 185101, (IF:3.2) Ministry points: 100, <https://doi.org/10.1063/5.0200717>
16. R. Babilas, K. Młynarek-Żak, A. Radoń, W. Łoński, M. Kądziołka-Gaweł, T. Warski, D. Rudomilova, **E. Wyszowska**, Ł. Kurpaska, *Effect of Cu and Cr addition on the structure, anticorrosion and nanomechanical properties of new Al-Ni-Fe-(Cr,Cu) alloys*, ***J. Alloys Compd.***, 960 (2023) 170839 (IF:6.37), Ministry points: 140, <https://doi.org/10.1016/j.jallcom.2023.170839>
17. A. Zaborowska, Ł. Kurpaska, **E. Wyszowska**, A. Azarov, M. Turek, A. Kosińska, M. Frelek-Kozak, J. Jagielski, *High versus low energy ion irradiation impact on functional properties of PLD-grown alumina coatings*, ***Nucl. Instr. Meth. B***, 540 (2023) 24-29, (IF:1.377), Ministry points: 70, <https://doi.org/10.1016/j.nimb.2023.03.027>
18. A. Olejarz, W.Y. Huo, M. Zieliński, R. Diduszko, **E. Wyszowska**, A. Kosińska, D. Kalita, I. Jóźwik, M. Chmielewski, F. Fang, Ł. Kurpaska, *Microstructure and mechanical properties of mechanically-alloyed CoCrFeNi high-entropy alloys using low ball-to-powder ratio*, ***J. Alloys Compd.***, 938 (2023) 168196, (IF:6.37), Ministry points: 140, <https://doi.org/10.1016/j.jallcom.2022.168196>
19. Anna Kosińska, Jacek Jagielski, Dariusz M. Bieliński, Olga Urbanek, Magdalena Wilczopolska, Małgorzata Frelek-Kozak, Agata Zaborowska, **Edyta Wyszowska**, and Iwona Jóźwik, *Structural and chemical changes in He⁺ bombarded polymers and related performance properties*, ***J. Appl. Phys.***, 132 (2022) 074701, (IF:3.2), Ministry points: 100, <https://doi.org/10.1063/5.0099137>
20. Ustrzycka A., Skoczeń B., Nowak M., Kurpaska Ł., **Wyszowska E.**, Jagielski J. „Evolution of ductile damage in the ion-irradiated materials during nanoindentation”. ***J. Damage Mech.***, 29

- (2020) 1271-1305, (IF:5.029), Ministry points: 100, <https://doi.org/10.1177/1056789520906209>
21. A. Zaborowska, Ł. Kurpaska, E. Wyszowska, M. Clozel, J. Jagielski, M. Vanazzi, F. DiFonzo. „Influence of ion irradiation on the nanomechanical properties of thin alumina coatings deposited on 316L SS by PLD”. *Surf. Coat. Technol.*, 386 (2020) 125491, (IF:5.4), Ministry points: 100, <https://doi.org/10.1016/j.surfcoat.2020.125491>
 22. I. Cieřlik, M. Duchna, T. Płociński, E. Wyszowska, A. Azarov, M. Zieniuk. „Ion irradiation effect on the microstructure of Inconel 625 obtained with additive manufactured 3D printing and with conventional technique”. *Surf. Coat. Technol.* 396, (2020) 125952, (IF:5.4), Ministry points: 100, <https://doi.org/10.1016/j.surfcoat.2020.125952>
 23. M. Clozel, Ł. Kurpaska, I. Józwick, J. Jagielski, M. Turek, R. Diduszko, E. Wyszowska. „Nanomechanical properties of low-energy Fe-ion implanted Eurofer97 and pure Fe”. *Surf. Coat. Technol.*, 393, (2020) 125833, (IF:5.4), Ministry points: 100, <https://doi.org/10.1016/j.surfcoat.2020.125833>
 24. A. Kosińska, J. Jagielski, Ł. Kurpaska, E. Wyszowska, M. Clozel, J. Zagórski, B. Staszkieicz, K. Gniadek. „Functional characteristics of ion-irradiated elastomers used as insulation materials: comparison between mechanical and electrical properties”. *Nucl. Instr. Meth. B*, 473, (2020) 6-9, (IF:1.377), Ministry points: 70, <https://doi.org/10.1016/j.nimb.2020.04.007>
 25. L. Kurpaska M. Frelek-Kozak, M. Wilczopolska W. Bonicki, R. Diduszko, A. Zaborowska, E. Wyszowska, M. Clozel, A. Kosinska, I. Cieslik, M. Duchna, I. Jozwick, W. Chmurzynski, G. Olszewski, B. Zajac, J. Jagielski. *Structural and mechanical properties of different types of graphite used in nuclear applications. J. Mol. Struct.*, (1217, (2020) 128370, (IF: 3.841), Ministry points: 70, <https://doi.org/10.1016/j.molstruc.2020.128370>
 26. Marcin Chmielewski, Szymon Nosewicz, Edyta Wyszowska, Łukasz Kurpaska, Agata Strojny-Nędzia, Anna Piątkowska, Piotr Bazarnik, Katarzyna Pietrzak. „Analysis of the micromechanical properties of copper-silicon carbide composites using nanoindentation measurements”, *Ceram. Int.*, 45 (7) Part A (2019) 9164-9173, (IF:5.2), Ministry points: 100, <https://doi.org/10.1016/j.ceramint.2019.01.257>
 27. A. Kosinska, J. Jagielski, U. Ostaszewska, E. Wyszowska, M. Clozel, L. Kurpaska, M. Romaniec. „Functional properties of low energy ion-irradiated acrylonitrile-butadiene rubber”. *Nucl. Instr. Meth. B.*, 443 (2019) 15-18, (IF:1.377), Ministry points: 70, <https://doi.org/10.1016/j.nimb.2018.12.052>
 28. M. Frelek-Kozak, L. Kurpaska, E. Wyszowska, J. Jagielski, M. Chmielewski. „Evaluation of consolidation method on mechanical and structural properties of ODS RAF steel”, *Appl. Surf. Sci.*, 446 (2018) 215-221, (IF:6.7), Ministry points: 140, <https://doi.org/10.1016/j.apsusc.2018.01.163>
 29. M. Frelek-Kozak, L. Kurpaska, E. Wyszowska, J. Jagielski, W. Pawlak, I. Jozwick, M. Chmielewski, K. Perkowski, M. Lewandowska. „Influence of consolidation process on functional properties of steels”. *Surf. Coat. Technol.*, 355 (2018) 234-239, (IF:5.4), Ministry points: 100, <https://doi.org/10.1016/j.surfcoat.2018.02.049>
 30. L. Kurpaska, J. Jasinski, E. Wyszowska, K. Nowakowska-Langier, M. Sitarz. „Influence of Ar-ion implantation on the structural and mechanical properties of zirconia as studied by Raman spectroscopy and nanoindentation techniques”. *Spectrochim. Acta A Mol. Biomol. Spectrosc.*, 195 (2018) 184-190, (IF:4.4), Ministry points: 140, <https://doi.org/10.1016/j.saa.2018.01.074>

Conference presentations

1. Nuclear Materials Conference - NuMat2024, 14-17.10.2024, Singapore Expo, Singapore
 - ✓ **Oral presentation:** Irradiation-induced hardening effects of fcc low-Fe Ni_xFe_{1-x} single crystals by experimental and simulated nanoindentation, E. Wyszowska, A. Aligayev, A. Azarov, W.

- Chromiński, F. J. Dominguez-Gutierrez, Ł. Kurpaska, A. Kosińska, C. Mieszczyński, K. Skrobias, J. Jagielski
- ✓ **Poster:** *Modeling of structural and mechanical high-temperature irradiation effects of equiatomic nickel-based alloys*, C. Mieszczyński, E. Wyszowska, A. Aligayev, F. J. Dominguez-Gutierrez, P. Jozwik, K. Skrobias, K. Stefanska-Skrobias, R. Ratajczak, K. Lorenz
2. **General Conference of the Condensed Matter Division of the European Physical Society (CMD31)**, 02-06.09.2024, Braga, Portugal
 - ✓ **Oral presentation:** *Point defects evolution in fcc Ni and Ni_xFe_{1-x} single crystals with low Fe content*, E. Wyszowska, C. Mieszczyński, A. Aligayev, F. J. Dominguez-Gutierrez, A. Azarov, W. Chromiński, Ł. Kurpaska, A. Kosińska, D. Kalita, I. Jóźwik, J. Jagielski
 3. **6th International Conference on Applied Surface Science (ICASS)**, 17-20 June 2024, Wuzhen, Zhejiang, China
 - ✓ **Poster 1:** *Assessment of the radiation defects evolution induced by ion beam surface modification of the of fcc Ni, Ni_{0.88}Fe_{0.12}, Ni_{0.77}Fe_{0.23} single crystals*, E. Wyszowska, C. Mieszczyński, W. Chromiński, Ł. Kurpaska, A. Azarov, I. Jóźwik, A. Kosińska, Damian Kalita, J. Jagielski
 - ✓ **Poster 2:** *Damage Kinetics in High-Temperature Irradiated Ni Crystals*, C. Mieszczyński, E. Wyszowska, P. Jozwik, K. Skrobias, K. Stefanska-Skrobias, M. Barlak, R. Ratajczak, A. Kosinska, W. Chrominski, K. Lorenz
 4. **Materials Today Conference 2023**, 2-5.08.2023, Singapore Expo, Singapore
 - ✓ **Poster:** *Unveiling mechanism of hardening in fcc-type Ni_xFe_{1-x} single crystals developed due to irradiation and high temperature*, E. Wyszowska, A. Esfandiarpour, A. Budzianowski, Ł. Kurpaska, A. Azarov, W. Chromiński, I. Jóźwik, D. Kalita, C. Mieszczyński, J. Jagielski, M. Alava
 5. **European Materials Research Society (E-MRS) 2023 Fall Meeting**, 18-21.09.2023 Warsaw University of Technology, Warsaw, Poland
 - ✓ **Oral presentation (invited speaker):** *Unveiling mechanism of hardening in fcc-type Ni_xFe_{1-x} single crystals developed due to irradiation and high temperature*, E. Wyszowska, A. Esfandiarpour, A. Budzianowski, Ł. Kurpaska, A. Azarov, W. Chromiński, I. Jóźwik, D. Kalita, C. Mieszczyński, J. Jagielski, M. Alava
 6. **Nuclear Materials Conference (NuMat2022)**, 24-28.10.2022, Gent, Belgium
 - ✓ **Poster:** *The Fe addition as an effective treatment of improving the radiation resistance properties in fcc Ni_xFe_{1-x} single-crystal alloys*, E. Wyszowska, C. Mieszczyński, Ł. Kurpaska, W. Chromiński, A. Azarov, I. Jóźwik, A. Esfandiarpour, A. Kosińska, D. Kalita, R. Diduszko, J. Jagielski, S. Nori, M. Alava

Other conference presentations (not related to the doctoral dissertation)

7. **21st International Conference on Ion Beam Modification of Materials (IBMM 2018)**, 24-29.06.2018, San Antonio, Texas, USA
 - ✓ **Oral presentation:** *Investigation of the nano-mechanical properties of ODS steels at high temperature using nano-indentation technique*, E. Wyszowska, Ł. Kurpaska, M. Frelek-Kozak, I. Jozwik, K. Perkowski, J. Jagielski.
8. **HTR 2018 - International Conference on High Temperature Reactor Technology** 8-10.10.2018, Warsaw, Poland – participant
9. **8th ERMSAR conference (European Review Meeting on Severe Accident Research)**, 16-18.05.2017, Warsaw, Poland (participant, organizer)

10. **EuCARD 2 kick-off meeting- Collimator Materials Conference**, 9-10.12.2013, CERN, Geneva, Switzerland, participant, preparation of material (results) for presentation
11. **EIROForum Science-Business WAMAS Workshop on Advanced Materials and Surfaces**, 19-20.11.2013, CERN, Geneva, Switzerland, participant, preparation of material (results) for presentation

Distinctions

1. Winner of the Preludium21 competition in December 2022, (2022/45/N/ST5/02980).
2. E-MRS 2023 conference, 18-21.09.2023 - The best presentation award “2023 Fall Meeting” in recognition of the oral presentation entitled “Unveiling mechanism of hardening in fcc-type Ni_xFe_{1-x} single crystals developed due to irradiation and high temperature” in Symposium D “Nuclear materials under extreme conditions II”.
3. Team Award for the scientific and research achievements at NCBJ in 2023, for a series of works presenting “*Experimental confirmation of the possibility of increasing the radiation resistance of construction materials by appropriate selection of their composition, with particular emphasis on Ni-Fe alloys*”.

Curriculum Vitae

Education	
Dates	March 2012 – March 2015 (including 1 year of scientific leave for the Technical Student programme at CERN)
Title of qualification awarded	Master of Science (Level II full-time studies), Major: Metallurgy Thesis topic: <i>Research and development of advanced aluminium/graphite composites for thermal management applications</i> , (https://cds.cern.ch/record/1995245), Thesis supervisors: Ph.D. Eng. Ewa Olejnik, Alessandro Bertarelli, Thesis awarded with distinctions in contests: „ <i>Diamonds of AGH</i> ”
Dates	October 2008 – February 2012
Title of qualification awarded	Bachelor of Science (Level I full-time studies), Major: Metallurgy Thesis topic: <i>Feasibility study of industry production of a casting block made of modified cast iron</i> , Thesis supervisor: Prof. Edward Guzik
Name of organization providing education	AGH University of Science and Technology, Faculty of Foundry Engineering , Kraków, Poland
Employment	
Dates	November 2016 – onwards
Employer	National Centre for Nuclear Research, Warszawa (Otwock-Świerk) , Poland
Organizational unit	Materials Research Laboratory, Nomaten CoE
Position held	Research and Technical Specialist
Internships	
Dates	March 2013 – April 2014 (1 year 2 months)
Employer	CERN, European Organization for Nuclear Research , Geneva, Switzerland, Mechanical & Materials Engineering Group, Engineering Department
Position held	“Technical Student” - engineering internship programme
Dates	July 2012 – February 2013 (5 months)
Employer	Foundry Research Institute , Kraków, Poland
Position held	Project associate/ participant of the “Zamat” project
Dates	July 2011 – August 2011 (1 month)
Employer	Pratt & Whitney Rzeszów S.A. Rzeszów, Poland
Position held	Summer Internship